

PHOTOELECTRON IMAGING OF MOLECULAR AND CLUSTER ANIONS

by

Sean Eric Surber

Copyright © Sean Eric Surber 2005

A Dissertation Submitted to the Faculty of the

DEPARTMENT OF CHEMISTRY

In Partial Fulfillment of the Requirements

For the Degree of

DOCTOR OF PHILOSOPHY

In the College of Science

THE UNIVERSITY OF ARIZONA

2 0 0 5

UMI Number: 3161673

Copyright 2005 by
Surber, Sean Eric

All rights reserved.



UMI Microform 3161673

Copyright 2005 by ProQuest Information and Learning Company.
All rights reserved. This microform edition is protected against
unauthorized copying under Title 17, United States Code.

ProQuest Information and Learning Company
300 North Zeeb Road
P.O. Box 1346
Ann Arbor, MI 48106-1346

THE UNIVERSITY OF ARIZONA
GRADUATE COLLEGE

As members of the Dissertation Committee, we certify that we have read the dissertation prepared by Sean Eric Surber entitled Photoelectron Imaging of Molecular and Cluster Anions and recommend that it be accepted as fulfilling the dissertation requirement for the Degree of Doctor of Philosophy

Dr. Andrei Sanov

Date: March 09, 2005

Dr. Oliver Monti

Date: March 09, 2005

Dr. Lucy Ziurys

Date: March 09, 2005

Dr. Bonner Denton

Date: March 09, 2005

Dr. Dom McGrath

Date: March 09, 2005

Final approval and acceptance of this dissertation is contingent upon the candidate's submission of the final copies of the dissertation to the Graduate College.

I hereby certify that I have read this dissertation prepared under my direction and recommend that it be accepted as fulfilling the dissertation requirement.

Dissertation Director: Andrei Sanov

Date: March 09, 2005

STATEMENT BY AUTHOR

This dissertation has been submitted in partial fulfillment of requirements for an advanced degree at The University of Arizona and is deposited in the University Library to be made available to borrowers under rules of the Library.

Brief quotations from this dissertation are allowable without special permission, provided that accurate acknowledgment of source is made. Requests for permission for extended quotation from or reproduction of this manuscript in whole or in part may be granted by the copyright holder.

SIGNED: _____

Acknowledgements

This work could not have been completed if it wasn't for guidance and tutorage of Andrei Sanov. His patience but yet encouraging support allowed not only completion of this work but also to my development as a scientist. The hard work from the machine shop, electronic shop and the University of Arizona Instrument Facility should not be overlook, for many a times they brought drawing of instrument components and circuits to life.

The recent expansions to the Sanov group has brought encouragement but also friendship (Terefe, Luis and Kosyta). Richard Mabbs arrival was critical for obtaining time resolved data. His scientific experience catapulted us ahead.

The love of my family especially my sister, my brother and my parents is appreciated. Many thanks to those in the dojo for training with me: bringing balance and peace within the chaos. To all those in my life, thank you for everything, for without Love there would be no life at all.

TABLE OF CONTENTS

5

LIST OF FIGURES	9
LIST OF TABLES	18
ABSTRACT	19
1 INTRODUCTION.....	20
2 EXPERIMENTAL DETAILS	24
2.1 GENERAL OVERVIEW OF THE APPARATUS	24
2.2 ION SOURCE CHAMBER.....	27
2.2.1 Pulsed Valve	29
2.2.2 Electron Gun	29
2.2.3 Faraday Cup	33
2.3 TIME OF FLIGHT MASS ANALYZER.....	33
2.4 PHOTOELECTRON IMAGING ASSEMBLY	55
2.5 LASER SYSTEM	63
2.6 DATA ACQUISITION.....	64
2.7 TIME RESOLVED SETUP	71
2.8 DATA ANALYSIS.....	72
3 PHOTOELECTRON IMAGING OF ATOMIC ANIONS.....	76
3.1 INTRODUCTION	76
3.2 RESULTS AND DISCUSSION	76
3.2.1 Iodide	76
3.2.2 Oxide.....	84
3.2.3 Sulfide	88

3.3 SUMMARY	91
4 PHOTOELECTRON IMAGING OF MOLECULAR ANIONS	92
4.1 INTRODUCTION:	92
4.2 RESULTS AND DISCUSSION:.....	93
4.2.1 Results for S_2^-	93
4.2.2 Analysis of S_2^- using the adapted Cooper-Zare Treatment	96
4.2.3 SO^- and O_2^- Results and Analysis	101
4.2.4 Results CS_2^-	103
4.3 THE S&P MODEL OF MOLECULAR ANION PHOTODETACHMENT	111
4.3.1 The s & p Treatment of CS_2^- Photodetachment.....	111
4.3.2 The s & p Treatment of S_2^- Photodetachment	115
4.4 SUMMARY:.....	118
5 NONEXISTENT ELECTRON AFFINITY OF CARBONYL SULFIDE AND ITS STABILIZATION BY GAS PHASE HYDRATION.....	120
5.1 INTRODUCTION	120
5.2 EXPERIMENTAL AND COMPUTATIONAL METHODS	122
5.2.1 Experimental Setup	122
5.2.2 Computational Details	123
5.3 RESULTS AND DISCUSSION	126
5.3.1 Indirect Mass Spectral Evidence of OCS^- Metastability	126
5.3.2 Theoretical Results and discussion	129
5.3.3 Photoelectron Imaging of Hydrated $OCS^-(H_2O)_k$	144

5.4 SUMMARY	148
6 ISOMER COEXISTENCE AND COMPETITION OF EXCITED STATE	
DECAY PATHWAYS OF $(\text{OCS})_n^-$	149
6.1 INTRODUCTION	149
6.2 RELEVANT EXPERIMENTAL DETAILS	151
6.3 RESULTS	152
6.4 ANALYSIS	154
6.5 DISCUSSION	162
6.6 SUMMARY	170
7 PHOTOELECTRON IMAGING OF HYDRATED AND HOMOGENEOUSLY SOLVATED CLUSTER ANIONS	
7.1 INTRODUCTION	172
7.2 RESULTS FROM HYDRATION AND SOLVATION OF $(\text{CO}_2)_N^-$	176
7.3 CORE SWITCHING $(\text{CO}_2)_N^-$ AND $[\text{CO}_2(\text{H}_2\text{O})_M]^-$	182
7.3.1 PADs of Monomer and Dimer Ionic Cores	183
7.3.2 Effects of Hydration and Solvation upon PADs	191
7.4 $(\text{CS}_2)_2^-$	197
7.5 SUMMARY	198
8 TIME-RESOLVED PHOTOELECTRON IMAGING	
8.1 INTRODUCTION	199
8.2 RESULTS	201
8.2.1 I_2^- Results	201

8.2.2 I^- channel of I_2Br^-	203
8.3 SUMMARY	214
9 FUTURE DIRECTIONS.....	216
9.1 CLUSTERS.....	216
9.2 TIME-RESOLVED EXPERIMENTS	218
10 REFERENCES.....	220

FIGURE 2.1, Negative-ion photoelectron imaging spectrometer	25
FIGURE 2.2, Exterior of ion source chamber	28
FIGURE 2.3, Electron gun: Overview.....	30
FIGURE 2.4, Electron gun: Filament mount	31
FIGURE 2.5, Electron gun: Electron optics	32
FIGURE 2.6, Faraday cup	34
FIGURE 2.7, TOF: Ion optics.....	35
FIGURE 2.8, TOF: Mass spectrometer and detection chamber vacuum components: (1) 6-way CF Cross 8" Flange OD, (2) 4-way CF Cross 8" Flange OD, (3-4) 6 way CF Cross 8" Flange OD, (5) 8" OD Flange, (6) Turbo molecular pump Leybold TMP 400, (7) 4" Gate Valve, (8) 8" to 4" Reducers	36
FIGURE 2.9, Ion repeller plate.....	41
FIGURE 2.10, TOF: Acceleration stack optic plate	42
FIGURE 2.11, TOF: Extraction plate	43
FIGURE 2.12, TOF: Housing extending into ion source chamber.....	44
FIGURE 2.13, TOF: Shielding tube with mounting base	45
FIGURE 2.14, TOF: Exterior of shielding tube	46
FIGURE 2.15, TOF: Deflectors and separator disc	47
FIGURE 2.16, TOF: Einzel lens.....	48
FIGURE 2.17, Potential switch	49
FIGURE 2.18, Willey-McLaren TOF spectrometer focusing	50
FIGURE 2.19, Ion detector – side view.....	51
FIGURE 2.20, Ion detector – front view	52

FIGURE 2.21, Ion detector components (A) Mesh mount (B) Detector shield (C) Ceramic stand-off.....	53
FIGURE 2.22, Ion detector - voltage divider and signal readout	54
FIGURE 2.23, Velocity map imaging assembly overview 1) Position sensitive electron detector, 2) Mesh, 3) Field-free e^- flight tube, 4) μ -metal cup, 5) Imaging lens, and 6) Ion deflector	58
FIGURE 2.24, Velocity map imaging lens plates.....	59
FIGURE 2.25, Electron flight tube's end flanges.....	60
FIGURE 2.26, Mesh mounting ring	61
FIGURE 2.27, Mesh stretching ring.....	62
FIGURE 2.28, μ -metal cup.....	65
FIGURE 2.29, Post-imaging ion deflector	66
FIGURE 2.30, Laser system	67
FIGURE 2.31, Negative ion mass spectrum – without flight tube	68
FIGURE 2.32, Preliminary positive ions - short flight tube and no ion optics.....	69
FIGURE 2.33, Mass spectrum of $(\text{OCS})_n^-$ cluster anions	70
FIGURE 3.1, The first photoelectron images captured with our negative-ion photoelectron imaging spectrometer. Photoelectron images of I^- at 400 nm and 267 nm. Below energy diagrams illustrating the photon energy in relation to the spin-orbit states of neutral Iodine. The laser polarization is in the vertical direction in the image plane.....	77
FIGURE 3.2, Left, photoelectron image of I^- at 267 nm. Right, Abel inversion of the photoelectron image. Laser polarization is vertical.	79
FIGURE 3.3, Photoelectron spectrum of I^- at 267 nm. The $^2\text{P}_{3/2}$ and $^2\text{P}_{1/2}$ states of the neutral are shown at 3.01 eV and 3.97 eV.....	80
FIGURE 3.4, Photoelectron angular distribution of the $^2\text{P}_{3/2}$ state of neutral Iodine at 267 nm. The solid line is the best fit of the angular distribution. θ is the angle between the laser polarization and the outgoing electron.	81

- FIGURE 3.5, Γ^- anisotropy parameter, β , experimental determine with the prediction from the Cooper-Zare model the solid line. The dashed line is the best fit line to the experimental data. The phase parameter of the dashed line is 0.81. The open circle is from Neumark's group² while the solid triangles is from Lineberger's group⁵. The error bars on our results are approximate and correspond to ± 0.0583
- FIGURE 3.6, Top photoelectron images of O^- at (a) 400 nm and (b) 800 nm. The laser polarization is vertical in the image plane. At the bottom are the photoelectron spectra for 800 and 400 nm; solid line and diamonds respectively.85
- FIGURE 3.7, Relative energy level diagram for photodetachment from O^- and S^-86
- FIGURE 3.8, Anisotropy parameter for photodetachment from O^- . The solid circles represent our values and the solid triangles are from Hanstorp et al¹. The solid line is the prediction from the Cooper-Zare model. The dashed line has a phase parameter of 0.925 which was chosen by Hanstorp et. al. to fit their data. The solid line's phase angle is 0.96 and it was chosen by Hanstorp et al. since it best fit the Cooper-Zare model.87
- FIGURE 3.9, (a) Photoelectron image of S^- at 267 nm (b) Abel transform of S^- at 267 nm (c)-(d) photoelectron image of S^- at 400nm velocity map focusing condition -V3/V1 450/150 V, 600/200 V, and 750/250 V respectively. ..89
- FIGURE 3.10, Photoelectron spectra of S^- at 267 and 400 nm. Both spin orbit states are evident in the 267 nm spectrum.90
- FIGURE 4.1, Top row: Photoelectron images recorded in the photodetachment of S_2^- at (a) 267, (b) 400, and (c) 530 nm. Bottom row [(d)-(f)]: Corresponding Abel-inverted images, reconstructed as described in the text. The images are shown on arbitrary velocity and intensity scales; see Figs. 4.3 and 4.4 for quantitative information. The laser polarization is always vertical in the figure plane. Arrows labeled X , a , b , c , and A' , indicate transitions assigned to the $X^3\Sigma_g^-$, $a^1\Delta_g$, $b^1\Sigma_g^+$, $c^1\Sigma_u^-$, and $A'^3\Delta_u$ states of S_2 , respectively.94
- FIGURE 4.2, Expanded half of the reconstructed 400 nm photoelectron image of S_2^- from Fig. 4.1(e). The electronic transition assignments correspond to neutral S_2 states formed in the detachment. The labels assigned to vibrational rings within the $b^1\Sigma_g^+$ transition are also shown.95

- FIGURE 4.3, Molecular orbital diagram for S_2^- . The X, a, and b neutral states result from detachment of an electron from the π_g^* molecular orbital.97
- FIGURE 4.4, Photoelectron spectra of S_2^- obtained from the images in Figs. 4.1(e) and (f). The spectrum represented by filled symbols/solid line corresponds to the 400 nm laser wavelength, open symbols/dotted line corresponds to 530 nm. Vertical dashed line represents the EA = 1.67 eV. The electronic state assignments correspond to neutral S_2 . The vibrational progression (α through ζ) within the b state corresponds to the similarly labeled rings in the image shown in Fig. 4.2.98
- FIGURE 4.5, Anisotropy of different components of the π_g^{-1} transition in S_2^- at three different wavelengths (as indicated), summarized as a function of eKE. The transition labels indicated on the graph correspond to 400 nm data. The Greek labels for vibrationally resolved transitions to the b $^1\Sigma_g^+$ state of S_2 are the same as in Figs. 4.2 and 4.3. (1) The 530 nm data corresponding to the X $^3\Sigma_g^-$ state. (2) Overall anisotropy of the peripheral feature in the 267 nm image shown in Figs. 4.1(a) and (d), corresponding to unresolved X $^3\Sigma_g^-$, a $^1\Delta_g$, and b $^1\Sigma_g^+$ states. The solid line corresponds to the Cooper-Zare model for photodetachment from a d orbital ($\ell = 2$) assuming a dipole radial matrix elements ratio of $R_{\ell+1}/R_{\ell-1} = (0.5 \text{ eV}^{-1}) \cdot \text{eKE}$ and a zero phase-shift between the $(\ell \pm 1)$ waves.100
- FIGURE 4.6, Photoelectron images (a) O_2^- at 400 nm (b) O_2^- at 800 nm (c) SO^- at 400 nm (d) SO^- at 800 nm102
- FIGURE 4.7, Photoelectron spectra of O_2^- and SO^- at 800 nm extracted from the Abel transforms of the images in Fig. 4.6 (b) and (d). The solid squares correspond to O_2^- while the open diamonds correspond to SO^-104
- FIGURE 4.8, Anisotropic parameters for the 800 nm images of SO^- (open diamonds) and O_2^- (solid squares) plotted against electron kinetic energy.105
- FIGURE 4.9, Top row: Photoelectron images recorded in the photodetachment of CS_2^- at (a) 267 nm, (b) 400 nm, (c) 530 nm, and (d) 800 nm, with the corresponding photon energies indicated. Bottom row: Abel-inversions of the above images, reconstructed as described in the text. The images are shown on arbitrary velocity and intensity scales; see Figs. 4.10 and 4.11 and the text for quantitative information. The laser polarization is always vertical in the figure plane. The arrows labeled X, a, and b indicate transitions accessing the X $^1\Sigma_g^+$, a 3B_2 , and b 3A_2 states of neutral CS_2 . The transition to the A 1A_2 state (not labeled) is just inside the b 3A_2 ring in (e), as discussed in the text and seen in Fig. 4.10. The dashed lines

- show correlations in the velocity-map domain of the selected eBE intervals between images taken at different wavelengths.106
- FIGURE 4.10, Half of the reconstructed 267 nm photoelectron image of CS_2^- reproduced from Fig. 4.9(e) (right) superimposed with the eKE scale (left) and neutral CS_2 state assignments for observed transitions.108
- FIGURE 4.11, 267 nm photoelectron spectrum of CS_2^- . (a) The spectrum obtained by integrating the reconstructed image in Fig. 4.10 over the entire angular range. (b) The spectrum obtained by integrating the same image from $\theta = 10^\circ$ to 25° . Peak assignments correspond to the electronic states of neutral CS_2109
- FIGURE 4.12, The s&p model treatment of CS_2^- photodetachment. First header row: principal anion orientations (solid line represents the bent frame of CS_2^-). Second header row: corresponding symmetries of the transition-dipole components driven by the laser radiation polarized along the LF z axis. Rows below the header indicate the symmetries and s and p components (dash contours) of ψ_f corresponding to the respective transitions and principal orientations. See the text for details.112
- FIGURE 4.13, The s&p model treatment of $\text{S}_2^- (\pi_g^{-1})$ photodetachment. Bold solid line is the S_2 molecular frame. Solid contours on the left represent the bound MO (π_g). Vertical arrows in the middle indicate the laser polarization direction, with the corresponding MF symmetry of the active transition dipole components shown. Dashed contours on the right represent the symmetry-allowed partial waves ($\ell \leq 1$) that contribute to ψ_f . The σ_u^- and δ_u waves corresponding to the $\pi_u(m_y)$ transition moment expands only in $\ell \geq 2$ waves, which are neglected in the model.116
- FIGURE 5.1, Negative ion mass spectra obtained with the OCS/Ar precursor containing a trace amount of water. The magnified ($\times 10$) spectra in (a) and (b) correspond to the experimental conditions optimized for the S^- and OCS^- anions, respectively. The latter shows the best OCS^- signal that could be achieved in the experiment. The ion peaks in (a) and (b) labeled in accordance with the corresponding anion mass (in a.m.u.) are assigned as follows: 66 = $^{32}\text{S}^{34}\text{S}^-$; 76 = CS_2^- ; 80 = $\text{OC}^{34}\text{S}^- \cdot \text{H}_2\text{O}$; 82 = $\text{S}_2^- \cdot \text{H}_2\text{O}$; 92 = OCS_2^- ; 124 = $\text{S}_2^- \cdot \text{OCS}$; 132 = $\text{OCS}^- \cdot (\text{H}_2\text{O})_4$; 150 = $\text{OCS}^- \cdot (\text{H}_2\text{O})_5$. In (c), the top of the three combs above the mass spectrum indicates the peak positions for the $(\text{OCS})_n^-$ cluster anions ($n = 4 - 10$). The two lower combs correspond to the monohydrated $(\text{OCS})_n^- \cdot \text{H}_2\text{O}$ and doubly hydrated $(\text{OCS})_n^- \cdot (\text{H}_2\text{O})_2$ cluster ions, respectively.127

FIGURE 5.2, The relaxed diabatic potential energy curves of OCS (curve I: filled circles), OCS^- (curve II: open circles, bold line), and $\text{S}^-\cdot\text{CO}$ (curve III: open symbols, thin line), calculated along the bending coordinate at the CCSD level with the 6-31+G(d) basis set. Curve I also corresponds to the $\text{OCS} + e^-$ detached-electron state. In the $\text{S}^-\cdot\text{CO}$ anion-neutral complex (curve III), the typical C-S distance is in the 3.2–3.7 Å range. The horizontal lines above the OCS and OCS^- potential minima indicate the ground state energies corrected for the ZPE.131

FIGURE 5.3, Some of the results for the adiabatic EA of OCS, including the ΔZPE correction. Open and filled circles: results obtained with the augmented correlation consistent basis sets of Dunning and the split valence basis sets of Pople, respectively. The error bars for the G2, G3, BLYP, and B3LYP results are determined as described in the text. The BLYP result was obtained with the 6-311+G(d) basis set, while both the 6-311+G(3df) and G3large basis sets yielded the B3LYP value shown with an error margin. Other data are as follows: 1 - MP2/6-31+G(d); 2 - MP2/aug-cc-pVTZ; 3 - MP3(Full)/aug-cc-pVDZ; 4 - MP4(Full)/6-31+G(d); 5 - MP4(Full)/aug-cc-pVDZ; 6 - CCSD/6-311+G(2df); 7 - CCSD/aug-cc-pVTZ; 8 - CCSD(T)/6-311+G(d); 9 - CCSD(T)/G3large; 10 - CCSD(T)/aug-cc-pVDZ; 11 - QCISD(T)/6-311+G(d); 12 - QCISD(T)/aug-cc-pVDZ; 13 - BLYP/aug-cc-pVQZ; 14 - B3LYP/aug-cc-pVQZ; 15 - mPW1PW91/6-31+G(3df); 16 - mPW1PW91/aug-cc-pVQZ.137

FIGURE 5.4, The equilibrium structures of four $\text{OCS}^-\cdot\text{H}_2\text{O}$ isomers. The relative hydration energies ΔE_h and VDEs are given in eV, while the intermolecular structural parameters are in Angstroms and degrees. The indicated values of ΔE_h are the purely electronic (excluding the ZPE correction) hydration energies, defined as the energy of $\text{OCS}^-\cdot\text{H}_2\text{O}$ relative to the sum of the separated OCS^- and H_2O energies. The energetic and structural parameters are determined from the following calculations: listed first (italics) – B3LYP/6-311++G(d,p); listed second (plain font) – CCSD/6-31+G(d). For the lowest-energy structure A, the parameters listed third (bold) are from CCSD/6-311++G(d,p), and those listed last (italics in parentheses) are at the mPW1PW91/aug-cc-pVTZ level.139

FIGURE 5.5, (a)–(c): Photoelectron images recorded in the photodetachment of $\text{OCS}^-\cdot\text{H}_2\text{O}$ at (a) 400, (b) 529, and (c) 800 nm. (d), (e): Photoelectron images of $\text{OCS}^-(\text{H}_2\text{O})_2$ at 400 and 529 nm, respectively. The images are shown on arbitrary velocity scales (see Fig. 5.6 for quantitative information). The laser polarization is vertical. (f) The HOMO of the most stable structure of $\text{OCS}^-\cdot\text{H}_2\text{O}$145

- FIGURE 5.6, Filled symbols: photoelectron energy spectra obtained from the $\text{OCS}^-\cdot\text{H}_2\text{O}$ images in Fig. 5.5(a)-(c). Open symbols: photoelectron spectra for $\text{OCS}^-\cdot(\text{H}_2\text{O})_2$, from Fig. 5.5(d) and (e). Different symbol types correspond to different wavelengths, as labeled. Solid lines: simulated photoelectron spectra obtained as described in the text, yielding $\text{VDE} = 2.07 \pm 0.07$ and 2.53 ± 0.07 eV for $\text{OCS}^-\cdot\text{H}_2\text{O}$ and $\text{OCS}^-\cdot(\text{H}_2\text{O})_2$, respectively.147
- FIGURE 6.1, Photoelectron images of $(\text{OCS})_{2-4}^-$ and $\text{OCS}^-\cdot\text{H}_2\text{O}$ recorded at 800, 530, 400, and 267 nm. The images are shown on arbitrary velocity and intensity scales (see Figs. 6.2-6.4 for quantitative information). Arrows indicate the contributions of autodetachment (AD) and direct detachment bands I, II, and III.153
- FIGURE 6.2, Experimental and simulated $(\text{OCS})_2^-$ photoelectron spectra in the energy and velocity domains (left and right columns, respectively). The experimental spectra (thin lines with apparent noise) are derived from the corresponding images in Fig. 6.1. The simulated spectra are shown by bold lines with the individual transitions (AD and bands I, II, and III) indicated by the thin curves, correspondingly labeled. The dashed curves in (a)-(c) [$P(\epsilon)$ column, this Figure only] are fits [Eq. (5)] to the $\text{OCS}^-\cdot\text{H}_2\text{O}$ spectra (not shown).155
- FIGURE 6.3, Experimental and model spectra for $(\text{OCS})_3^-$. See Fig. 6.2 caption for further details. The $P(v)$ distributions in (b) and (c) are magnified $\times 5$ and $\times 10$, respectively, to highlight the autodetachment components.156
- FIGURE 6.4, Experimental and model spectra for $(\text{OCS})_4^-$. See Fig. 6.2 caption for further details. The $P(v)$ distributions in (b) and (c) are magnified $\times 5$ and $\times 10$, respectively, to highlight the autodetachment components.157
- FIGURE 7.1, Photoelectron images of $[(\text{CO}_2)_n(\text{H}_2\text{O})_m]^-$ cluster anions. The images are recorded with the same velocity-map imaging focusing conditions except for $(\text{CO}_2)_{10}^-$ and $\text{CO}_2^-\cdot\text{H}_2\text{O}$; however, the latter two have been rescaled to account for the discrepancy in the imaging voltages and are shown on the same velocity scale as the rest of the data. Hence, all images presented are shown on the same velocity scale allowing for direct visual comparison. In graph (a) the $e\text{BE}_{\text{max}}$ in eV is plotted versus the total number of molecules ($n + m$) in each cluster. In graphs (b) and (c) the photoelectron anisotropy parameter β is plotted versus the total number of molecules ($n + m$) in each cluster. The \diamond , \bullet , and \square symbols correspond to $(\text{CO}_2)_{4-11}$, $(\text{CO}_2)_n(\text{H}_2\text{O})_{n-1}$ and $\text{CO}_2(\text{H}_2\text{O})_m$ respectively. In (c), β is integrated over

- the range 0.12-0.53 eV, while in (b) the it is integrated over the over the entire image area.178
- FIGURE 7.2, Molecular orbital plots for dimer based cluster anion HOMOs (a.1), (b.1), (b.2) and monomer anion HOMO (a.2). Geometries (shown above the HOMO for each species) are taken from Ref. ³ and correspond to the potential minima calculated at the MP2/6-31+G* level. Above left is the view perpendicular to CC bond axis and above right is along the CC bond axis. (a.1) $(\text{CO}_2)_2^-$, D_{2d} symmetry. (a.2) Two monomer CO_2^- HOMOs arranged with D_{2d} symmetry. (b.1) lowest energy $(\text{CO}_2)_2^- \cdot \text{H}_2\text{O}$ structure in which the dimeric core anion is distorted from D_{2d} to C_2 symmetry by the bridging H_2O group. (b.2) $(\text{CO}_2)_2^- \cdot \text{H}_2\text{O}$ with H_2O in the end position. .185
- FIGURE 7.3, Qualitative treatment of $(\text{CO}_2)_2^-$ photodetachment. For each orientation I and II, the parent orbital (left column) is described as an LCMO superposition of the orbitals of two monomers α and β (second column). The partial wave pairs sketched on the right represent a dual-source description of the free-electron wavefunction in the limit of s and p components only. The symmetries of the bound and free electron wavefunctions and the laser polarization vector are given in the irreducible representations of the dimer and monomer point groups (D_{2d} and C_{2v} , respectively).189
- FIGURE 7.4, Predicted structures for $\text{CO}_2(\text{H}_2\text{O})_m$ Optimized by the MP2/6-31+G* method.193
- FIGURE 7.5, Abel-transformed 400 nm photoelectron images of (a) CS_2^- and (b) $(\text{CS}_2)_2^-$. The laser polarization is vertical. Arrows I point to the transitions corresponding to electron detachment from the CS_2^- HOMO (either in the isolated anion or in the $\text{CS}_2^- \cdot \text{CS}_2$ cluster). Arrow II marks the lowest-energy detachment transition from covalent $(\text{CS}_2)_2^-$196
- FIGURE 8.1, *Left* time-resolved photoelectron images of I_2^- each the time interval between images is 33 fs. The bottom image has a delay of approximately -50 fs, while the top is ~ 450 fs. *Top-right*: Contour spectra of the images with time as the y-axis. *Bottom*: Schematic of potential surfaces of I_2^- where arrows represent the photon energies of the pump and the probe beams.202
- FIGURE 8.2, Two dimensional photoelectron images (shown on the right in order of increasing delay time) are Abel inverted to reproduce the photoelectron energy domain spectra (shown on the left) and the photoelectron angular distributions. The insert on the 100 fs spectrum shows an increased energy

range, clearly indicating the presence of a second electronic transition as seen in the image by the outer ring. This outer ring is absent in all of the other (longer delay time) images. The peak in the 0.0-0.2 eV energy range becomes narrower and shifts to higher eKE as the delay time increases, becoming increasingly like that seen in atomic anion detachment. The final image in the series is from the single photon detachment of I^- at 388 nm which effectively represents an infinite delay time between the two lasers.204

FIGURE 8.3, Evolution of the photoelectron band ascribed to the $\text{I}_2\text{Br}^- \rightarrow \text{I}^-$ channel (388 nm pump – 388 nm probe): (a) eKE corresponding to the transition maximum and (b) transition width (defined as FWHM) as functions of pump-probe delay. Filled symbols correspond to time-resolved data from I_2Br^- pump-probe measurements. Open symbols correspond to a one-photon measurement on isolated I^- , representing the $\text{I}_2\text{Br}^- \rightarrow \text{I}^-$ channel in the asymptotic limit of infinite delay. The peak positions and widths are determined by fitting the 0–0.2 eV band in the spectra in Fig. 8.2 with Gaussian functions. The dashed trend lines, added merely to guide the eye, do not represent quantitative fits to the data.208

FIGURE 8.4, Evolution of the anisotropy parameters (a) β_2 and (b) β_4 as functions of pump-probe delay in I_2Br^- dissociation via the I^- channel (388 nm pump – 388 nm probe). Filled symbols correspond to time-resolved data; open symbols on the right represent one-photon (388 nm) detachment from isolated I^- , representing the $\text{I}_2\text{Br}^- \rightarrow \text{I}^-$ channel in the asymptotic limit of infinite delay. The anisotropy parameters were determined by fitting the 0 – 0.2 eV band in the photoelectron images shown in Fig. 8.2 using Eq. (1), as described in more detail in the text.211

FIGURE 8.5, Comparison of the time-resolved β_2 values obtained in this work to the eKE-dependent values expected for one-photon detachment from I^- . In the main panel, filled symbols represent the time-resolved data with the corresponding pump-probe delays indicated next to the data points. The open circle corresponds to one-photon detachment from isolated I^- at 388 nm, representing the limit of infinite pump-probe delay in the I_2Br^- experiment. The solid line represents a fit to the one-photon data using the Hanstorp model,¹ as described in the text. The inset shows the one-photon detachment data for isolated I^- (symbols), for which the model parameters were optimized, and the fit curve (same as in the main panel) over a broad eKE-range. The open circles represent data obtained in this work. The open squares are from ref. 48 and the open triangle is from ref. 33.213

Table 5.1,	Calculated ab initio values of the electron affinity of OCS, excluding the zero-point vibrational energy corrections (ΔZPE), except where noted. 134
Table 5.2,	Calculated DFT values of the electron affinity of OCS, excluding the zero-point vibrational energy corrections (ΔZPE).135
Table 5.3,	Calculated equilibrium geometries and vibrational frequencies of OCS and OCS^-136
Table 5.4,	Equilibrium parameters and harmonic vibrational frequencies of $OCS^- \cdot H_2O$ structure A (ground state) shown in Fig. 4 calculated at the CCSD level with the 6-311++G(d,p) basis set.142
Table 6.1,	TE temperatures (in K) calculated with Eq. (3).160
Table 6.2,	Optimal ϵ_0 and w values for direct detachment bands in $(OCS)_n^-$ modeled with Eq. (5). Values are listed in eV in the format ϵ_0 (w). The VDEs are obtained by averaging ϵ_0 for different wavelengths. Parameters for $OCS^- \cdot H_2O$ (from Ref. 30) are given for comparison.164
Table 7.1,	Electron binding energy (in electron-volts) at spectral maximum for selected $[(CO_2)_n(H_2O)_m]^-$ cluster anions determined from the presented photoelectron images.180
Table 7.2,	Total energies, eBE_{max} and VDE of $[CO_2(H_2O)_n]^-$ cluster anions using the MP2/6-311++G** theory level and basis set or determined from photoelectron spectra through fitting with Gaussians.....194

Abstract

Femtosecond negative-ion photoelectron imaging spectroscopy allows the probing of dynamics resulting from solvation and photodissociation in both the time-resolved and solvent domains. First, the basic premise of photoelectron imaging shall be presented, followed by a discussion of qualitative approaches for interpreting photoelectron angular distributions as illustrated by application to the photoelectron images of S_2^- and CS_2^- . The photoelectron images of CS_2^- serve as a reference for interpreting the results for homogeneous and heterogeneous solvation in CO_2 and OCS cluster anions. The effects of solvation upon the photoelectron angular distribution and the photoelectron energy spectrum are discussed in relation to $(OCS)_n^-$, $OCS^- \cdot H_2O$, $(CO_2)_n^-$, and $(CO_2)_n(H_2O)_m^-$. The $(OCS)_2^-$ cluster anion images show evidence of competition of excited state decay pathways and coexistence of isomers. The evolution of photoelectron images, resulting from I_2Br^- dissociation shows the evolving electronic structure of the I^- channel as the anion dissociates.

1 INTRODUCTION

This dissertation describes the development, construction and initial experiments on a femtosecond negative-ion photoelectron imaging spectrometer. The calibration and initial experiments served as a stepping stone to more complex systems and time-resolved studies. Through these experiments qualitative methods for analyzing photoelectron angular distributions were developed.

Through time-resolved negative ion spectroscopy we aim to understand chemical reaction at a detailed molecular-orbital (MO) level with an emphasis on evolving electronic wave functions. For it is the electronic wave functions which control chemical binding and define the potential energy surface upon which the nuclei move challenging the traditionally description that nuclear rearrangement determines chemical reactions. The driving force of chemical reaction, electron dynamics, is explored through femtosecond negative-ion photoelectron spectroscopy.

Our instrument combines the advantages of negative-ion photoelectron spectroscopy,⁹ pump-probe techniques and the imaging technique.¹⁰ Photoelectron imaging affords the reconstruction of a complete 3D velocity distribution of the ejected electrons including the speed and angular distributions from the photoelectron images. The radial or speed distribution corresponds to the photoelectron energy spectrum. From angular distributions the symmetry of the electronic wave function can be retrieved, conveying information of the parent anion's MO.^{11,12} A photoelectron image in short contains all the observable information about the ejected electrons, which relate back to the electronic wave functions of the parent anion.

While other methods measure the electron's energy or the angular distribution, only photoelectron imaging detects both simultaneously with good resolution and sensitivity. The imaging technique was developed by Chandler and Houston for photofragment spectroscopy. It has been applied successfully to photodissociation and ionization of neutral molecules.^{10,13-19} The addition of velocity mapping²⁰ by Parker and Eppink has improved the resolution of imaging allowing for the popularity of imaging to surge. At the start of this project there were no reported photoelectron imaging studies for negative ions. Now others are following suit including Bordas's group imaged tungsten cluster anions^{21,22} and Neumark's time resolved photoelectron images of I_2^- dissociation,² C_2^- dynamic study,²³ and C_6^- relaxation.²⁴

Time-resolved photoelectron spectroscopy (TRPES) was first introduced in 1985 to study electronic dynamics on semiconductor surfaces.²⁵ The temporal resolution of the laser system determines the type of dynamics that can be followed. Nanosecond or picosecond experiments have been used to probe lifetimes and radiationless decay pathways of excited electronic states.²⁵ Femtosecond resolution allows one to monitor vibrational dynamics such as dissociations and coherent wavepacks. In addition short-lived electronic states can also be studied with femtosecond resolved experiments. TRPES allows the excited state dynamics to be monitored over the entire reaction coordinate. It also provides full Frank-Condon mapping of the evolving wavepacket at each delay. TRPES provides info about the energy content of the species of interest as a function of time. In 1996 Neumark was the first to apply femtosecond TRPES to a negative ion, I_2^- .

We focus on negative ions, because they are instrumental for probing the transition state of chemical reactions. Anions are conveniently mass-selected allowing cluster and solvation studies upon size-selected clusters. The excess electron occupies a diffused outer-shell orbital that is sensitive to its environment; hence, it serves as a probe for intermolecular interactions. Less energy is needed to photodetach an electron from an anion than to photoionize a neutral. Typically only one visible/UV photon is needed allowing for experimental straightforwardness.

Each successive chapter builds from the foundation developed in its preceding chapter. Chapter 2 describes the building of time-resolved photoelectron imaging spectrometer. Data collection and analysis are also discussed in that chapter. Chapter 3 discusses photoelectron imaging of atomic anions. Chapter 4 extends photoelectron imaging to molecules. Two models that qualitatively explain the photoelectron angular distributions are introduced in chapter 4. The results described in chapter 4 have been published in refs.^{26,27} The principles of image analysis developed in chapters 3 and 4 are applied to photoelectron images of clusters in chapters 5, 6, and 7. Chapter 5 focuses on the metastability of OCS^- . The non-existent electron affinity of OCS is predicted from theoretical calculation and estimated through indirect measurements. Chapter 5 is a summary of previous publications.^{26,28} Chapter 6 deals with the coexistence of isomers and competition of excited state decay pathways of $(\text{OCS})_n^-$, which have been reported previously.²⁹ Hydration and homogeneous solvation of anions are analyzed in chapter 7. Most of the results in chapter 7 are in preparation for publication, others have been

published.^{30,31} Finally Chapter 8 deals with time-resolved imaging of negative-ions.

These results have been published in ref.³²

2 EXPERIMENTAL DETAILS

2.1 GENERAL OVERVIEW OF THE APPARATUS

The negative ion photoelectron imaging spectrometer consists of an ion source, time of flight mass analyzer and position sensitive photoelectron detector. The instrument's design employs concepts of negative ion and photoelectron spectroscopy developed by Carl Lineberger³³ and combines them with the novel imaging scheme for detection of the photoelectrons. Figure 2.1 shows a diagram of the experimental apparatus.

The source chamber is pumped by a 10" diffusion pump (Varian VHS 10) connected by an 10" I.D. elbow. A base pressure of 2.5×10^{-7} Torr is achieved in the source chamber. The first, pre-detection section of the time of flight (TOF) tube consists of two differentially pumped stages, is pumped by a 6" diffusion pump and a 400 l/s turbo pump (VHS-6 and Leybold TMP-361). The detection region is differentially pumped with a second 400 l/s turbo pump (Leybold TMP-361). The TOF region achieves pressures of $0.8\text{--}3 \times 10^{-7}$ Torr while the detection region has a base pressure of 2.2×10^{-9} Torr. The TOF region and detection region are separated by a 4' gate valve. Under operating conditions the source chamber is $1.5\text{--}5 \times 10^{-5}$ Torr depending upon the sample and the detection region rises to 1.4×10^{-8} Torr.

Anions are created by electron impact of molecules in a pulsed-supersonic expansion. First, molecules enter the chamber through a General Valve Series 9 pulsed valve with a 0.3 mm orifice. Then a 1kV electron gun produces a beam of electrons that intersects the supersonic expansion 1-3 mm downstream of the valve. Secondary

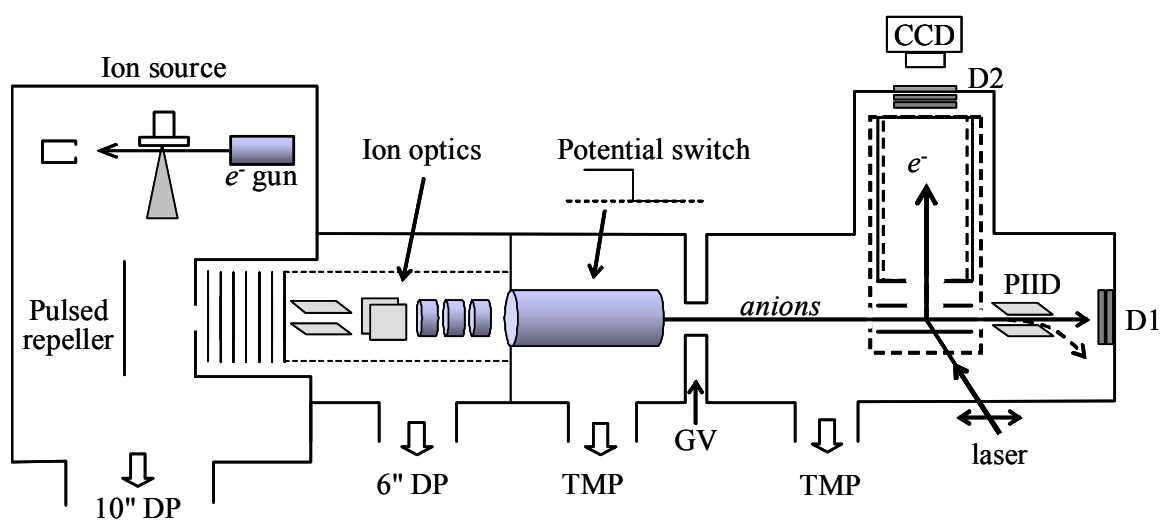


Figure 2.1 Negative-ion photoelectron imaging spectrometer

electrons are generated from the ionization of neutral molecules. The secondary electrons attach to neutral molecules to form negative ions. Fourteen centimeters downstream the anions are extracted into a Wiley-McLaren TOF mass analyzer³⁴, which is mounted perpendicular to the molecular beam.

The Wiley-McLaren TOF mass analyzer focuses the anions in time through adjusting the ratio of voltages between the repeller plate and the acceleration stack so that ions of the same mass arrive at the detector at the same time regardless of their initial position in the extraction region. An einzel lens, operated in the ion-decelerating regime, focuses the anions in space. Vertical and horizontal deflectors steer the anions. A potential switch drops the potential of the beam. The ions are detected by a 25 mm microchannel plate detector positioned at the end of the flight tube at the terminus of the detection chamber.

Next, within the detection region we intersect the anion beam with a pulsed laser beam. The laser photodetaches valence electrons in order to probe the electronic structure. For dynamic (time-resolved) experiments a (pump) femtosecond laser pulse first excites the anions to a higher electronic state while, a predetermined delay later, another (probe) laser pulse probes the evolution of the excited electronic state. Through sampling over several different delays, the evolution of the wave packet can be studied.

The photodetached electrons are projected onto a position sensitive imaging detector via a velocity-map focusing lens. The position sensitive detector (Burle, Inc.) consists of two 40 mm diameter microchannel plates linked to a P-47 phosphor screen,

which is monitored by a CCD camera (Roper Scientific HQ CoolSnap). The following sections give more detailed descriptions of the individual components of the apparatus.

2.2 ION SOURCE CHAMBER

The ion source produces anions through secondary electron attachment. The ion source chamber includes a supersonic nozzle, electron gun, Faraday cup and a pulsed repeller plate. The 1 keV electron beam ($\sim 100 \mu\text{A}$ DC) intersects the molecular expansion less than 4 mm after the nozzle orifice. There is 14 cm between the nozzle and the center of the extraction region. The Faraday cup prevents reflection of the electron beam by collecting the electrons. The Vacuum chamber housing these components was built at the University of Arizona Research Instrument Center. The exterior of the ion source region is pictured in Fig 2.2. There are many ports on the source chamber to make it as adjustable as possible. Briefly side A has four 3" and a 6" half nipples with ASA flanges on the end. One of the 3" nipples serves as the sample gas intake. The 6" port has electrical feedthroughs. There are two eight pin feedthroughs, one 2 pin high voltage feedthrough, and 2 MHV feedthroughs. Side B has a port 10" port that connects to an elbow. At the other end of the elbow the 10" diffusion pump (VHS-10) resides. Side C has two 4" ID half nipples that are blanked off, a 3" ID half nipple which has a vacuum gauge mounted on a blank ASA flange, and a 6" ID conflat half nipple of which the time-of-flight tube extends out. Side D has more ports to make the chamber more versatile. The 10" port on this side assisted with insertion of components into the TOF tube. The lid lifts off so that easy access to the interior of the source chamber is achieved. On the

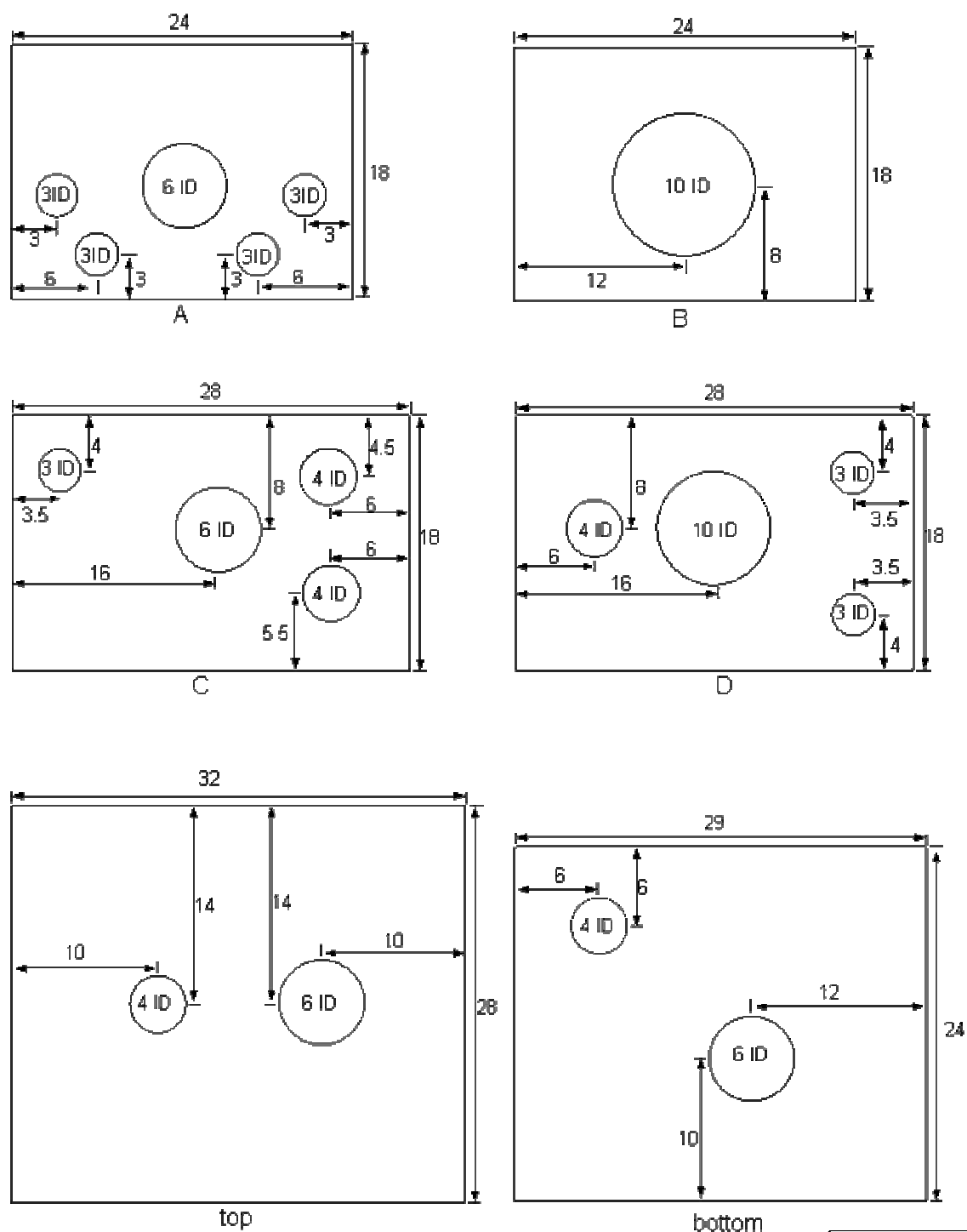


Figure 2.2 Exterior of ion source chamber

lid are two ports; one of which holds an Ion gauge. There are two ports on the bottom of the chamber and to one the roughing pump attaches.

2.2.1 Pulsed Valve

The pulsed solenoid valve (General Valve, series 9, Parker Inc.) has an orifice of 0.3 mm; later we used a valve with a 0.8 mm orifice. The pulsed valve is driven by a General Valve IOTA driver. It is triggered by a TTL pulse from a Stanford Instruments Pulse Generator (model 535), which receives its trigger from a BNC pulse generator that divides the trigger from the laser's pockel cells by 14 which is adjustable. Hence, the valve is triggered at a repetition rate of 71 Hz which is the highest rep rate possible with this nozzle to produce stable ions. The sample is seeded in 1-3 atm of a carrier gas (Ar, He, or CO₂). For example, I₂ is introduced by passing the carrier gas through a reservoir of Iodide crystals before it reaches the nozzle. For OCS, a lecture bottle containing 7% OCS in Argon is used.

2.2.2 Electron Gun

The Electron gun was designed in house and its components were built at the University of Arizona Research Instrument Center. Figure 2.3 illustrates the electron gun's components which are the filament assembly that irradiates e^- , a three component einzel lens for focusing, and deflectors for steering. The details of the filament assembly are shown in Fig. 2.4. A thorated tungsten filament is mounted in the filament assembly so that the bent filament tip sits just above the anode plate. The voltage difference between the anode plate and the filament extracts electrons from the filament. -1 kV is applied to the filament while the anode plate is approximately -1.2 kV. The

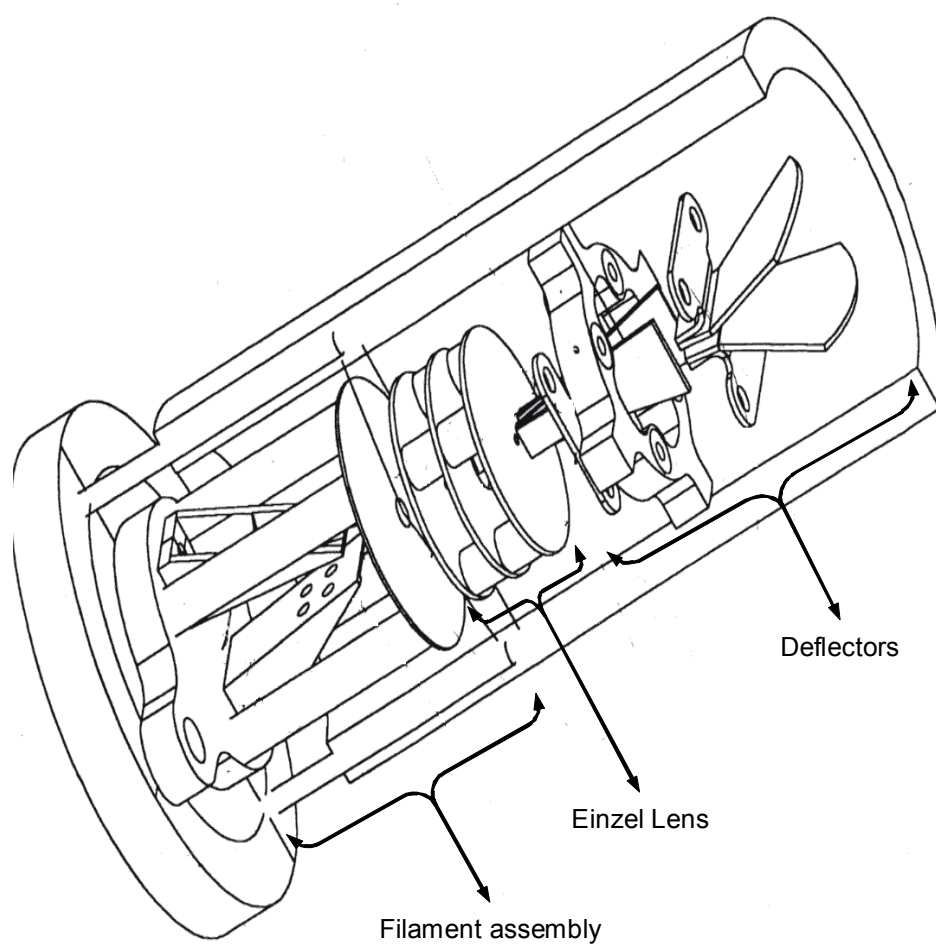


Figure 2.3 Electron gun: Overview

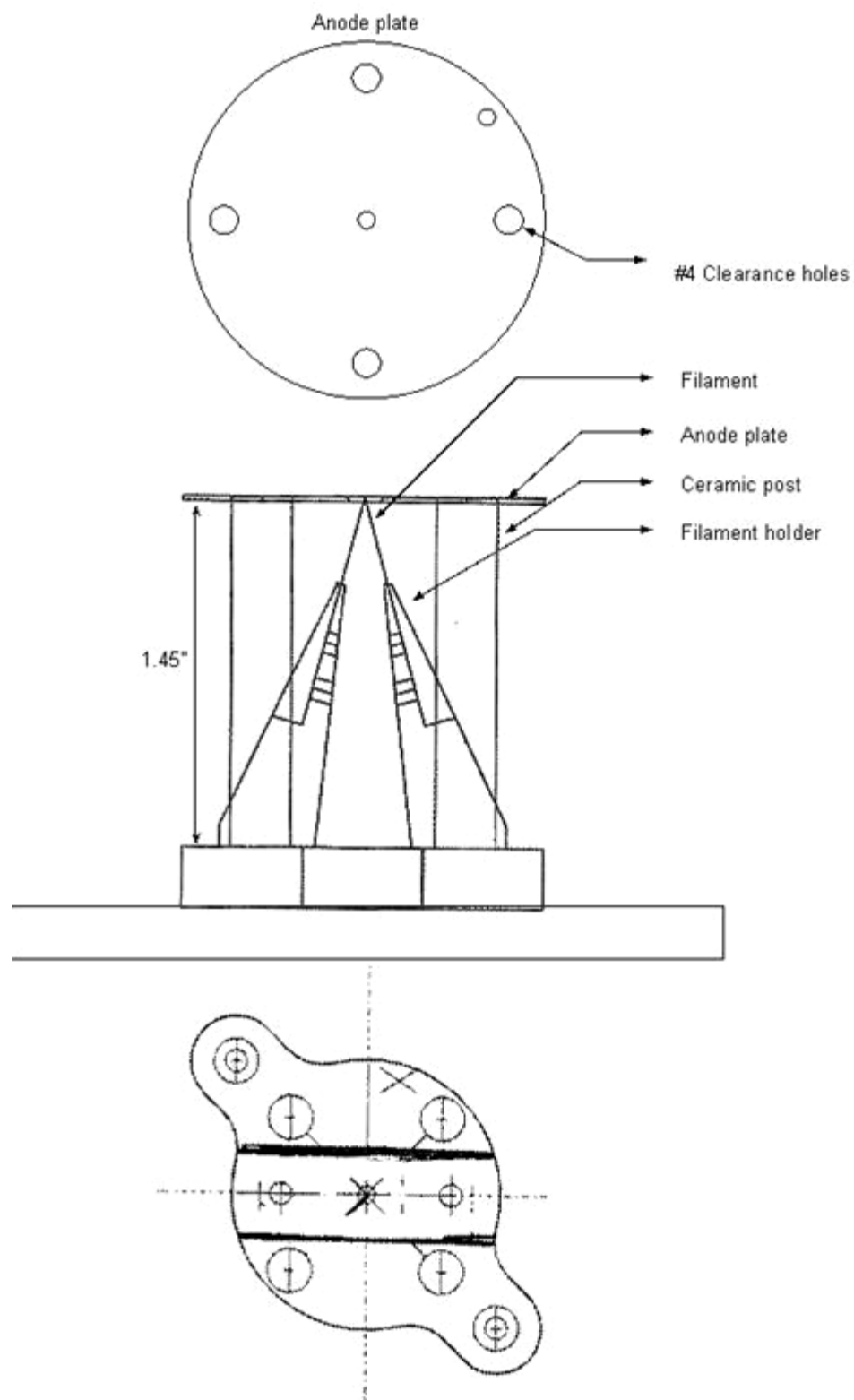


Figure 2.4 Electron gun: Filament mount

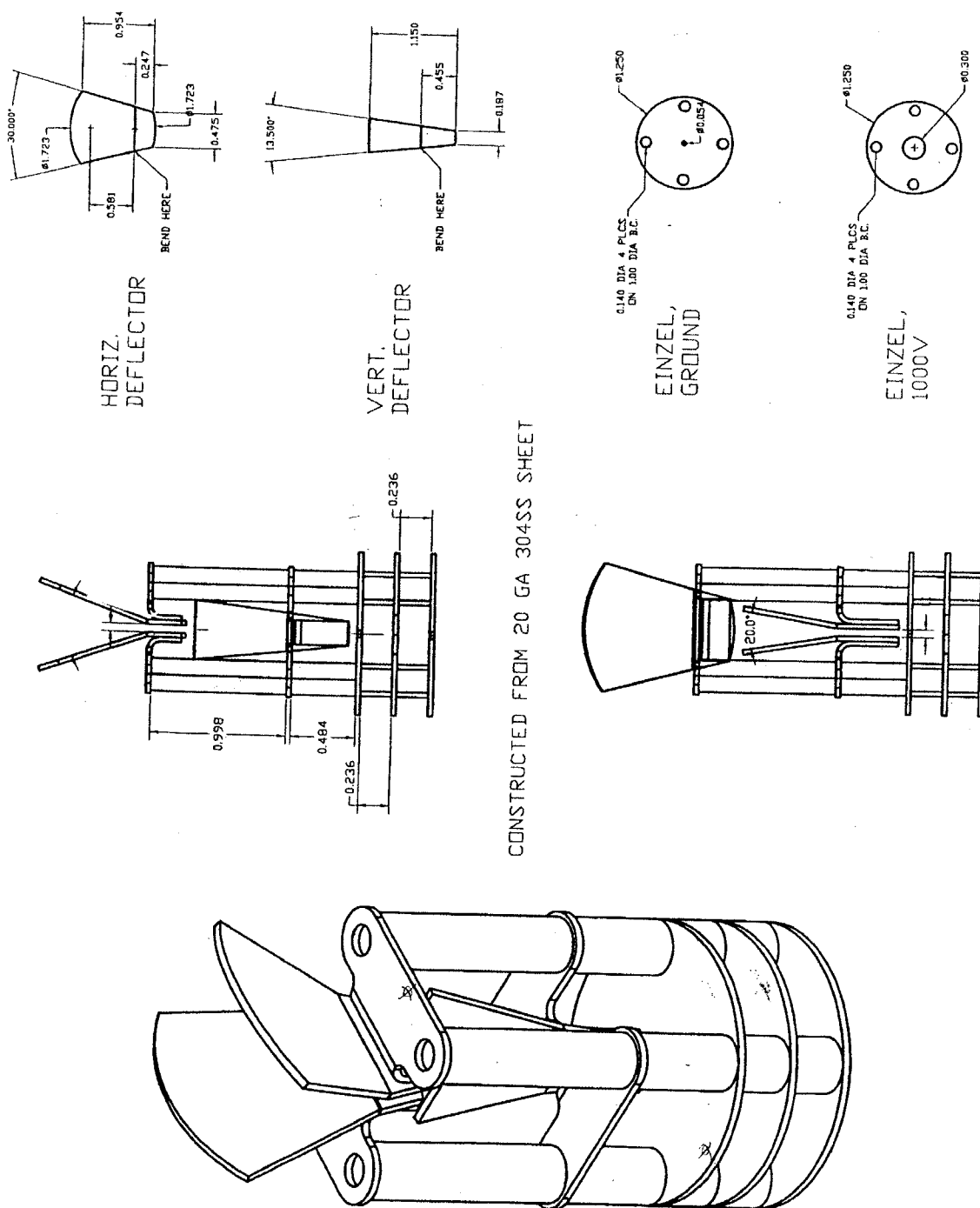


Figure 2.5 Electron gun: Electron optics

schematics of the deflectors and the einzel lens are given in Fig. 2.5. The ceramic posts insulate the electrode components from each other. The first and third components of the einzel lens are grounded, while the middle plate is typically -600 to 980 Volts.

2.2.3 Faraday Cup

The Faraday cup, shown in Fig. 2.6, is a four inch long cylinder that is two inches in diameter. There is a half inch lip at the front to decrease the possibility of reflected electrons from escaping. The back slopes to a point which deflects the electron beam; scattering it toward the walls of the cup. The cup is not grounded, but it is attached to an ammeter via a wire. Typically the current measured, when the electron gun is operating, is 20-80 μA .

2.3 TIME OF FLIGHT MASS ANALYZER

A Wiley-McLaren Time of Flight Mass Analyzer separates the ions by mass, and focuses them in time and space. In brief, ions of different mass fly at different velocities through the flight tube. The difference in speed arises from heavy ions getting less acceleration than lighter ions in an electric field. Approximately the ions flight time is proportional to the square of the ions mass. Spreadsheet modeling and the software Simion (Scientific Instrument Services, Inc., Ringoes, NJ) was used to assist in designing the instrument. Simion allows the simulation of charged particle behavior in electric fields. A schematic overview of the acceleration and ion-optics components of the TOF mass analyzer is shown in Fig. 2.7. Not shown in the figure is the ion repeller plate, which injects ions into the mass analyzer through the 4mm diameter orifice in the extraction

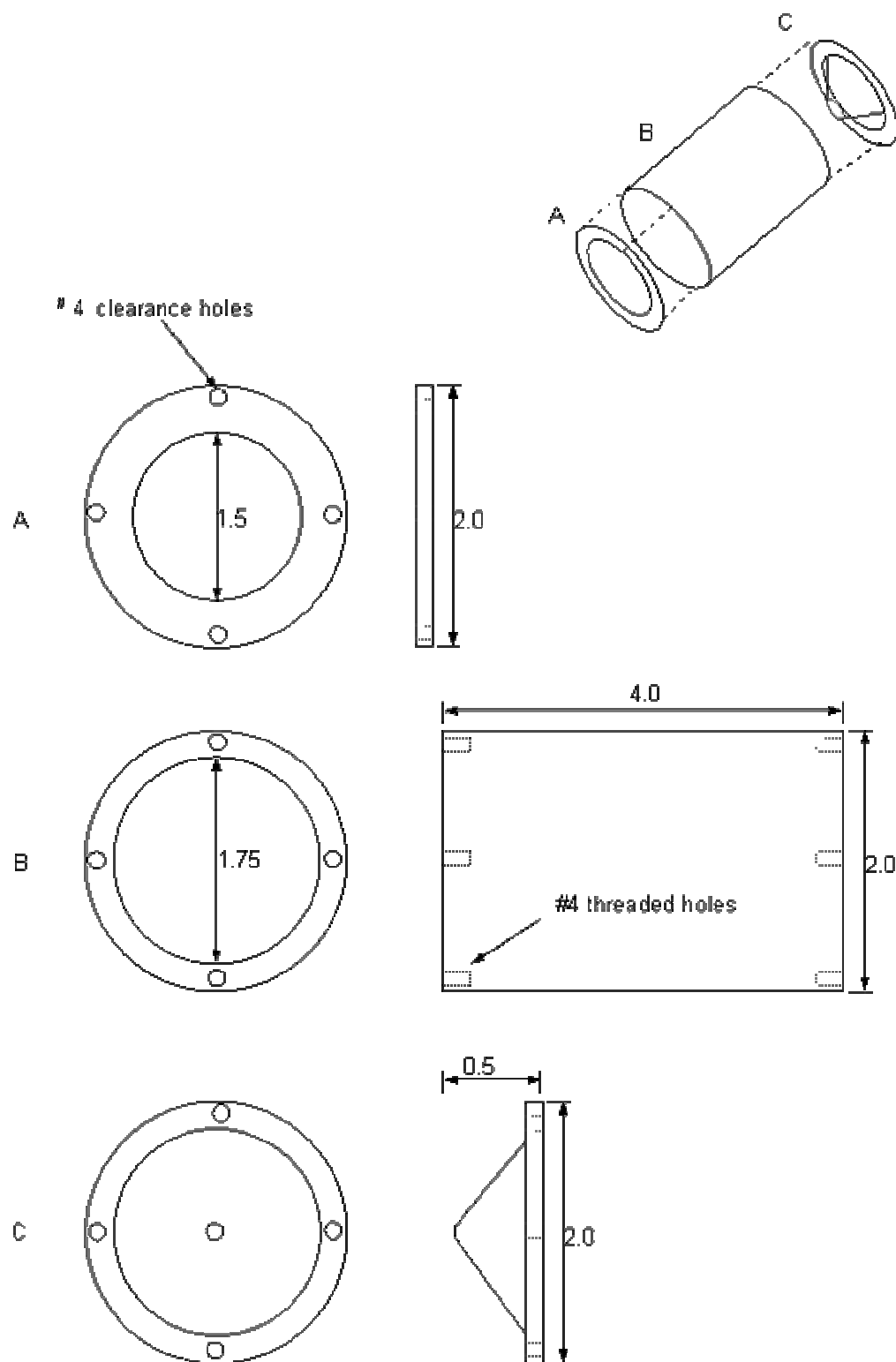


Figure 2.6 Faraday cup

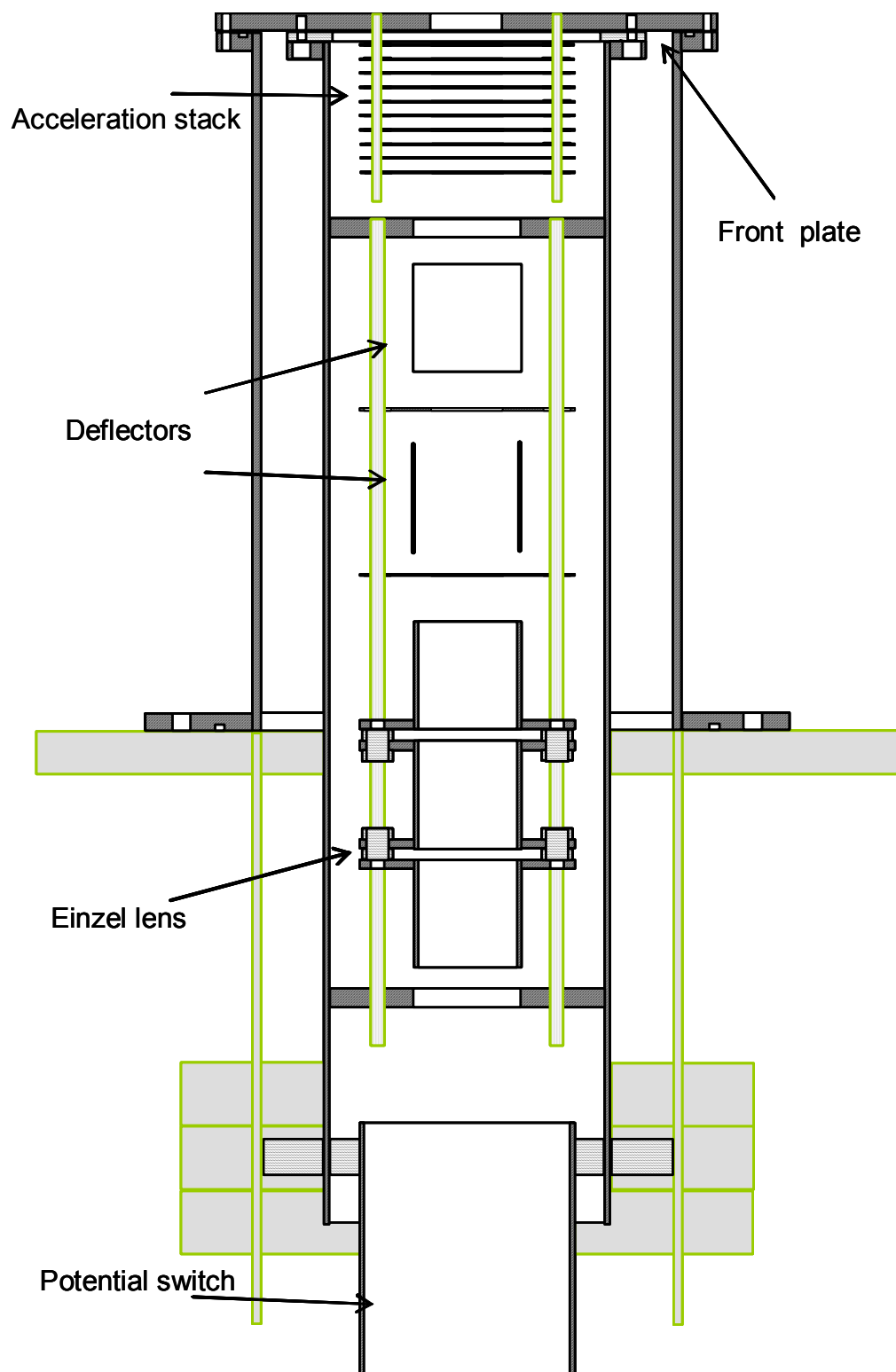


Figure 2.7 TOF: Ion optics

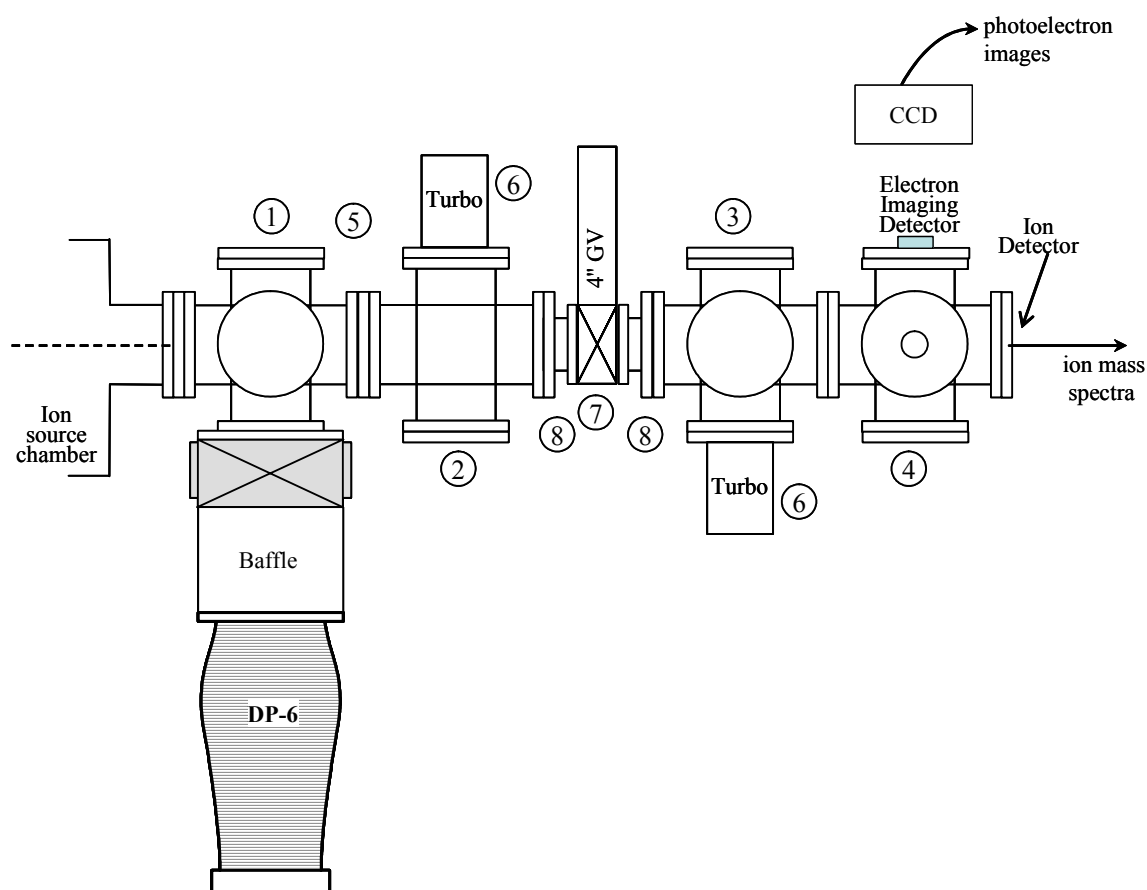


Figure 2.8 TOF: Mass spectrometer and detection chamber vacuum components: (1) 6-way CF Cross 8" Flange OD, (2) 4-way CF Cross 8" Flange OD, (3-4) 6 way CF Cross 8" Flange OD, (5) 8" OD Flange, (6) Turbo molecular pump Leybold TMP 400, (7) 4" Gate Valve, (8) 8" to 4" Reducers

plate. The extraction plate is grounded and serves as a partition between the source chamber and the rest of the instrument. The TOF and detection regions are encased in four vacuum crosses that extend out from the source chamber, and a gate valve separates the two regions. Figure 2.8 illustrates the arrangement of the vacuum components. The acceleration stack (see Fig 2.7) accelerates the ions which are then steered by the deflectors (Fig. 2.7). The Einzel lens (Fig. 2.7) focuses the ions in space. The focal point is 50 inches from the extraction plate. The ions then enter a potential switch which references the ion beam's potential to ground without altering the ion kinetic energy.

The ion repeller plate is depicted in Fig. 2.9. It sits parallel to the extraction plate; when it is pulsed ions enter the mass spectrometer. A 10 ns rise/fall-time high-voltage pulse generator (Directed Energy PVM-4210) drives the repeller plate. It is pulsed 600-1100 μ s after the nozzle trigger pulse. The extraction pulse is 250-900V in amplitude and 10-50 μ s in duration. The amplitude of the extraction pulse is adjusted for optimum Wiley-McLaren focusing. The variation in pulse length is arbitrary. However, since its trigger is linked to the potential switch for convenience, it varies as the potential switch is varied to accommodate ion size. Ions are accelerated according to their initial position in the extraction region and the amplitude of the extraction pulse. In conjunction with the acceleration stack, the ion repeller plate determines the velocity of ions through the mass-spectrometer flight tube.

The acceleration stack is composed of ten identical plates. Each plate's thickness is 0.03125" and the diameter is 3" as is shown in Fig. 2.10. The plates are mounted to the extraction plate by 2-56 threaded rods that are insulated with Teflon tubes, 1/8" I.D x 1/4"

O.D. Teflon spacers ($1/4'' \times 3/8'' \times 0.16''$) separate the plates. The acceleration stack plates are connected in series with $1\text{ M}\Omega$ vacuum-grade resistors, creating a uniform potential gradient to accelerate the ions. The extraction plate is at ground and the last acceleration plate is adjustable, typically at -1950 V . The extraction plate (shown in Fig. 2.11) is attached to the housing that encases the acceleration stack and the ion optics. The housing is illustrated in Fig. 2.12. The ion optics are secured in place by four threaded rods held within a shielding tube, which is mounted to the extraction plate, and it is held in place on the opposite end by a Teflon inset inside the six way cross. Figures 2.13 and 2.14 illustrate the shielding tube arrangement.

The deflectors are mounted so that they are electrically isolated from the supporting rods by Teflon washers ($3/16'' \times 5/16'' \times 0.40''$ and $5/16'' \times 7/16'' \times 0.16''$). The power supplies that control the deflectors are floated at -1950 V . The 110 V AC for the floated power supplies is supplied via a 110 V transformer. The deflectors' elements are shown in Fig. 2.15. They are two sets of stainless steel plates $1.5''$ by $2.25''$. One pair sits above and below the ion beam path. The other pair sits to the left and right of the ion beam, horizontal. The horizontal deflectors' voltage is typically set relative to the beam potential at $\pm \sim 70\text{ V}$ to account for momentum from the supersonic expansion, and the vertical deflectors' voltage is usually relative to the beam potential $\pm \sim 10\text{ V}$.

The Einzel Lens is depicted in Fig. 2.16. It is composed of three 1.5 long cylinders. The lens is operated in the ion deceleration regime; hence, the first and last cylinders are floated at the beam's potential, typically -1950 V , while the middle is varied

between 600-900 V. It is electrically isolated from rest of the flight tube components by Teflon washers in similar fashion as the deflectors.

After passing through the Einzel Lens, the ions then enter the potential switch, shown in Fig. 2.17. The potential switch is a 60 cm long stainless tube that is 7.5 cm in diameter. The potential switch is pulsed from the beam potential, -1950 V, to ground by a 25 ns rise/fall time high-voltage pulse generator (Directed Energy, PVX-4140). The potential switch decreases the potential of the ions within the tube without disturbing their flight path.³⁵

The previously described components interact with each other to focus anions in time and space at the point of laser interaction. Figure 2.18 shows the beam's diameter at various points within the Wiley-McLaren TOF spectrometer. The fractional numbers correspond to the diameter of the apertures of the spectrometer; three quarters of an inch corresponds to the aperture at the end of the potential switch. The decimal numbers refer to the beam's size at those aperture points with the corresponding distance at the bottom of the Fig. 2.18.

The ions are detected by a set of Chevron-type dual micro-channel plates (MCP, Burle, Inc.) with a 25 mm diameter and a metal anode. Before impacting the detector, the ions are post-accelerated by an additional 1 kV, raising their kinetic energy to >3 keV. The MCPs are mounted on the flange at the end of the time of flight tube 58 inches from the extraction plate. Figures 2.19 and 2.20 portray the detector flange from the side and inside, respectively. There is a 70 lines per inch nickel mesh in front of the micro-channel plates, which is also mounted to the flange as illustrated in Fig. 2.21. In short,

three ceramic posts are attached to the flange by 0-80 threaded rods. Three more 0-80 threaded rods extend out from the ceramic post. The MCPs detector assembly rest on the posts with ceramic washers separating the MCPs from the detector shield. The mesh is secured between two stainless steel rings that attach to the flange via the aforementioned ceramic posts. Nuts top off the threaded rods. The mesh is grounded. A voltage divider supplies the anode with the input voltage while supplying the rear MCP with input voltage minus 200V and the front MCP receives 66% of the voltage that is supplied to the Voltage divider. For example, if 2400 volts is applied to the voltage divider box, then ~2400, 2200, ~1500 is supplied to the anode, rear MCP and front MCP respectively. The electrical schematic of the voltage divider box is illustrated in Fig. 2.22.

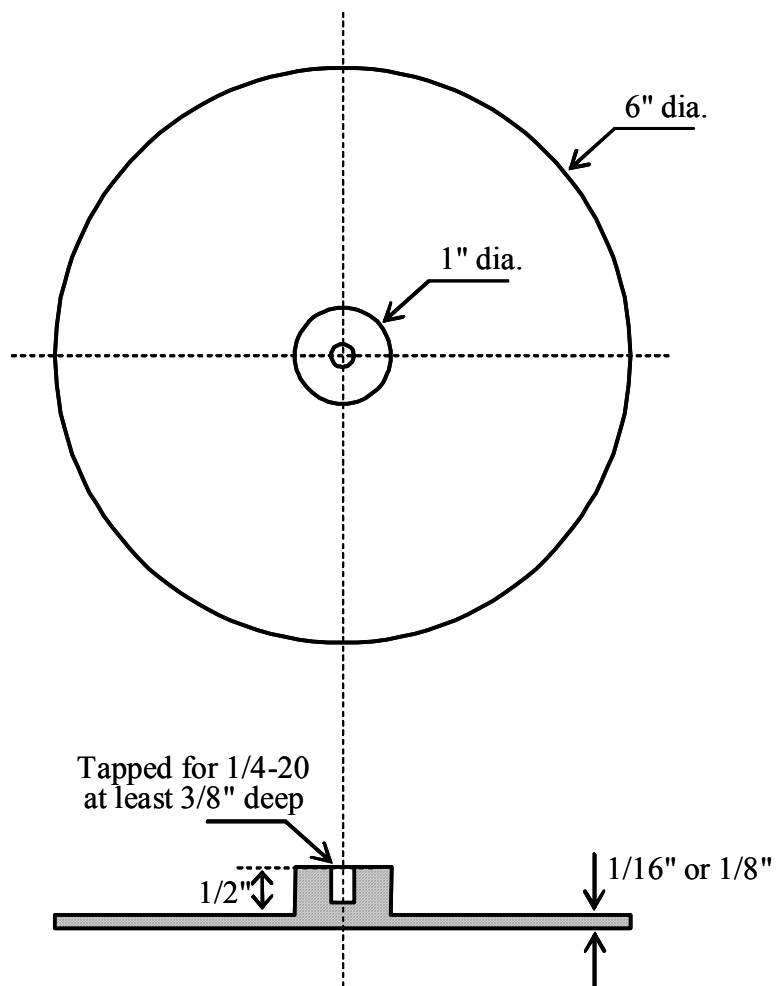


Figure 2.9 Ion repeller plate

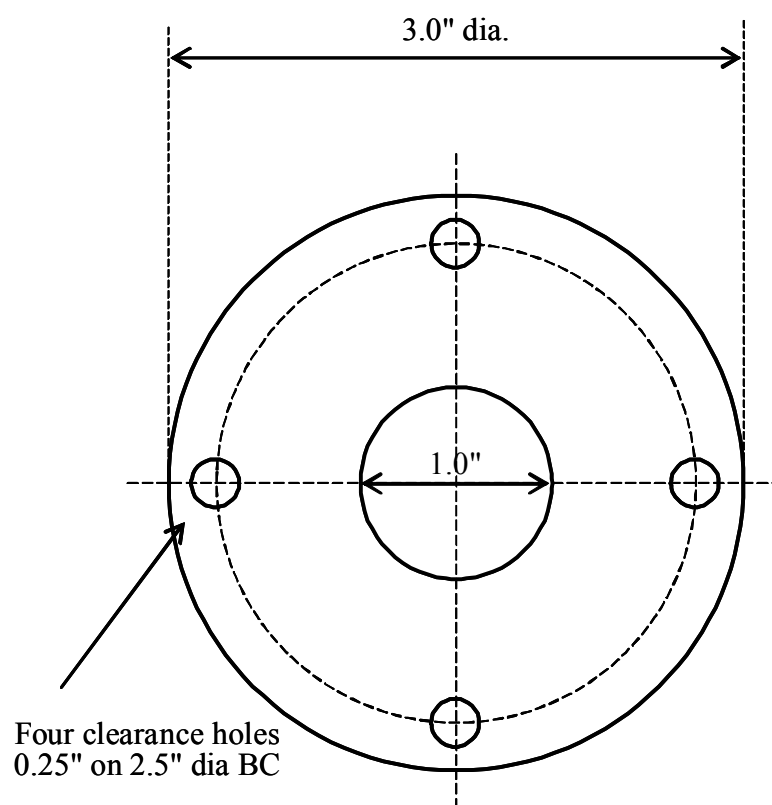


Figure 2.10 TOF: Acceleration stack optic plates

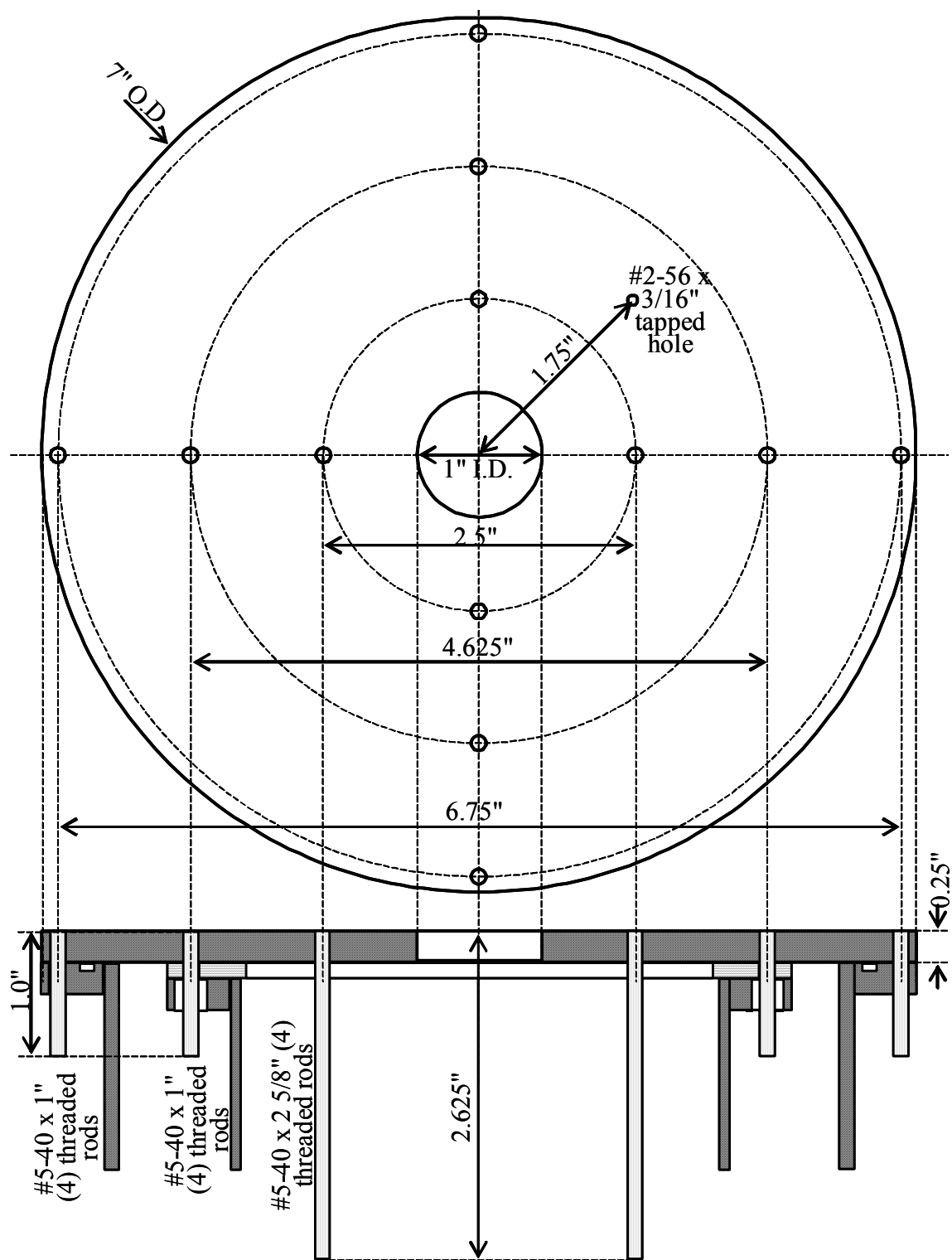


Figure 2.11 TOF: Extraction plate

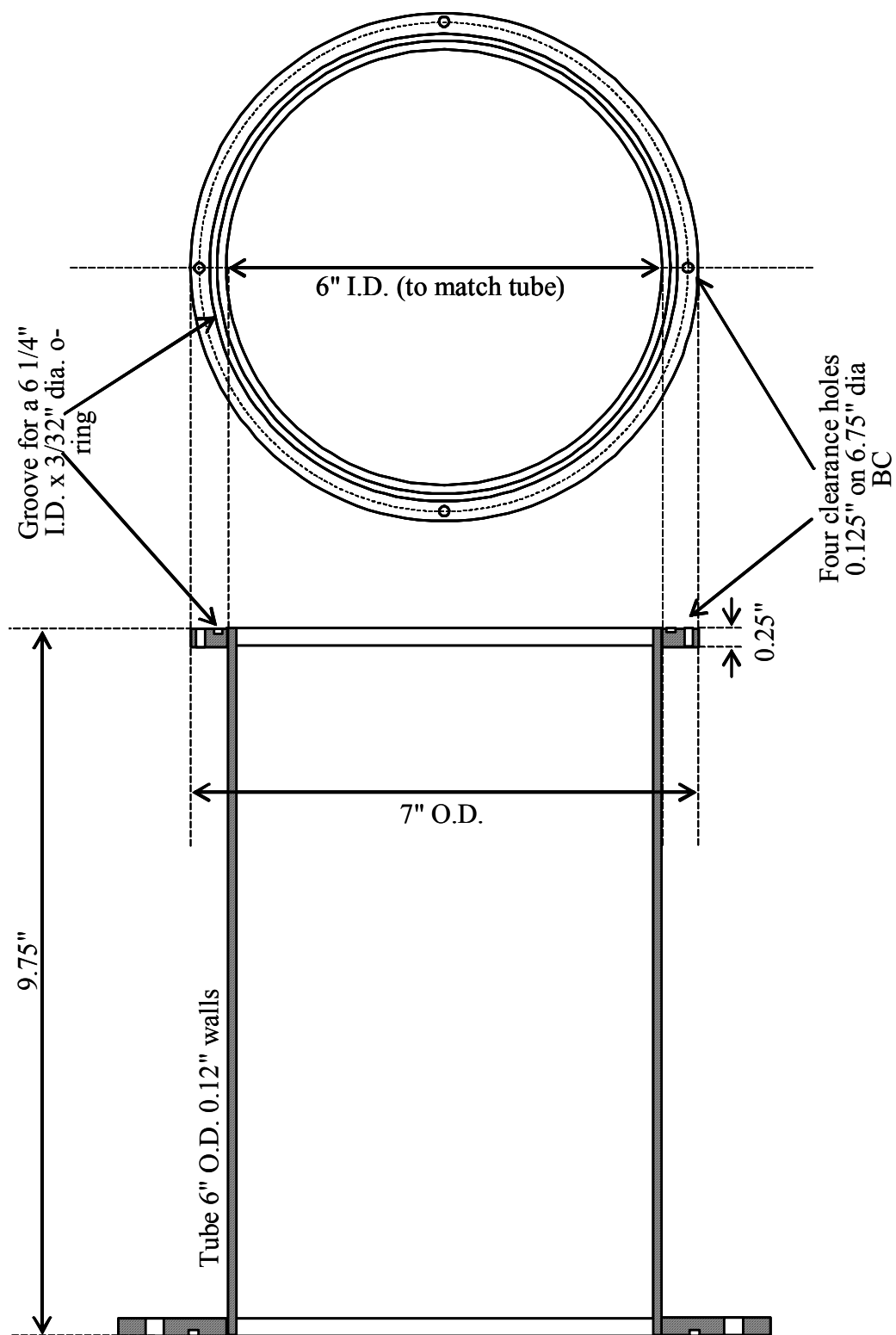


Figure 2.12 TOF: Housing extending into the ion source chamber

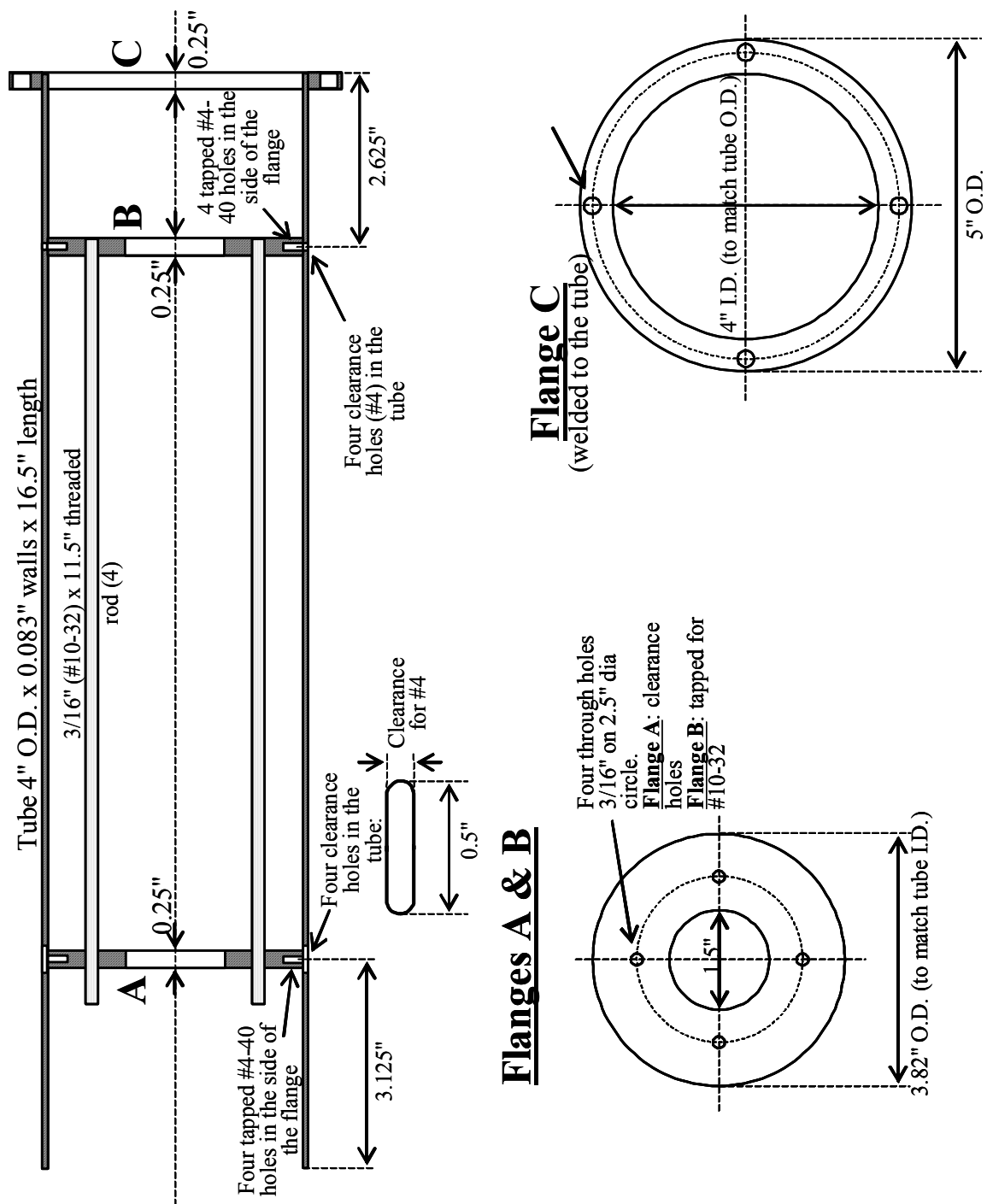


Figure 2.13 TOF: Shielding tube with mounting base

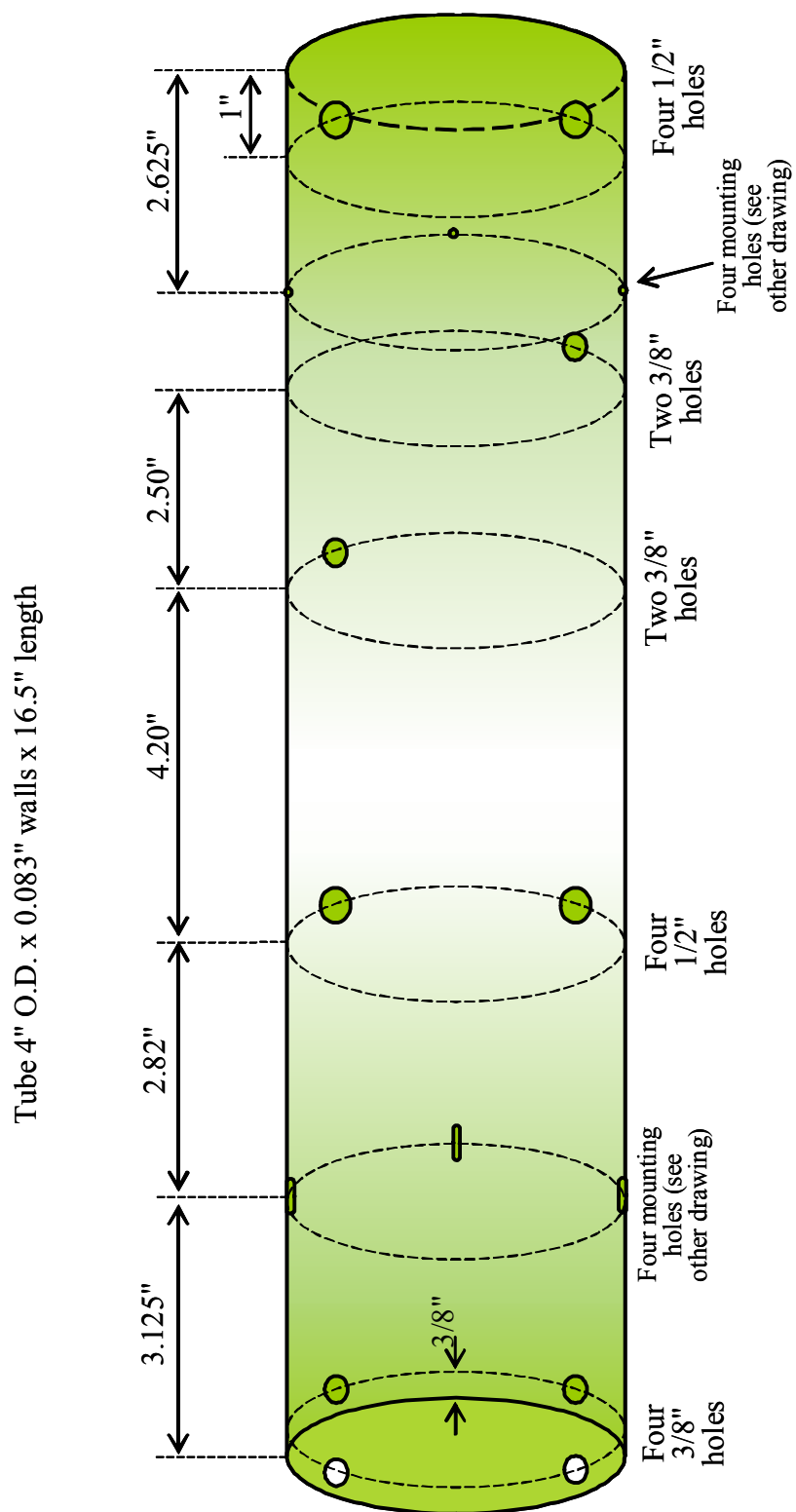


Figure 2.14 TOF: Exterior of shielding tube

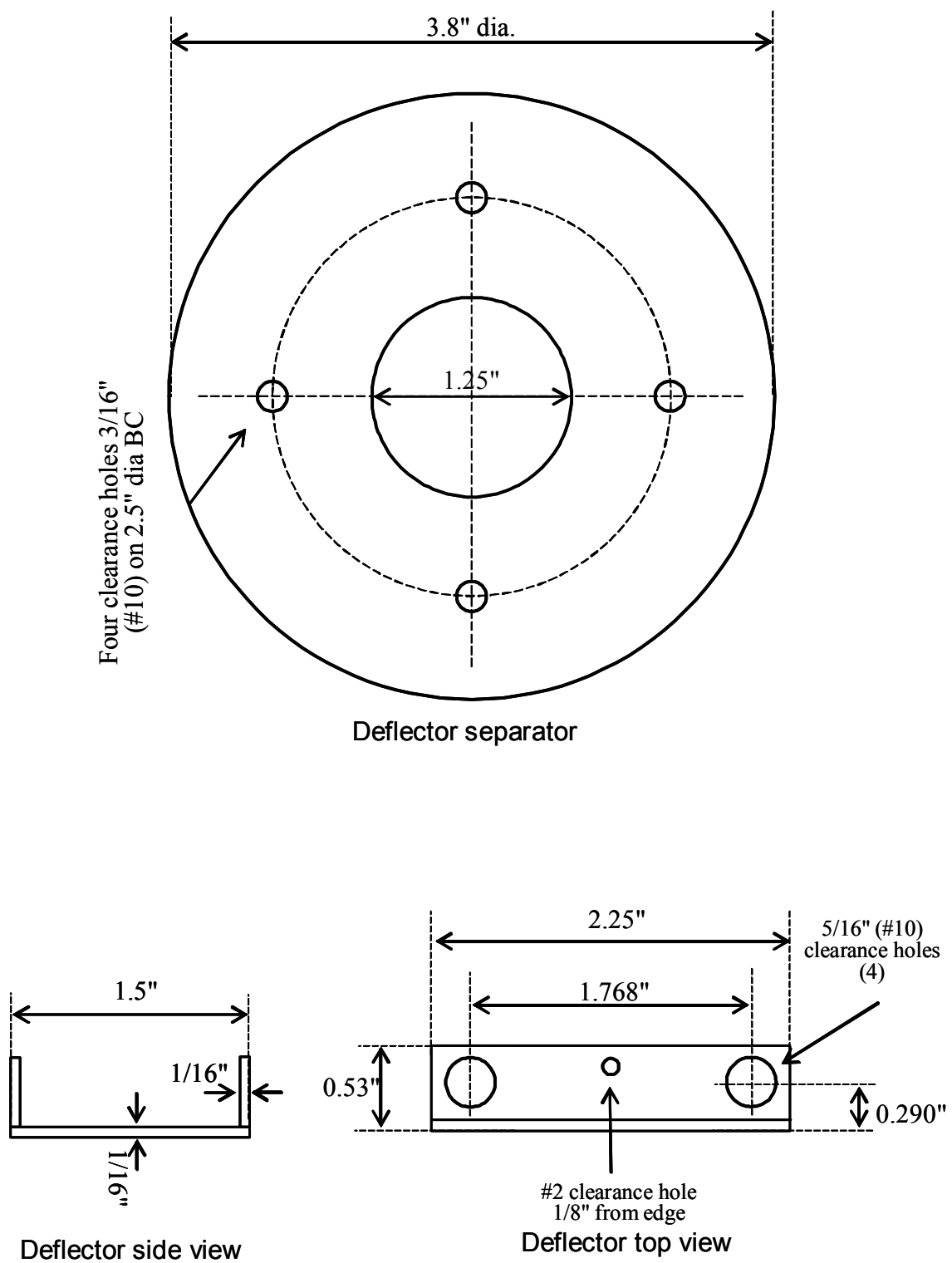


Figure 2.15 TOF: Deflectors and separator disc

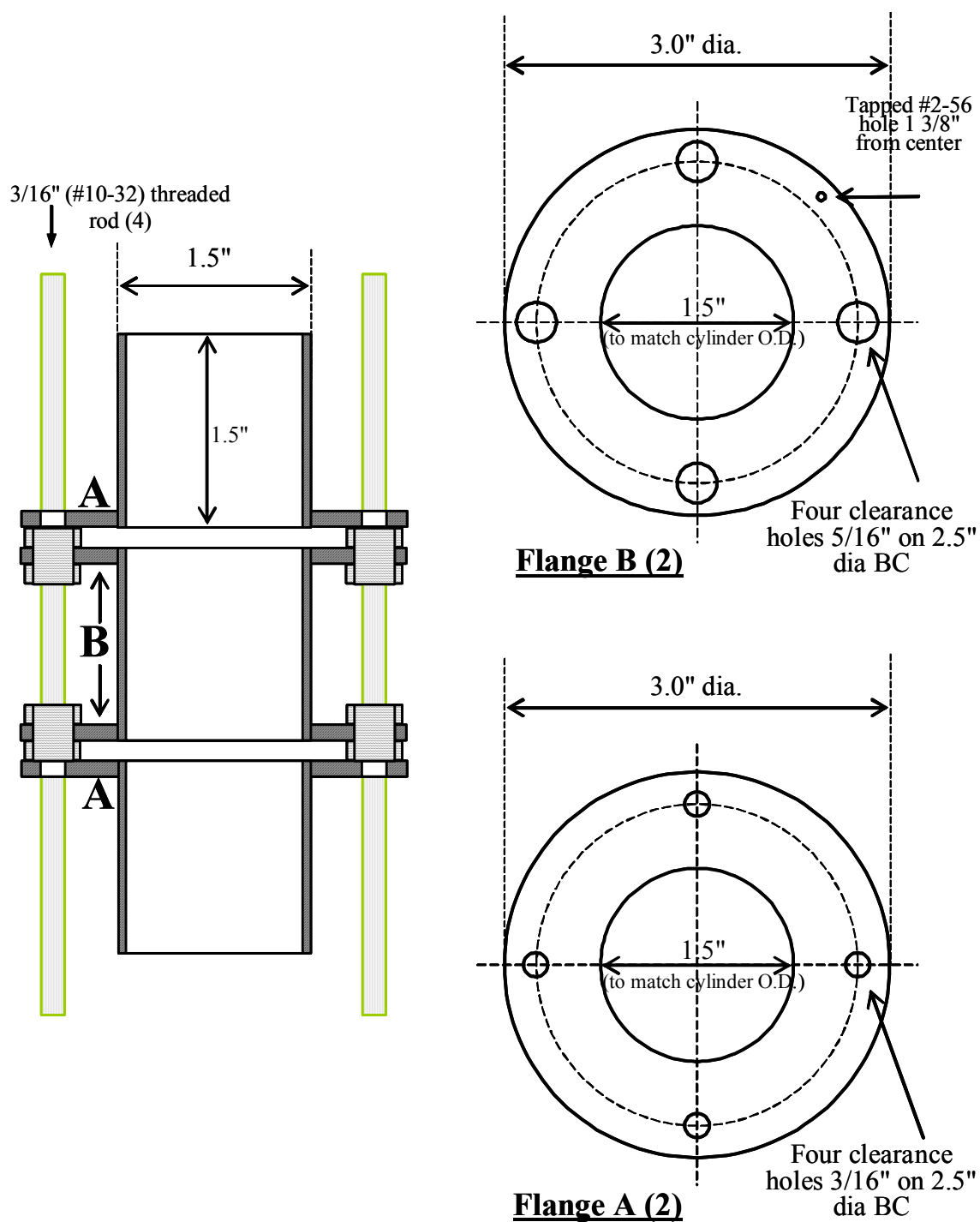


Figure 2.16 TOF: Einzel lens

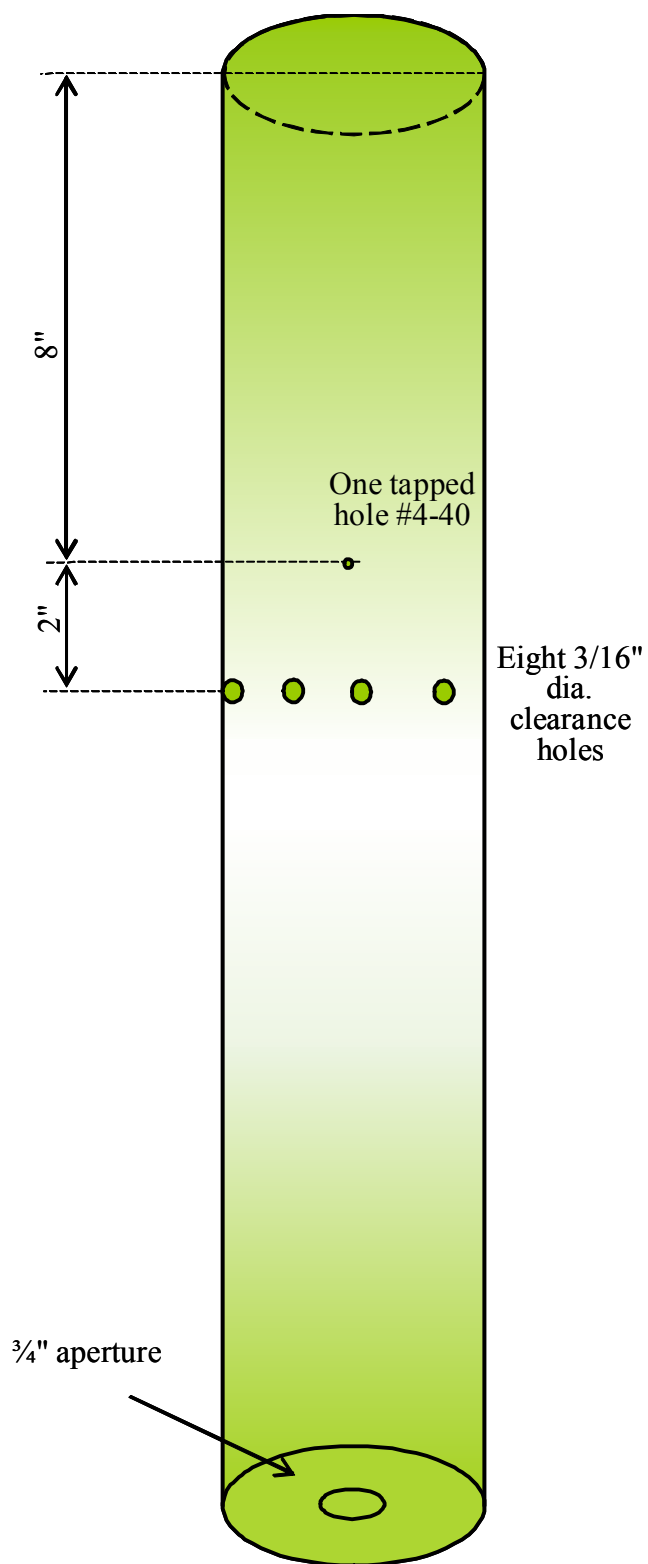


Figure 2.17 Potential switch

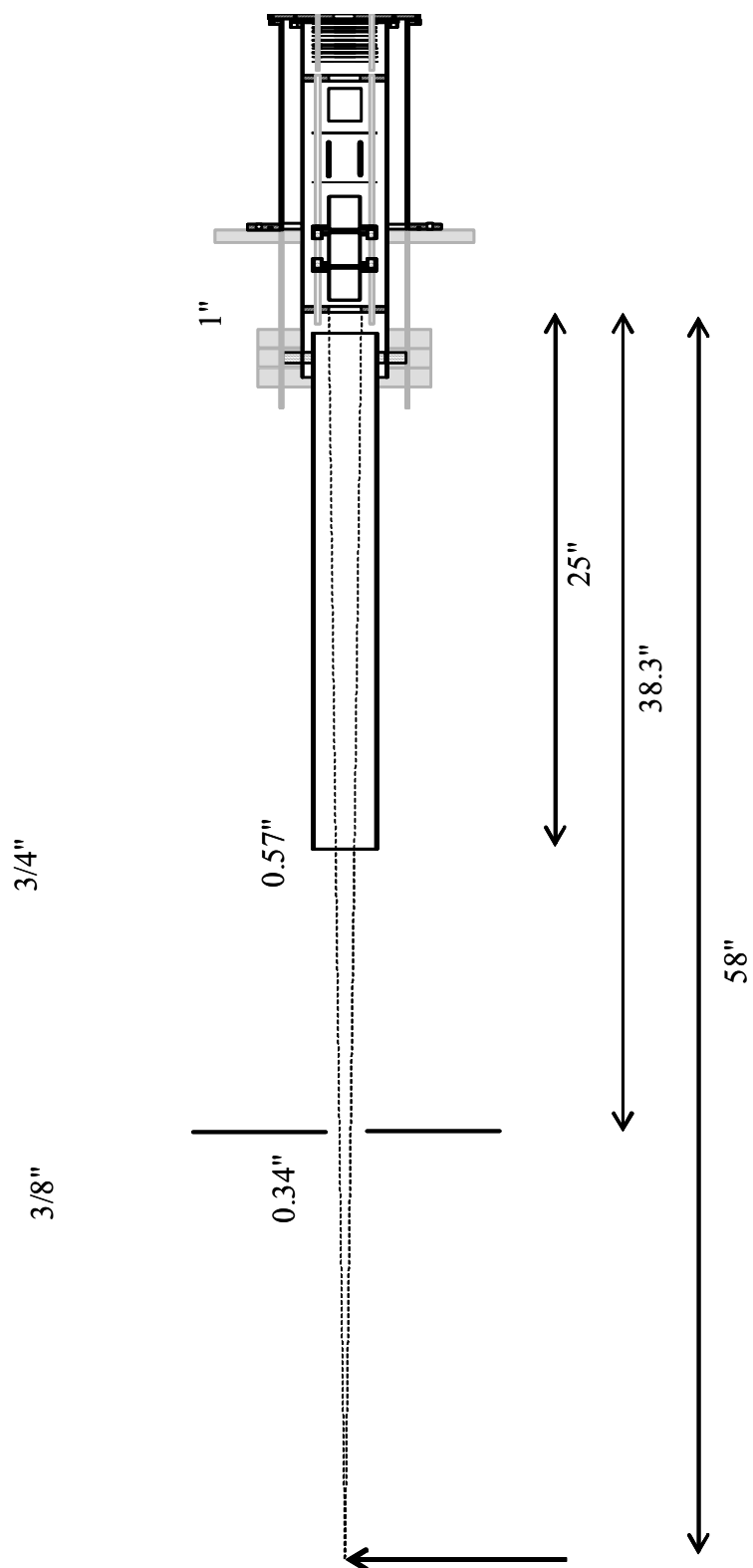


Figure 2.18 Wiley-McLaren TOF spectrometer focusing

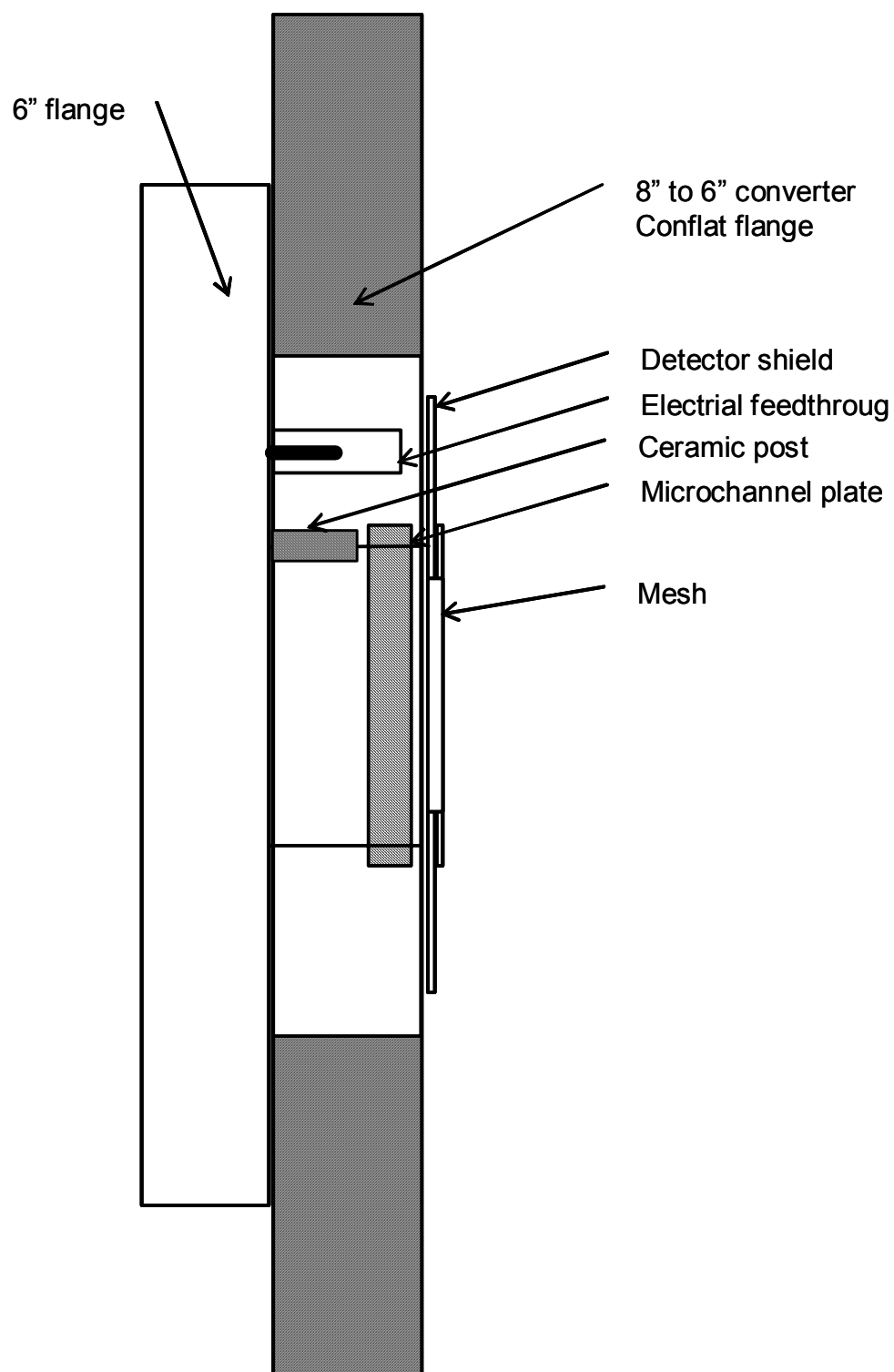


Figure 2.19 Ion detector - side view

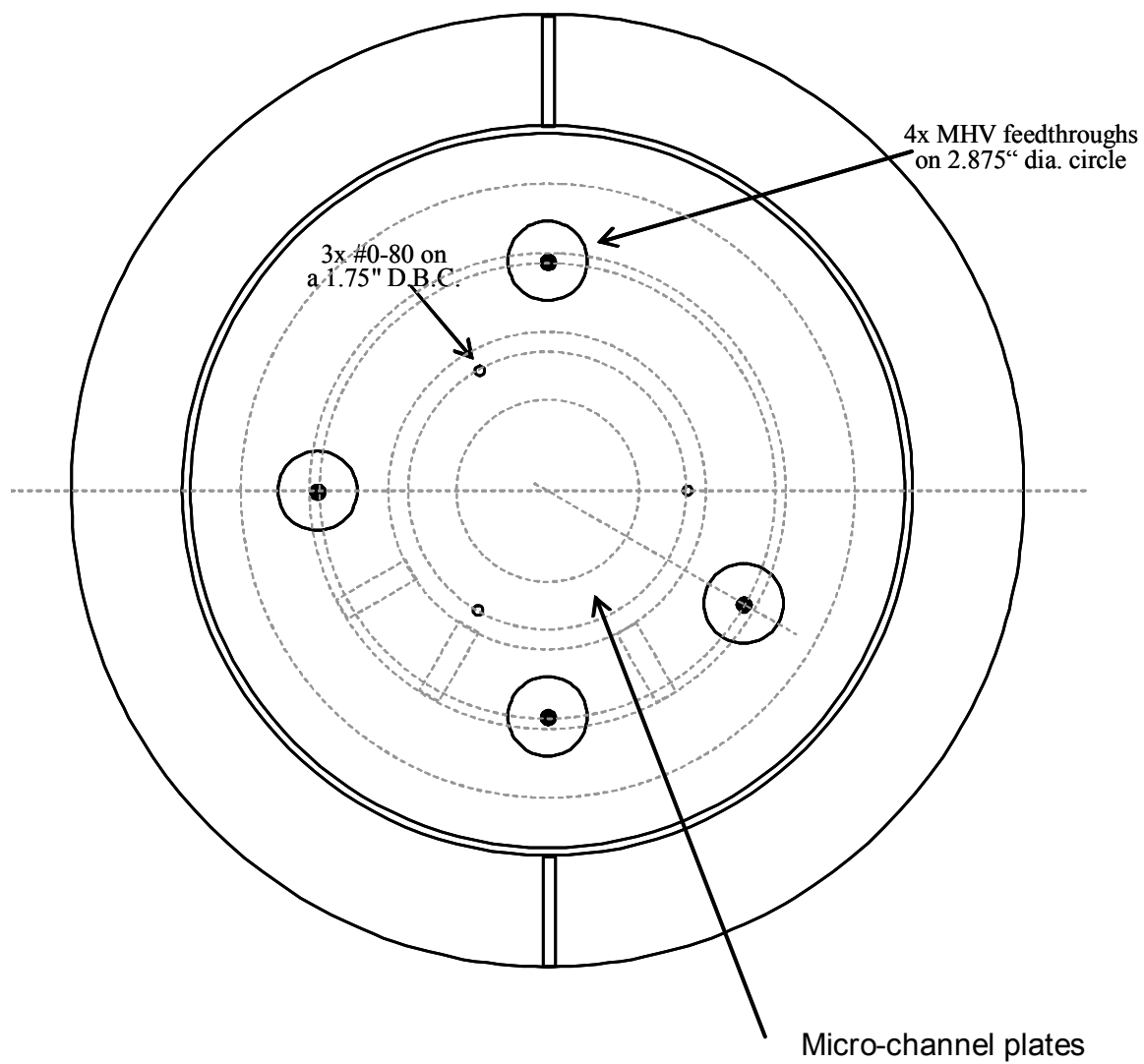


Figure 2.20 Ion detector - front view

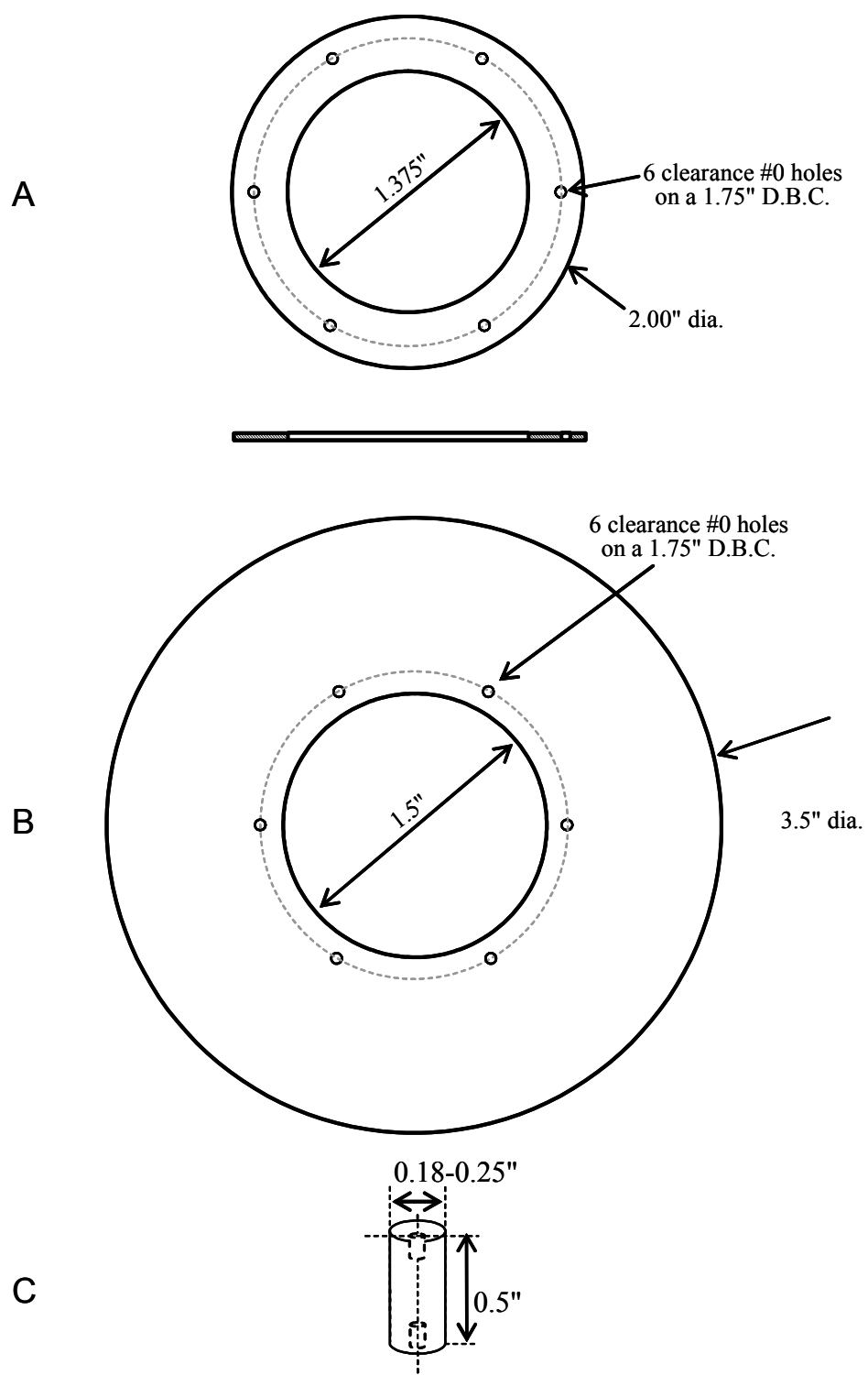


Figure 2.21 Ion detector components (A) Mesh mount (B) Detector shield (C) Ceramic stand-off

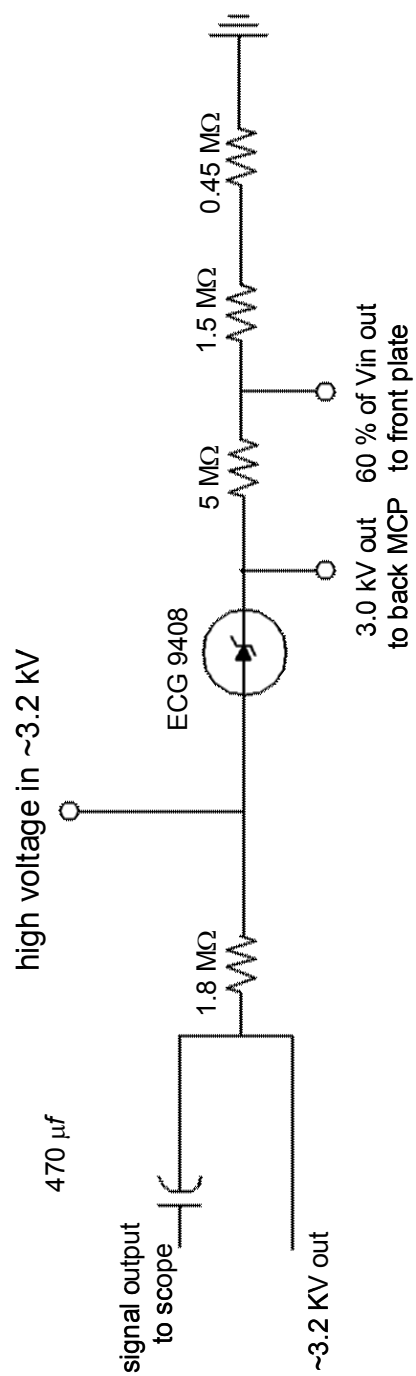


Figure 2.22 Ion detector - voltage divider and signal readout

2.4 PHOTOELECTRON IMAGING ASSEMBLY

The photoelectrons detached from the mass-selected negative ions are analyzed using the imaging technique pioneered by Chandler and Houston in 1987.¹⁰ The imaging assembly employs the velocity map imaging arrangement as introduced in 1997 by Parker and Eppink.²⁰ The velocity mapping approach effectively eliminates image blurring due to the finite size of the parent ion (or neutral) and laser beams. As a result the resolution is improved significantly. The principle is as follows. If two electrons originated from the same point in space with different velocities, they will impact the detector in different places according to the projection of their velocity vectors on the plane of the detector. If two electrons originate in different positions and have the same vector velocities, they will impact the detector at the same spot. Hence, this experimental arrangement indeed provides a velocity map of the electron detachment (or ionization process)

The imaging assembly is sketched in Fig. 2.23. Its components are a position sensitive electron detector (1), mesh (2), field free electron flight tube (3), μ -metal shielding cup (4), imaging lens (5), and post-imaging ion deflector (6). The focused ion beam crosses the laser beam at the center of the extraction region of the imaging lens. Electrons are photodetached and accelerated towards the detector by the field of the lens. The assembly is mounted vertically, with its axis perpendicular to the ion and laser beams. Electrons pass through the mesh before impacting the MCP. The mesh serves to shield the field-free electron flight tube from the potential at the front of the detector. A CCD camera monitors the phosphor screen recording the position the electrons impact on the detector.

The imaging lens is composed of three OFHC (oxygen free high-conductivity) copper plates, shown schematically in Fig. 2.24. The middle plate (see Fig. 2.23) is grounded, while the bottom and top plates are at $-V_0$ and $+3 V_0$ typically -200 V and 600 V respectively. To increase the image size these voltages are reduced; however, the ratio of one to three must be conserved. Aluminum oxide (Al_2O_3) tubes are used to insulate the plates from the 0-80 rods and nuts that are holding the lens in place.

After being accelerated by the imaging lens, the photodetached electrons pass through a field-free flight tube, 4.90" in length and $\sim 3"$ I.D. The flanges for the flight tube are shown in Fig. 2.25. Flange A is the bottom of the flight tube while flange B is the top of the flight tube. The electron flight tube is secured to the 8" to 6" CF reducing flange with four #4 socket-cap screws. The other four holes in flange B are used to secure the mesh mount to the top of the flight tube. The four holes in flange A attach the top plate of the velocity imaging lens to the flight tube. The cutaways in flange A allow the threaded rods, which connect the other two imaging lens plates together, to terminate without electrical interference. A 0.014 inch thick μ -metal sheet is wrapped around the flight tube twice to protect against the earth's magnetic field. Another layer of μ -metal covers the inside of the flight tube. The Nickel mesh (Buckbee-Mears Inc) has 333 lines per inch, and it has 70% transmission. It is stretched over a ring (Fig. 2.26) and held in place by the stretching ring which is pictured in Fig. 2.27. The mesh mount is electrically isolated from the flight tube so that it can be pulsed depending upon the needs of the experiment. The expanding electron cloud passes through the mesh and is then accelerated into the front MCP by an additional $\sim 1\text{kV}$.

The imaging detector (Burle, Inc.) includes two imaging quality 40 mm diameter MCPs and a P47 phosphor screen coupled to an outside window by a fiber-optic bundle. To discriminate against noise, the MCPs are operated in a pulsed-bias mode. The total bias across the two plates, normally kept at 1.0-1.2 kV is pulsed up to 1.6-1.8 kV for 200-300 ns window timed to coincide with the arrival of the photoelectrons. The high-voltage pulses are provided by a <25 ns rise/fall-time pulse generator (Directed Energy PVM-4150), whose output is connected to the floated detector via a 390 μ F capacitor.

The phosphor screen is monitored with a thermoelectrically cooled CCD camera (CoolSnap, Roper Scientific). The images are typically averaged for 10,000 to 30,000 experimental cycles and sent to the computer.

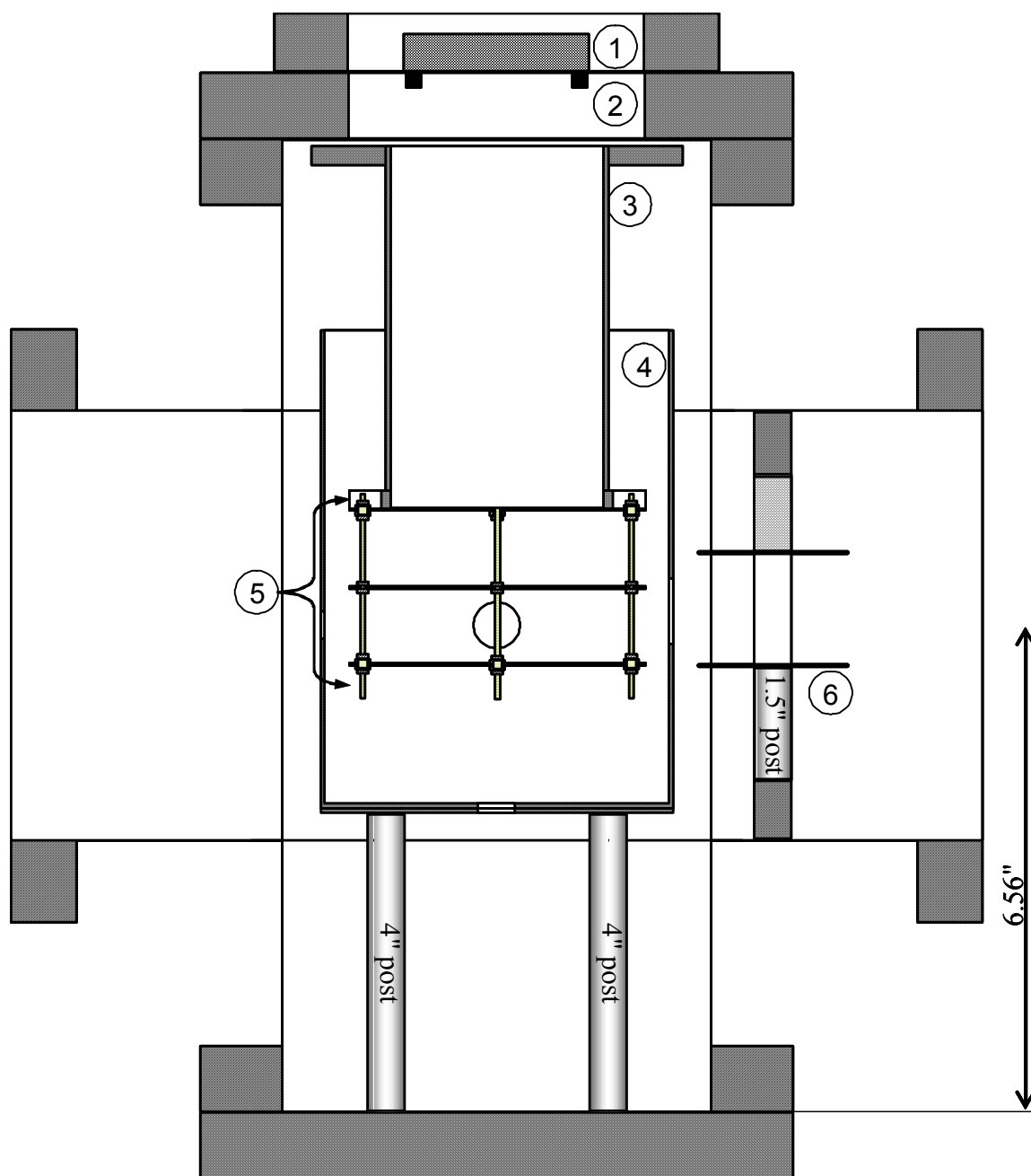


Figure 2.23 Velocity map imaging assembly overview 1) Position sensitive electron detector 2) Mesh 3) Field-free e^- flight tube 4) u-metal cup 5) Imaging lens 6) Ion deflector.

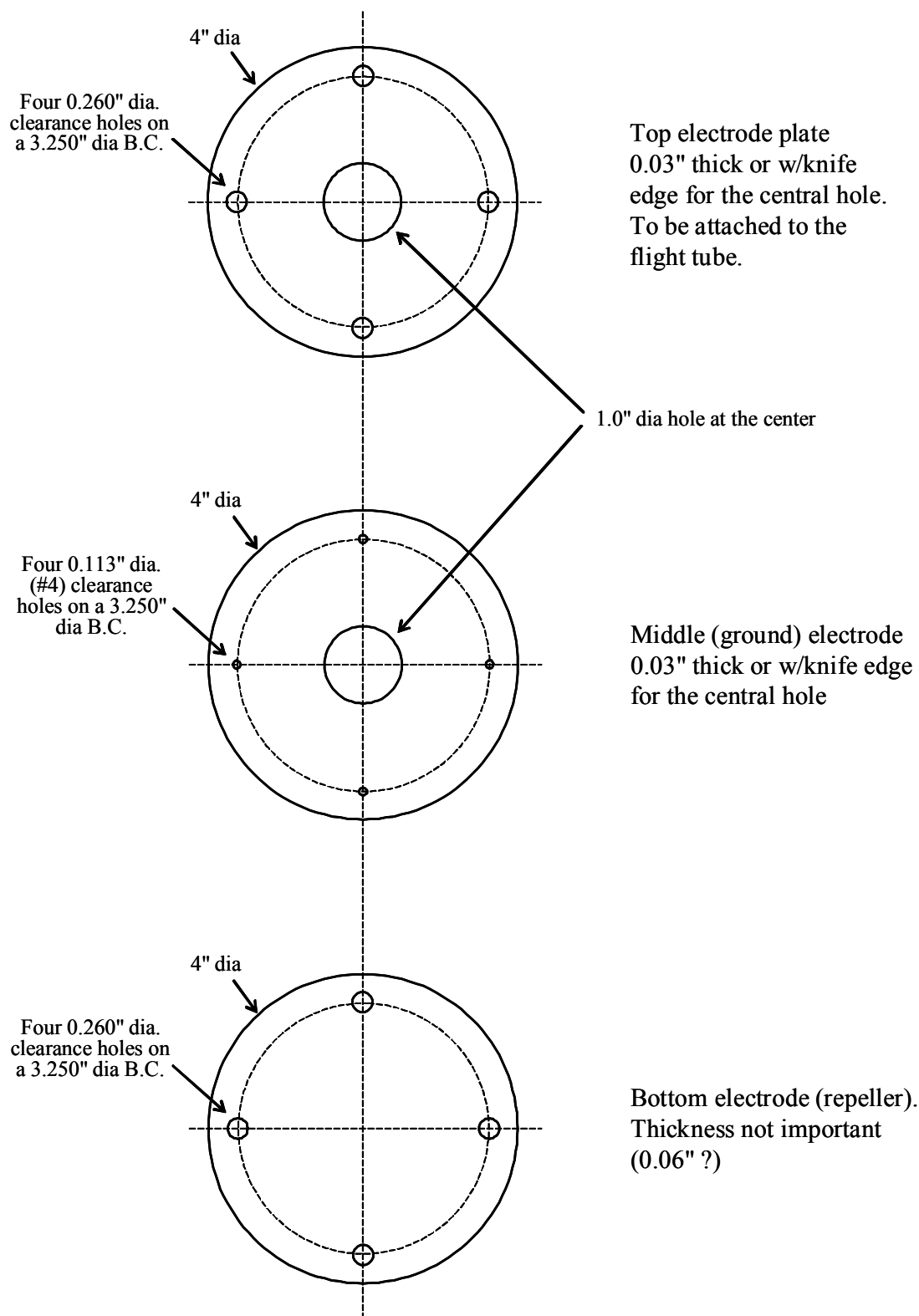


Figure 2.24 Velocity map imaging lens plates

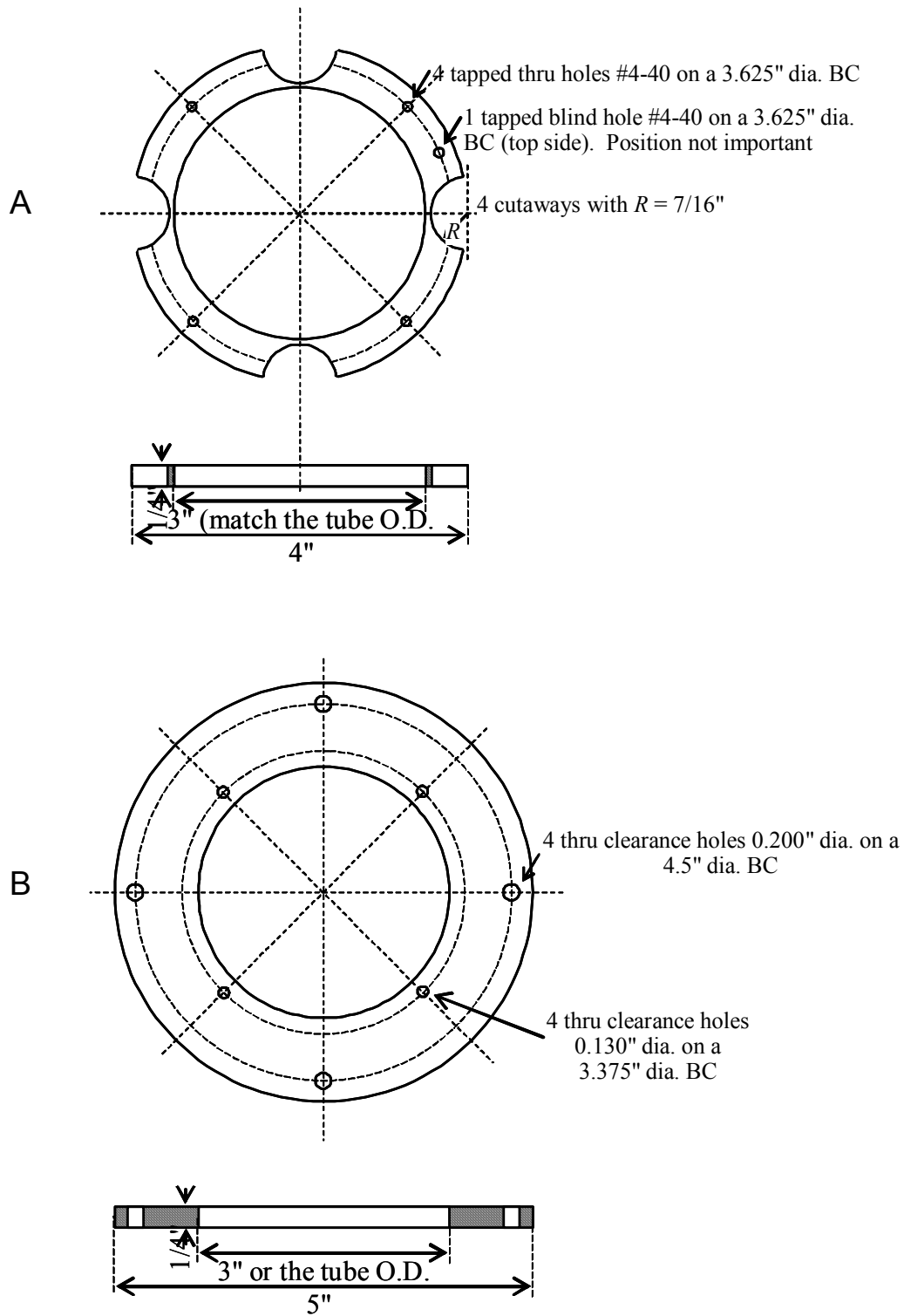


Figure 2.25 Electron flight tube's end flanges

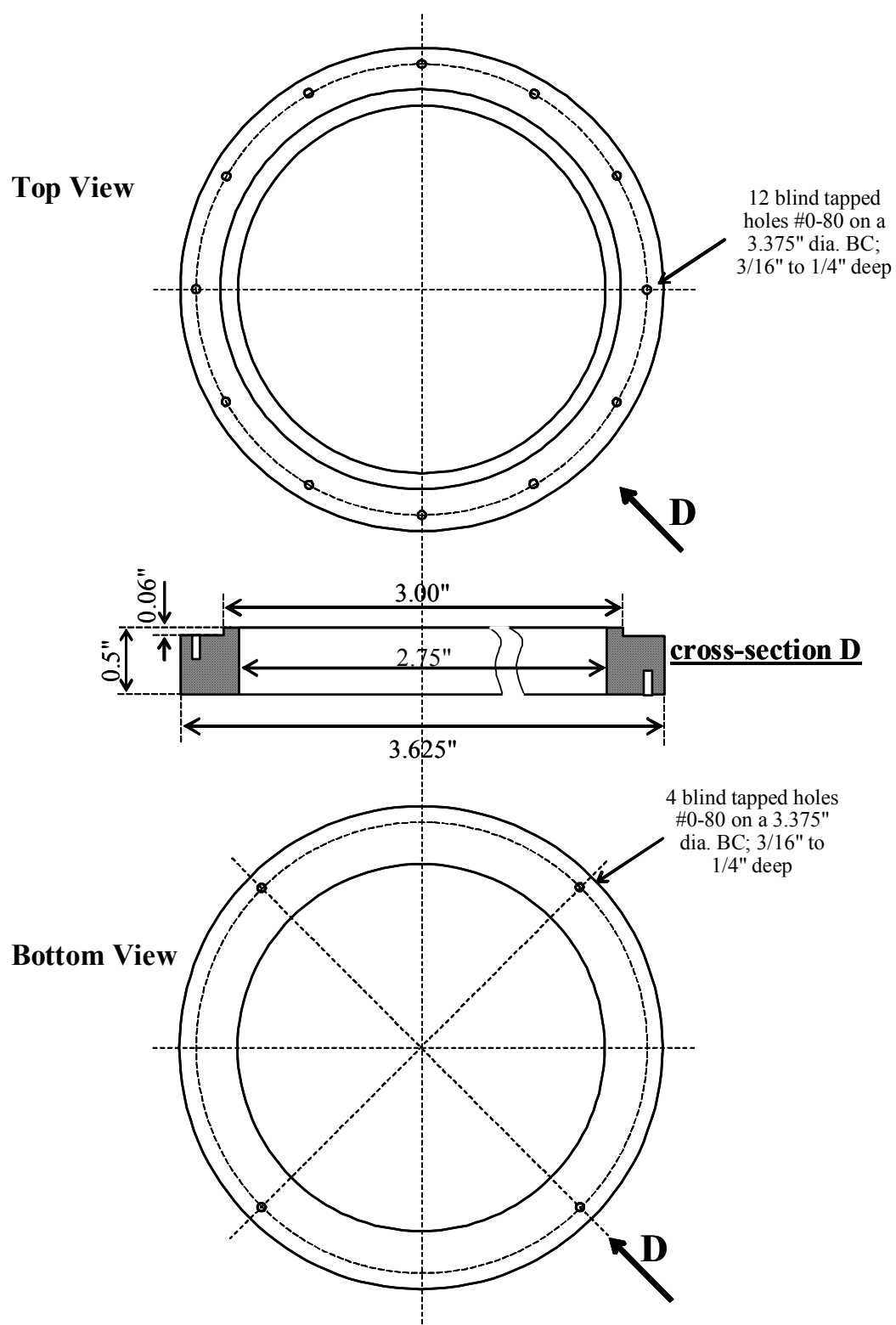


Figure 2.26 Mesh mounting ring

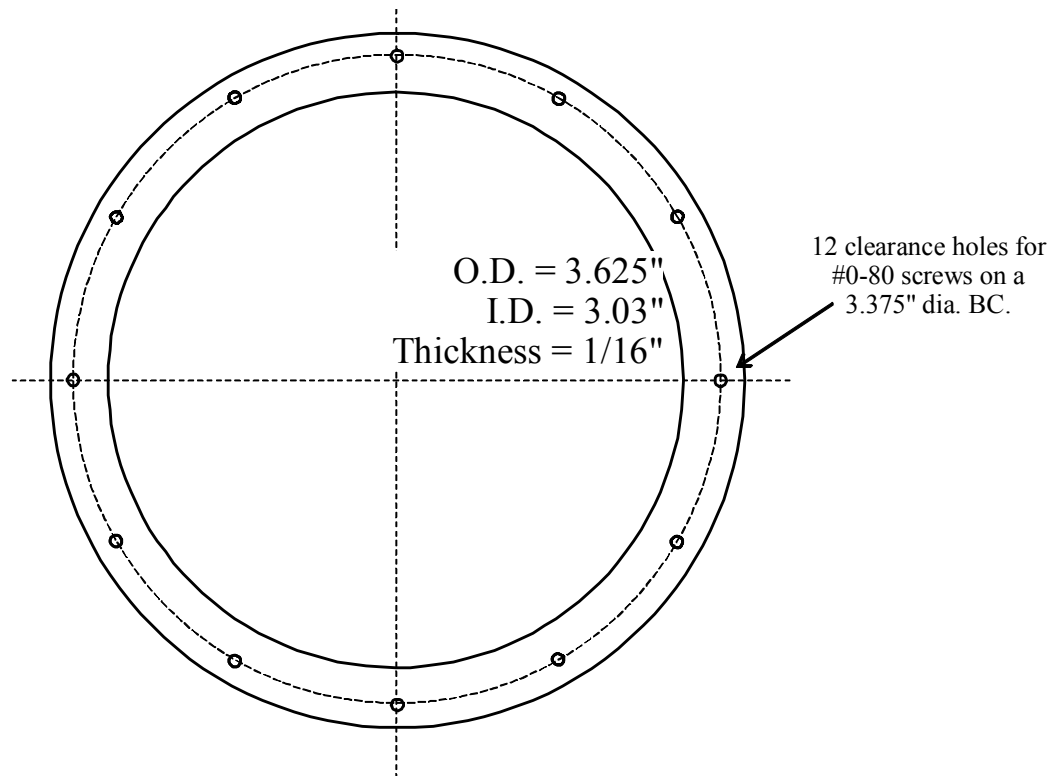


Figure 2.27 Mesh stretching ring

A μ -metal cup surrounds the velocity map imaging lens. It is schematically shown in Fig. 2.28. It has two orifices for the laser and two for the ion beam. After the ion beam leaves the μ -metal cup, the post-imaging ion deflector (see Fig. 2.23) can either correct for the beam deflection or by the imaging lens or deflect the ions away from the ion detector, allowing rapid optimization of photodetachment through maximizing laser ion pulse temporal overlap. The deflector is a set of two stainless steel plates mounted to an aluminum ring as shown in Fig. 2.29. The aluminum rings fits snugly into the nipple of the six-way cross.

2.5 LASER SYSTEM

The laser system is a commercial Ti- Sapphire based system from Spectra Physics Inc. A block diagram of the laser system is shown Fig. 2.30. It consists of a regenerative amplifier seeded by a Tsunami laser which is pumped by Millennia, a diode pumped continuous wave laser. The amplifier is pumped by an Evolution X diode pumped Nd:YLF laser. The fundamental is 800 nm with 1 mJ of power. An autocorrelator measures the beam width to be <100 fs. The beam is split in half, and then half of it enters the OPA, which can then tune the beam from ~ 300 nm to ~ 600 nm. The other half passes through a Super Tripler femtosecond harmonics generator (Super Optonics, Inc.) to frequency double the beam to 400 nm at $120 \mu\text{J/pulse}$. On some experiments the third harmonic, 267 nm $20 \mu\text{J}$, is used, which is also generated by the Super Tripler through mixing the 2nd harmonic with the fundamental in another BBO crystal.

2.6 DATA ACQUISITION

Crucial to experimental success is precise timing of all experimental components. The apparatus is timed off the laser's Pockel cells which fire at a repetition rate of 1000 Hz. A multichannel delay generator (model 555, BNC Inc) receives the trigger from the laser and after it reduces the repetition frequency to ~ 70 Hz it then triggers another multichannel delay generator (Stanford Research System, model DG535), which triggers the pulse valve via its T_0 channel. 0.5 to 1.2 ms after T_0 the repeller plate is triggered and the potential switch is simultaneously fired up to 1950 V.

The imaging MCP plates are pulsed for 200 ns. This pulse is adjusted in time to overlap with the arrival of the photoelectrons. Thus the imaging MCP plates are only on when the electrons are collected to decrease the background signal. To align the laser with the ions of interest the delay on the BNC pulse generator is adjusted shifting the entire pulse sequence of ion generation and detection as a unit.

The ion mass spectrum is measured and recorded by a digital oscilloscope (Tektronics, Inc. TDK 300). The first mass spectra of negative and positive ions recorded by the apparatus are shown in Figs 2.31 and 2.32, respectively. Note, the resolution of these mass spectra is poor because they were taken with a short ion TOF tube and without any ion optics. Figure 2.33 contains the mass spectrum of $(\text{OCS})_n^-$ cluster anions with a completed mass spectrometer and demonstrates greatly improved resolution. For static experiments, the computer records images through Winview, a software package from Roper Scientific. Most images are recorded for a five minute run or 21,300 experimental

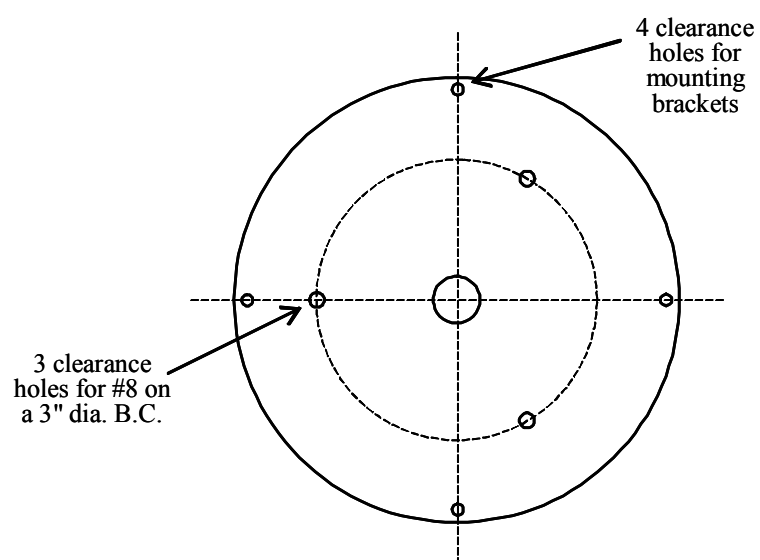
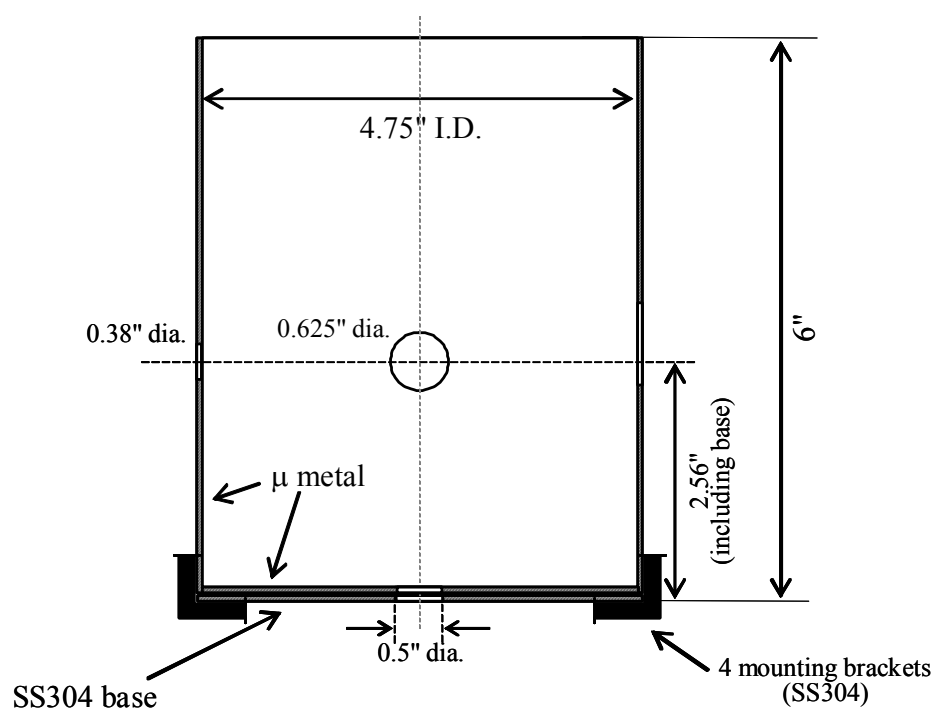


Figure 2.28 μ -metal cup

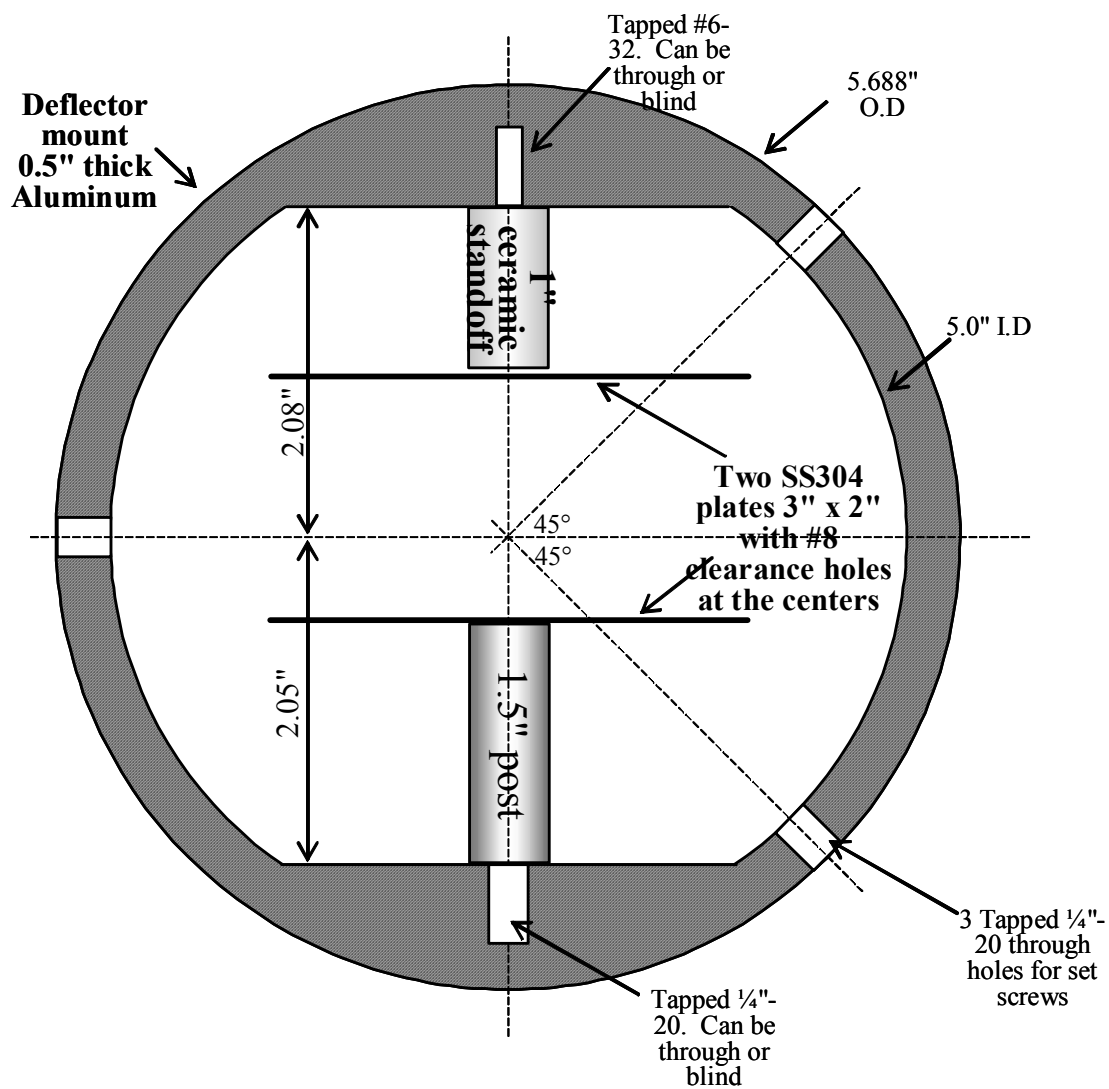


Figure 2.29 Post-imaging ion deflector

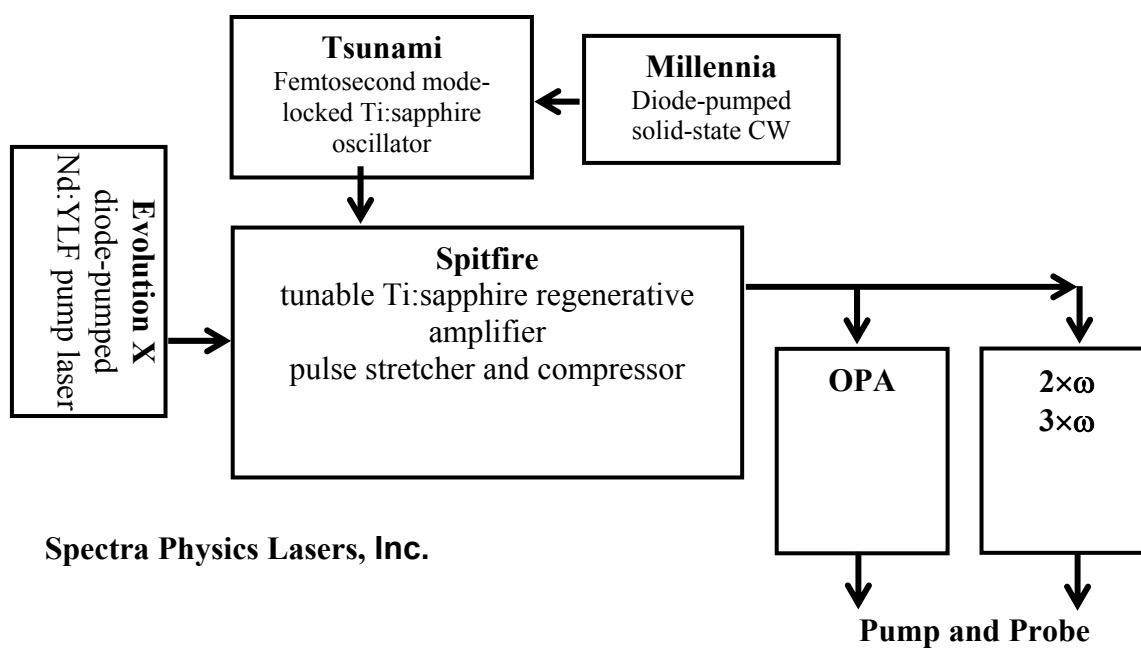


Figure 2.30 Laser system

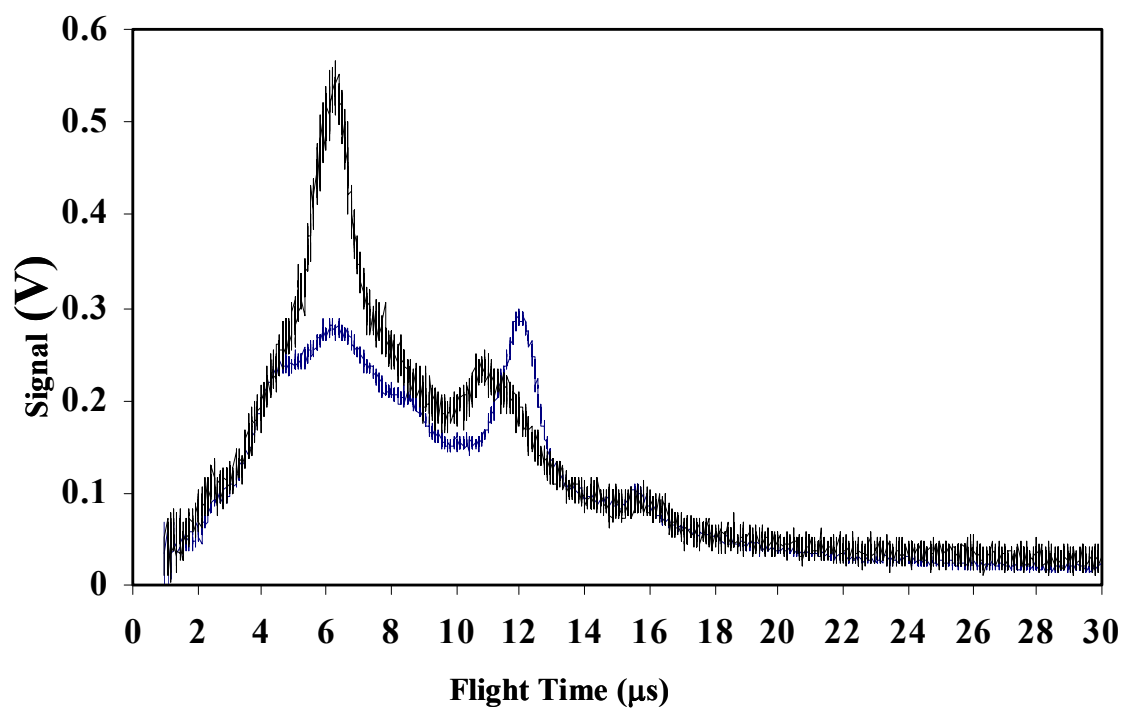


Figure 2.31 Negative ion mass spectra, without flight tube

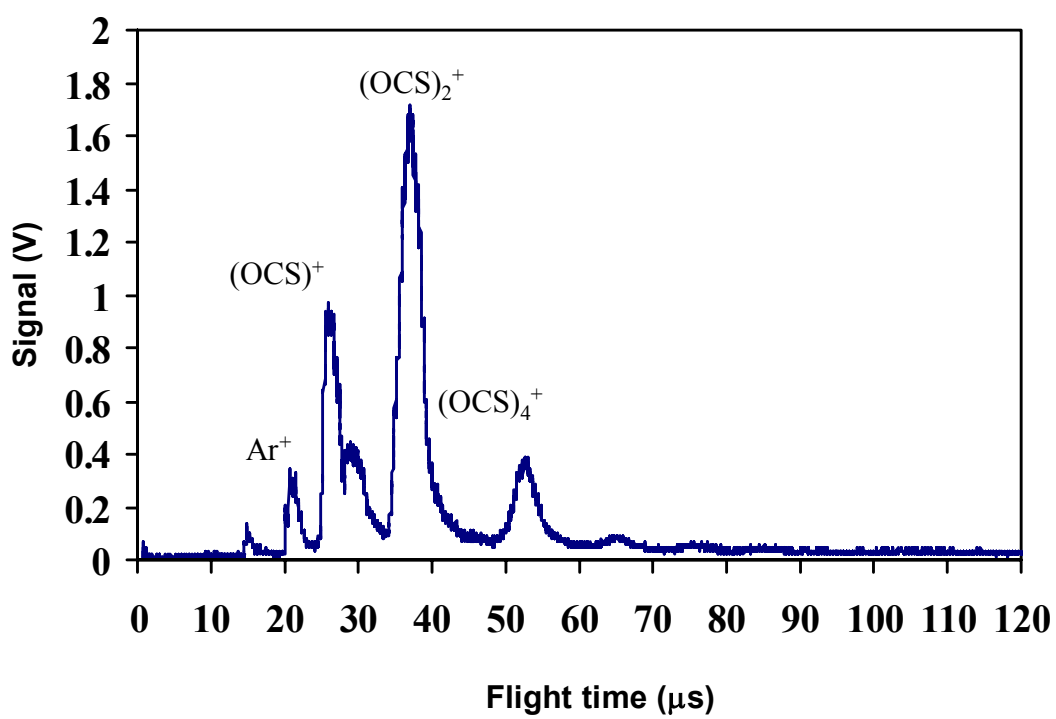


Figure 2.32 Preliminary positive ions -- short flight tube and no ion optics

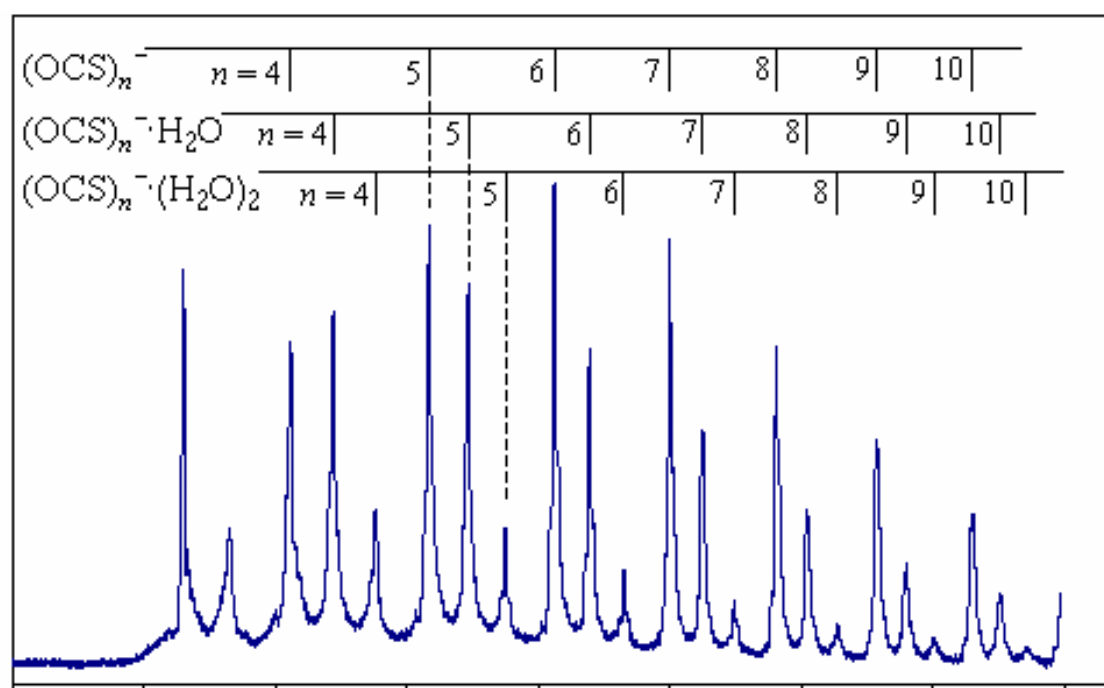


Figure 2.33 Mass spectrum of $(\text{OCS})_n^-$ cluster anions – full length flight tube

cycles. Several five minute runs are summed together to provide the final image. Time Resolved data acquisition details are provided in Sec. 2.7

2.7 TIME RESOLVED SETUP

For time resolved experiments the laser beam is divided by a 50/50 beam splitter into a pump and a probe beams. The pump pulse excites or photolyses a molecular system while a second pulse probes the evolving electronic structure through electron photodetachment. Varying the delay between the pump and probe pulses, allows the evolution of the electronic wave-function to be observed. Controlled temporal separation of the pump and probe pulses results from passing one pulse through a motorized translation stage (Newport ESP300 Universal Motion controller). By varying laser's beam path, a delay between the two beams is generated and controlled. A change of 0.03 mm in the path length corresponds to 100 fs. The beams are recombined before entering the reaction chamber using another 50/50 beam splitter. The polarization of the two beams is parallel to each other and to the ion beam. The combined beams are mildly focused with a 1 m focal length lens positioned ~45 cm before the intersection with the ion beam.

The position of zero pump-probe delay for one color experiments is determined by observing interference fringe patterns when the two laser pulses overlap both in time and space. The variation of the pattern contrast ratio as the delay stage is moved gives an indication of the temporal overlap (cross-correlation) of the pump and probe pulses. The cross-correlation width measured before the entrance into the vacuum chamber was

determined to be approximately 250 fs. This value defines the approximation time resolution of the experiment at 388 nm.

The pump-probe photoelectron images may contain signal from either the probe and/or the pump alone. A sequence of four images is obtained to account for the background signals from the probe and the pump. Mechanical shutters (Uniblitz, Vincent Associates, Inc) are used to block and unblock the laser beams in 10 second intervals in the following pattern: (1) pump-probe together (2) probe alone (3) pump alone and (4) neither laser entering the reaction chamber. A one second delay occurs between intervals to allow the shutters to open and close. The shutters are controlled remotely by the data acquisition software, V++ by Digital Optics. The pump-probe signal is obtained from subtraction of (2) and (3) from (1) and the dark-count (4) is added to correct for its double subtraction incurred in the above procedure. At each pump-probe delay, the experiment is continuously cycled through stages (1)-(4) until a suitable-quality pump-probe image is accumulated. A typical experimental run entails accumulating for 100 cycles of the above four-stage loops a total of 280,000 experimental cycles.

2.8 DATA ANALYSIS

Below is an overview of the analysis procedure applied to the images. The raw photoelectron images collected in the experiments are reconstructed by Abel inversion.¹⁶ All images are obtained with the laser polarization set parallel to the detector and vertical in the image plane. Raw images are two-dimensional projections of the three-dimensional (3D) distributions of photoelectron velocity vectors, while the reconstructed images show the cross-sections through the original 3D distributions in a plane containing the

cylindrical symmetry axis, defined by the laser polarization direction.¹⁶ These cross-sections are obtained from the experimental images using the Basis Set Expansion method developed by Reisler and co-workers.³⁶ The method uses a fitting procedure, which relies on the expansion of the raw image with a large basis set of functions that are the analytical Abel transforms of narrow Gaussian functions. The latter constitute the basis set for the reconstructed image.

In the images obtained in this work, electronic and in some cases vibrational transitions can be resolved. The imaging resolution is defined in absolute terms as Δv in the velocity domain. Because of the $eKE \propto v^2$ scaling, the best energy resolution is achieved for the slowest electrons. Taking advantage of this feature, the photodetachment transitions to different neutral states can be brought into “focus” through changing the photon energy.

Photoelectron energy spectra and PADs are obtained by integrating the reconstructed images, including the necessary Jacobian factors.¹⁶ The spectra are plotted versus electron binding energy $eBE = h\nu - eKE$, allowing for direct comparison of the data obtained at different wavelengths. The PADs are extracted by integrating the signal intensity at a specific angle over the range of radii that encompass the ring (transition) of interest. The asymmetry parameter β is determined by fitting the PADs using the expression for differential cross-sections:³⁷

$$d\sigma / d\Omega = (\sigma / 4\pi) [1 + \beta P_2(\cos \theta)], \quad (2-1)$$

where θ is the angle between the laser polarization and the velocity vector of the ejected

electron and $P_2(\cos\theta) = (3\cos^2\theta - 1)/2$ is a Legendre polynomial. The asymmetry parameter describes the PAD's symmetry. It can range from -1 to 2. $\beta = 0$ corresponds to an isotropic PAD, while $\beta = 2$ signifies a transition that has its peak intensity along the laser polarization axis. On the other hand a $\beta = -1$ signifies a transition's peak intensity is perpendicular to the laser polarization axis.

The wave function of the free electron produced upon detachment from a bound orbital can be expanded in terms of partial waves characterized by definite values of the orbital angular momentum. For example, in the one electron approximation, an electron detached from an atomic p orbital produces s and d waves, in accordance with the selection rule $\Delta\ell = \pm 1$. Near the detachment threshold, the cross-section for each wave is well approximated by the Wigner law,³⁸ and thus the relative weight of the isotropic s wave is expected to be greater for slower electrons.¹ While the threshold scaling of the cross-section depends only on the ℓ quantum number (in the absence of long-range interactions), the corresponding PAD is dependent on both ℓ and m_ℓ . For example, for p waves the angular distribution corresponding to a p_z wave peaks along the z axis, while combinations of p_x and p_y waves produce a peak in the direction perpendicular to z , the laser's polarization vector.

For molecular wave functions, ℓ is not a good quantum number. Reed et al approached molecular detachment from two conceptually different viewpoints.¹² The first expands the parent MO as linear combination of atomic orbital centered in the molecular frame. This is an expansion of the central-potential model for atomic ionization and

photodetachment.³⁷ In the other approach symmetry arguments and dipole selection rules are used to determine the symmetry of the free (photodetached) electron wave function. We then expand the free electron wave function as a summation of s and p atomic orbitals, relying on the approximate Wigner threshold law for anion photodetachment.³⁸ These methods are described with examples in subsequent chapters.

3 PHOTOELECTRON IMAGING OF ATOMIC ANIONS

3.1 INTRODUCTION

This chapter describes the photoelectron imaging of atomic anions. Atomic Anions were imaged first for their narrow well studied photoelectron spectra enabling us to test and calibrate our apparatus. Interpretation of atomic anions allowed us to develop approaches for analysis of the spectral profile and photoelectron angular distribution (PAD) of the photoelectron images. Photodetachment from atomic anions such as I^- , O^- and S^- demonstrate the Cooper-Zare model for PAD. The electron affinity of neutral I, O S corresponding to detachment energies of I^- , O^- , and S^- are 3.06 eV, 1.46 eV, and 2.08 eV.^{39,40}

3.2 RESULTS AND DISCUSSION

3.2.1 Iodide

Iodide Results

Gas phase I^- was produced by flowing argon gas at a pressure of 1.5 atm over iodine crystals and expanding into the chamber via a pulsed valve. The first Photoelectron images of I^- at 400 nm and 267 nm are shown in Fig. 3.1 along with energy level diagrams showing the photon energy at each wavelength in relation to the spin-orbit states of I. The 267 nm image is significantly larger than the 400nm image due to the greater kinetic energy imparted to the electrons by the higher photon energy (4.6 eV vs. 3.1 eV) causing them to fly faster. The images are projections of the 3D distribution of the photodetached electrons on to the 2-D surface. To obtain a slice

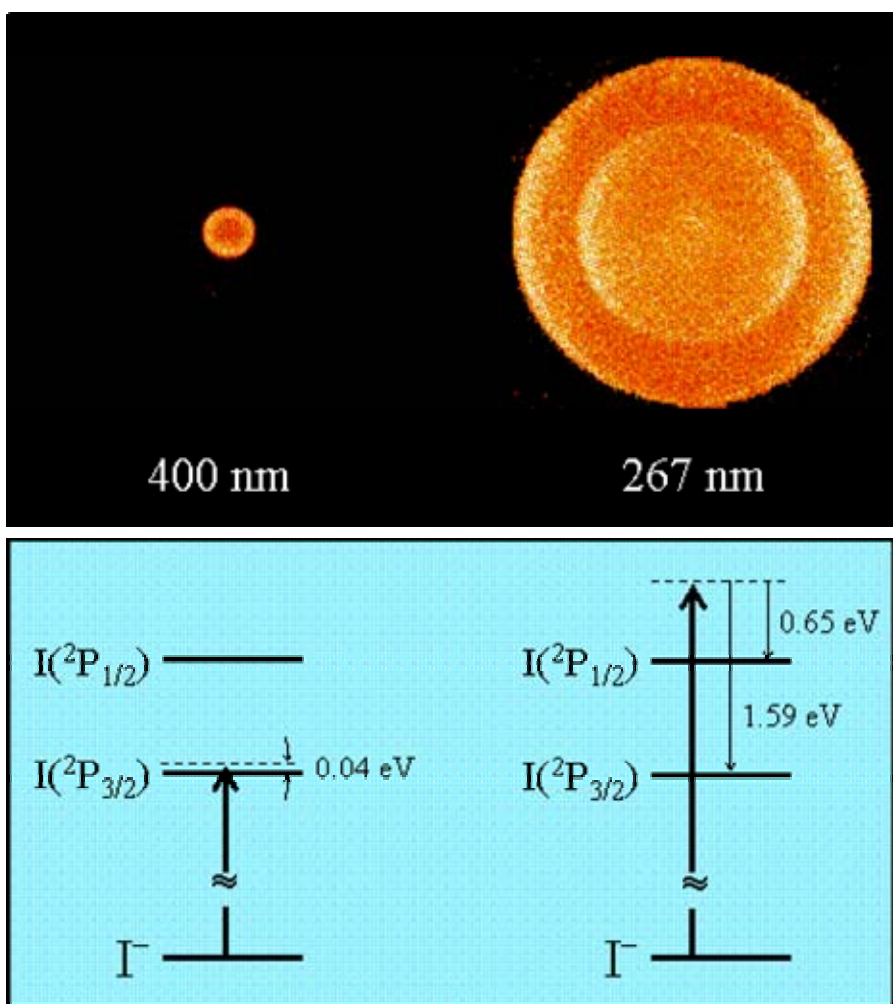


Figure 3.1 The first photoelectron images captured with our negative-ion photoelectron imaging spectrometer. Photoelectron images of I^- at 400 and 267 nm. Below energy diagrams illustrating the photon energy in relation to the spin-orbit states of the neutral Iodine. The laser polarization is in the vertical direction in the image plane.

through the center of the 3D distribution we apply an inverse Abel transform providing a reconstruction of the distribution. The reconstructed Γ^- image at 267 nm is shown in Fig. 3.2 (b). For comparison the original image is also shown. The difference between the raw images in 3.1 and 3.2 is due to the difference of the mesh. Our initial images were collected with a 70 lpi mesh which was later replaced with a 333 lpi mesh with 70% transmission greatly improving image quality. The faster an electron flies the further from the image center it tends to be detected. Since *velocity* is proportional to the square root of eKE, the photoelectron spectrum P(eKE) can be extracted from the reconstructed images.

The photoelectron spectrum for Γ^- at 267 nm is shown in Fig. 3.3. Two peaks corresponding to the $^2P_{3/2}$ and $^2P_{1/2}$ spin-orbit states of Γ^- . The electron affinity of I is 3.06 eV.⁴⁰ At 400 nm the photoelectrons only have 0.04 eV of kinetic energy.

Note the difference in the angular distributions between the 400 nm and 267 nm images (Fig. 3.1). The 400 nm image is nearly isotropic while the 267 nm rings are more intense to the right and left of the image. The photoelectron angular distribution is plotted in Fig. 3.4 for the $^2P_{3/2}$ transition at 267 nm.

Iodide Data Analysis

For linearly polarized light the angular distribution³⁷ has the form

$$\frac{d\sigma}{d\Omega} = \left(\frac{\sigma_{total}}{4\pi} \right) [1 + \beta P_2(\cos \theta)], \quad (1)$$

where $P_2(\cos \theta) = \frac{1}{2} (3 \cos^2 \theta - 1)$, σ_{total} represents the total cross section, θ is the angle between the laser polarization and direction of electron ejection, β is the asymmetry

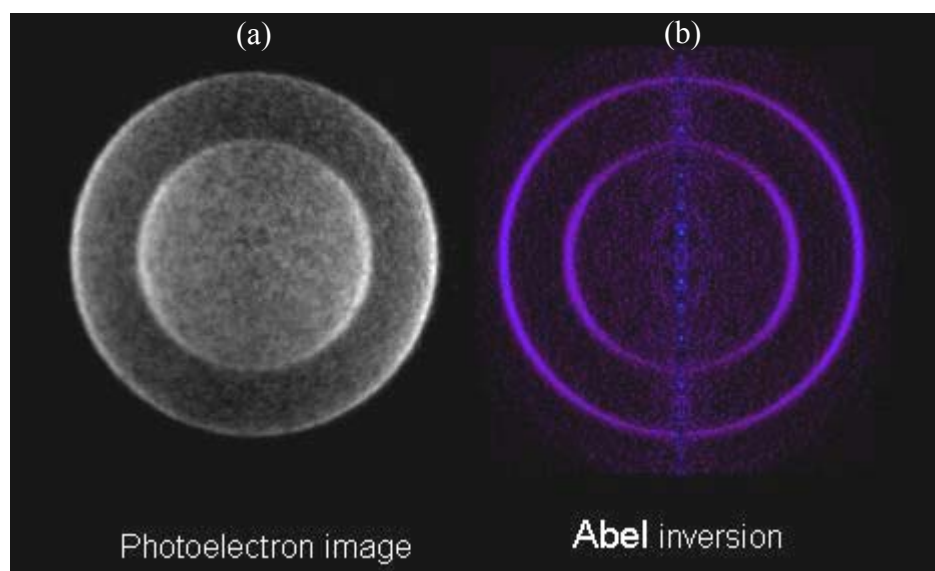


Figure 3.2 (a) photoelectron image of I^- at 267 nm. (b) Abel inversion of the photoelectron image. Laser polarization is vertical.

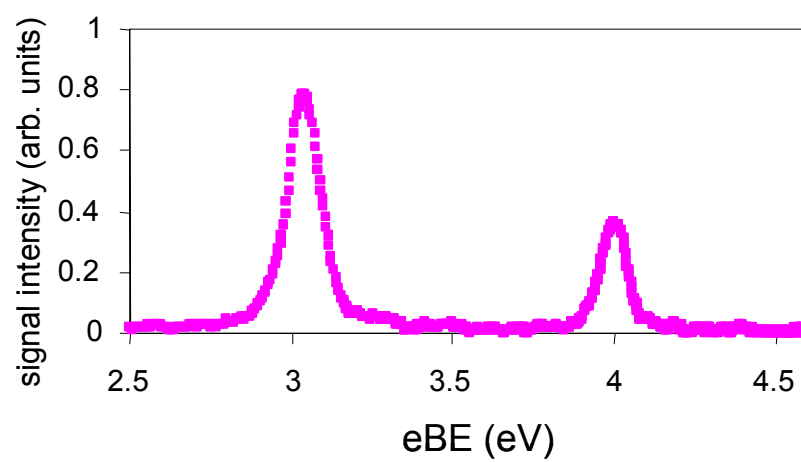


Figure 3.3 Photoelectron spectrum of I^- at 267 nm. The $^2\text{P}_{3/2}$ and $^2\text{P}_{1/2}$ states of the neutral are shown at 3.01 eV and 3.97 eV.

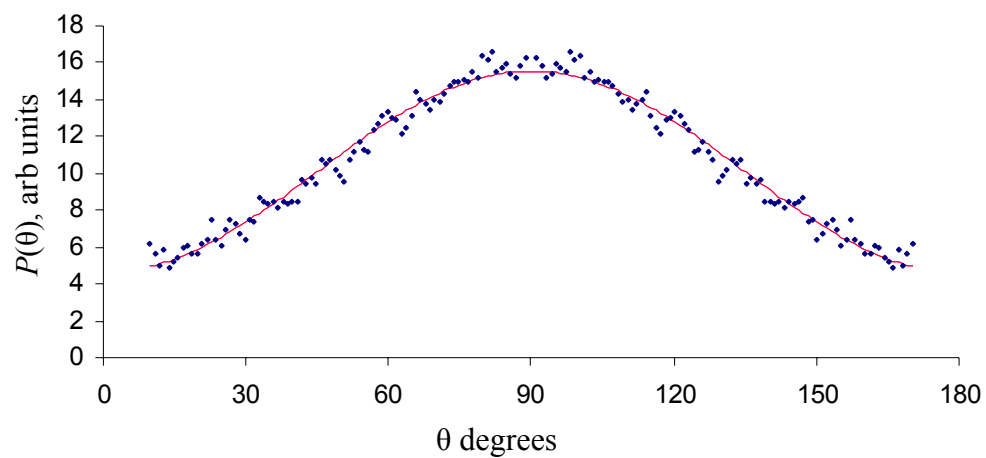


Figure 3.4 Photoelectron angular distribution of the $^2P_{3/2}$ state of the neutral at 267 nm. The solid line is the best fit of the angular distribution. θ is the angle between the laser polarization and the outgoing electron.

parameter. We fit the experimental photoelectron angular distribution, Fig 3.4, with the preceding equation to determine β . β can range from -1 to +2: a β of zero corresponds to an isotropic image while a negative β corresponds to an image with more intensity perpendicular to the laser polarization. In the 400 nm image $\beta = -0.02$, while in the 267 nm image of Γ^- $\beta = -0.61$ and -0.67 for the $^2P_{3/2}$ and $^2P_{1/2}$ bands, respectively. In this case β depends upon the kinetic energy because photoejection occurs from a non- s -type orbital. The anisotropy depends upon the interference between the partial waves, $\ell' = \ell \pm 1$.³⁷ Applying the Wigner threshold law, at lower kinetic energies the lower ℓ wave will dominate. Since $\ell = 1$ for the Γ^- photoejected electron, the outgoing waves are s and d waves. Near threshold the s wave will dominate producing the nearly isotropic image observed in the Γ^- image in Fig. 3.1. At greater photon energies the d wave will contribute significantly giving a negative β .

Cooper and Zare reported¹¹ that the asymmetry parameter, β , for a given ℓ is modeled by the following equation:

$$\beta = \frac{\ell(\ell-1)\sigma_{\ell-1}^2 + (\ell+1)(\ell+2)\sigma_{\ell+1}^2 - 6\ell(\ell+1)\sigma_{\ell+1}\sigma_{\ell-1}\cos(\delta_{\ell+1} - \delta_{\ell-1})}{(2\ell+1)[\ell\sigma_{\ell-1}^2 + (\ell+1)\sigma_{\ell+1}^2]}, \quad (2)$$

where δ_ℓ is the phase shift of the ℓ^{th} partial wave and $\sigma_{\ell\pm 1} = \int_0^\infty R_{n\ell} r R_{k\ell\pm 1} dr$ is the dipole radial matrix element. Figure 3.5 compares the experimental results for β with Cooper and Zare's model. There is good agreement between the experimental values and the model.

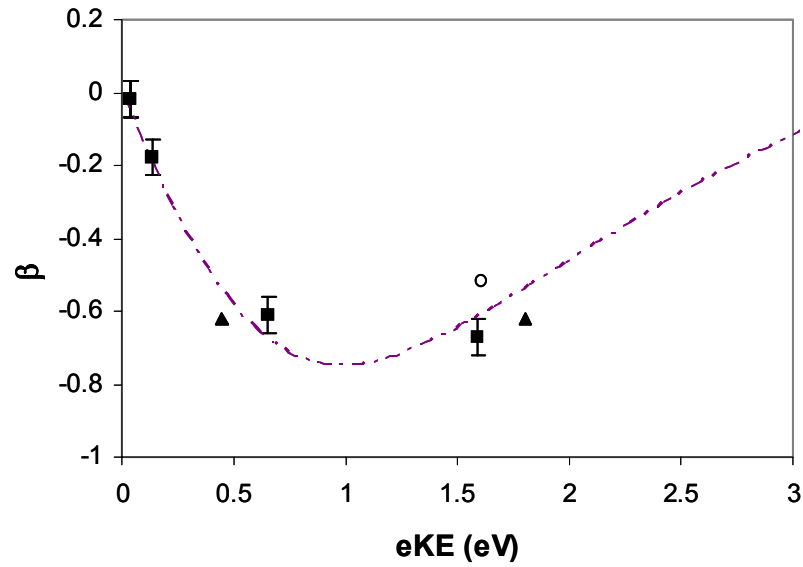


Figure 3.5 Γ^- anisotropy parameter, β , experimental determine with the prediction from the Cooper-Zare model the solid line. The dashed line is the best fit line to the experimental data. The phase parameter of the dashed line is 0.81. The open circle is Neumark's² while the solid triangles is Lineberger's⁵. The error bars on our results are approximate and correspond to ± 0.05 .

3.2.2 Oxide

Photoelectron imaging of O^- and S^- represents another case of atomic – anion photodetachment, where the electrons are ejected from a p atomic orbital.

The photoelectron images of O^- at 800 and 400 nm are shown in Fig. 3.6(a) and (b). Figure 3.6(c) shows the corresponding photoelectron energy spectra. The electron affinity is 1.46 eV⁴¹. Only one narrow transition is apparent in each image which is expected for atomic transitions at this energy. A schematic of the energy levels for atomic oxygen is shown in Fig. 3.7. The spin-orbit splitting of the 3P_2 , 3P_1 , and 3P_0 states is smaller than the FWHM (0.10 eV) of peak in the spectral profile. Notice the increase in anisotropy with the higher kinetic energy electrons in figure 3.6(a) at 400 nm versus the 800 nm image in Fig. 3.6(b).

The outgoing free electron wave, ψ_f , is determined so that the direct product of the irreducible representations of the bound atomic orbital (ψ_{AO}), ψ_f , and dipole operator ($\hat{\mu}$) are invariant, $\langle \psi_{AO} | \hat{\mu} | \psi_f \rangle \neq 0$. Detachment from a p_z orbital will produce an s wave and a d wave. This is a partial case of when the dipole selection rule of $\ell \pm 1$ also produces the similar results. Since the detached electron in O^- much like in I^- and S^- is from a p atomic orbital with $\ell = 1$, the outgoing free electron wavefunction will consist of both s and d waves. Applying the Wigner threshold law the s waves will dominate near threshold, producing an isotropic ring in the image as observed in Fig. 3.6 (b). $\beta = -0.063 \pm 0.017$ in the 800 nm image. Further from threshold the d wave dominates accounting for the negative $\beta = -0.33 \pm 0.05$ which is composed of five 400 nm images of O^- averaged together. Figure 3.8 compares our experimental anisotropy parameter with the

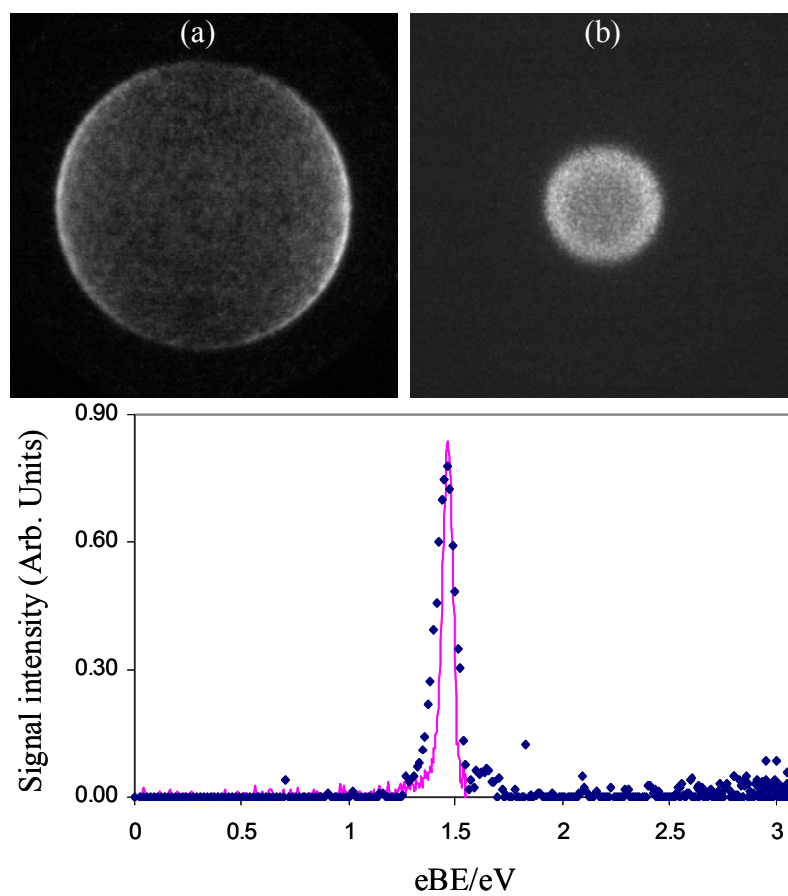


Figure 3.6 Top photoelectron images of O^- at (a) 400 nm and (b) 800 nm. The laser polarization is vertical in the image plane. At the bottom are the photoelectron spectra for 800 and 400 nm; solid line and diamonds respectively.

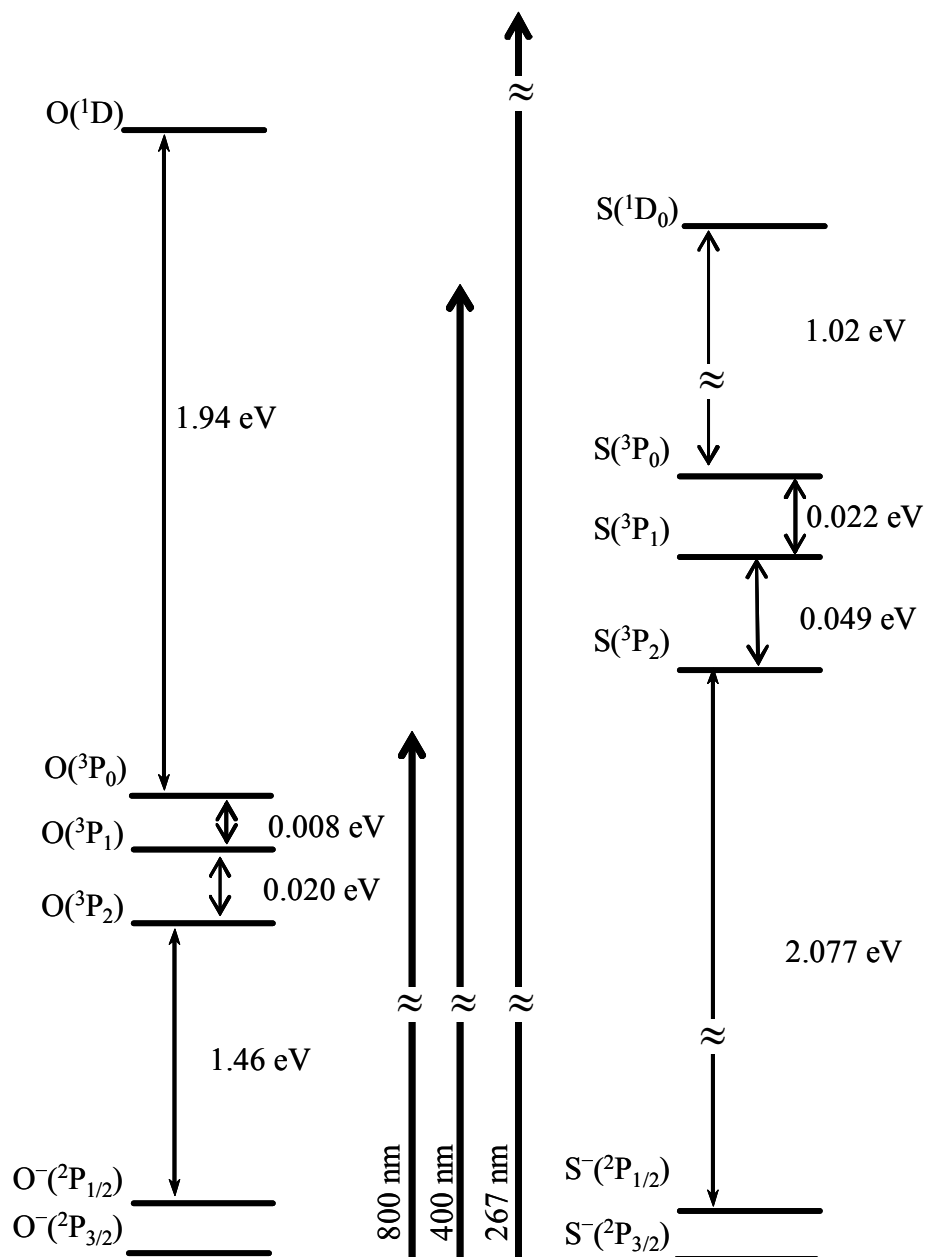


Figure 3.7 Relative energy levels diagram for photodetachment O^- and S^- .^{7,8}

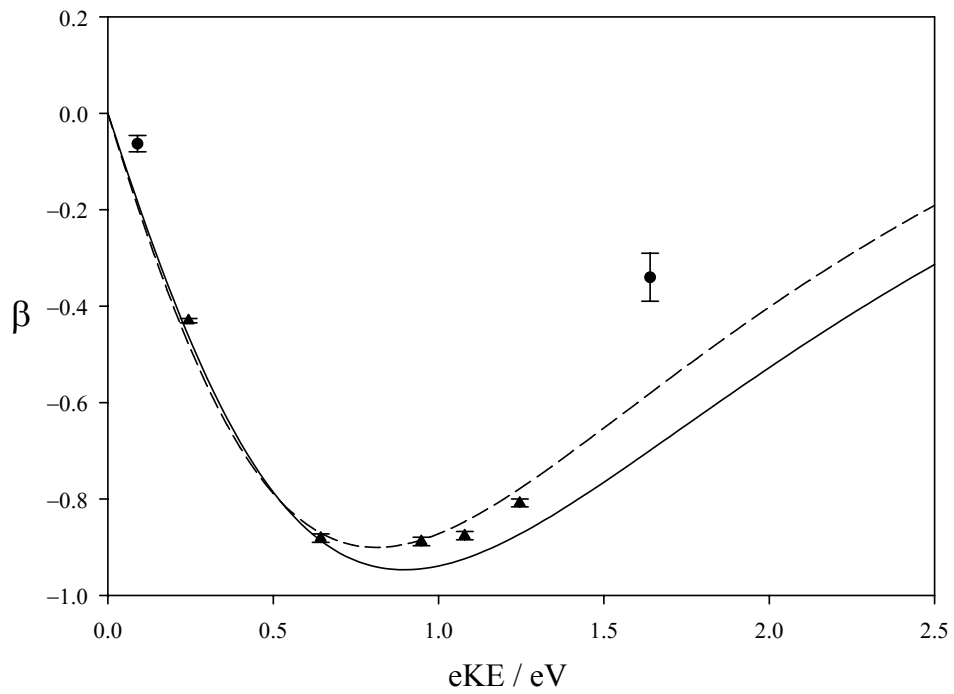


Figure 3.8 Anisotropy parameter for photodetachment from O^- . The solid circles represent our values and the solid triangles are Hanstorp et al.¹. The solid line is the prediction from the Cooper-Zare model. The dashed line has a phase parameter of 0.925 which was chosen by Hanstorp et. al. to fit their data. The solid line's phase angle is 0.96 and it was chosen by Hanstorp et al. since it best fit the Cooper-Zare model.

Cooper-Zare model and an approximation of the Cooper-Zare model by Hanstorp et. al¹ based on their experimental results.

3.2.3 Sulfide

Sulfide Results

The photoelectron image and Abel transform for S^- at 267 nm are shown in the top row of Fig 3.9. The bottom row of Fig 3.9 contains raw photoelectron images of S^- obtained at 400 nm at three different velocity-map imaging focusing conditions. The images decrease in size as the voltage applied to the imaging lens is increased. This capability is useful for expanding low electron kinetic energy images to fill the detector. Figure 3.10 contains the photoelectron spectra at both 267 nm and 400 nm. The 400 nm spectrum was also used to recalibrate the instrument along with the I^- data. The ring in the 400 nm image has $\beta = -0.80 \pm 0.1$ and corresponds to the unresolved $^3P_{2,1,0}$ states of the neutral S atom. In the 267 nm image two peaks are present; the second peak is just more than 1 eV above the other peak. It corresponds to the 1D state of the neutral. The spectral band in the 400 nm image of S^- is wider than the spectral band in the 400 nm image of O^- . It is more clearly observed in the FWHM of the spectral peaks, where the peaks corresponding to $^3P_{2,1,0}$ of oxygen and for sulfur has a FWHM of 0.104 and 0.11 respectively. The outer ring is more isotropic than the inner ring; $\beta = -0.64$ and -0.02 ± 0.1 , respectively.

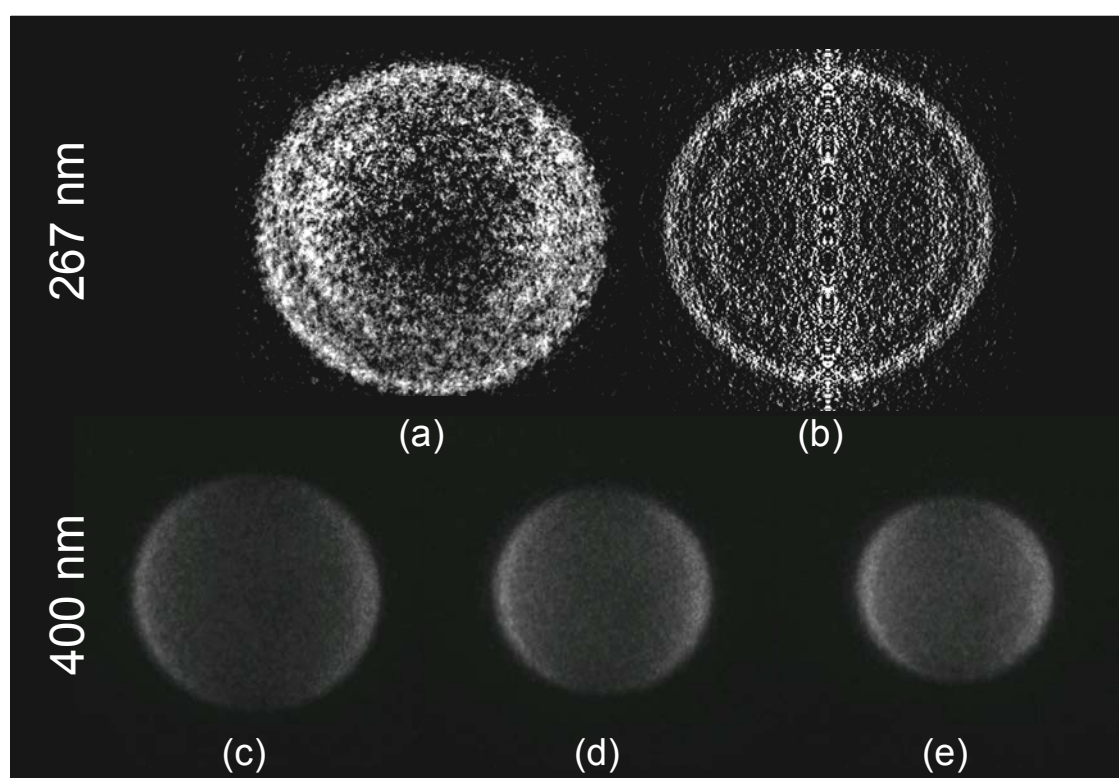


Figure 3.9 (a) photoelectron image of S^- at 267 nm (b) Abel transform of S^- at 267 nm (c)-(e) photoelectron image of S^- at 400 nm velocity map focusing condition $-V_3/V_1$ 450/150, 600/200, and 750/250 respectively.

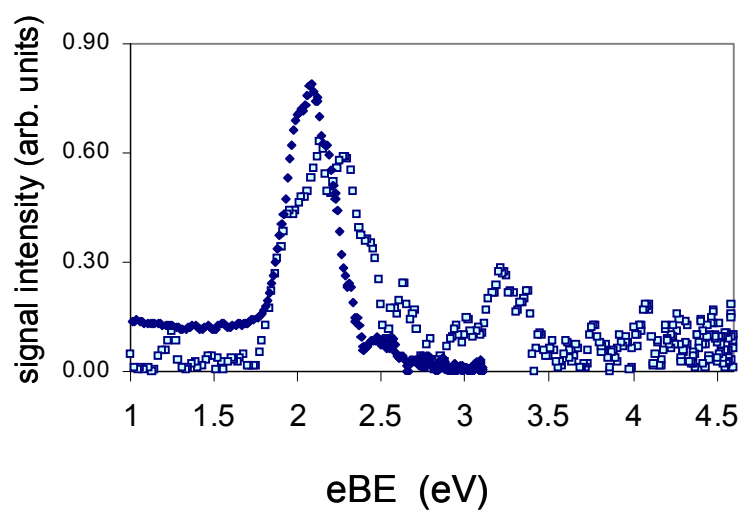


Figure 3.10 Photoelectron spectra of S^- at 267 and 400 nm respectively label as \square and \blacklozenge . Both spin orbit states are evident in the 267 nm.

Sulfide Analysis

As in the case of Γ^- detachment occurs from a bound p orbital, therefore we expect similar anisotropy for S^- images. The 400 nm detachment of Γ^- produced a nearly isotropic band ($\beta = -0.02 \pm 0.1$), however in the 400 nm detachment from S^- , the band is anisotropic ($\beta = -0.80 \pm 0.1$). The dependence of PADs upon energy accounts for the differences between in β . In the Γ^- the photon energy is only 0.04 eV above threshold while in S^- the photon energy is 1.01 eV greater than EA of S.

In the 267 nm image the outer band is nearly isotropic ($\beta = -0.02 \pm 0.1$) and the inner band is anisotropic ($\beta = -0.64 \pm 0.1$). This isotropic band is the same band that was anisotropic in 400 nm image; it corresponds to the transition to the 3P state of the neutral. Note in the Cooper-Zare model (Fig. 3.5) the asymmetry parameter starts above zero, dips to below almost -1 and returns to zero. This is why the 3P band changes from being anisotropic in the 400 nm to isotropic in the in 267 nm image.

3.3 SUMMARY

Photoelectron imaging of Γ^- , S^- , and O^- assisted in the development of our femtosecond negative-ion photoelectron imaging spectrometer. Iodide anion was the first negative ion examined with our instrument. It demonstrated proof of concept and allowed for calibration of the instrument. Application of the Cooper-Zare central potential model to PADs assisted in our understanding of PADs and development of approaches to analyze the PADs in molecules discussed in the next chapter.

4 PHOTOELECTRON IMAGING OF MOLECULAR ANIONS

4.1 INTRODUCTION:

This chapter presents the results for molecular anions, S_2^- , SO^- , O_2^- , and CS_2^- . Analyzing these systems allowed us to develop two methods of interpreting the PADs. The first model builds upon the Cooper-Zare treatment that was introduced in chapter 3, by expanding of the model to molecules. The other method is called the *s & p* model and is applied to more complex molecules. These studies serve as the foundation to understanding cluster and time-resolved studies by serving as a reference and a stepping stone to bigger systems. The molecular orbital signatures of these molecules are used for comparison with images from future experiments.

Traditional photoelectron spectroscopy has been applied to both S_2^- and CS_2^- in the past. A photoelectron spectrum of S_2^- at 2.54 eV was obtained by Ellison and co-workers,⁴² revealing a vibrational progression assigned to the $X^3\Sigma_g^-$ state of S_2 . We recorded a series of S_2^- photoelectron images recorded between 2.34 eV and 4.64 eV photon energy, revealing the structure of the detachment transitions assigned to the $X^3\Sigma_g^-$, $a^1\Delta_g$, $b^1\Sigma_g^+$, $c^1\Sigma_g^-$, and $A^3\Delta_u$ states of the neutral. For CS_2^- a 2.54 eV photoelectron spectrum revealed a single electronic transition assigned to the $X^1\Sigma_g^+$ state of the neutral. A higher photon-energy spectrum (4.66 eV) showed additional peaks assigned to the a^3B_2 , b^3A_2 , and A^1A_2 neutral states.⁴³ There was no discussion of PADs in the previous work. A comparison of the earlier results to the present results illustrates the advantages of photoelectron imaging.

This chapter is organized as follows. The next section presents the results and analysis for each molecule. A subsection is provided for the application each of the two qualitative PADs models. The final section is a summary.

4.2 RESULTS AND DISCUSSION:

4.2.1 Results for S_2^-

S_2^- was produced by electron impact ionization of a supersonic expansion of 7% OCS in argon. S_2^- was photodetached at 267, 400, 530 and 800 nm. An overview of the photoelectron images of S_2^- are presented in Fig. 4.1. Using the assignments from Swope *et al.*,⁴⁴ the diffuse feature at the center of the 267 nm image [Fig. 4.1(a) and (d)] is assigned to the transitions yielding the neutral $c^1\Sigma_u^-$ and/or $A'^3\Delta_u$ states. This part of the image is nearly isotropic with $\beta \approx -0.14$. The outer ring in the 267 nm image is comprised of unresolved contributions of three electronic transitions: $^2\Pi_g \rightarrow X^3\Sigma_g^-$, $a^1\Delta_g$, and $b^1\Sigma_g^+$. Changing the laser wavelength to 400 nm, we “zoom in” on these transitions and they become resolved in the images shown in Fig. 4.1(b) and (e). In the MO picture, each of these three transitions involves the removal of an electron from the doubly degenerate π_g^* HOMO of S_2^- . Therefore, their comparative analysis is particularly instructive, as the observed anisotropy trends can be attributed to eKE-dependent photodetachment dynamics and/or deficiencies of the one-electron MO description.

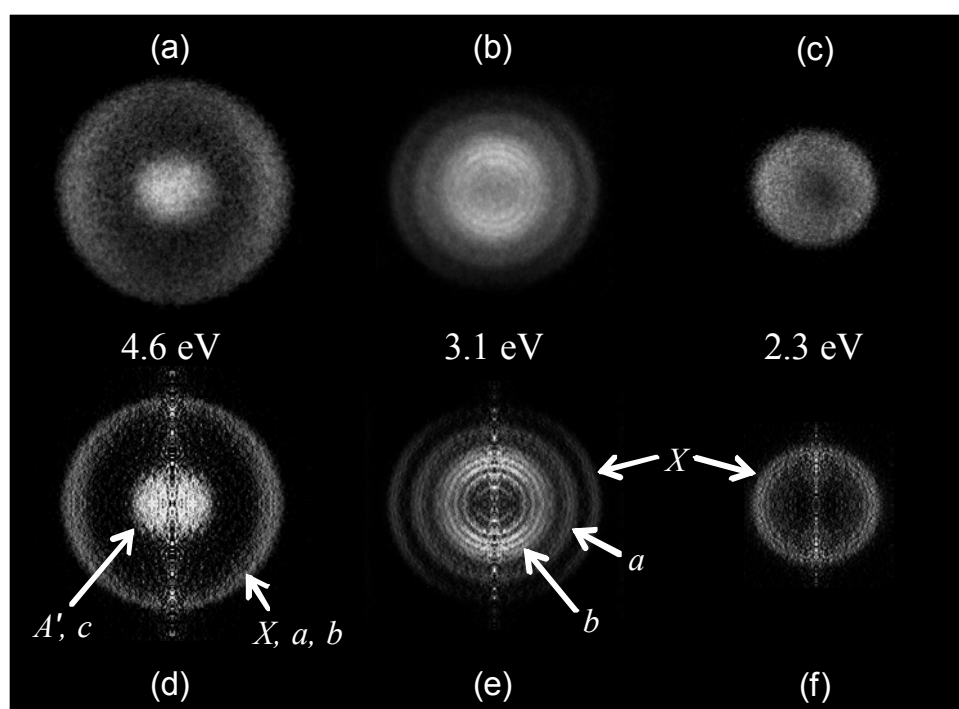


Figure 4.1 Top row: Photoelectron images recorded in the photodetachment of S_2^- at (a) 267, (b) 400, and (c) 530 nm. Bottom row [(d)-(f)]: Corresponding Abel-inverted images, reconstructed as described in the text. The images are shown on arbitrary velocity and intensity scales; see Figs. 4.3 and 4.4 for quantitative information. The laser polarization is always vertical in the figure plane. Arrows labeled X , a , b , c , and A' , indicate transitions assigned to the $X^3\Sigma_g^-$, $a^1\Delta_g$, $b^1\Sigma_g^+$, $c^1\Sigma_u^-$, and $A'^3\Delta_u$ states of S_2 , respectively.

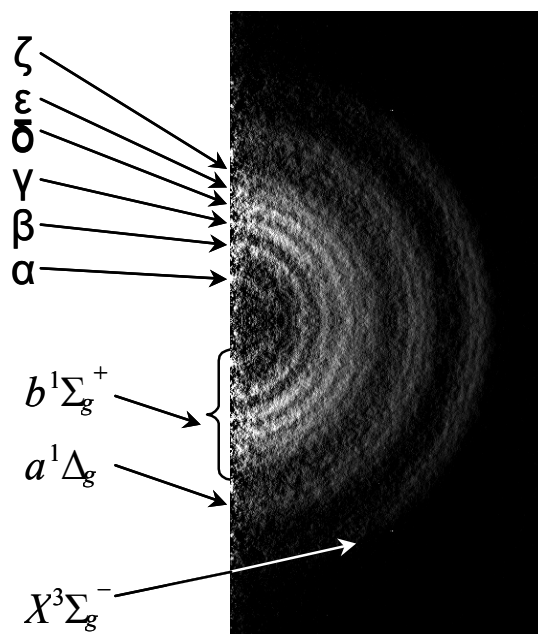


Figure 4.2 Expanded half of the reconstructed 400 nm photoelectron image of S_2^- from Fig. 4.1(e). The electronic transition assignments correspond to neutral S_2 states formed in the detachment. The labels assigned to vibrational rings within the $b^1\Sigma_g^+$ transition are also shown.

The reconstructed 400 nm image from Fig. 4.1(e) is enlarged in Fig. 4.2. The electronic transitions are labeled with regard to the resulting neutral states. Vibrational rings are evident in the Figure for all three electronic states with the slowest electrons, corresponding to the $b^1\Sigma_g^+$ neutral state, being better resolved. A MO diagram is shown in Fig. 4.3. The HOMO has three degenerate electrons; detachment of these is responsible for producing the X, a, and b neutral states. The A and C states are produced from detachment from the HOMO-1. The photoelectron spectra in Fig. 4.4 correspond to 400 and 530 nm S_2^- images. Partial vibrational resolution is achieved for all three electronic transitions. The vibrational peaks for the $b^1\Sigma_g^+$ state transition are labeled using the assignments given to the corresponding rings in Figure 4. 4. The peaks are spaced by $\sim 600\text{ cm}^{-1}$, compared to the reported vibrational frequency for the $b^1\Sigma_g^+$ state of S_2 $\omega_e = 699.7\text{ cm}^{-1}$.⁴⁵ The discrepancy can be attributed, at least partially, to anharmonicity. The leading shoulder of the X band agrees with the known EA of S_2 ($1.670 \pm 0.015\text{ eV}$),⁴² indicated by the dashed line in Fig. 4.4. The signal at $eBE < EA$ corresponds to hot bands and uncorrected backgrounds in the experimental image.

Upon visual inspection of 400 nm S_2^- image, the rings corresponding to the b state are anisotropic peaking in the direction of the laser polarization. The outer rings peak perpendicular to the laser polarization.

4.2.2 Analysis of S_2^- using the adapted Cooper-Zare Treatment

Photodetachment of S_2^- is an excellent candidate for the adapted Cooper-Zare treatment, with the core ideas used here having been applied previously to O_2^- threshold photodetachment.⁴⁶⁻⁴⁹ The π_g HOMO of S_2^- has two nodal planes, resembling an atomic d

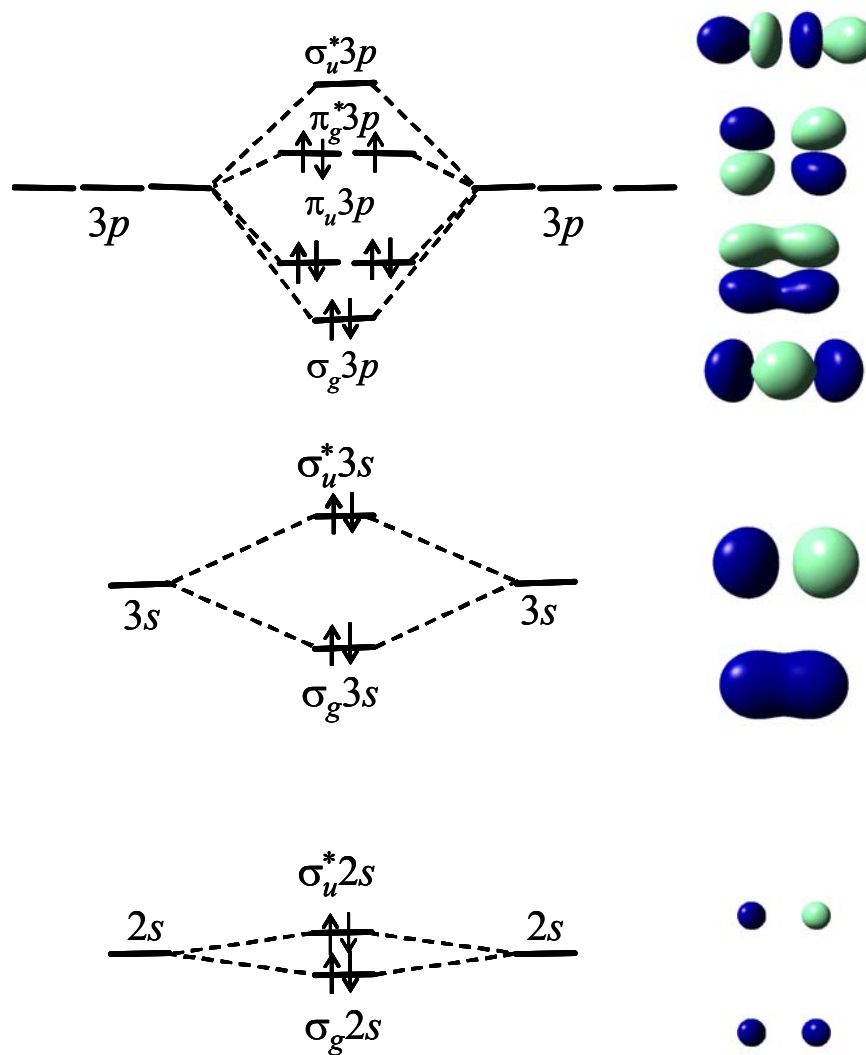


Figure 4.3 Molecular orbital diagram for S_2^- . The X, a, and b neutral states result from detachment of an electron from the π_g^* Molecular orbital.

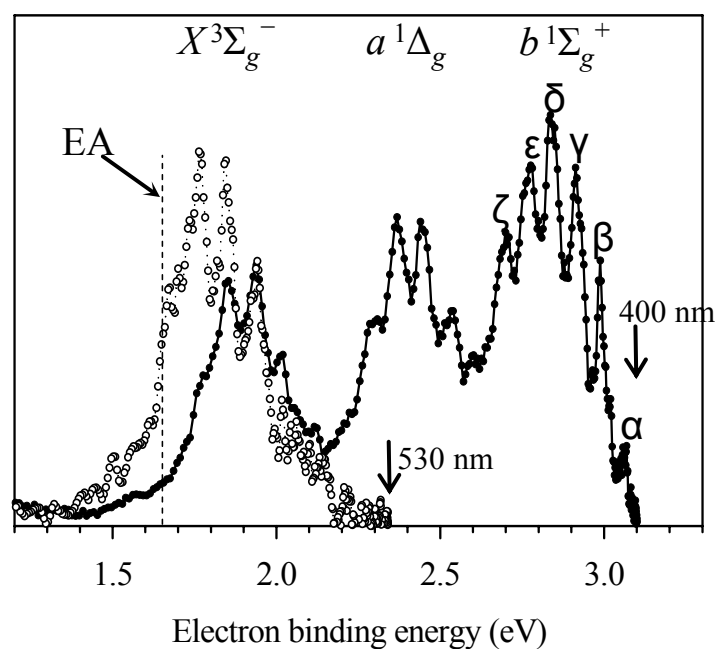


Figure 4.4 Photoelectron spectra of S_2^- obtained from the images in Figs. 4.1(e) and (f). The spectrum represented by filled symbols/solid line corresponds to the 400 nm laser wavelength, open symbols/dotted line corresponds to 530 nm. The vertical dashed line represents the EA = 1.67 eV. The electronic states assignments correspond to neutral S_2 . The vibrational progression (α through ζ) within the b state corresponds to the similarly labeled rings in the image shown in Fig. 4.2.

orbital (d_{xy} , if x = molecular axis, $y \perp$ to it, in the plane of the orbital). Hence, for the π_g^{-1} transitions yielding the $X^3\Sigma_g^-$, $a^1\Delta_g$, and $b^1\Sigma_g^+$ neutral states the initial orbital angular momentum quantum number of the electron can be taken as $\ell = 2$ and the qualitative trends in β can be explained by considering the interference of p and f partial waves. The Cooper-Zare formula³⁷ for $\ell = 2$ predicts that the asymmetry parameter will be positive at small eKEs, before reaching negative values. Figure 4.5 compares the experimental data for S_2^- with the trend predicted by the Cooper-Zare central-potential model for detachment from a d orbital. The phase difference between the $(\ell \pm 1)$ partial waves was set to zero. Although this supposition is somewhat arbitrary, there is no physical basis for assuming a non-vanishing phase difference, at least in considering the qualitative trends in the detachment. In the relevant energy range, the final-state de Broglie wavelength is quite large ($\sim 14 \text{ \AA}$) compared to the initial state and therefore no significant phase-shift between the outgoing waves excited by the same laser field is expected.¹ Another model parameter, namely the ratio of the dipole radial matrix elements (affecting the position of the turnaround point on the curve), was chosen to simulate the trend in the data.

Although the experimental data in Fig. 4.5 correspond to different wavelengths, as well as different final states, the anisotropy parameter appears to depend mainly on eKE, following a qualitative trend consistent with the Cooper-Zare model. This collective behavior is consistent with the MO picture, in which the X , a , and b neutral states are formed via different spin components of the same π_g^{-1} one-electron detachment transition. Quantitative differences between the data and the model can be attributed, in part,

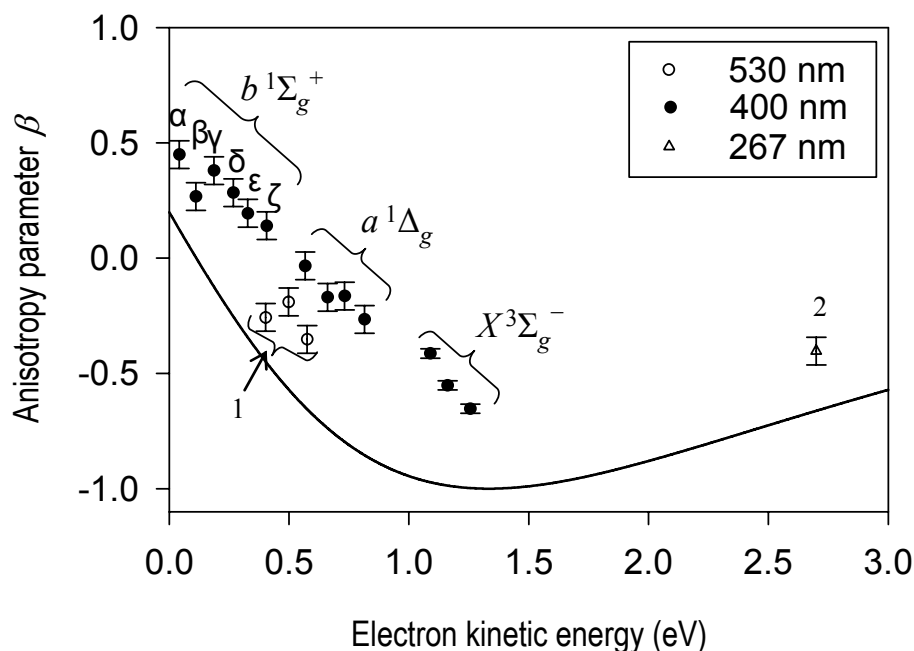


Figure 4.5 Anisotropy of different components of the π_g^{-1} transition in S_2^- at three different wavelengths (as indicated), summarized as a function of eKE. The transition labels indicated on the graph correspond to 400 nm data. The Greek labels for vibrationally resolved transitions to the $b^1\Sigma_g^+$ state of S_2 are the same as in Figs. 4.2 and 4.3. (1) The 530 nm data corresponding to the $X^3\Sigma_g^-$ state. (2) Overall anisotropy of the peripheral feature in the 267 nm image shown in Figs. 4.1(a) and (d), corresponding to unresolved $X^3\Sigma_g^-$, $a^1\Delta_g$, and $b^1\Sigma_g^+$ states. The solid line corresponds to the Cooper-Zare model for photodetachment from a d orbital ($\ell = 2$) assuming a dipole radial matrix elements ratio of $R_{\ell+1}/R_{\ell-1} = (0.5 \text{ eV}^{-1}) \cdot \text{eKE}$ and a zero phase-shift between the $(\ell \pm 1)$ waves. See the text for details.

to the neglected MO components, as well as electron interaction and intramolecular dynamics. In addition, the assumption of a central potential in the Cooper-Zare (atomic) model is not accurate in the case of the non-spherically symmetric molecular potential. Despite the quantitative discrepancies, this method is an effective qualitative tool for understanding the dependence of the PAD on eKE.

A similar approach can be applied to electrons originating from the orbitals below the HOMO. For example the A' and c states of S₂ originate from electron detachment from the π_u (HOMO-1), the lowest- ℓ contributions to the single-center AO expansion of this MO correspond to p functions, followed by f functions, etc. If the p functions dominate the AO expansion then the detached waves will comprise of mainly s and d waves. Near threshold with slow electrons the s waves will dominate giving an isotropic ring, which is evident in the inner ring of S₂⁻ at 267 nm (Fig. 4.1(a)). The slightly negative value of (-0.14 ± 0.06) arises from contributions of the d wave.

4.2.3 SO⁻ and O₂⁻ Results and Analysis

Photoelectron images of O₂⁻ and SO⁻ are presented in Fig. 4.6. It is interesting to compare these to S₂⁻ and amongst each other for they are isovalent. At 400 nm O₂⁻ and SO⁻ both present a very broad inner ring and a narrower outer ring. At 800 nm the difference is much more evident. In both images the ground state of the neutral is vibrationally resolved. The O₂⁻ 800 nm image (Fig. 4.6(b)) has five narrow rings that are further from the image center than the rings in the SO⁻ image, Fig. 4.6(d).

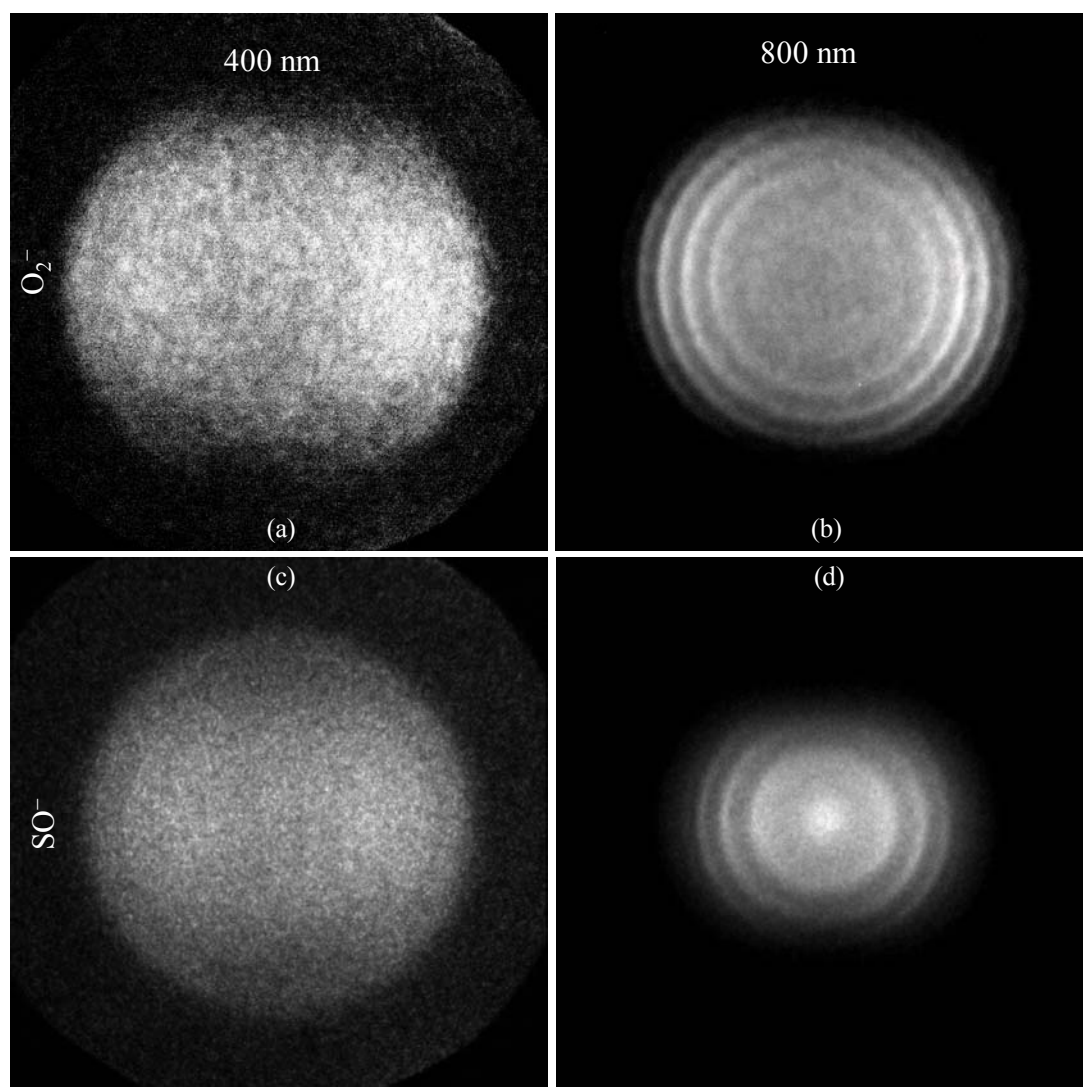


Figure 4.6 Photoelectron images (a) O_2^- at 400 nm (b) O_2^- at 800 nm (c) SO^- at 400 nm (d) SO^- at 800 nm

The photoelectron spectra from the 800 nm images in Fig. 4.6 are presented in Fig. 4.7. O_2^- first detaches at 0.42 eV and the mean separation between the peaks in the O_2^- spectrum is $1540 \pm 60 \text{ cm}^{-1}$, in good agreement with Lineberger's results of 0.45 eV for the adiabatic electron detachment energy of $\text{O}_2^- X^2\Pi_g$ ground state and $\text{O}_2 X^3\Sigma_g$ ground state has a vibrational progression of 1558.6 cm^{-1} .⁵⁰ We are unable to resolve the spin-orbit splitting in O_2^- . Substituting one oxygen with sulfur increases the electron detachment energy by about 0.5 eV as observed in the 800 nm spectra in Fig. 4.7. The mean separation between SO peaks is 1137 cm^{-1} . A second substitution of sulfur for the other oxygen increases the detachment energy for S_2^- to $1.67 \pm 0.015 \text{ eV}$ ⁴², which is in excess of the 800 nm laser probe.

The photoelectron angular distributions in the outer ring of the 400 nm images for O_2^- and SO^- appear to be more intense perpendicular to the laser polarization. Upon visual inspection the inner ring of 800 nm SO^- appears to be isotropic, while the outer rings are less isotropic. The β for each vibration band versus eKE is plotted in Fig. 4.8. β becomes more negative as eKE increases.

4.2.4 Results CS_2^-

The photoelectron images of CS_2^- are shown in the top row of Fig. 4.9, while the bottom row contains the reconstructed images. At least three electronic transitions are visible in the reconstructed 267 nm image of CS_2^- . The rings are labeled in Fig. 4.9(e) as X , a , b , corresponding respectively to the $X^1\Sigma_g^+$, a^3B_2 , and b^3A_2 states of the neutral. As the photon energy is decreased, the X state is brought into focus, revealing vibrational

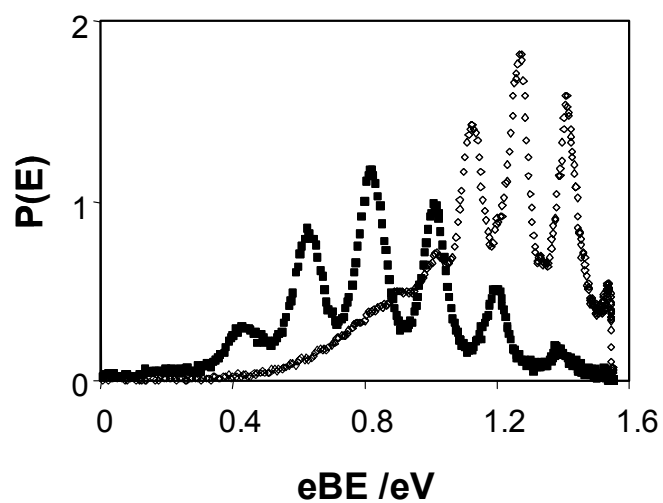


Figure 4.7 Photoelectron spectra of O_2^- and SO^- at 800 nm extracted from the Abel transforms of the images in Fig. 4.6 (b) and (d). The solid squares correspond to O_2^- while the open diamonds correspond to SO^- .

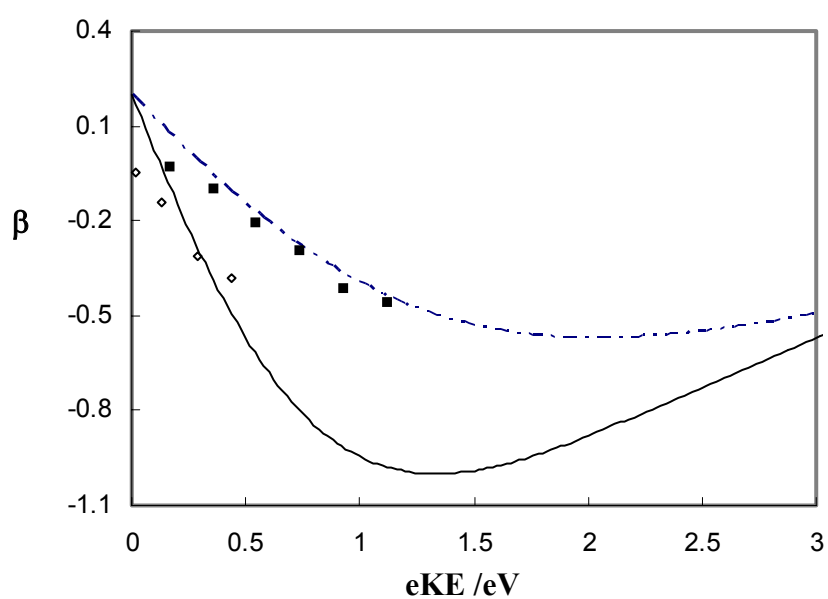


Figure 4.8 Anisotropic parameters for the 800 nm images of SO^- (open diamonds) and O_2^- (solid squares) plotted against electron kinetic energy.

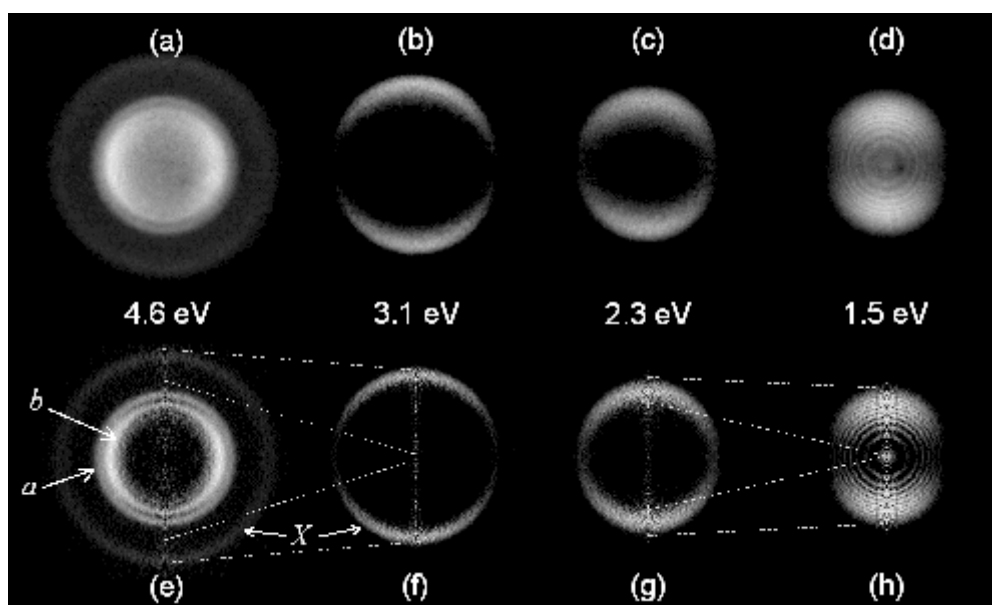


Figure 4.9 Top row: Photoelectron images recorded in the photodetachment of CS_2^- at (a) 267 nm, (b) 400 nm, (c) 530 nm, and (d) 800 nm, with the corresponding photon energies indicated. Bottom row: Abel-inversions of the above images, reconstructed as described in the text. The images are shown on arbitrary velocity and intensity scales; see Figs. 4.10 and 4.11 and the text for quantitative information. The laser polarization is always vertical in the figure plane. The arrows labeled X , a , and b indicate transitions accessing the $X^1\Sigma_g^+$, a^3B_2 , and b^3A_2 states of neutral CS_2 . The transition to the A^1A_2 state (not labeled) is just inside the b^3A_2 ring in (e), as discussed in the text and seen in Fig. 4.10. The dashed lines show correlations in the velocity-map domain of the selected eBE intervals between images taken at different wavelengths.

structure in the 800 nm image (Fig. 4.9(d)). Only the ground state, $X^1\Sigma_g^+$, is observed in the 400, 530 and 800 nm images. The term symbol for the neutral ground state corresponds to the linear equilibrium geometry of the neutral molecule. The equilibrium geometry of CS_2^- is bent, corresponding to the 2A_1 electronic state.

The series of rings observed in the 800 nm image arise from the vibrational progression in the neutral state excited during photodetachment of the electron from the anion. The progression originates from the vertical transition from the bent ground state of the anion to the highly excited bending vibrational levels of neutral CS_2 , whose equilibrium geometry is linear.⁵¹ The analysis of the 800 nm image²⁶ yields an average energy interval between the rings of $415 \pm 10 \text{ cm}^{-1}$, consistent with the bending vibrational frequency in neutral CS_2 .^{6,51,52}

Upon more careful inspection of the CS_2^- 267 nm reconstructed image, a fourth electronic state, A^1A_2 , is revealed as a shadow of the ring labeled *b*. Figure 4.10 is an enlarged Fig. 4.9(e), reconstructed CS_2^- at 267 nm, with an eKE scale. The *X* ground state is a peripheral ring with its intensity peaking in the direction parallel to the laser polarization, giving a positive β . The other three states are crowded together between 0.5 eV and 1.5 eV from the center. Each state exhibits distinct anisotropy. At 267 nm the anisotropy parameters corresponding to the formation of the $X^1\Sigma_g^+$, a^3B_2 , b^3A_2 , and A^1A_2 states of the neutral CS_2 are $\beta = 0.29 \pm 0.1$, -0.24 ± 0.1 , -0.44 ± 0.1 , and -0.42 ± 0.1 respectively. Due to the overlap of corresponding transitions, these β values should be taken as estimates only.

The photoelectron spectra of CS_2^- obtained from the 267 nm photoelectron images

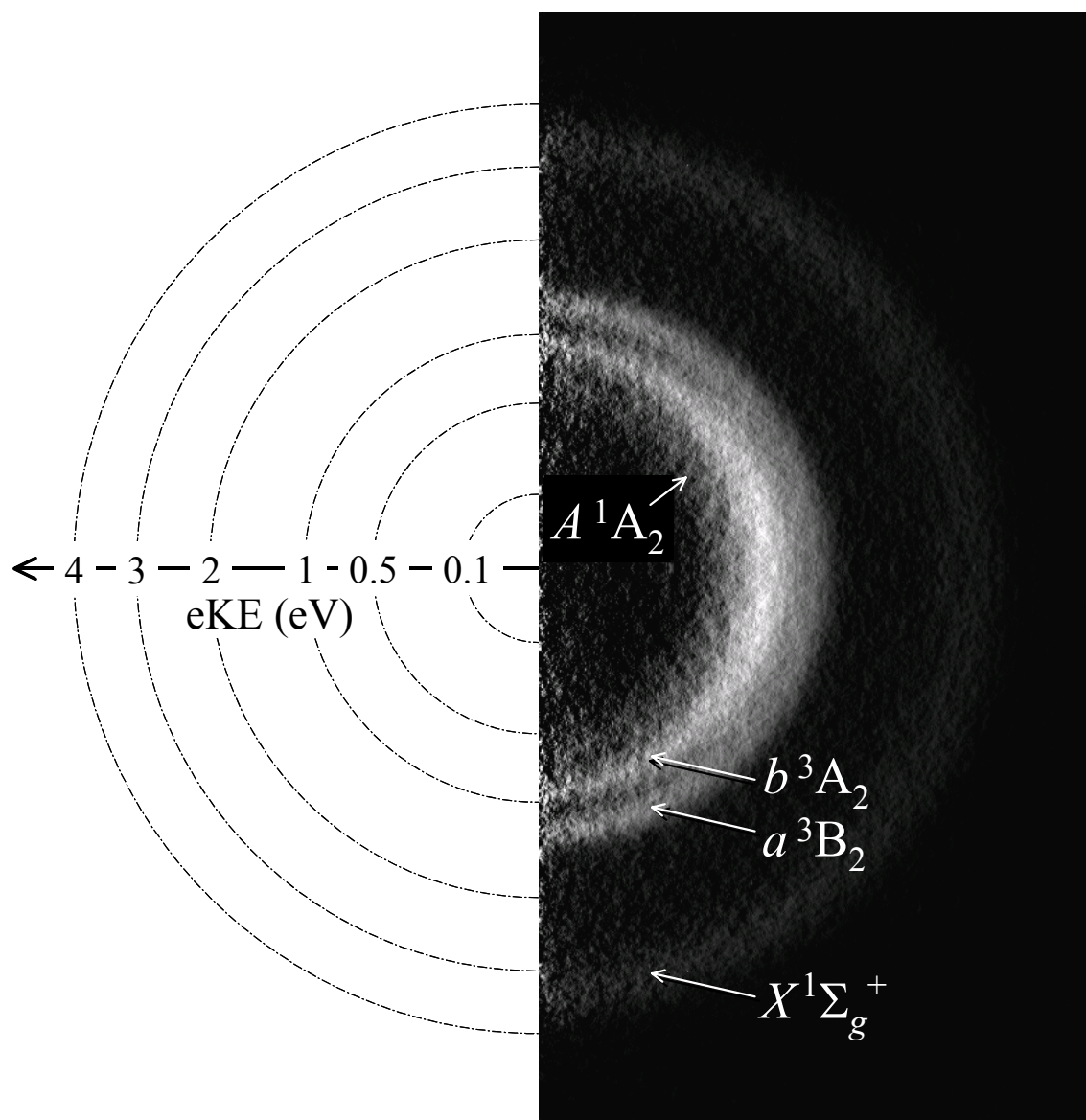


Figure 4.10 Half of the reconstructed 267 nm photoelectron image of CS_2^- reproduced from Fig. 4.9(e) (right) superimposed with the eKE scale (left) and neutral CS_2 state assignments for observed transitions.

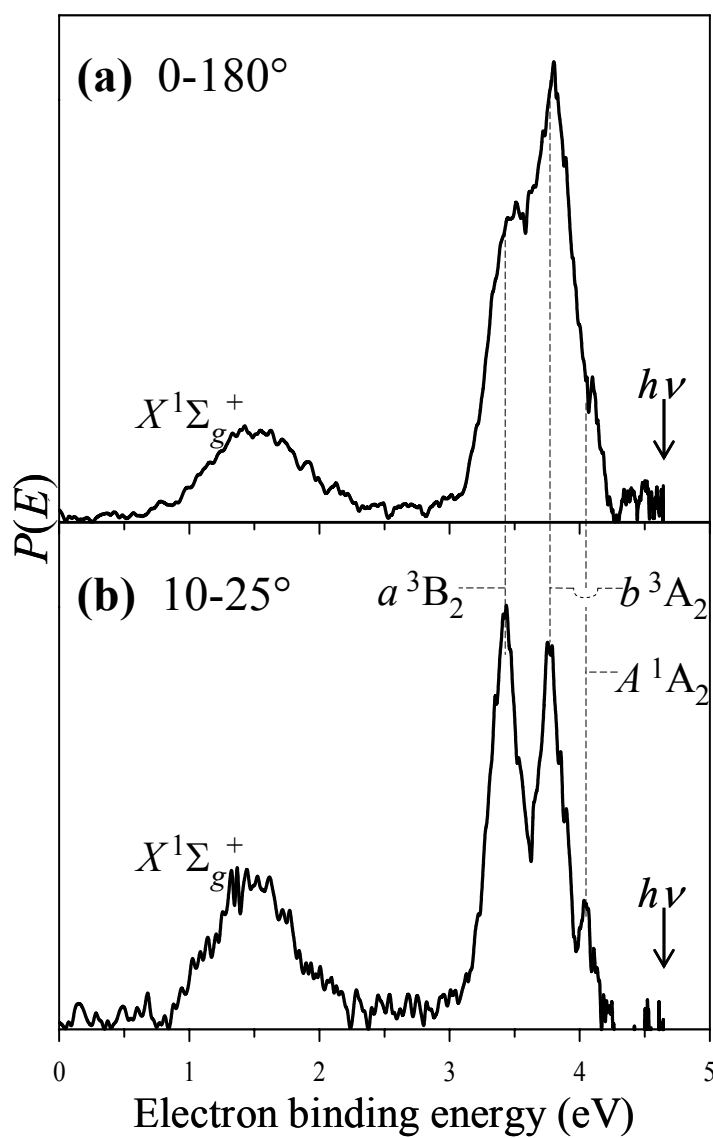


Figure 4.11 267 nm photoelectron spectrum of CS_2^- . (a) The spectrum obtained by integrating the reconstructed image in Fig. 4.7 over the entire angular range. (b) The spectrum obtained by integrating the same image from $q = 10^\circ$ to 25° . Peak assignments correspond to the electronic states of neutral CS_2 .

in Fig. 4.9 and Fig. 4.10 are shown in Fig. 4.11. The spectrum in Fig. 4.11(a) shows the photoelectron signal integrated over the entire angular range from $\theta = 0$ to 180 degrees (zero corresponds to the top of the image and the direction of laser polarization). The Spectrum in Fig. 4.11(b) was obtained by integrating within only a narrow angular range, $\theta = 10$ -25 degrees. The photoelectron spectrum in Fig. 4.11(a) poorly resolves the three excited states of neutral CS₂. The a^3B_2 and A^1A_2 states are shoulders of the intense b^3A_2 state. In Fig 4.11(b), the partial integrated spectrum, the resolution of the three excited states is comparable to that achieved using traditional time-of-flight photoelectron spectroscopy,⁴³ with an added advantage of examining in detail the near zero-eKE range. Restricting the angular integration range improves the resolution by minimizing the effects of distortions, such as possible imperfect roundness of the image and blurring due to a velocity spread in the ion beam. These effects are not observable by eye, but are felt in the quantitative analysis. The states are labeled in accordance with the electronic states of CS₂ formed in the photodetachment, and the state assignments are taken from Tsukuda *et al.*⁴³

In Fig. 4.11(b), the range of integration was chosen close to the laser polarization direction in order to reduce the relative intensity of the b^3A_2 peak, dominating the fully integrated spectrum in Fig 4.11(a). Since the spectrum in Fig. 4.11(b) does not account for all the electrons produced in the photodetachment, the relative band intensities are not reflected properly.

4.3 THE s&p MODEL OF MOLECULAR ANION PHOTODETACHMENT

For many molecular anions, the parent MO cannot be approximated, even qualitatively as a single AO. In these cases the Cooper-Zare treatment is not practical. Hence a different approach is needed to describe the PAD. We have developed a model, which uses group theory to predict the anisotropy properties of the free electron (ψ_f). Here the model is described using the examples of CS_2^- and S_2^- .

4.3.1 The s & p Treatment of CS_2^- Photodetachment

The detachment is first considered from molecular frame (MF) perspective. CS_2^- belongs to the C_{2v} point group. The direct product of the irreducible representations of the molecular orbital's wave function (ψ_{MO}), ψ_f , and dipole operator ($\hat{\mu}$) must be invariant under the symmetry operations of this group. After determining the allowed symmetries of the free-electron waves, ψ_f can be expanded in a single-center AO basis. We then make a further approximation (best justified for slow electrons),³⁸ considering only the waves with $\ell \leq 1$. These s and p waves must then be referenced from the MF to the LF axes. The LF PAD is determined by integrating over all molecular orientations. This is done accounting for the proportionality of transition amplitudes to the cosine of the angle between $\vec{\mu}$ and the laser polarization axis, defined to be the LF z axis (z_{LF}). Qualitative insights into the nature of the PADs can be gained by considering only three “principal” orientations of the anion. These orientations are chosen so that one of the principal molecular axes is aligned along z_{LF} . This substitute for proper orientation averaging is, of

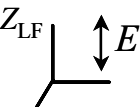

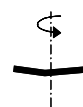



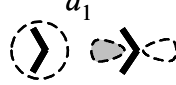


<div style="display: flex; align-items: center;"> <div style="margin-right: 10px;"> Z_{LF}  </div> <div> s and p partial waves for principal anion orientations </div> </div>			
Orientation			
Active $\vec{\mu}$ component	a_1	b_1	b_2
Detachment transition / Neutral state(s)	a_1^{-1} X^1A_1	b_1^{-1} 	b_2^{-1} 
	b_2^{-1} a^3B_2	a_2 $\ell \geq 2$	a_1 
	a_2^{-1} b^3A_2 A^1A_2	b_2 	b_1 
	a_2 $\ell \geq 2$		

Figure 4.12 The s&p model treatment of CS_2^- photodetachment. First header row: principal anion orientations (solid line represents the bent frame of CS_2^-). Second header row: corresponding symmetries of the transition-dipole components driven by the laser radiation polarized along the LF z axis. Rows below the header indicate the symmetries and s and p components (dash contours) of ψ corresponding to the respective transitions and principal orientations. See the text for details.

course, a very coarse approximation, designed to give a qualitative picture of the detachment dynamics without embarking on complete quantum calculations.

The principal orientations of CS_2^- in relation to Z_{LF} are shown in the top row of Fig. 4.12. For each orientation, only the transitions with non-zero $\bar{\mu}$ components along z_{LF} are active. The second header row of Fig 4.12 denotes the symmetry species of the MF active dipole operator. The symmetry species are the irreducible representations corresponding to z_{LF} for the given molecular orientation. Since only the irreducible representation of the $\bar{\mu}$ component along z_{LF} is important in the following discussion, all conclusions remain valid if the molecule is rotated about z_{LF} , as indicated in Figure 4.12, or inverted in the plane perpendicular to z_{LF} .

The MF symmetry of ψ_f is determined by requiring $\langle \psi_f | \hat{\mu} | \psi_{\text{MO}} \rangle \neq 0$. Photodetachment from the a_1 anion MO yields the X^1A_1 neutral state, while the a_2^{-1} transition yields b^3A_2 or the A^1A_2 . Similarly, the b_2^{-1} transition yields both the 3B_2 and 1B_2 states, but only the triplet is observed due to the higher energy of 1B_2 .⁴³ In Fig. 4.12, the three rows below the header list the orientation-dependent ψ_f symmetries allowed in the indicated transitions. For example, in the b_2^{-1} transition, the free-electron waves detached from the anion orientations corresponding to the a_1 , b_1 , and b_2 active $\bar{\mu}$ components are of b_2 ; a_2 ; and a_1 symmetries, respectively.

In the next step of the analysis, ψ_f is expanded in a single-center AO basis, as done previously for the bound MOs. We then make a second core approximation, limiting the consideration to s and p partial waves only. An s wave always corresponds to the a_1 representation, but p waves can transform as a_1 , b_1 , or b_2 symmetry species, depending on

the wave polarization in the MF. The dashed contours in Fig. 4.12 show schematically the s and p components of ψ_f under the symmetry constraints determined above.

The ejected electron can have both s and p partial components if the ψ_f transforms as a_1 . The s waves are isotropic while the p waves' LF orientation is chosen from the MF symmetry and the orientation of the anion being considered. For ψ_f of b_1 and b_2 symmetries, only the p waves are considered in the model. For a_2 waves, the smallest- ℓ components correspond to d -orbitals; therefore, a_2 waves are neglected under the $\ell \leq 1$ approximation.

Considering the wave sketches in Fig. 4.12, the qualitative nature of the expected PADs becomes immediately clear. For the $a_1^{-1} (X^1A_1)$ transition, the free-electron wave function is characterized by interference of the isotropic s waves and anisotropic p waves with amplitudes peaking along z_{LF} . Thus, a PAD with positive β is expected, in agreement with the experimental results. For example, the 800 nm PAD for the X^1A_1 transition integrated over all eKEs is characterized by $\beta = 0.68$. Similar values are obtained at 530 and 400 nm.²⁶ The eKE-dependence of the anisotropy of the vibrational rings in Figures 4.9(d) and (h) can also be understood qualitatively using the s & p analysis. Compared to the s waves, the p wave amplitude is small for slow electrons, increasing with increasing eKE (Wigner law). Therefore, the anisotropy for this transition should increase with increasing eKE. This predicted behavior can be seen in the 800 nm data [see Fig. 4.9(h)].

In the $b_2^{-1} (a^3B_2)$ transition the s and p model predicts a b_2 and an a_2 ψ_f to be produced corresponding to an s wave and two p waves which are perpendicular to the

laser polarization. Thus β is expected to be less negative as observed in experimental image in Fig 4.10.

In the a_2^{-1} (b^3A_2 and A^1A_2) transition the s & p model predicts only p waves contribute to the PAD. No s waves are allowed by selection rules. Therefore, a very negative β is predicted for these transitions. Qualitatively we can predict that these transitions will be more anisotropic than the b_2^{-1} (a^3B_2) transition due to the contributions of the s wave to the b_2^{-1} (a^3B_2) transition. It is also observed in the experimental image Fig 4.10 that the b_2^{-1} (a^3B_2) transition is more isotropic than either (b^3A_2 or A^1A_2) states. The a_2^{-1} transition does indeed exhibit a more negative anisotropy ($\beta = -0.44$ and -0.42 for b^3A_2 and A^1A_2 , respectively) than the b_2^{-1} transition ($\beta = -0.24$ for a^3B_2).

4.3.2 The s & p Treatment of S_2^- Photodetachment

The application of the $s&p$ model to CS_2^- photodetachment makes use of the specific properties of the C_{2v} point group. Nonetheless, the same general approach can be applied to other molecular anions, such as, for example, S_2^- . In this case, the model can be compared to the Cooper-Zare method adapted to the molecular case as described above. Although the application of the Cooper-Zare method to S_2^- is straightforward, in our view the $s&p$ model has an important pedagogical advantage, as long as the detachment is considered in a qualitative manner only. We refer, of course, to the ease of visualization, which contrasts the $s&p$ model with the Cooper-Zare formalism.³⁷

Figure 4.13 illustrates the application of the s and p model to S_2^- . The left column shows the principal orientations of S_2^- . Moving across the top row of Fig 4.13 the π_g

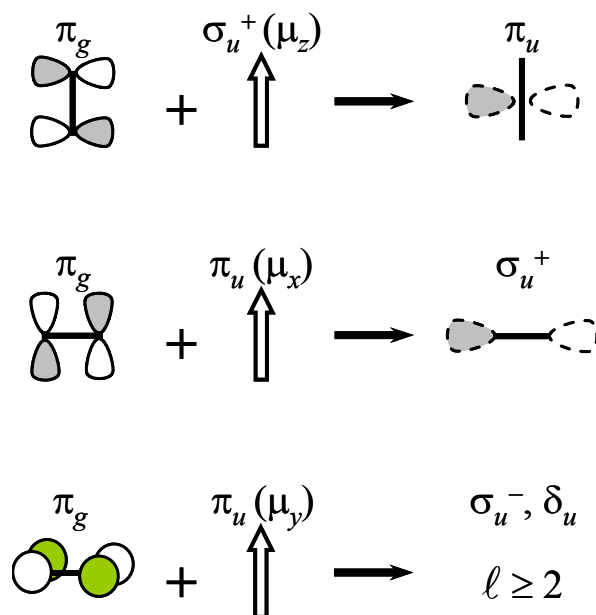


Figure 4.13 The *s&p* model treatment of $S_2^- (\pi_g^{-1})$ photodetachment. Bold solid line is the S_2 molecular frame. Solid contours on the left represent the bound MO (π_g). Vertical arrows in the middle indicate the laser polarization direction, with the corresponding MF symmetry of the active transition dipole components shown. Dashed contours on the right represent the symmetry-allowed partial waves ($\ell \leq 1$) that contribute to ψ_f . The σ_u^- and δ_u waves corresponding to the $\pi_u(m_y)$ transition moment expands only in $\ell \geq 2$ waves, which are neglected in the model.

principal orientation interacts with the σ_u active dipole moment to produce a π_u free electron wave. The second and third principal orientation interacts with the degenerate π_u active components of the transition dipole. The μ_x component produces σ_u^+ while the μ_y component produces both σ_u^- and δ_u waves when interacted with their respective principal orientations. Expanding ψ_f in the AO basis with the $\ell < 2$ model approximation, only p waves are produced for the first two orientations. The third orientation only produces waves with $\ell \geq 2$. The p waves produced are all perpendicular to the laser polarization; hence, the s and p model predicts $\beta < 0$.

Thus, the $s\&p$ model predicts $\beta < 0$ for all three π_g^{-1} transitions yielding the $X^3\Sigma_g^-$, $a^1\Delta_g$, and $b^1\Sigma_g^+$ neutral states. The 400 nm experiment shows that β is indeed substantially negative for the X state ($\beta = -0.54 \pm 0.02$, integrated over all vibrational components). However, the overall anisotropies are almost zero ($\beta = -0.16 \pm 0.06$) and even positive ($\beta = 0.29 \pm 0.06$) for the a and b states, respectively. Although the β values for the a and b states tend to become negative as eKE increases, this case highlights the limitations of the model inherent in its qualitative nature. The Cooper-Zare wave composition depends on the initial state orbital angular momentum, while the $s\&p$ model in its present formulation always includes only s and p waves. (However, some generalization of the model to include higher-order waves is in principle possible.) As a consequence of this limitation, only p -wave contributions are considered in the photodetachment of S_2^- . Thus, the $s\&p$ model may serve as an insightful tool for determining the overall nature of the detachment process, as reflected in its anisotropy at

intermediate eKEs, while predicting the anisotropy at any given eKE requires a more rigorous, quantitative approach.

For the transitions arising from the π_u (HOMO-1) of S_2^- , the allowed partial waves are σ_g^+ , σ_g^- , δ_g , and π_g . Of these, only the σ_g^+ wave contains partial waves with $\ell < 2$, namely, the isotropic s functions. All other waves formed under the above symmetry restrictions expand in $\ell \geq 2$ AO functions. Thus, p waves are forbidden for this transition under the one-electron, electric-dipole approximations. The s partial wave is responsible for a nearly isotropic PAD predicted for this case, in agreement with the nearly isotropic ($\beta = -0.14 \pm 0.06$) A', c feature in Figs. 4.1(a) and (d).

4.4 SUMMARY:

The utility of photoelectron imaging to probe the electronic structure of molecular anions was discussed. The results of S_2^- , O_2^- , SO^- , and CS_2^- were presented over a series of wavelengths examining the electronic structure and electron ejection dynamics.

Two approaches to describing the photodetachment process and interpreting the PADs of small molecular anions were illustrated with model system, S_2^- and CS_2^- . The first approach extends the central-potential model of Cooper and Zare to molecules whose MO closely resembles an AO. However since most MO do not resemble AO a second approach was developed for more complicated system such as CS_2^- . It relies upon group theory and dipole transition selection rules to determine the symmetry of the outgoing free electron waves, which are then expanded in AO basis and restricted to only s and p waves.

These results provide a tutorial foundation for the interpretation of anion photoelectron images, which will be useful in developing more sophisticated approaches to more complex systems.

5 NONEXISTENT ELECTRON AFFINITY OF CARBONYL SULFIDE AND ITS STABILIZATION BY GAS PHASE HYDRATION

5.1 INTRODUCTION

Gas-phase clusters serve as microlaboratories to investigate electronic structure, chemical interactions and reaction dynamics. Solvation stabilizes molecular anions through electrostatic effects, displaying dramatic changes in electronic structure and dynamics. Ion-neutral interactions decrease the energy of an anion relative to its neutral species. Of particular interest are cases that the corresponding neutral cannot bind an electron, yet the anion can be stabilized and studied within a cluster. The effects of both heterogeneous and homogenous solvation are examined with photoelectron imaging experiments.

This chapter describes the determination of carbonyl sulfide's electron affinity (EA) through theoretical calculations and indirect experiment observations such as photoelectron imaging of hydrated carbonyl sulfide cluster anions and mass spectrometry of $(\text{OCS})_n^-$ cluster anions.

A fundamental question in regard to the isovalent $(\text{CO}_2)_n^-$, $(\text{OCS})_n^-$ and $(\text{CS}_2)_n^-$ anionic clusters is whether the excess electron localizes on a single monomer or is shared between two (or more) monomer moieties.^{43,53-60} CS_2^- and CO_2^- cluster anions have been the subject of several experimental and theoretical studies^{43,54-58,61-72} compared to the relatively few studies conducted on OCS^- clusters anions.^{6,60,69} OCS is a hybrid of CO_2 and CS_2 . Its fundamental properties are in between those of CO_2 and CS_2 . In particular, the electron affinity of OCS has remained uncertain. As in CO_2 and CS_2 the

determination of the EA is complicated by differences between the equilibrium geometries of the neutral and the anion. CO_2 electron affinity is negative (-0.6eV), while in CS_2 it is positive ($0.9\text{-}1.0\text{ eV}$). In either case the sign of the EA isn't in doubt, but in OCS even the sign is not known. Since OCS is a hybrid of its isovalent companions its EA is close to zero. Hence it is crucial to carefully determine its EA even for a qualitative description of the stability and other properties of carbonyl sulfide anions.

The only experimental evidence of the EA of OCS reported in the literature is $0.46 \pm 0.2\text{ eV}$.⁷³ However, this result is difficult to reconcile with the observed absence of the OCS^- monomer anions in the $(\text{OCS})_n^-$ family.⁶⁰ It is also inconsistent with a theoretical study by Gutsev et al., who predicted the EA to be 0.22 eV at CCSD(T) level.⁶ Presented below is indirect evidence that OCS^- is metastable, the most extensive (to date) theoretical investigation of the EA of OCS, and an experimental estimate of the EA of OCS determined through photoelectron imaging of $[\text{OCS}\cdot\text{H}_2\text{O}]^-$. By investigating the hydrated clusters, we aim to unravel the properties of OCS^- .

OCS^- is not formed effectively in our ion source. Its absence in the ion beam is an indirect indication that OCS^- has no electron affinity. The appearance of OCS^- fragments (with a lifetime $\geq 5\text{ }\mu\text{s}$), resulting from photodissociation of $(\text{OCS})_n^-$, is another piece of the puzzle,⁶⁰ suggesting the metastable nature of OCS^- . However, these observations are inconclusive because the absence of the monomer in the $(\text{OCS})_n^-$ ion beam can be explained by the mechanism of cluster formation rather than by OCS^- energetics.

A possible mechanism for formation of $(\text{OCS})_n^-$ cluster anions is the attachment of slow electrons to neutral $(\text{OCS})_n$ clusters, followed by cluster cooling via the loss of

solvent molecules. The solvent shell then grows through long range ion-neutral interactions in the supersonic expansion.³³ Because of the geometry difference between neutral OCS, (linear) and OCS^- (bent), an isolated OCS cannot attach an electron. Due to evidence of the covalently bound dimer core, $(\text{OCS})_2^-$, it is possible that the formation of small $(\text{OCS})_n^-$ cluster ions always involves a molecular rearrangement leading to the stable dimer core. In this case, the monomer anions may not be formed because the solvent loss stops at the dimer level, not because OCS^- is unstable. However, the presence of hydrated OCS cluster anions in the ion beam would direct us away from the explanation of dimer core formation, for the lack of OCS^- formation, leading us toward the instability of OCS^- in the absence of stabilization through solvation.

The experimental and theoretical methods employed in this study are provided in section 5.2. The indirect experiment results are presented in section 5.3.1 while the theoretical investigation of the EA OCS and study of $\text{OCS}^- \cdot \text{H}_2\text{O}$ are presented in section 5.3.2. Photoelectron imaging studies of $\text{OCS}^- \cdot \text{H}_2\text{O}$ are presented in section 5.3.3. and section 5.4 summarizes the conclusions.

5.2 EXPERIMENTAL AND COMPUTATIONAL METHODS

5.2.1 Experimental Setup

The negative-ion photoelectron imaging spectrometer described in chapter two was used. Important details are briefly given here. A room temperature mixture of 7 % OCS in Ar with trace amounts of water is expanded through a pulsed supersonic valve operated with a backing pressure of 1.5 atm at a repetition rate of 50 Hz. The expansion is ionized by secondary electron attachment, and the anions are extracted in a TOF mass

spectrometer, which records the mass spectrum. A 100 fs laser pulse at 800, 529 and 400 nm photodetaches electrons from mass selected anions. The electrons are then projected onto a 2D imaging detector.

The anion TOF spectra are converted into mass spectra by first relying on the calibration of the mass spectrometer based on the known experimental parameters. The exact assignment is achieved by choosing pairs of prominent peaks with unambiguous preliminary assignments and adjusting the flight-time to mass conversion parameters to satisfy the chosen time–mass pairs.

5.2.2 Computational Details

The calculations are carried out with the GAUSSIAN 98 suite of programs,⁷⁴ employing a range of ab initio and hybrid Hartree-Fock density functional theory (DFT) methods with two classes of basis sets: the split-valence sets of Pople with added diffuse and polarization functions [6-31+G(d,p), 6-311+G(d,p), and others], and the augmented correlation-consistent basis sets of Dunning (aug-cc-pVXZ, where X = D, T, Q, for double, triple, and quadruple- ζ). The new G3large basis set,⁷⁵ not available in GAUSSIAN 98, was also used in some calculations.

The ab initio calculations were carried out using several methods accounting for electron correlation: the Møller-Plesset perturbation theory,⁷⁶ the coupled-cluster theory,^{6,77} and the non-variational quadratic configuration interaction (CI) method.⁷⁸ The Møller-Plesset correlation energy correction was computed to the second,^{76,77,79} third,^{77,80} and fourth⁷⁷ orders (MP2, MP3, and MP4, respectively). The fourth-order Møller-Plesset calculations were complete with single, double, triple, and quadruple substitutions (MP4-

SDTQ). The coupled-cluster theory and quadratic CI calculations included single and double excitations, with triple excitations treated perturbatively, where indicated [CCSD, CCSD(T), and QCISD(T)].^{78,81-83}

The EA of OCS was also determined using the Gaussian-2 (G2)⁸⁴ and Gaussian-3 (G3) composite ab initio theories.⁸⁵ The final G2 and G3 energies are effectively at the QCISD(T) level used with the 6-311+G(3df) and G3large basis sets, respectively,^{75,86} with the high-level accuracy achieved at significantly lower computational cost than that of a direct calculation. The Gaussian theories are attractive for the present study, because their performance in calculating the total energies and EAs has been thoroughly tested on the sets of reliable experimental data, known as the G2/97^{75,87} and G3/99⁸⁸ test sets. The availability of published test data statistics^{75,85} enables us to assign meaningful margins of trust to the computed EA values.

The G2 calculations were carried out using the standard procedure in GAUSSIAN 98.⁷⁴ The G3 method is not included in the GAUSSIAN 98 package, and neither is the G3large basis set [which is an improved version of 6-311+G(3df,2p) with modified polarization functions].⁷⁵ The G3large basis for O, C, and S was downloaded as instructed by its developers,⁷⁵ and all computational steps comprising the G3 method were carried out separately with GAUSSIAN 98,⁷⁴ after which the necessary energy corrections were determined and combined to yield the total energies of OCS and OCS⁻ at 0 K, referred to as the G3 energies.⁷⁵ Unlike the anion, the neutral OCS molecule is included in the G2/97 test set, which enabled us to compare the calculated G3 energy of OCS to the published value⁷⁵ and thus verify the accuracy of our G3 procedure. To the

best of our knowledge, the G3 energy of OCS^- has not been calculated previously. Since the zero-point vibrational energy is included in the G2 and G3 energies, the corresponding adiabatic EAs were directly determined as the difference between the G_n energies of the neutral and the anion.

The DFT was chosen for its computational efficiency, which is particularly important for the cluster ion calculations, as well as for its track record in predicting electron affinities.⁸⁹ The specific DFT methods used in this study are BLYP, B3LYP, and *mPW1PW*. The first two employ the 1988 functional⁹⁰ and the three-parameter exchange functional⁹¹ of Becke, respectively, in conjunction with the correlation functional of Lee, Young, and Parr.⁹² The *mPW1PW* method is based on Barone and Adamo's Becke-style one-parameter hybrid functional with modified Perdew-Wang exchange and correlation and improved long-range behavior.⁹³

The spin-unrestricted methods were used for open-shell systems, while spin-restricted calculations were carried out in the closed-shell cases. By default, only the outer-shell electrons were included in the correlation calculations. However, in several cases (identified by the 'full' keyword), full correlation calculations were carried out in order to quantify the effect of including the inner-shell electrons. For geometry optimizations, the Berny algorithm⁹⁴ was used by default. However, in calculations on some cluster ion conformations involving rather flat potential energy surfaces, the convergence was achieved using the modified GDIIIS method (geometry by direct inversion in the iterative subspace).⁹⁵

5.3 RESULTS AND DISCUSSION

5.3.1 Indirect Mass Spectral Evidence of OCS^- Metastability

Three mass spectra of $(\text{OCS})_n^-$ and S^- are shown in Fig. 5.1. Each is at a different mass range adjusted by shifting the delay between the ion extraction pulse and when potential switch turns off. Mass spectra 5.1(a), (b), and (c) correspond to delays of 11.8, 13.6, and 26.6 μs respectively. The experimental conditions are optimized for each mass range to provide sharp S^- and OCS^- peaks. To check the calibration of the mass spectrometer we examine the magnified ($\times 10$) spectra in Fig. 5.1(a) of S^- . The isotope peaks at 34 and 33 atomic mass units (amu) correspond in size and location to their natural abundance (4.21 % and 0.75%)⁴⁰ for $^{34}\text{S}^-$ and $^{33}\text{S}^-$ respectively.

The dominant peak in spectra (a) and (b) is S_2^- at 64 amu. Since sulfide does not reside in the source, it must arise from OCS clusters. To reinforce that it is not OCS^- at 60 amu the satellite peak at 66 has the correct natural abundance ratio for $^{32}\text{S}^{34}\text{S}^-$ (0.08).

There is almost no signal at 60 amu. The barely measurable peak at 60 amu in the magnified spectrum depends upon the conditions of the supersonic expansion and

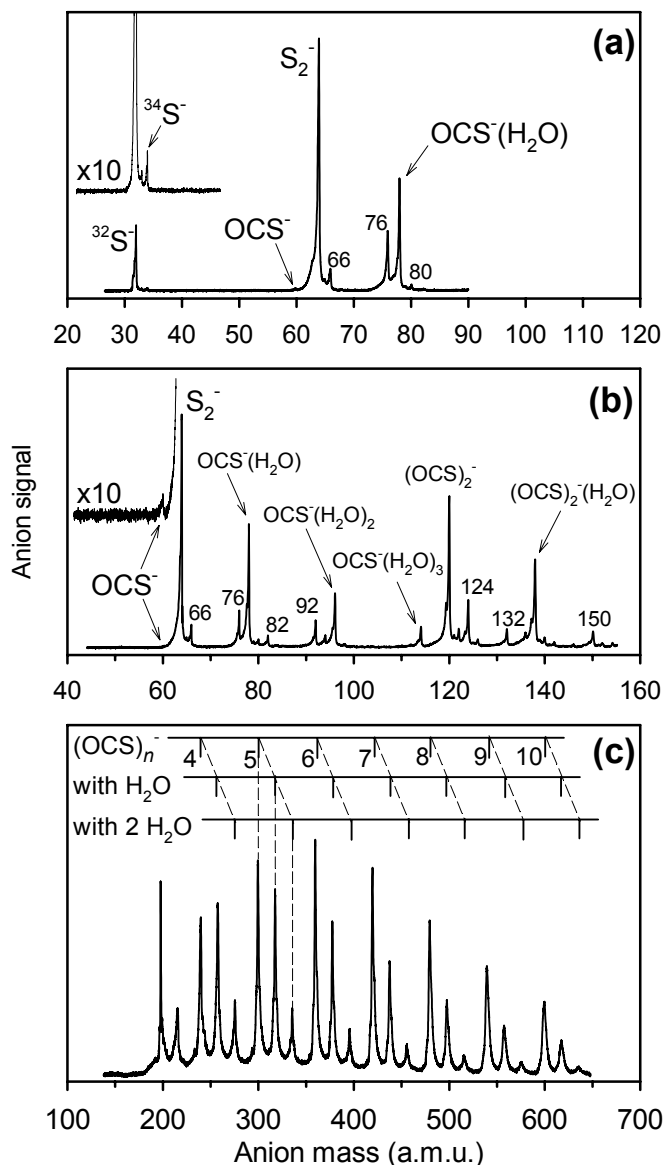


Figure 5.1. Negative ion mass spectra obtained with the OCS/Ar precursor containing a trace amount of water. The magnified ($\times 10$) spectra in (a) and (b) correspond to the experimental conditions optimized for the S^- and OCS^- anions, respectively. The latter shows the best OCS^- signal that could be achieved in the experiment. The ion peaks in (a) and (b) labeled in accordance with the corresponding anion mass (in a.m.u.) are assigned as follows: 66 = $^{32}S^{34}S^-$; 76 = CS_2^- ; 80 = $OC^{34}S_2^- \cdot H_2O$; 82 = $S_2^- \cdot H_2O$; 92 = OCS_2^- ; 124 = $S_2^- \cdot OCS$; 132 = $OCS^- \cdot (H_2O)_4$; 150 = $OCS^- \cdot (H_2O)_5$. In (c), the top of the three combs above the mass spectrum indicates the peak positions for the $(OCS)_n^-$ cluster anions ($n = 4 - 10$). The two lower combs correspond to the monohydrated $(OCS)_n^- \cdot H_2O$ and doubly hydrated $(OCS)_n^- \cdot (H_2O)_2$ cluster ions, respectively.

particularly upon the position of the 1 keV electron beam relative to the nozzle. The magnified spectrum was recorded with the experimental conditions optimized for OCS^- and represents the best OCS^- signal that could be achieved.

The intense progression of hydrated OCS^- is noteworthy due to the lack of OCS^- in the mass spectrum. The first $[\text{OCS} \cdot (\text{H}_2\text{O})_k]^-$ at 78 amu when $k=1$ is the third most intense peak in the spectrum in Fig. 5.1 (b). Since a single water molecule cannot bind an electron,⁹⁶⁻¹⁰⁴ the excess electron in hydrated OCS should reside on the OCS monomer giving the structure $\text{OCS}^- \cdot \text{H}_2\text{O}$. When $k > 1$ the question of electron localization is open but in analogy with $\text{CO}_2^- \cdot (\text{H}_2\text{O})_k$,¹⁰⁵⁻¹⁰⁸ it is reasonable to assume that the electron is localized on the OCS^- cluster core. In view of the insignificant OCS^- signal, the efficient formation of the $\text{OCS}^- (\text{H}_2\text{O})_k$ cluster ions is quite revealing. In particular, it is remarkable that the $\text{OCS}^- \cdot \text{H}_2\text{O}$ peak is one of the most intense peaks in the spectrum, while the seemingly simpler OCS^- anion is barely observed at all. In this light the hypothesis of dimer ion core formation does not explain the lack of OCS^- in the mass spectrum. In the mass spectrum (Fig. 5.1 (b)) $\text{OCS}^- \cdot (\text{H}_2\text{O})_k$ $K = 1-5$ is observed. Peaks 132 and 150 correspond to $k = 4$ and 5 respectively. These all have the characteristic isotope satellite peaks for anions containing one sulfur atom.

Another intense peak in Fig. 5.1(b) with a series of satellite peaks characteristic of an anion containing two sulfur atoms is $(\text{OCS})_2^-$ anion. Lineberegger and co-workers⁶⁰ argued that this peak is the covalent dimer anion and not $\text{OCS}^- \cdot \text{OCS}$ cluster. However, photoelectron imaging of this peak and others, which will be discussed in subsequent

chapters, reveals that both isomers coexist. The question of whether the $(\text{OCS})_n^-(\text{H}_2\text{O})_k$ cluster ions possess a monomer or dimer anion core will remain open until we examine the photoelectron images of these clusters.

Figure 5.1 (c) shows a mass spectrum optimized for heavy ions. The sharp onset of signal at 200 amu is due to the truncation of the spectrum by the potential switch. At the top of the spectrum in Fig 5.1(c) are three combs indicating the peak positions for $(\text{OCS})_n^-$ cluster anions ($n = 4 - 10$), monohydrated $\text{OCS}^-\cdot\text{H}_2\text{O}$ and the doubly hydrated $\text{OCS}^-\cdot\text{H}_2\text{O}$ cluster anion series.

To summarize the experimental results, the OCS^- anions are formed extremely inefficiently in an electron-impact ionized OCS/Ar expansion; nonetheless, the hydrated cluster ions, in particular $\text{OCS}^-\cdot\text{H}_2\text{O}$, are produced readily and in abundance. We have also observed the hydrated carbonyl sulfide dimer ion, as well as larger $[(\text{OCS})_n(\text{H}_2\text{O})_k]^-$ cluster ions. In the next Section, we combine these observations with theoretical evidence that the OCS monomer has no electron affinity and discuss the stabilization of metastable OCS^- by gas phase hydration, as the effect responsible for the observation of the $\text{OCS}^-(\text{H}_2\text{O})_k$ clusters.

5.3.2 Theoretical Results and discussion

Adiabatic electron affinity of OCS

The definition of adiabatic EA as the energy difference between the lowest-energy states of the neutral and the anion becomes ambiguous if the calculated EA turns out negative. A negative EA implies that the relaxed neutral species lies lower in energy than the corresponding anion (e.g., CO_2 vs. CO_2^-). However, it immediately follows that

in such a case the most stable anionic state is a relaxed neutral molecule plus a free electron (e^-), and therefore, the truly adiabatic EA is not negative, but zero, or – it is said – nonexistent. Accordingly, a calculation within the Born-Oppenheimer limit sampling the entire coordinate space and employing a sufficiently large basis set must yield an EA approaching zero. Unfortunately, this conclusion tells little about the structure of the metastable anion of interest. It does show, however, that it is important to clarify what is meant by reporting negative values of adiabatic EA.

We begin our investigation of the EA of OCS by exploring the OCS and OCS^- bending potentials with relatively inexpensive calculations. Figure 5.2 shows portions of the OCS and OCS^- potential energy curves calculated along the bending coordinate using the CCSD theory with the 6-31+G(d) basis set. For each OCS angle, the CO and CS bond lengths in both the neutral and the anion were optimized to yield the relaxed potential energy curves. The three curves in Fig. 5.2 correspond to the following *diabatic* states: (I) the neutral OCS molecule *or* the $\text{OCS} + e^-$ (detached-electron) state; (II) the OCS^- molecular anion; and (III) the $\text{S}^- \cdots \text{CO}$ anion-neutral complex (corresponding to C-S distances of 3.2–3.7 Å). The horizontal lines above the OCS and OCS^- potential minima indicate the ground state energies corrected for the zero-point vibrational energy (ZPE). The relaxed OCS has lower energy than OCS^- , indicating that the EA, defined as the difference between the two potential minima, is negative.

The crossing between curves I and II, corresponding to the diabatic $\text{OCS} + e^-$ and OCS^- states, defines the adiabatic ground state of the anionic system, which has an electron-bound (OCS^-) and free-electron characters to the left and to the right of the I/II

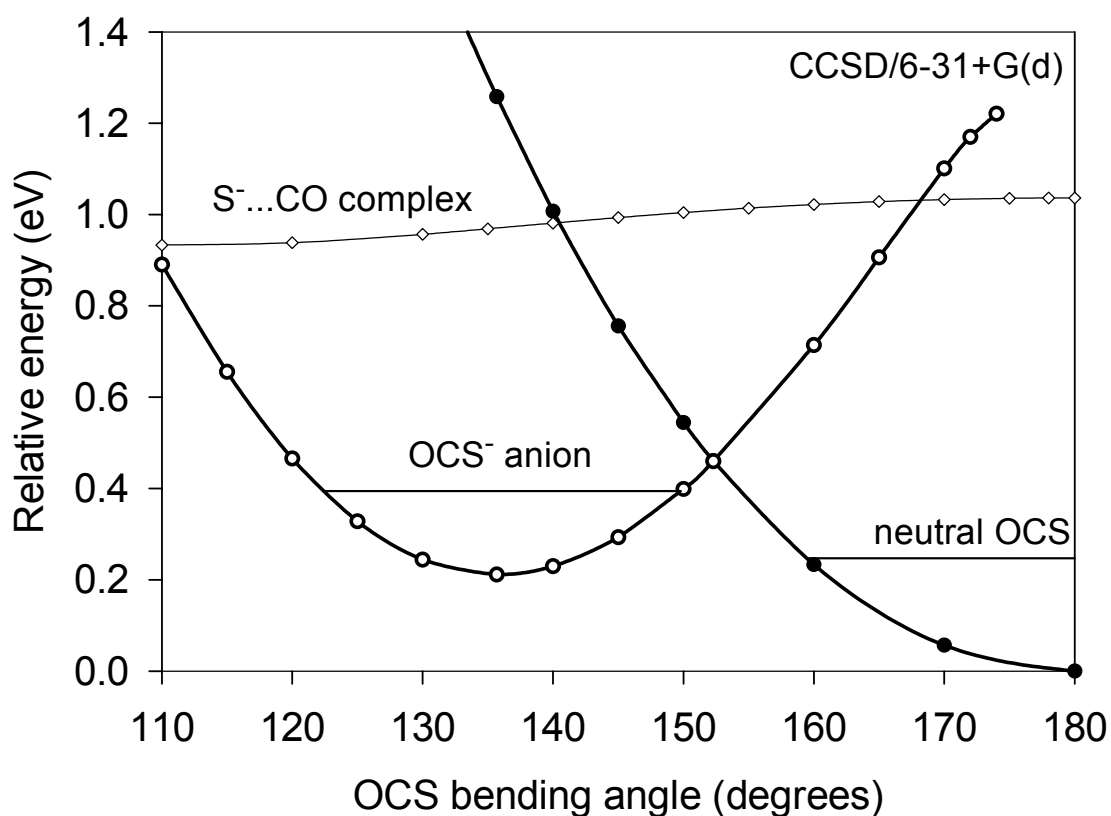


Figure 5.2. The relaxed diabatic potential energy curves of OCS (curve I: filled circles), OCS⁻ (curve II: open circles, bold line), and S⁻·CO (curve III: open symbols, thin line), calculated along the bending coordinate at the CCSD theory level with the 6-31+G(d) basis set. Curve I also corresponds to the OCS + *e*⁻ detached-electron state. In the S⁻·CO anion-neutral complex (curve III), the typical C-S distance is in the 3.2–3.7 Å range. The horizontal lines above the OCS and OCS⁻ potential minima indicate the ground state energies corrected for the ZPE.

crossing point in Fig. 5.2, respectively. Thus, there is a potential barrier on the adiabatic bending potential, separating the bent OCS^- equilibrium from the more energetically favorable linear $\text{OCS} + e^-$ system. If OCS^- is formed within the potential well corresponding to the electron-bound state, it is isolated from the part of the potential energy surface where the autodetachment would occur. The barrier separating the OCS^- and $\text{OCS} + e^-$ equilibria is actually higher than the I/II intersection point at $\angle\text{OCS} = 152.3^\circ$ in Fig. 5.2, because this point in fact corresponds to two different geometries of the neutral and the anion ($R_{\text{CO}} = 1.171$ vs. 1.216 Å, respectively, and $R_{\text{CS}} = 1.587$ vs. 1.685 Å, respectively) and does not represent the top of the barrier. Approximating the barrier top location with an intermediate geometry halfway between the partially relaxed neutral and anion geometries at $\angle\text{OCS} = 152.3^\circ$, we estimate that the barrier height is about 0.32 eV relative to the electronic potential minimum on the OCS^- side. Including the ZPE, the CCSD/6-31+G(d) method predicts that the barrier lies about 0.14 eV or 1100 cm^{-1} above the OCS^- ground state. The metastable OCS^- state may explain the observation of the minor quantities of OCS^- in the present experiment, as well as the unsolvated OCS^- fragments in the $(\text{OCS})_2^-$ photodissociation, which were found to be stable on a $>5\text{ }\mu\text{s}$ timescale.⁶⁰

Defining the EA as the energy difference between the neutral state and the (metastable) electron-bound OCS^- state, the EA of OCS was calculated at several ab initio and DFT theory levels, employing a variety of basis sets. Except where single-point calculations are indicated, the geometries of OCS and OCS^- were fully optimized at

the indicated theory level until the gradients fell below the threshold values (typically, $\sim 4.5 \times 10^{-4}$ and 3×10^{-4} a.u. for the maximum and rms force, respectively, and 0.001 and 0.0006 Å for the maximum and rms displacements, respectively). The results of the ab initio calculations are summarized in Table 5.1, which lists the values of purely electronic EA, excluding the ZPE corrections (except for the composite Gaussian methods). The EA values determined by Gutsev et al.⁶ are also included. For comparison, Table 5.2 lists the EAs determined by several DFT methods.

The optimized geometries and vibrational frequencies determined at selected theory levels are given in Table 5.3, along with the zero-point vibrational energies and Δ ZPE corrections to the EA (Δ ZPE is defined as the difference between the ZPEs of OCS and OCS⁻). The EA of OCS, corrected for the ZPEs, is obtained by adding Δ ZPE to the purely electronic EA values listed in Tables I and II. While Δ ZPE varies slightly with the theory level and basis set, the rounded-off correction Δ ZPE = 0.07 eV, consistent with most calculations, is sufficient for this discussion.

Some of the results for EA(OCS), including the Δ ZPE correction, are summarized in a graphic form in Fig. 5.3. Our strategy in selecting data for this plot has been for each type of calculations to choose the results obtained with the largest basis set. The ab initio results are generally arranged in the order of increasing the level of electron correlation. All ab initio methods predict that the adiabatic EA is either negative or essentially zero. The largest in magnitude negative values of EA are predicted by the second-order Møller-Plesset perturbation theory. While almost always remaining negative, the absolute magnitude of the EA tends to decrease, approaching zero, as the correlation effects

Table 5.1. Calculated ab initio values of the electron affinity of OCS, excluding the zero-point vibrational energy corrections (Δ ZPE), except where noted.

Method	Basis set	EA, eV (excluding Δ ZPE)
HF	6-31+G(d)	-0.209
	6-311+G(3df)	-0.394 ^[G]
MP2	6-31+G(d)	-0.510
	aug-cc-pVDZ	-0.315 [†]
	aug-cc-pVTZ	-0.335 [†]
MP2 (full)	aug-cc-pVDZ	-0.338 [†]
MP3 (full)	aug-cc-pVDZ	-0.100 [†]
MP4-SDTQ	6-31+G(d)	-0.459 [†]
MP4-SDTQ (full)	aug-cc-pVDZ	-0.239 [†]
CCSD	6-31+G(d)	-0.211
	6-311+G(d)	-0.284
	6-311+G(2df)	-0.203
	aug-cc-pVDZ	-0.035
	aug-cc-pVTZ	-0.059 [‡]
CCSD (full)	6-31+G(d)	-0.237
	6-311+G(d)	-0.295
	aug-cc-pVDZ	-0.058
CCSD(T)	6-311+G(d)	-0.342
	6-311+G(3df)	-0.295 ^[G]
	aug-cc-pVDZ	-0.071
CCSD(T)	G3large	
MP2		-0.439
MP3		-0.217
MP4-SDTQ		-0.336
CCSD		-0.162
CCSD(T)		-0.190
QCISD(T)	6-31+G(d)	-0.276
	6-311+G(d)	-0.342
	aug-cc-pVDZ	-0.067
Composite theories (incl. ZPE):		
	Gaussian-1 (G1)	-0.107 [*]
	Gaussian-2 (G2)	-0.095 [*]
	Gaussian-3 (G3)	-0.059 [*]

^[G] from Gutsev et al.⁶[†] From single-point calculations at the geometries optimized at the MP2/6-31+G(d) level.[‡] From single-point calculations at the geometries optimized at the CCSD/aug-cc-pVDZ level.^{*} Includes the Δ ZPE correction.

Table 5.2. Calculated DFT values of the electron affinity of OCS, excluding the zero-point vibrational energy corrections (ΔZPE).

Method	Basis set	EA, eV (excluding ΔZPE)
BLYP	6-31+G(d)	0.065
	6-311+G(d)	0.021
	aug-cc-pVDZ	0.074
	aug-cc-pVTZ	−0.020
	aug-cc-pVQZ	−0.033
B3LYP	6-31+G(d)	0.226
	6-311+G(d)	0.164
	6-311+G(3df)	0.059
	G3large	0.061
	aug-cc-pVDZ	0.208
	aug-cc-pVTZ	0.103
	aug-cc-pVQZ	0.085
<i>m</i>PW1PW91	6-31+G(d)	0.170
	6-311+G(d)	0.104
	6-311+G(3df)	−0.003
	aug-cc-pVDZ	0.149
	aug-cc-pVTZ	0.041
	aug-cc-pVQZ	−0.147

beyond the second-order perturbation theory are included. The basis sets of Dunning (open circles in Fig. 5.3) tend to yield higher (less negative) values of EA than the basis sets of Pople (filled circles).

Special consideration is given to the G3 theory value of $EA = -0.059$ eV. Not surprisingly, the largest corrections for the EA within the G2 and G3 calculations come from the inclusion of diffuse basis functions, underscoring their importance for proper modeling of the electronic structure of OCS^- . In the G3 theory, the total energy correction for diffuse functions $\Delta E(+)$ is -0.03099 hartrees for the anion compared to -0.00840 hartrees for the neutral, increasing the calculated value of EA by 0.615 eV.

The known test statistics for the G2 and G3 theories are used here to arrive

Table 5.3. Calculated equilibrium geometries and vibrational frequencies of OCS and OCS⁻.

	HF 6- 31G(d)	CCSD 6- 31+G(d)	CCSD 6- 311+G(d)	CCSD(T) G3large	B3LYP G3large
<i>Neutral</i>					
<i>OCS</i>					
R_{CO} , Å	1.1314	1.1670	1.1557	1.1598	1.1555
R_{CS} , Å	1.5723	1.5703	1.5683	1.5675	1.5616
ω_1 , cm ⁻¹	794 [*]	884	888		880
ω_2 , cm ⁻¹	506 [*]	493	505		530
ω_3 , cm ⁻¹	2059 [*]	2118	2137		2112
ZPE, eV	0.2396 [*]	0.2472	0.2501		0.2512
<i>OCS⁻</i>					
<i>Anion</i>					
R_{CO} , Å	1.1869	1.2175	1.2074	1.2103	1.2058
R_{CS} , Å	1.7318	1.7116	1.7103	1.7067	1.7013
$\angle\text{OCS}$, °	135.12	135.69	135.69	136.69	136.98
ω_1 , cm ⁻¹	676 [*]	740	735		703
ω_2 , cm ⁻¹	463 [*]	498	500		487
ω_3 , cm ⁻¹	1717 [*]	1712	1718		1684
ZPE, eV	0.1771 [*]	0.1829	0.1831		0.1782
55ΔZPE, eV	0.063 [*]	0.064	0.067		0.073

Note: the experimental values for OCS are: $R_{\text{CO}} = 1.1562$ Å, $R_{\text{CS}} = 1.5614$ Å, and vibrational frequencies 875.3, 524.4, and 2093.7 cm⁻¹.⁴

^{*} The HF/6-31G(d) frequencies and ZPEs are scaled by a factor of 0.8929.

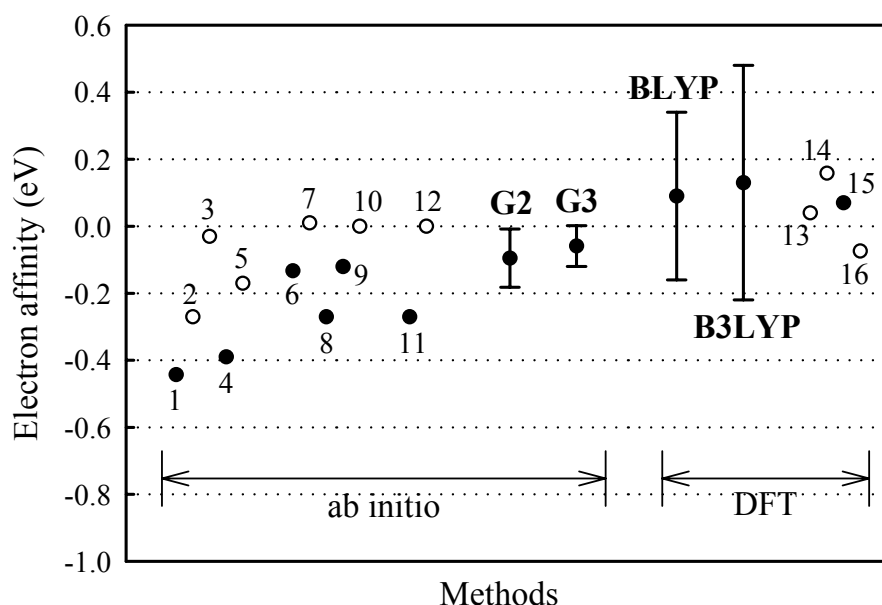


Figure 5.3. Some of the results for the adiabatic EA of OCS, including the Δ ZPE correction. Open and filled circles: results obtained with the augmented correlation consistent basis sets of Dunning and the split valence basis sets of Pople, respectively. The error bars for the G2, G3, BLYP, and B3LYP results are determined as described in the text. The BLYP result was obtained with the 6-311+G(d) basis set, while both the 6-311+G(3df) and G3large basis sets yielded the B3LYP value shown with an error margin. Other data are as follows: 1 - MP2/6-31+G(d); 2 - MP2/aug-cc-pVTZ; 3 - MP3(Full)/aug-cc-pVDZ; 4 - MP4(Full)/6-31+G(d); 5 - MP4(Full)/aug-cc-pVDZ; 6 - CCSD/6-311+G(2df); 7 - CCSD/aug-cc-pVTZ; 8 - CCSD(T)/6-311+G(d); 9 - CCSD(T)/G3large; 10 - CCSD(T)/aug-cc-pVDZ; 11 - QCISD(T)/6-311+G(d); 12 - QCISD(T)/aug-cc-pVDZ; 13 - BLYP/aug-cc-pVQZ; 14 - B3LYP/aug-cc-pVQZ; 15 - mPW1PW91/6-31+G(3df); 16 - mPW1PW91/aug-cc-pVQZ.

at meaningful trust margins for the calculated values of EA. The average absolute deviation of the G3 electron affinities from the experimental data has been determined to be 1.00 kcal/mol, or 43 meV, compared to 1.41 kcal/mol, or 61 meV for the predecessor G2 theory.⁷⁵ More importantly, 62% of the EAs calculated using the G3 method fall within 1.0 kcal/mol of the experimental values for the G2/97 test set species, while 76% fall within 1.4 kcal/mol (61 meV).⁷⁵ For G2, the corresponding measures are: 55% within 1.4 kcal/mol of the experiment and 76% within 2.0 kcal/mol (87 meV).⁷⁵ Based on these assessments, we assign the following margins of trust (with estimated 76% confidence) for the EAs calculated here using the G3 and G2 theories: EA(OCS) = -0.059 ± 0.061 eV for G3 and -0.095 ± 0.087 eV for G2.

Unlike the ab initio methods, the DFT calculations with moderate-size basis sets yield positive values of the adiabatic EA of OCS. However, the calculated EA decreases consistently as the size of the basis set is increased. For example, the *m*PW1PW91 method employed with Dunning's basis sets predicts the values of EA that reverse sign from positive to negative as the basis set is expanded from double to quadruple- ζ (see Table II).

Tschumper and Schaefer estimated average absolute errors of 0.25 and 0.18 eV for the EAs of triatomics predicted using the B3LYP and BLYP methods, respectively.⁸⁹ Scaling these average values by a factor of 1.4, for a higher confidence level similar to the above G3 and G2 analyses, we arrive at the following margins of trust for some of our DFT results (including the Δ ZPE corrections): EA(OCS) = 0.13 ± 0.35 eV for the B3LYP calculations with both the 6-311+G(3df) and G3large basis sets and 0.09 ± 0.25 eV for

the BLYP/6-311+G(d) result.

The margins of trust for the G2, G3, BLYP, and B3LYP calculations are indicated as error bars in Fig. 5.3. Given the large margins estimated for DFT, there is no discrepancy between the G3 and G2 predictions on the one hand, and the DFT results on the other. The G3 and G2 values are also consistent with most coupled-cluster and quadruple CI theories results. We thus conclude that the EA of OCS is either slightly negative or zero. In the strict adiabatic sense, our overall conclusion is that OCS has no electron affinity.

This conclusion is in disagreement with the 1975 collisional detachment measurement, which placed the EA of OCS at 0.46 ± 0.2 eV.⁷³ However, the preponderance of theoretical evidence, corroborated by the indirect experimental observations, indicates that the EA cannot be substantially positive. Even so, the metastable OCS^- anions can be formed via a dynamic process involving a favorable (bent) geometry, as in the case of $(\text{OCS})_2^-$ dissociation, where the parent dimer anion has two covalently joined, bent OCS moieties.⁶⁰

Structure and Energetics of $\text{OCS}^- \cdot \text{H}_2\text{O}$

Given the nonexistent EA of OCS, the corresponding anions exist in the stable, hydrated form due to the additional stabilization resulting from the strong ion–neutral interactions between OCS^- and H_2O . The experiment indicates that the addition of one water molecule is sufficient to offset the negative value of the EA. This is not surprising, considering the small absolute values of the negative EA predicted above.

We determined theoretically the structures of four $\text{OCS}^- \cdot \text{H}_2\text{O}$ isomers, which are

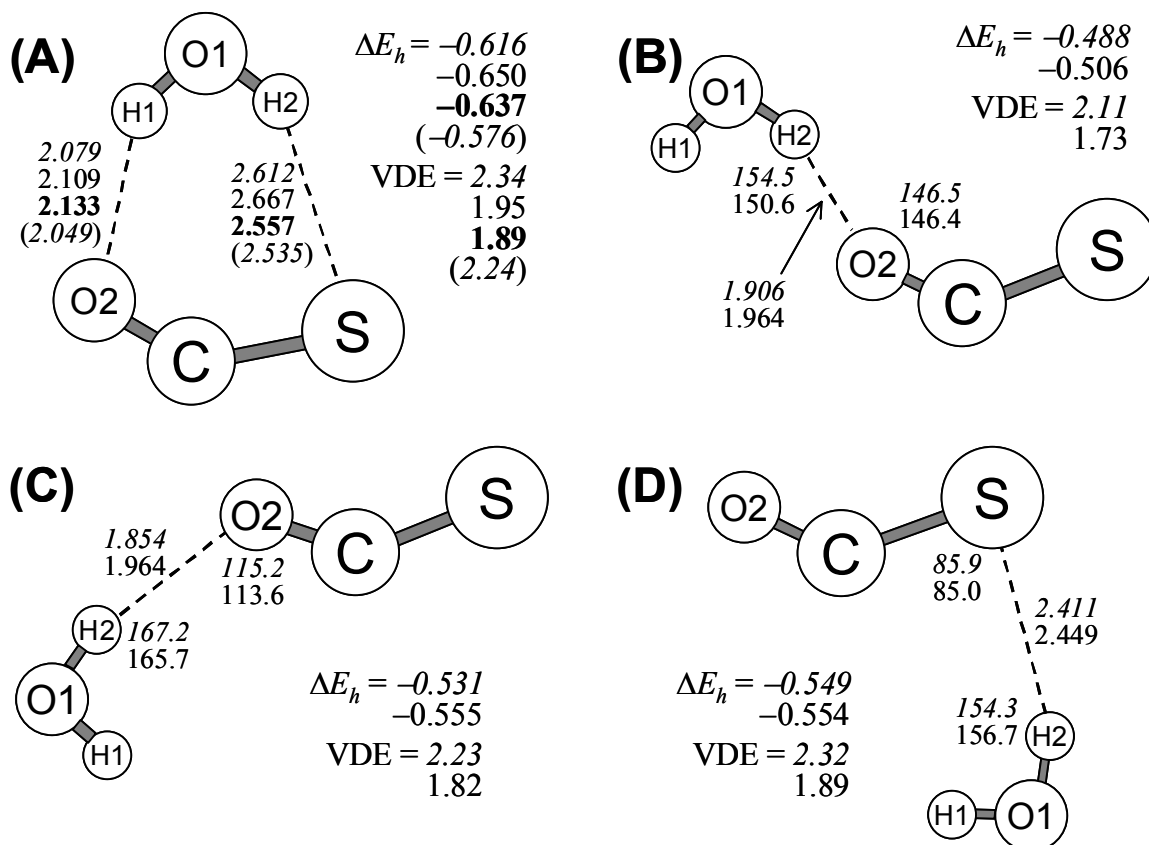


Figure 5.4. The equilibrium structures of four $\text{OCS}^- \cdot \text{H}_2\text{O}$ isomers. The relative hydration energies ΔE_h and VDEs are given in eV, while the intermolecular structural parameters are in Angstroms and degrees. The indicated values of ΔE_h are the purely electronic (excluding the ZPE correction) hydration energies, defined as the energy of $\text{OCS}^- \cdot \text{H}_2\text{O}$ relative to the sum of the separated OCS^- and H_2O energies. The energetic and structural parameters are determined from the following calculations: listed first (italics) – B3LYP/6-311++G(d,p); listed second (plain font) – CCSD/6-31+G(d). For the lowest-energy structure A, the parameters listed third (bold) are from CCSD/6-311++G(d,p), and those listed last (italics in parentheses) are at the *m*PW1PW91/aug-cc-pVTZ level.

shown in Fig. 5.4. Structures (A)-(D) were first obtained from a B3LYP/6-311++G(d,p) geometry optimization (the corresponding structural and energetic parameters are given in italics in Fig. 5.4) and then re-optimized at the CCSD level with the 6-31+G(d) basis set (plain font in Fig. 5.4). In addition, the most stable structure A was optimized at the CCSD level with the 6-311++G(d,p) basis set (bold in Fig. 5.4) and the *m*PW1PW91 DFT level with the aug-cc-pVTZ basis (italics in parentheses in Fig. 5.4). Only the most important intermolecular parameters are given in Fig. 5.4, while Table 5.4 lists the complete set of parameters and the harmonic vibrational frequencies of the ground-state structure A, as determined from the CCSD/6-311++G(d,p) calculation.

All structures are characterized by the excess electron localized on OCS and all four have planar equilibrium geometries. They correspond to true potential minima, as verified by their harmonic frequencies. Care was taken to determine all possible structural isomers by starting the optimization from different initial configurations. The initial intermolecular coordinates for the optimizations were chosen to be analogous to the three isomers predicted for $\text{CO}_2^-\cdot\text{H}_2\text{O}$, which are: one of the C_{2v} symmetry with two equivalent electrostatic O-H “bonds” and two C_s structures with single O-H “bonds”, one each in the *cis* and *trans* configurations of the dangling H atom with respect to CO_2^- .^{3,105} Considering the reduced symmetry of OCS^- , five different structures might be expected for $\text{OCS}^-\cdot\text{H}_2\text{O}$: a doubly bound isomer with the electrostatic O-H and S-H bonds, in addition to two *trans* and two *cis* structures with dangling hydrogen atoms, one each on the oxygen and sulfur sides of OCS^- . However, one of the sulfur-side structures proved to be a saddle point on the potential leading to the global minimum structure A shown in

Table 5.4. Equilibrium parameters and harmonic vibrational frequencies of $\text{OCS}^- \cdot \text{H}_2\text{O}$ structure A (ground state) shown in Fig. 5.4 calculated at the CCSD level with the 6-311++G(d,p) basis set.

Structural parameters (Å and degrees)		Harmonic vibrational frequencies	
		Symmetry	cm^{-1}
C-O2	1.211	a'	101.7
C-S	1.707	a''	107.1
O2-C-S	135.5	a'	158.6
S-H2	2.557	a''	327.6
H2-S-C	84.0	a'	338.4
O1-H2	0.966	a'	512.0
O1-H1	0.964	a''	618.0
H1-O1-H2	99.1	a'	748.3
O1-H2-S	146.6	a'	1699.8
O2-H1	2.133	a'	1744.5
		a'	3802.3
		a'	3859.9

Fig. 5.4, and thus only four isomers corresponding to true potential minima were found.

The important energetic parameter describing the relative stability of the cluster is the hydration energy ΔE_h , defined here as the electronic energy (excluding the ZPE) of $\text{OCS}^- \cdot \text{H}_2\text{O}$ relative to the separated $\text{OCS}^- + \text{H}_2\text{O}$ limit. The calculated values of ΔE_h are indicated in Fig. 5.4, along with the predicted vertical detachment energies (VDE) for each isomer. The predicted values of $\Delta E_h \approx -0.6$ eV are in line with the typical stabilization expected for an ion-dipole interaction^{109,110} and similar to the stabilization energy observed for CO_2 anion hydrates.¹⁰⁵

Comparison of the Hydrated Anions of CO_2 , OCS , and CS_2

The present results allow for a comparison of the hydration dynamics of the isovalent CO_2^- , OCS^- , and CS_2^- anions, with OCS^- bridging the gap between the other two.

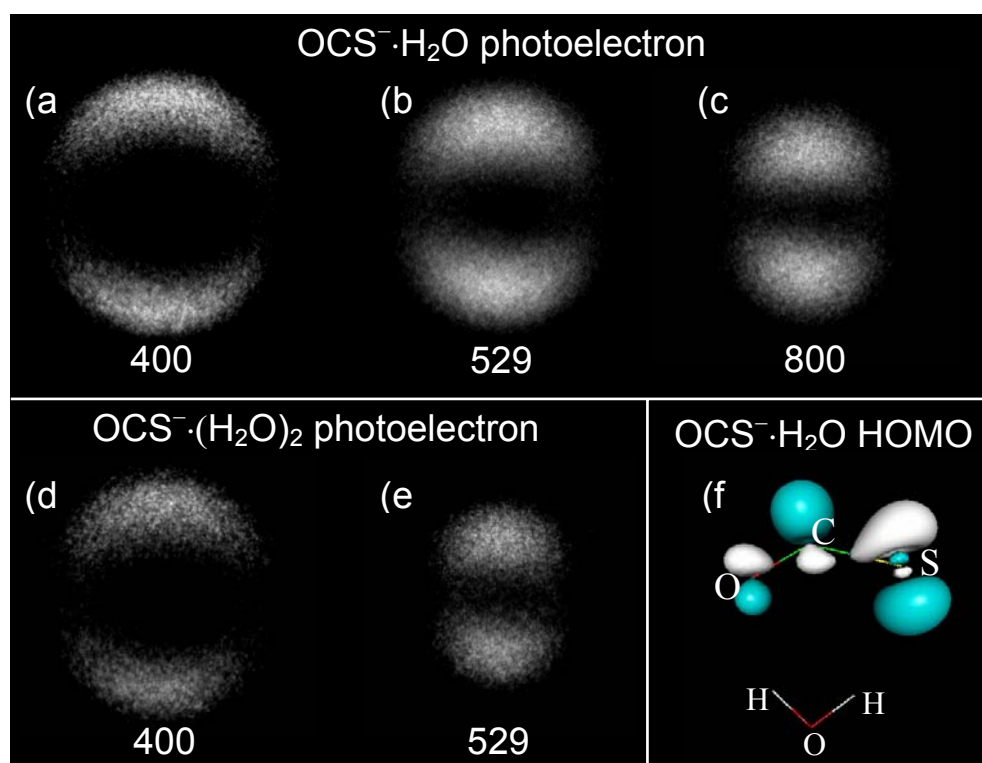
For CO_2 (experimental EA = -0.6 eV),⁷³ the unhydrated anion is metastable, and it takes at least two H_2O molecules for the efficient formation of hydrated CO_2^- in an electron-impact source, i.e., the smallest hydrated cluster anion that is formed in abundance under normal conditions similar to ours is $\text{CO}_2^-(\text{H}_2\text{O})_2$.^{105,108} In Sec. 5.3.2.1 we showed that the corresponding minimum number of water molecules needed in the hydration of OCS^- is reduced to one. Finally, the CS_2^- anion requires no external stabilization, as the EA of CS_2 is in the 0.9–1.0 eV range.^{51,73}

Another parallel can be drawn for the hydration of the corresponding dimer anions, where a similar trend of the diminishing required hydration is observed. Indeed, although $(\text{CO}_2)_2^-$ can be formed,^{55,56,63} its abundance is small compared to the

$(\text{CO}_2)_2^-\cdot\text{H}_2\text{O}$ cluster anion.¹⁰⁵ Thus, one water molecule is needed to stabilize effectively $(\text{CO}_2)_2^-$, while $(\text{OCS})_2^-$ and $(\text{CS}_2)_2^-$ are both stable and abundant in the isolated form.^{54,60} These observations can be summarized in an empirical 3-2-1 rule: for the efficient formation of stable $\text{X}_n^-(\text{H}_2\text{O})_k$ cluster ions ($\text{X} = \text{CO}_2, \text{OCS}, \text{or } \text{CS}_2$) with $n \geq 1$, the total number of molecules ($n + k$) must be at least 3, 2, and 1, respectively.

5.3.3 Photoelectron Imaging of Hydrated $\text{OCS}^-(\text{H}_2\text{O})_k$

Fig. 5.5 (a-c) contains the images obtained in the detachment of $\text{OCS}^-\cdot\text{H}_2\text{O}$ at 400, 529 and 800 nm respectively, while images of the photodetachment of $\text{OCS}^-\cdot\text{H}_2\text{O}$ at 400 and 529 are shown in Fig. 5.5(d) and (e), respectively. $\text{OCS}^-\cdot\text{H}_2\text{O}$ at 800 is not shown due to its weak intensity. All the images are quite similar especially their anisotropies: $\beta = 1.13 \pm 0.06$, 1.20 ± 0.06 , and 1.16 ± 0.05 at 400, 529, and 800 nm, respectively for $\text{OCS}^-\cdot\text{H}_2\text{O}$. They are practically independent of energy. This is probably a consequence of the highly integrated nature of these PADs, including a wide energy range and different structural isomers as discussed above. Compare to CS_2^- the images of $\text{OCS}^-(\text{H}_2\text{O})_{1,2}^-$ lack vibration resolution due to the dissociative nature of the cluster ion detachment, but overall they are similar suggesting a qualitatively similar orbital for the excess electron. OCS^- and CS_2^- have similar HOMOs; hence, their PADs are expected to be similar. The results indicate that one or two water molecules do not alter greatly the excess electron orbital on OCS^- , in agreement with the calculated HOMO of $\text{OCS}^-\cdot\text{H}_2\text{O}$ shown in Fig. 5.5 (f).



(a)–(c): Photoelectron images recorded in the photodetachment of OCS⁻·H₂O at (a) 400, (b) 529, and (c) 800 nm. (d), (e): Photoelectron images of OCS⁻·(H₂O)₂ at 400 and 529 nm, respectively. The images are shown on arbitrary velocity scales (see Fig. 4 for quantitative information). The laser polarization is vertical. (f) The HOMO of the most stable structure of OCS⁻·H₂O.

The $\text{OCS}^-\cdot\text{H}_2\text{O}$ structure of the monohydrated cluster is expected, since water does not bind an electron. For $[\text{OCS}(\text{H}_2\text{O})_2]^-$ a water dimer anionic core is conceivable, but the similarity of the images in Figs. 5.5 (d) and (e) to the monohydrated clusters in Figs. 5.5 (a-c) favors the excess electron to be localized on OCS in the dihydrated clusters, $\text{OCS}^-\cdot(\text{H}_2\text{O})_2$.

The Photoelectron spectra shown in Fig. 5.6 reveal more structural information. The filled and open symbols represents $\text{OCS}^-\cdot\text{H}_2\text{O}$ and $\text{OCS}^-\cdot(\text{H}_2\text{O})_2$, respectively. The shape of the symbols denotes the photon wavelength as labeled in the plot. The 400 nm spectrum of $\text{OCS}^-\cdot\text{H}_2\text{O}$ peaks at 1.87 ± 0.05 eV agreeing with the predicted VDE of 1.89 eV for the most stable isomer of $\text{OCS}^-\cdot\text{H}_2\text{O}$, based on CCSD/6-311++G(d,p) calculations. The observed maximum position varies with photon energy due to the overlap of the Frank-Condon envelope and the electronic cross-section $\sigma(\text{eKE})$, as seen in Fig. 5.6. Therefore, the spectral maximum does not correspond directly to the anion VDE.

Accounting for this effect, the solid lines in Fig. 5.4 indicate the spectra simulated by superimposing the Franck-Condon envelope (assumed Gaussian) with $\sigma(\text{eKE})$, obtained by modeling the superposition of $\ell = 0, 1$, and 2 waves and disregarding all others.²⁶ Neglecting the long-range interaction between the electron and neutral $\text{OCS}\cdot\text{H}_2\text{O}$, the scaling of the partial cross-sections was approximated by the Wigner law.³⁸ The consistent modeling of the 400, 529, and 800 nm $\text{OCS}^-\cdot\text{H}_2\text{O}$ photoelectron spectra yields a VDE of 2.07 ± 0.07 eV, which is 0.18 eV larger than the theoretical

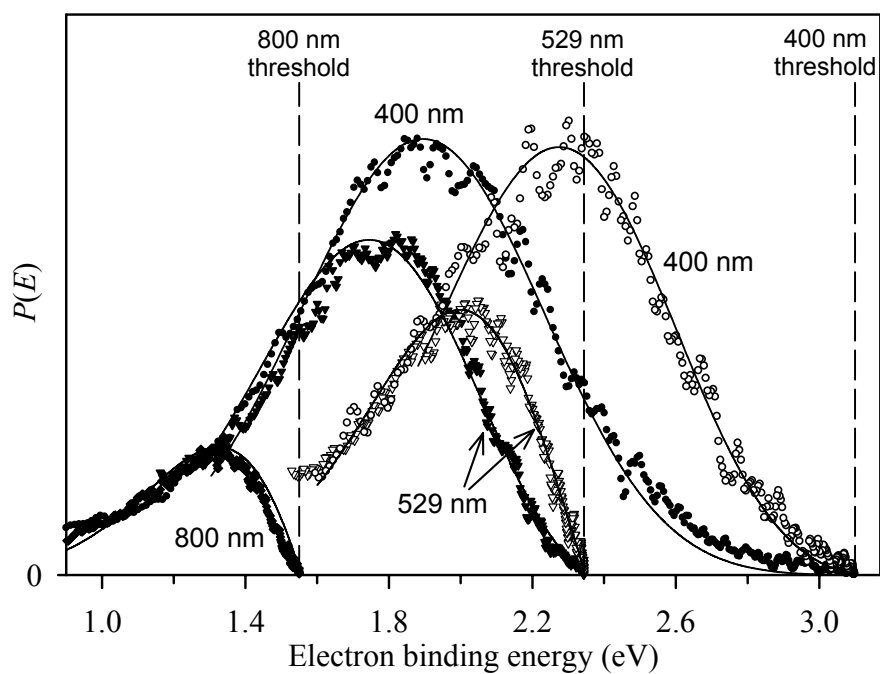


Figure 5.6. Filled symbols: photoelectron energy spectra obtained from the $\text{OCS}^- \cdot \text{H}_2\text{O}$ images in Fig. 3(a)-(c). Open symbols: photoelectron spectra for $\text{OCS}^- \cdot (\text{H}_2\text{O})_2$, from Fig. 3(d) and (e). Different symbol types correspond to different wavelengths, as labeled. Solid lines: simulated photoelectron spectra obtained as described in the text, yielding $\text{VDE} = 2.07 \pm 0.07$ and 2.53 ± 0.07 eV for $\text{OCS}^- \cdot \text{H}_2\text{O}$ and $\text{OCS}^- \cdot (\text{H}_2\text{O})_2$, respectively.

prediction. This result has implications for the EA of OCS. At the CCSD/6-311+G(d) level, the adiabatic EA was predicted to be -0.217 eV. Assuming that the coupled-cluster theory underestimates the EA of OCS by the same error as the VDE of $\text{OCS}^-\cdot\text{H}_2\text{O}$, the correct EA value can be estimated as the CCSD prediction plus the experimental correction giving -0.04 eV. It is in remarkable agreement with higher-level theoretical prediction obtain by gaussian-3 theory of -0.059 ± 0.061 eV.

The VDE for $\text{OCS}^-\cdot(\text{H}_2\text{O})_2$ is 2.53 ± 0.07 eV a value obtained by modeling the 400 and 529 nm photoelectron spectra of $\text{OCS}^-\cdot(\text{H}_2\text{O})_2$ with the same parameters as above except for VDE. The addition of a water molecule to $\text{OCS}^-\cdot\text{H}_2\text{O}$ increases the VDE by 0.46 eV. This is consistent with the 0.52 eV increase of VDE from $\text{CO}_2^-\cdot\text{H}_2\text{O}$ to $\text{CO}_2^-\cdot(\text{H}_2\text{O})_2$ ¹⁰⁵

5.4 SUMMARY

The electron-impact ion source is ineffective at producing OCS^- . The EA for OCS has been extensively investigated with theoretical methods predicting an EA of -0.059 ± 0.061 eV at the G3 level of theory. It was also estimated as -0.04 eV, using the CCSD experimental correction of 0.18 eV, determined from photoelectron imaging of $\text{OCS}^-\cdot\text{H}_2\text{O}$. The VDE of $\text{OCS}^-\cdot\text{H}_2\text{O}$ and $\text{OCS}^-\cdot(\text{H}_2\text{O})_2$ are 2.07 ± 0.07 and 2.53 ± 0.07 eV respectively. The structures of hydrated OCS cluster anions have been calculated.

6 ISOMER COEXISTENCE AND COMPETITION OF EXCITED STATE DECAY PATHWAYS OF $(\text{OCS})_n^-$

6.1 INTRODUCTION

Gas phase clusters serve as micro laboratories to study chemical interaction and dynamics within condensed environments. Clusters bridge the gap between the condensed and gas phases with a definable geometry that can be reconstructed, and they are small enough to compare with high level theoretical calculations. Within these “microlaboratories” both molecular and “bulk” properties are manifested in single-photon excitation of small cluster anions. The transition between gas-phase and bulk properties has been the subject of extensive research.⁵³ The focus has been in regards to how much matter is needed for physical laws associated with bulk materials to be applicable.¹¹¹

An autodetachment (AD) signal has been observed in the photodetachment of $(\text{OCS})_n^-$ cluster anions. This AD can be modeled as a gas-phase analog of thermionic emission, which is a characteristic of bulk material. This chapter discusses autodetachment and direct photoelectron detachment process observed in $(\text{OCS})_n^-$ cluster anions. The results illustrate that the electronic structure of the cluster determines whether a cluster manifests bulk material properties rather than due to its size. The photoelectron images also reveal the coexistence of the $\text{OCS}^- \cdot (\text{OCS})_{n-1}$ and $(\text{OCS})_2^- \cdot (\text{OCS})_{n-2}$ clusters.

As discussed in the previous chapter isolated OCS^- is believed to be metastable,^{6,26} but the addition of solvent molecules yields a stable cluster anion. The monohydrated anion was predicted to have a straightforward, electrostatically bound ion

molecule combination $\text{OCS}^- \cdot \text{H}_2\text{O}$. The homogeneous cluster can assume either an ion molecule $\text{OCS}^- \cdot \text{OCS}$ configuration or one of two covalently bound isomers. The most stable of these has C_{2v} symmetry, a C - C bond and a S - S bond with bond orders of 1 and 1/2. The existence of the covalent dimer anion and its solvated species was indirectly indicated in $(\text{OCS})_n^-$ photofragmentation experiments.⁶⁰

The photofragmentation and photodetachment studies complement each other, exploring competing reaction pathways. Due to low thresholds for both detachment and dissociation, the competition between electron emission and fragmentation plays an important role in $(\text{OCS})_n^-$. In some of the fragmentation channels, autodetaching products may be formed, while, on the other hand, the parent autodetachment (AD) itself can be safely assumed to be dissociative. Thus the excited-state decay ties the ionic fragmentation and AD into an entangled knot of decomposition reactions, which involve several competing pathways potentially leading to the same final products.

To distinguish between the electro statically and covalently bound anions of $(\text{OCS})_2^-$, the results are compared to the previous results for $\text{OCS}^- \cdot \text{H}_2\text{O}$.²⁶ In the latter case there is no AD; therefore, it is hypothesized that $\text{OCS}^- \cdot \text{OCS}$ also does not participate in this process. AD is then attributed to the covalent dimer. It is predicted that $\text{OCS}^- \cdot \text{OCS}$ and $\text{OCS}^- \cdot \text{H}_2\text{O}$ would have similar photoelectron images, since solvation does not alter the HOMO of the ion core.

The bulk thermionic emission TE model assumes that efficient electron - photon coupling leads to rapid thermalization of the excitation energy among the electronic and nuclear degrees of freedom.^{22,112} Analogs of TE have been previously seen in the gas

phase, for example in fullerenes.^{112,113} The gas-phase manifestation of TE includes a thermal electron kinetic energy (eKE) distribution, and the delayed and consequently isotropic nature of electron emission. In contrast, direct photoelectron detachment is fast and in general anisotropic. Concerning negative ions, the Neumark group described TE in the multiphoton detachment of C_4^- , C_6^- , and C_8^- .¹¹⁴ Baguenard et al. observed this effect in the ultraviolet photodetachment of carbon²¹ and tungsten²² cluster anions.

The $(OCS)_n^-$ clusters described here present special interest, because their decay involves acute competition between autodetachment and fragmentation. In this work, we exploit the crucial advantages of imaging¹⁰ to obtain evidence of the existence and dynamics of excited anionic states of $(OCS)_n^-$. Imaging is ideally suited to detection of both slow and fast photoelectrons, which is important for the simultaneous observation of autodetachment and direct photodetachment. The photoelectron angular distributions are also easily visualized, helping elucidate the emission mechanisms.

Reported below are the photoelectron images of $(OCS)_n^-$ $n = 2, 3, 4$ recorded at photon energies of 800, 530, 400, and 267 nm. Variations in the relative abundances of OCS^- $(OCS)_{n-1}$ and $(OCS)_2^-$ $(OCS)_{n-2}$ isomers are explored under the conditions of stepwise solvation and the competition between AD and ionic fragments. These results have been published previously.^{29,115}

The next section describes the experimental approach used in this study. Section 6.3 presents the results followed by model and analysis in section 6.4

6.2 RELEVANT EXPERIMENTAL DETAILS

The $(OCS)_n^-$ cluster ions are formed as described previously,^{28,60} using published

cluster-ion techniques.³³ The ions are generated in an electron-impact ionized pulsed supersonic expansion of a 7% mixture of OCS in Ar.

The 530, 400, and 267 nm beams were mildly focused with a 2 m focal-length lens, positioned 1.3 m before the interaction region. The polarization axis was always arranged parallel to the imaging detector plane. The single-photon nature of the observed transitions was verified using the signal power dependence.

6.3 RESULTS

Figure 6.1 compiles the images of $(\text{OCS})_{2,3,4}^-$ at photon energies 800, 530, 400, and 267 nm. The laser polarization is vertical in the image plane for all the photoelectron images. For comparison the photoelectron images of $\text{OCS}^- \cdot \text{H}_2\text{O}$ are shown at the right at 800, 530 and 400 nm. Despite the overall differences between the homogeneous and heterogeneous clusters anions, the higher-eKE parts of $(\text{OCS})_n^-$ images resemble those of $\text{OCS}^- \cdot \text{H}_2\text{O}$ at all wavelengths for which comparison is available. To the contrary, the mid and low-eKE parts are qualitatively different. In particular, the central spots in the $(\text{OCS})_n^-$ images are not present in the $\text{OCS}^- \cdot \text{H}_2\text{O}$ results, nor were they observed in $\text{OCS}^- \cdot (\text{H}_2\text{O})_2$ detachment.²⁶

The analyses of the images were performed with the inverse Abel transformation, which produced the velocity and angular distribution. The Abel inversion and subsequent integration of the transformed images was carried out using the basis set expansion (BASEX) method of Reisler and co-workers.³⁶ The velocity distributions, $P(v)$, are converted into photoelectron energy spectra, $P(\epsilon)$ ($\epsilon \equiv \text{eKE}$), according to the straightforward relation

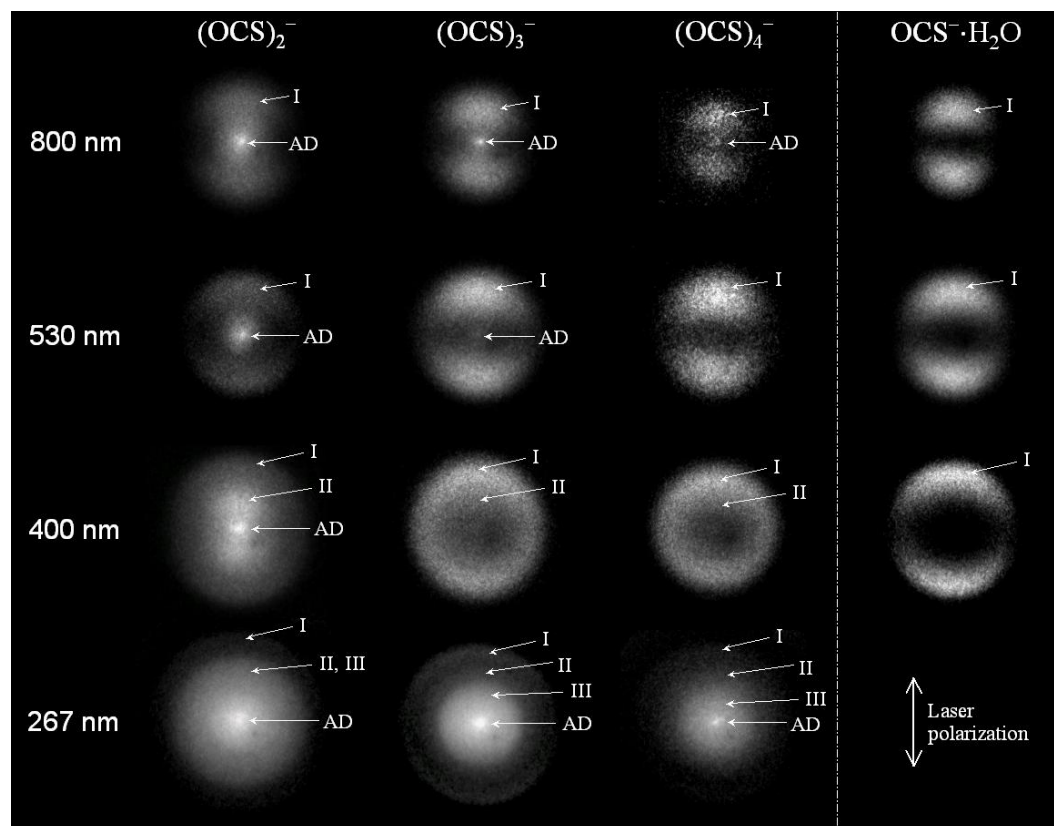


Figure 6.1 Photoelectron images of $(\text{OCS})_{2-4}^-$ and $\text{OCS}^- \cdot \text{H}_2\text{O}$ recorded at 800, 530, 400, and 267 nm. The images are shown on arbitrary velocity and intensity scales (see Figs. 2-4 for quantitative information). Arrows indicate the contributions of autodetachment (AD) and direct detachment bands I, II, and III.

$$P(\varepsilon) = P(v)dv/d\varepsilon \propto P(v)/v. \quad (6.1)$$

The $P(\varepsilon)$ and $P(v)$ distribution obtained for $(\text{OCS})_n^-$ $n = 2, 3$, and 4 are shown in figs. 6.2, 6.3, and 6.4 respectively. Traditionally, photoelectron spectra are analyzed in the energy domain; however imaging experiments provide velocity rather than energy maps of the detachment process. The information seen in the velocity spectra is not always clear in the energy domain, particularly for slow electrons. Note, also that imaging allows discernment of some transitions that are unresolved in the spectra. A particular case is $(\text{OCS})_2^-$ at 400nm. In the spectra (shown in Fig. 6.2(c)) only 2 transitions are obvious compared to the three seen in the image (Fig. 6.1).

6.4 ANALYSIS

Two different electron-emission mechanisms have been observed in the images of $(\text{OCS})_n^-$. The results are modeled to account for both mechanisms through spectral stimulation. The first mechanism is direct photodetachment which is characterized by high energy electrons and an anisotropic PAD. Direct photodetachment is modeled by a simplified Frank-Condon model. The second mechanism of electron-emission is manifested by isotropic spots at the image center corresponding to indirect decay via delayed electron emission (autodetachment). The spot that appears at the image center is independent of wavelength, which is uncharacteristic of direct photodetachment. The AD bands are modeled using the delayed thermionic emission formalism,¹¹² as employed by Baguenard et al.^{21,22} Our core assumption is that the available energy is distributed statistically among all product degrees of freedom. Despite the competition between AD and ionic fragmentation, the TE

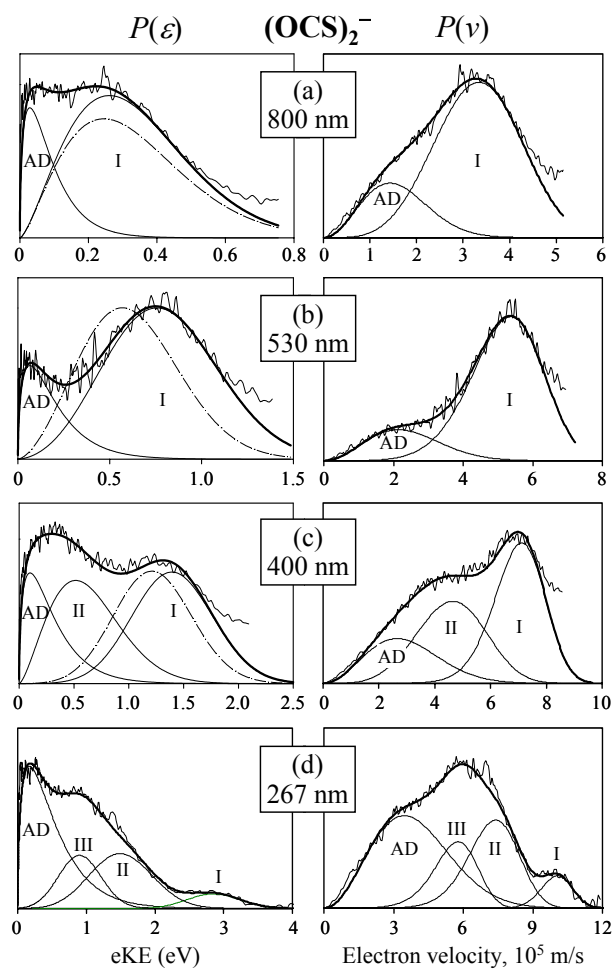


Figure 6.2 Experimental and simulated $(\text{OCS})_2^-$ photoelectron spectra in the energy and velocity domains (left and right columns, respectively). The experimental spectra (thin lines with apparent noise) are derived from the corresponding images in Fig. 6.1. The simulated spectra are shown by bold lines with the individual transitions (AD and bands I, II, and III) indicated by the thin curves, correspondingly labeled. The dashed curves in (a)-(c) [$P(\varepsilon)$ column, this Figure only] are fits [Eq. (6-5)] to the $\text{OCS}^- \cdot \text{H}_2\text{O}$ spectra (not shown).

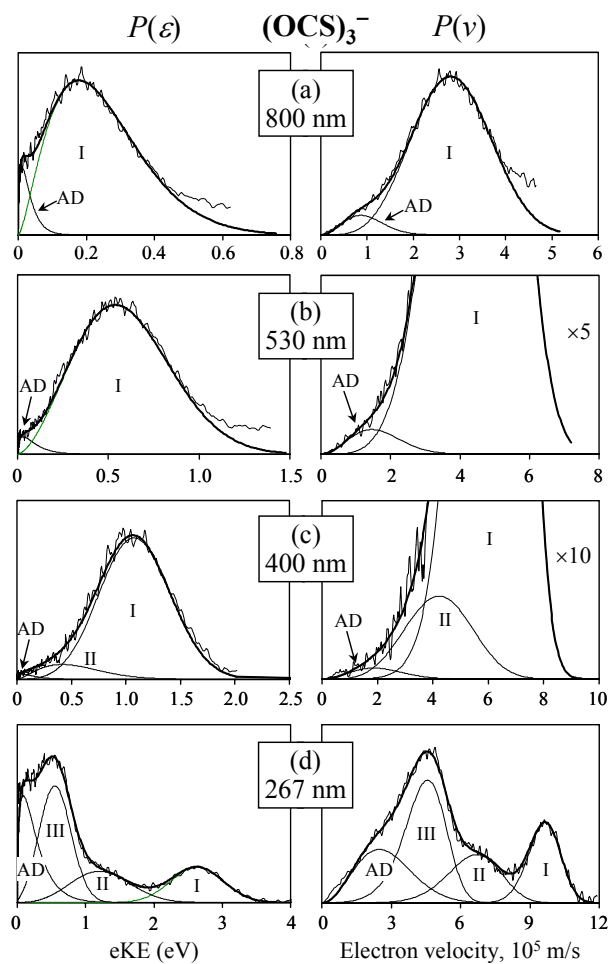


Figure 6.3 Experimental and model spectra for $(\text{OCS})_3^-$. See Fig. 6.2 caption for further details. The $P(v)$ distributions in (b) and (c) are magnified $\times 5$ and $\times 10$, respectively, to highlight the autodetachment components.

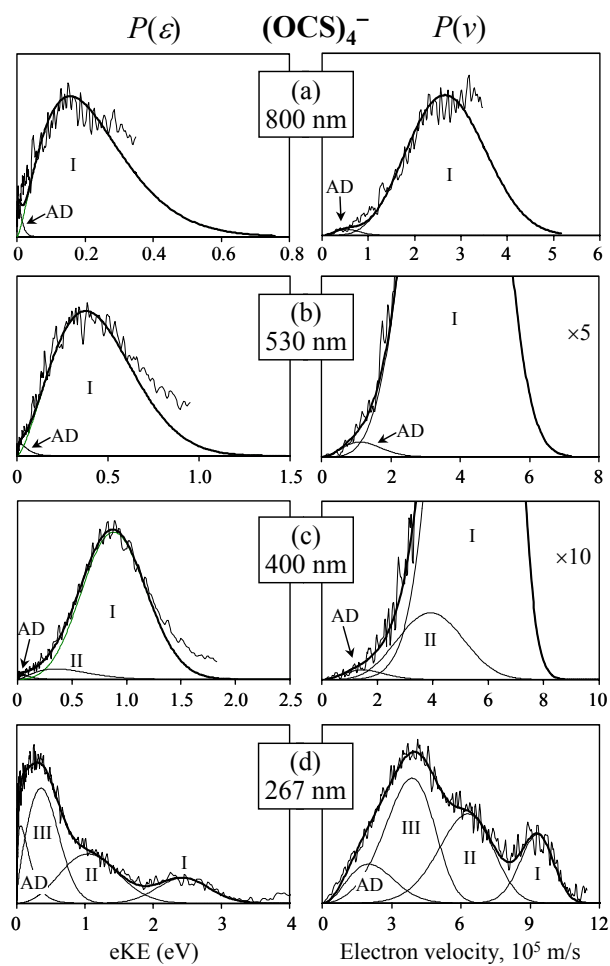


Figure 6.4 Experimental and model spectra for $(\text{OCS})_3^-$. See Fig. 6.2 caption for further details. The $P(v)$ distributions in (b) and (c) are magnified $\times 5$ and $\times 10$, respectively, to highlight the autodetachment components.

model is applicable to the final product distributions (i.e., the photoelectron spectra), provided the statistical assumption is valid at all decay stages.

Autodetachment. In the TE model applied to negative ions, the eKE distribution of the emitted electrons is approximated by Klots' formula:^{22,112,116}

$$P_{TE}(\varepsilon) \propto \varepsilon^{1/2} \exp(-\varepsilon / k_B T_{TE}). \quad (6.2)$$

It assumes a completely statistical emission process within the constraints of the detailed balance principle. The pre-Boltzmann factor reflects the cross-section scaling due to the effect of the centrifugal barrier and T_{TE} describes the effective temperature of the emission spectrum. Under the condition of thermal equilibrium, T_{TE} equals the microcanonical “daughter” temperature of the remaining neutral cluster (not to be confused with the emission temperature, determining the TE rate).¹¹² Following the thermalization of the excitation energy $h\nu$, T_{TE} is determined by the microcanonical temperature of the parent cluster corrected for the energy required to emit an electron, i.e., the adiabatic electron affinity (EA):^{21,22}

$$T_{TE} \approx T_0 + (h\nu - \text{EA}) / C_v. \quad (6.3)$$

Here, T_0 is the cluster temperature prior to photon absorption, which we take as ~ 70 K,³³ and C_v is the microcanonical heat capacity.¹¹⁷ For an ensemble of N atoms, i.e., $(3N - 6)$ internal degrees of freedom, in a high-temperature harmonic approximation C_v is given by:^{22,117}

$$C_v = (3N - 7)k_B \quad (6.4)$$

This definition differs from canonical heat capacity by one unit of k_B . The microcanonical temperature of an isolated cluster describes the average energetic content of an individual degree of freedom, determined by its couplings with the remaining $(3N - 7)$ oscillators.¹¹⁷

The $(\text{OCS})_n^-$ cluster ions have a variety of modes, not all of which are necessarily equally active in the energy randomization. This can be further complicated by competition with ionic fragmentation. If the electronic-vibrational energy exchange is incomplete on the autodetachment timescale,¹¹² one could factor in an effective number of degrees of freedom and use it as an adjustable parameter to fit the data. However, we found no need to deviate from the microcanonical limit. The microcanonical heat capacity was calculated using Eq. (4) with $N = 6, 9$, and 12 for $(\text{OCS})_2^-$, $(\text{OCS})_3^-$, and $(\text{OCS})_4^-$, respectively. While the agreement with the experiment does not prove that the decay process is completely statistical, the data do not provide evidence of deviations from the statistical model.

The EAs corresponding to the formation of covalent $(\text{OCS})_2^-$ and its clustered species are not known. As an estimate, we compared the calculated energy of the C_{2v} symmetry dimer anion⁶⁰ to the combined energy of two relaxed OCS molecules, as the detachment of $(\text{OCS})_2^-$ can be assumed to be dissociative. The previous study⁶⁰ of $(\text{OCS})_2^-$ employed the second-order Møller-Plesset perturbation theory with the 6-31+G(d) basis set. However, this method performs poorly in predicting the EA of the OCS monomer. Based on more recent results,²⁸ we chose a minimal-cost density-functional approach that works well for OCS. In calculations using Gaussian 98,⁷⁴ the

B3LYP method was used with the 6-31+G(d) and aug-cc-pVDZ basis sets. The results predict the covalent $(\text{OCS})_2^-$ anion to lie 1.01 and 0.98 eV, respectively, lower in energy than two OCS molecules (excluding the zero-point vibrational energy correction). The latter value was adopted as $(\text{OCS})_2^-$ EA in Eq. (6.3). Accounting for stepwise solvation, the EAs corresponding to $(\text{OCS})_3^-$ and $(\text{OCS})_4^-$ were taken to be 1.25 and 1.5 eV, respectively. The assumed increments correspond to the typical binding energy of OCS in small cluster anions.¹¹⁸

The T_{TE} values calculated according to Eqs. (6.3) and (6.4) for different cluster sizes and excitation wavelengths are summarized in Table 6.1. These temperatures describe the eKE distributions of the emitted electrons. The high-temperature assumption made in the preceding discussion concerns the significantly higher temperatures of the excited parent clusters, which can be estimated using Eq. (6.3) without the EA term. Besides, the lowest parent and TE temperatures correspond to the measurements in which only a minor AD component is observed, providing no basis for more careful modeling of the emission process.

Table 6.1 TE temperatures (in K) calculated with Eq. (6.3).

λ , nm	$(\text{OCS})_2^-$	$(\text{OCS})_3^-$	$(\text{OCS})_4^-$
800	674	246	91
530	1508	704	407
400	2311	1146	712
267	3942	2043	1331

The T_{TE} values from Table 6.1 were used with Eq. (6.2) to model the AD bands in the photoelectron spectra. Their contributions are shown in Figs. 6.2-6.4.

Direct photodetachment. The direct photodetachment transitions are characterized in general by anisotropic angular distributions and non-thermal eKE distributions. We model the spectral profile of each of the observed direct detachment bands with

$$P(\varepsilon) = A\varepsilon^{\ell+1/2} \exp\left[-(h\nu - \varepsilon - \varepsilon_0)^2 / w^2\right], \quad (6.5)$$

where $(h\nu - \varepsilon)$ is the electron binding energy (eBE). This equation involves two approximations. First, a Gaussian Franck-Condon profile is assumed, with ε_0 corresponding to the VDE and w defining the width. Second, the electronic cross-section scaling is approximated by the pre-Gaussian factor in the form of the Wigner law,³⁸ assuming an effective free-electron angular momentum quantum number ℓ . This factor is most important for slow electrons, for which the Wigner law is best justified. The coefficient A is proportional (among other factors) to the population of the species responsible for the transition. The variations in A for different transitions as functions of n can be used to gain qualitative insights into the changes in isomer abundances under stepwise solvation.

Except for very slow electrons, ℓ is not as critical in modeling energy spectra as it is for angular distributions.^{37,119} Instead of considering the effects of wave interference (nearly impossible in the case of not-well-known electronic structure), we used the dominant ℓ values based on angular anisotropy. In Fig. 6.1, bands I and II exhibit angular distributions with markedly positive anisotropy parameters,^{37,119} characteristic of p_z par-

tial waves (where z is the laser polarization axis). The $\beta > 0$ type of transition I is evident in all images, consistent with the detachment from the OCS^- HOMO, previously discussed in the context of photoelectron imaging of $\text{OCS}^- \cdot \text{H}_2\text{O}$.²⁶ The $\beta > 0$ character of band II is best seen in the 400 nm $(\text{OCS})_2^-$ image. Thus, we used $\ell = 1$ in modeling bands I and II, while the nearly isotropic band III was described by $\ell = 0$.

The contributions of bands I, II, and III modeled with Eq. (6.5) are shown in Figs. 6.2-6.4. The sum of all bands, including AD, yields the total simulated spectra shown by bold lines. The only parameter adjusted for AD was its intensity. The low-eKE parts of the spectra, where AD is most important, are best viewed in the velocity domain. For the direct bands, A , ε_0 and w were adjusted for agreement with the experiment. Discrepancies at the high-eKE tails of the spectra are attributed to the uncorrected backgrounds (proportional to integration area, increasing for faster electrons and minimally affecting the slow ones) and edge-related artifacts in the images. The contributions of different transitions to the photoelectron images are marked in Fig. 6.1, while the optimum values of ε_0 and w are summarized in Table 6.2. The VDE values for different transitions in a given cluster, which are also summarized in Table 6.2, were estimated by averaging ε_0 determined at different wavelengths.

6.5 DISCUSSION

Band assignments. The direct photodetachment bands' VDEs increase by 0.2 -0.3 eV with the addition of each solvent molecule (see Table 6.2). This increase is consistent with the binding energy of OCS to an anionic cluster core.^{60,118}

λ , nm	(OCS) ₂ ⁻	(OCS) ₃ ⁻	(OCS) ₄ ⁻	OCS ⁻ ·H ₂ O
<u>Band I</u>				
800	1.87 (0.45)	2.15 (0.43)	2.5 (0.48)	2.07 (0.50)
530	1.85 (0.52)	2.15 (0.50)	2.4 (0.48)	2.08 (0.50)
400	1.87 (0.55)	2.20 (0.50)	2.4 (0.48)	2.07 (0.54)
267	1.87 (0.55)	2.10 (0.55)	2.3 (0.55)	
VDE	1.87	2.15	2.4	2.07
<u>Band II</u>				
400	3.40 (0.75)	3.70 (0.75)	3.95 (0.75)	
267	3.40 (0.70)	3.75 (0.70)	3.95 (0.70)	
VDE	3.40	3.73	3.95	
<u>Band III</u>				
267	3.80 (0.45)	4.15 (0.35)	4.40 (0.40)	
VDE	3.80	4.15	4.40	

Table 6.2 Optimal ε_0 and w values for direct detachment bands in (OCS)_n⁻ modeled with Eq. (5). Values are listed in eV in the format ε_0 (w). The VDEs are obtained by averaging ε_0 for different wavelengths. Parameters for OCS⁻·H₂O (from Ref. 30) are given for comparison.

Band I is consistent with the $\text{OCS}^-\cdot(\text{OCS})_{n-1}$ structure of the anions responsible for these parts of the images. Through comparison with $\text{OCS}^-\cdot\text{H}_2\text{O}$ images with band I at the same wavelength, we expect similar electronic structure due to the similar photoelectron signatures (Fig. 6.1). Also the spectral profiles of band I in Fig 6.2 (a) – (c) can be compared with the dashed curves representing the fits from Eq. (6.5) to the $\text{OCS}^-\cdot\text{H}_2\text{O}$ (see previous chapter).

The VDE of band I in $(\text{OCS})_2^-$ is 1.87 eV, compared to $\text{VDE} = 2.07$ eV for $\text{OCS}^-\cdot\text{H}_2\text{O}$.²⁶ The mismatch is in line with the difference in solvent binding energies expected for OCS and H_2O (~ 0.3 eV^{60,118} and $0.5\text{--}0.6$ eV,^{105,110} respectively). The similarity of the spectra and angular distributions of band I in $(\text{OCS})_2^-$ and $\text{OCS}^-\cdot\text{H}_2\text{O}$ suggests that the structure of the $(\text{OCS})_2^-$ species responsible is likely to be similar to that of $\text{OCS}^-\cdot\text{H}_2\text{O}$. In the latter case, the electrons are ejected from the OCS^- HOMO.²⁸ Therefore, we attribute band I in $(\text{OCS})_2^-$ to an electro statically bound isomer described as $\text{OCS}^-\cdot\text{OCS}$ and the nature of this band is similar to that observed in the photodetachment of $\text{OCS}^-\cdot\text{H}_2\text{O}$.

The significant presence of $\text{OCS}^-\cdot\text{OCS}$ suggests stability for this cluster anion. Since OCS^- is metastable and not formed efficiently in our ion source, the stability of $\text{OCS}^-\cdot\text{OCS}$ indicates that the EA of OCS is only slightly negative, with its absolute value not exceeding the stabilization energy of a OCS molecule. This observation alone brackets the EA of OCS between approximately -0.3 eV and zero, consistent with the recent indirect estimate of -0.04 eV.²⁶

On the other hand, the presence of other species in $(\text{OCS})_2^-$ and $(\text{OCS})_{3,4}^-$ is

indicated by AD bands in the images. The monomer based $\text{OCS}^- \cdot (\text{OCS})_{n-1}$ cluster anions are unlikely to produce the AD components of the images because neither $\text{OCS}^- \cdot \text{H}_2\text{O}$ nor $\text{OCS}^- \cdot (\text{H}_2\text{O})_2$ produced similar bands. The lack of anisotropy and the spot remaining in the center of the image regardless of photon energy for $(\text{OCS})_2^-$ cluster anion images allows these bands to be attributed to a indirect process involving excited anionic states of the covalent dimer. In the trimer and tetramer, the same excited states of the $(\text{OCS})_2^-$ cluster core are involved. The AD electrons can originate either from the excited covalent dimer states or from the internally excited products of anionic fragmentation, known to occur in $(\text{OCS})_2^-$,⁶⁰ or from any intermediate configuration.

Band II, seen in $(\text{OCS})_n^-$ at 400 and 267 nm, is assigned to direct photodetachment of the covalent dimer, $(\text{OCS})_2^-$. This band was also not observed in $\text{OCS}^- \cdot (\text{H}_2\text{O})_{1,2}$.²⁶ This band's VDE of 3.4 eV compares well with the predicted value, 3.35 eV, for the covalent C_{2v} form of $(\text{OCS})_2^-$.^{26,60} Also of note a similar 2.7 eV band in the photoelectron spectrum of $(\text{CS}_2)_2^-$ was attributed to a covalent C_2S_4^- anion of C_{2v} symmetry.⁴³

Band III observed in the 267 nm images cannot be assigned unambiguously to any single transition. First, in the energy range where band III is observed, several direct detachment transitions are possible from solvated OCS^- accessing the excited states of the neutral. In a similar fashion, 267 nm photodetachment from CS_2^- yields transitions to the $a^3\text{B}_2$, $b^3\text{A}_2$, and $A^1\text{A}_2$ neutral states which were observed in the range of eBE = 3.3-4.1 eV.^{27,43} These bands exhibit either negative or slightly negative anisotropy,²⁷

consistent with band III in $(\text{OCS})_{2-4}^-$. Hence, this band is tentatively assigned to the analogous neutral states formed in the photodetachment of $\text{OCS}^-(\text{OCS})_{1-3}^-$. However, at the same energy range contributions from several singlet and triplet neutral states of the covalent $(\text{OCS})_2^-$ are accessed.

Coexistence of isomers. It was previously proposed that the relative abundances of OCS and $(\text{OCS})_2^-$ based cluster may change with cluster size, in a similar fashion as the core-switching^{55,56} observed in $(\text{CO}_2)_n^-$ and isomer coexistence⁴³ in $(\text{CS}_2)_n^-$. In this work, the relative intensities of the bands assigned to the monomer core (bands I and III) and the dimer core (AD, band II, possibly part of band III) shed light on coexistence of the $(\text{OCS})_n^-$ isomers.

Band III and AD are excluded from this analysis due to band's III ambiguity and the differing mechanism of AD and competition processes involved. The relative abundances of the dimer and the monomer can be determined by comparing the A factor [Eq. (6.5)] for bands I and II to clusters of a different size. For example, at 400 nm, the I/II ratio defined as

$$I/II(n) = \frac{A_I(n) / A_{II}(n)}{A_I(2) / A_{II}(2)} , \quad (6.6)$$

has approximate values of 1, 6, and 4 for $n = 2, 3$, and 4, respectively. This implies that the percentage of dimer based anions is six times smaller in $(\text{OCS})_3^-$ cluster than $(\text{OCS})_2^-$. Likewise $(\text{OCS})_4^-$ has fourfold smaller percentage of dimer based anions than $(\text{OCS})_2^-$.

Qualitatively, this trend is observed in Figs 6.2(c), 6.3(c) and 6.4(c). A similar conclusion can be drawn from the 267-nm data [Figs 6.2(d), 6.3(d) and 6.4(d)]. Note the decrease of band II as the cluster size increases. The numbers calculated with Eq. (6.6) should be viewed as crude estimates, because of the approximations inherent in Eq. (6.5) and the disregard for changes in the electronic cross-sections and Frank-Condon factors upon solvation. Finally, the observed band intensity variations do not correspond exactly to the changes in natural isomer abundances, as these observations are likely affected by the ion source conditions.

Competition of decay mechanisms. Ionic fragmentation of excited $(\text{OCS})_n^-$ complicates understanding of the origin of autodetached electrons. In principle, the AD electrons can be emitted from (i) the excited parent cluster, (ii) the internally excited anionic fragments, or (iii) an intermediate state of cluster decomposition. The discussion focuses on autodetachment pathways in the decay of covalent $(\text{OCS})_2^-$, since this same anion is presumed to act as a chromophore and controls the decay dynamics in larger dimer based clusters. The most likely AD products of excited $(\text{OCS})_2^-$ are two OCS molecules plus an electron via dissociation. In the ionic fragmentation channels of $(\text{OCS})_2^-$ near 800 nm the products⁶⁰ were OCS^- , S_2^- , and OCS_2^- . At 400 nm the products also include S^- . Of these OCS^- is a plausible candidate for fragmentation AD, because the EAs of OCS, S_2 , and S (-0.04 ,²⁶ 1.67 and 2.1 eV, respectively) and the $(\text{OCS})_2^-$ dissociation energetics,⁶⁰ the adiabatic thresholds for the formation of OCS^- , S_2^- , S^- , and OCS_2^- followed by their AD can be crudely estimated as 0.6, 2.8, 3.7, and 2.8 eV, respectively. Hence, at 800 and 530 nm, only the OCS^- fragment AD is possible. At 400 nm

two other pathways open up, but the images do not support them with any significant increase in AD signal. Therefore we restrict the discussion to OCS^- as the most plausible source of fragment AD. At 267 nm, all of the above ionic fragments can be formed above their respective detachment thresholds, which may account for the sharp increase in AD at 267 nm compared to the other wavelengths.

Considering the 800-400 nm excitations, two AD pathways are most likely for $(\text{OCS})_2^-$:



where * denotes the excited parent state. The TE model of autodetachment employed in Sec. IV does not distinguish between these pathways. It assumes only that the energy is divided randomly among all product degrees of freedom. Since the final products are the same, (6.7a) and (6.7b) describe different pathways of the same decomposition reaction. In a statistical regime, one cannot specify at what stage of complex disintegration the electron leaves the nuclear framework. However, if the ionic fragmentation were fast, pathway (7b) could possibly dominate. In this case, the impulsive dissociation would be expected to result in non-statistical energy partitioning.

Although there is not enough information to conclusively discriminate between pathways (7a) and (7b), or in fact to provide a rigorous proof of the statistical nature of the decay process, the performance of the TE model gives no justification for invoking non-statistical dynamics. The multiple fragmentation channels active in the decay also

point away from impulsive dissociation. Finally, recent experiments on $(\text{CS}_2)_2^-$ by Mabbs *et al.*³¹ revealed no significant reduction in AD at 400 and 530 nm, compared to $(\text{OCS})_2^-$. This observation is inconsistent with the AD originating primarily from the fragments, because CS_2^- , the most likely source of fragment AD in the $(\text{CS}_2)_2^-$ case, is 0.9 eV more stable to detachment than OCS^- .

We now consider the sharp drop in relative AD intensity from $(\text{OCS})_2^-$ to $(\text{OCS})_3^-$, followed by a less significant decrease in $(\text{OCS})_4^-$. While the drop is particularly drastic at 400 nm and longer wavelengths, it is also significant at 267 nm longer wavelengths. There are two possible reasons for this effect: (i) the decrease in the relative abundance of $(\text{OCS})_2^-(\text{OCS})_{n-2}$; (ii) the competition of electron emission with cluster fragmentation.

First, there is a decrease in the relative abundance of $(\text{OCS})_2^-(\text{OCS})_{n-2}$ ions for $n = 3$ and 4, compared to $n = 2$. This is revealed in the images (Fig. 6.1) and spectra (Figs. 6.2-6.4) by the weakening intensity of band II relative to band I. However, comparing Figs. 6.2(c) and 6.3(c), we note that the decrease in AD from $(\text{OCS})_2^-$ to $(\text{OCS})_{3,4}^-$ is more significant than the corresponding drop in band II intensity. If the same cluster type (dimer-based) is responsible for both AD and band II, the isomer abundance argument is not sufficient to describe the observed trend. The greater number of degrees of freedom in larger clusters, resulting in lower TE temperatures and longer emission lifetimes, can contribute to lowering the AD intensity, but only if the electron emission competes with another excited-state decay mechanism.

The drop in AD intensity should be considered in the context of changes

occurring in the ionic fragmentation channels. In $(\text{OCS})_n^-$ dissociation, the fractional yield of S_2^- nearly doubles for $(\text{OCS})_3^-$ compared to $(\text{OCS})_2^-$ at both 790 and 395 nm, while the 395 nm yield of OCS^- drops from 8% to zero.⁶⁰ These changes in the fragmentation channels show that solvation affects the excited cluster decay mechanism.

In covalent $(\text{OCS})_2^-$, dissociation involves the breaking of covalent bonds. The energy barriers involved, which could be comparable to the electron emission barrier, indirectly contribute to making the competing process, the autodetachment, more favorable. In $(\text{OCS})_{3,4}^-$, solvation increases the electron detachment energy, while enabling cluster relaxation by solvent evaporation. Fragmentation can thus become a preferred decay mechanism.

For all cluster sizes studied, the relative AD intensity increases sharply at 267 nm compared to longer wavelengths. This could be a consequence of two effects: (i) a decrease in the parent AD lifetime, favoring electron emission over ionic fragmentation; (ii) an increase in fragment-ion internal excitation leading to a corresponding increase in fragment AD. The congestion of low-eKE bands at 267 nm does not allow for a careful analysis of the separate transitions. In particular, our confidence in the assigned TE temperatures (Table 6.1) and even the applicability of the statistical description at 267 nm is not as high as at lower photon energies.

6.6 SUMMARY

This chapter attempts to decipher the structure of $(\text{OCS})_n^-$ with photoelectron imaging spectroscopy. This approach allows the simultaneous detection of fast and slow electrons, which is useful for observing the possible transitions.

In $(\text{OCS})_n^-$ electronic and structural isomer were found to coexist. Both dimer and monomer based clusters were found to coexist in $(\text{OCS})_n^-$. The $\text{OCS}^-\cdots\text{OCS}$ and the covalent $(\text{OCS})_2^-$ exhibit different response to photoexcitation. $\text{OCS}^-\cdots\text{OCS}$ only pathway is direct photodetachment while $(\text{OCS})_2^-$ can either photodetach or promote to an excited anionic state where subsequent autodetachment or fragmentation occurs.

Autodetachment can originate from either the excited parent clusters or internally excited anionic fragments. Regardless of origin, the electron spectra are described successfully using a thermionic-emission model, which assumes strong electronic – vibrational coupling and statistical energy partitioning among product degrees of freedom. The AD cross section in the trimer and tetramer anions decreases relative to the dimer anion. It is suggest that this reflects the competition between the AD and fragmentation channels.

7 PHOTOELECTRON IMAGING OF HYDRATED AND HOMOGENEOUSLY SOLVATED CLUSTER ANIONS

7.1 INTRODUCTION

This chapter analyzes the effects of solvation upon the energy spectra and photoelectron angular distributions of negative ions. PADs resulting from heterogeneous and homogenous solvated anions are compared and contrasted revealing how the electronic structure alters upon solvation. In chapter 5 we observed that hydration stabilizes carbonyl sulfide anions. Chapter 6 discussed isomer coexistence and competition of excited state decay pathways from $(\text{OCS})_n^-$. Now this chapter addresses hydration and homogenous solvation of CO_2^- resulting in cluster anions of the form $[(\text{CO}_2)_n(\text{H}_2\text{O})_m]^-$ where $n = 1-12$ and $m = 0-6$. This chapter concludes with a comparison of the photoelectron signatures of $(\text{CS}_2)_2^-$ and $(\text{CO}_2)_2^-$.

The arrangement of the solvation-shell around a solute anion has drawn much attention recently. Thorough studies of the solvation of halide anions have recently been accomplished,¹²⁰⁻¹⁴⁷ in which not only the structure of the solvation shell was studied with IR^{148,149} and *ab initio* calculations,^{120,139-141,150} but also the dynamics¹²² including charge transfer from solute to solvent. For example, charge transfer to solvent occurs in $\text{I}^-(\text{H}_2\text{O})_n$ when $n \geq 5$. The structural studies conclude that water molecules bind the halide ion in a strong, single ionic hydrogen bond allowing network formation between the remaining OH groups. In larger solutes e.g. the superoxide¹⁵¹⁻¹⁵⁵ and hydroxide ion¹⁵⁶ the water networks form differently. It was observed that $\text{O}_2^-(\text{H}_2\text{O})_4$ does not show evidence of a cyclic water network. Instead evidenced for two dimeric subunits that

bridge the gap between the oxygen atoms of superoxide exist. Seta et al. have calculated the structure of hydrated O^- , O_2^- , and O_3^- clusters, suggesting that none of these portray the cyclic water networks observed within the solvated halides.¹⁵³ Contrarily NO^- favors cyclic hydration with greater than three waters.¹⁵⁷ Recently, the monohydration of small anions SO_2^- , OCS^- , NO_2^- , CH_3CO_2^- and CH_3NO_2^- has also been studied by Johnson and coworkers,¹⁵⁸ finding that symmetric hydration occurs in molecules with a domain larger than 2.2 Å.

Since Klots and Compton first observed $(\text{CO}_2)_n\text{H}_2\text{O}$,¹⁰⁸ few studies have been performed on hydrated carbon dioxide. These include Nagata's and coworkers' examination of the electronic structure of $(\text{CO}_2)_n\text{ROH}$ ($\text{R} = \text{H}$ and CH_3).^{3,105,106} Johnson et al. reacted water clusters with CO_2^- to examine the scavenging of the excess electron.¹⁰³ Photoelectron spectroscopy of $(\text{CO}_2)_n^-$ and $(\text{CO}_2)_n^-\cdot\text{H}_2\text{O}$ revealed evidence for different anionic core structures within these clusters as well.^{55,56,105-107}

A fundamental question in regard to the isovalent $(\text{CO}_2)_n^-$, $(\text{OCS})_n^-$ and $(\text{CS}_2)_n^-$ anionic cluster is whether the excess electron localizes on a single monomer or is shared between two (or more) monomer moieties.^{43,53-60} The closed-shell CO_2 molecule has no electron affinity,⁷³ and CO_2^- is not stable as an isolated species. Small amounts of CO_2^- can be observed in the gas phase under certain ion source conditions,^{55,57,105} as the metastable anion owes its limited existence ($<100 \mu\text{s}$)^{73,159,160} to the potential barrier separating its bent equilibrium geometry from the linear region of the adiabatic potential, which corresponds to the autodetached state. On the other hand, since the pioneering work of Klots and Compton⁶³ it has been known that homogeneous $(\text{CO}_2)_n^-$ cluster

anions can be prepared by low-energy electron attachment to neutral clusters of carbon dioxide.^{43,54-58,61,62,64-72} It is also known that the excess electron in carbon dioxide cluster anions localizes on a single monomer only at select cluster sizes. When $n = 7$ to 13 the excess electron is localized on a single monomer, but when $n \leq 6$ and $n \geq 13$ the excess electron resides on a dimer moiety. Thus the CO_2^- anion is stabilized by homogeneous solvation, but only when certain coordination requirements are met. A similar picture emerges in $(\text{CO}_2)_n^- \cdot \text{H}_2\text{O}$, where the coexistence of different core types is seen for $n = 2-4$, followed by an apparent switch to just one type (the monomer anion) for $n > 4$.^{105,106} Calculations indicate that there are several close lying structures associated with these isomers, but they all are either dimer or monomer based.^{3,59} On the other hand, small CS_2^- clusters ($n \leq 4$) form dimer anion cores^{54,58,161} even though CS_2^- has a positive electron affinity.^{6,51,73} Coexistence of dimer and monomer cores has not been ruled out in $(\text{CS}_2)_n^-$.⁴³

We recently examined the core-switching in $(\text{CO}_2)_n^-$ and $(\text{CO}_2)_n^- \cdot \text{H}_2\text{O}$ with an emphasis on the photoelectron angular distributions. Our previous experiments³⁰ corroborated the evidence for different anionic core species dependent upon the size of the clusters first uncovered by Johnson.⁵⁵ The smaller clusters $n = 2-5$ are comprised of a covalently bound dimer anion solvated by the remaining neutral molecules. For $n > 6$, the cluster core switches to a monomer anion solvated by $n-1$ neutral CO_2 . A similar picture emerges for $(\text{CO}_2)_n^- \cdot \text{H}_2\text{O}$, where the coexistence of the different core types is seen for $n = 2-4$,^{106,107} followed by an apparent switch to just the monomer anion for $n > 4$. Our recent photoelectron imaging experiments reveal that the two different anionic cores both

exhibit quantitatively similar PADs (skewed along the laser polarization). One might expect different PADs, since the molecular orbitals for the each anionic core are different. The analysis, based on the linear combination of molecular orbitals (LCMO) description of the dimer anion's highest-occupied molecular orbital (HOMO), combined with the dual-source interference picture of the detachment process, rationalized the similar PADs as resulting from the similar origin of the monomer and dimer-anion orbitals. Those studies complement the study present in this chapter on $[(\text{CO}_2)_n(\text{H}_2\text{O})_m]^-$. Through these studies the effects of hydration and homogenous solvation on the PADs of anionic carbon dioxide clusters are characterized. Knowledge of the effects of hydration upon the PADs is an important step in understanding solvation. Information of the nature of the excess electron allows us to determine the structure of the clusters.

Homogenous clusters are clusters whose solvating molecules are identical to the ion core or solute. For example, $\text{CO}_2^-(\text{CO}_2)_n$ is a homogenous cluster anion. Contrarily, heterogeneous cluster anions have ion cores that are solvated by molecules or atoms that are different from the core ion. Hydrated cluster anions are a prime example of heterogeneous cluster anions.

This chapter is organized as follows. The following Section presents photoelectron images of homogenous and heterogeneous solvation of CO_2^- at a photodetachment energy of 3.1 eV. Section 7.3 discusses core-switching in $(\text{CO}_2)_n^-$ and $(\text{CO}_2)_n\text{H}_2\text{O}^-$ with an emphasis on the PADs. The retention of PAD in $(\text{CO}_2)_n^-$ upon homogeneous solvation is contrasted with $(\text{CS}_2)_2^-$ in section 7.4. A summary is given in found in section 7.5.

7.2 RESULTS FROM HYDRATION AND SOLVATION OF $(\text{CO}_2)_n^-$

A summary of the 400 nm photoelectron images of $(\text{CO}_2)_n^-$ and $[(\text{CO}_2)_n(\text{H}_2\text{O})_m]^-$ is presented in the form of a $n \times m$ table in Fig. 7.1. The effects of homogenous and heterogeneous solvation can be examined through the $(\text{CO}_2)_n^-$ and $[(\text{CO}_2)_1(\text{H}_2\text{O})_m]^-$ image series of the top row and the first column, respectively. All images are displayed on the same velocity scale, allowing for direct comparison of the corresponding eKE distributions. The consistent scaling of the images was achieved by using the same electrostatic potentials on the imaging lens for all cluster anions studied, with the exception of $(\text{CO}_2)_{10}^-$ and $\text{CO}_2(\text{H}_2\text{O})^-$. For these clusters, different velocity-map imaging conditions were used, but the corresponding images were subsequently rescaled for consistency with the rest of the data.

Most images display a single broad and anisotropic band corresponding to direct photodetachment. A few images in Fig. 7.1, particularly for $(\text{CO}_2)_2^- \cdot \text{H}_2\text{O}$, $\text{CO}_2^- \cdot \text{H}_2\text{O}$, and $(\text{CO}_2)_2^- \cdot (\text{H}_2\text{O})_2$, contain a central spot corresponding to near-zero-eKE electrons. These features were found to be laser-independent and therefore must originate from either autodetachment or field-induced electron detachment occurring within the electron imaging lens. For analysis purposes, the laser-independent signals were subtracted from the images and disregarded.

The most striking results are revealed in the photoelectron angular distributions. Upon visual inspection, the PADs remain qualitatively similar across the rows of images in Fig. 7.1, particularly in the top row ($m = 0$), which corresponds to pure CO_2 cluster anions. On the other hand, the image series presented in the first column in Fig. 7.1,

corresponding to $\text{CO}_2^-(\text{H}_2\text{O})_m$, $m = 1-6$, shows a striking decrease in anisotropy with increasing number of water molecules. The following section will expand

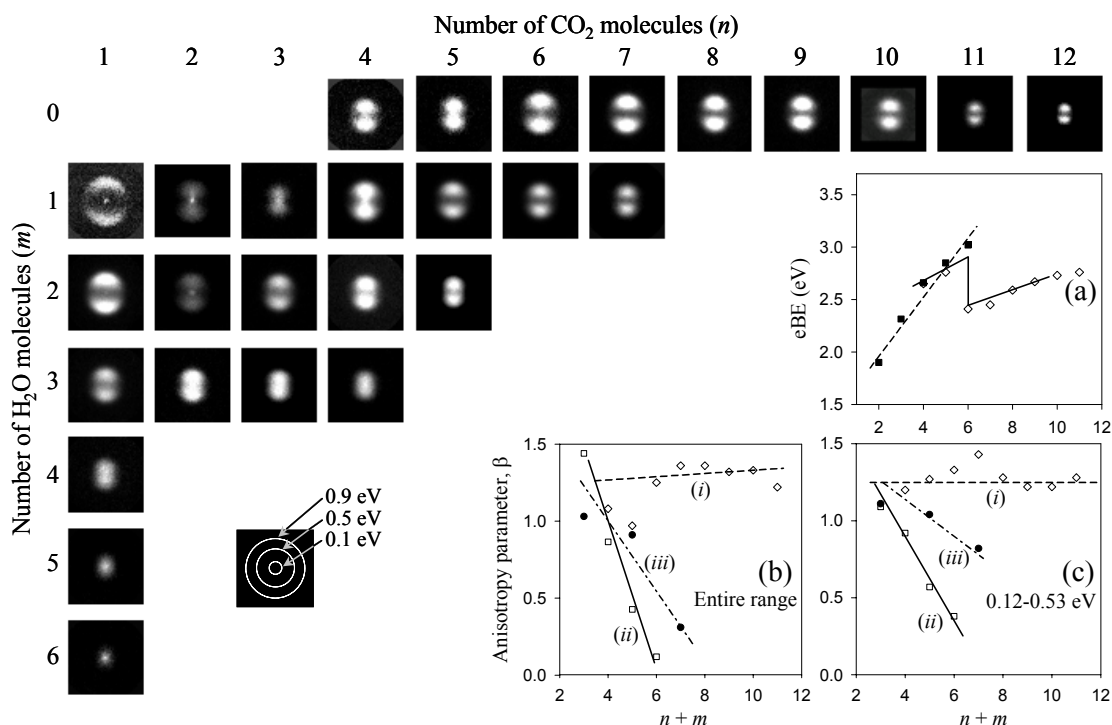


Figure 7.1 Photoelectron images of $[(\text{CO}_2)_n(\text{H}_2\text{O})_m]^-$ cluster anions. The images are recorded with the same velocity-map imaging focusing conditions except for $(\text{CO}_2)_{10}^-$ and $\text{CO}_2^-\cdot\text{H}_2\text{O}$; however, the latter two have been rescaled to account for the discrepancy in the imaging voltages and are shown on the same velocity scale as the rest of the data. Hence, all images presented are shown on the same velocity scale allowing for direct visual comparison. In graph (a) the eBE_{max} in eV is plotted versus the total number of molecules ($n + m$) in each cluster. In graphs (b) and (c) the photoelectron anisotropy parameter β is plotted versus the total number of molecules ($n + m$) in each cluster. The \diamond , \bullet , and \square symbols correspond to $(\text{CO}_2)_{4-11}$, $(\text{CO}_2)_n(\text{H}_2\text{O})_{n-1}$ and $\text{CO}_2(\text{H}_2\text{O})_m$ respectively. In (c), β is integrated over the range 0.12-0.53 eV, while in (b) the it is integrated over the over the entire image area.

upon the PAD.

Turning to the energy domain, one finds that the photoelectron bands generally shrink towards the image centers as the size of the clusters studied increases. This trend is observed both across the rows and down the columns in the table of images in Fig. 7.1. As expected, the shift towards smaller eKEs reflects the energetics of anion solvation. Notable exceptions from this general behavior are observed for $(\text{CO}_2)_6^-$, $(\text{CO}_2)_4^- \cdot \text{H}_2\text{O}$, and $[(\text{CO}_2)_3(\text{H}_2\text{O})_2]^-$. For example, in the $(\text{CO}_2)_n^-$ series the detachment band for $n = 6$ covers a larger portion of the imaging detector than that for $n = 5$, suggesting a lower detachment energy for the larger-size cluster. This discontinuity in the VDE, uncharacteristic of conventional solvation interactions, has been seen previously as evidence of the dimer-to-monomer cluster-core switching.^{30,55,106,107} Similar behavior, also suggestive of core switching, is observed in the $(\text{CO}_2)_n^- \cdot \text{H}_2\text{O}$ series between $n = 3$ and 4,³⁰ and the $[(\text{CO}_2)_n(\text{H}_2\text{O})_2]^-$ series between $n = 2$ and 3.

While the qualitative effects observed in the energy/velocity and angular domains can be seen by visual inspection of the images, quantitative analysis calls for the extraction of the photoelectron spectra and PADs from the Abel-inverted images. Following the image analysis using the BASEX program,³⁶ the photoelectron bands in the resulting energy-domain spectra were fitted with Gaussian functions, allowing for systematic determination of the vertical detachment energies. Photoelectron energy spectra extracted from the images were fitted with Gaussian functions. Allowing for systematic determination of the electron binding energy at the maximum point of the spectral profile, referred to as eBE_{max} . These are presented in Table 7.1. eBE_{max} values are not necessarily the same as

VDEs. For example, when the VDE is at or above the photon energy, as in many of the spectra here, the maximum of the spectral profile will be below the VDE. Typically an s-wave correction from the Wigner threshold law can extrapolate the VDE when the photon energy is near threshold, but in low signal to noise ratio spectra very near threshold it can lead to an over estimate. The type I and type II transitions listed in Table 7.1 correspond to clusters with monomer, CO_2^- , and dimer, $(\text{CO}_2)_2^-$, anion cores,¹⁰⁵ respectively. A subset of the data from Table 7.1 is also presented in Graph (a) in Fig. 7.1, where the eBE_{max} values for the $(\text{CO}_2)_n^-$ and $\text{CO}_2^-(\text{H}_2\text{O})_m$ series are plotted versus the total number of molecular moieties ($n + m$) in the cluster. The eBE_{max} for the $(\text{CO}_2)_n^-$ series exhibits a drop at $n = 6$ corresponding to an increase in image size observed in the photoelectron images. This dis-

Table 7.1. Electron binding energy (in electron-volts) at spectral maximum for selected $[(\text{CO}_2)_n(\text{H}_2\text{O})_m]^-$ cluster anions determined from the present photoelectron images.

n	$m = 0:$ $(\text{CO}_2)_n^-$		$m = 1:$ $(\text{CO}_2)_n^-\cdot\text{H}_2\text{O}$		$m = 2:$ $[(\text{CO}_2)_n\cdot(\text{H}_2\text{O})_2]^-$		$m = 3:$ $[(\text{CO}_2)_n\cdot(\text{H}_2\text{O})_3]^-$
	Type I	Type II	Type I	Type II	Type I	Type II	Type I
1			1.90		2.32		2.66
2			2.17	2.67	2.54	2.54	2.69
3			2.38	2.79	2.34		2.77
4		2.65	2.45	2.87	2.66		2.84
5		2.76	2.53		2.74		
6	2.41		2.64		2.73		
7	2.45		2.73				
8	2.57						
9	2.65						
10	2.73						
11	2.90						

continuity in eBE_{\max} , uncharacteristic of conventional solvation interactions, has been seen previously as evidence of the dimer-to-monomer cluster-core switching.^{30,55,106,107}

The angular distributions observed in the images have been characterized in terms of the anisotropy parameter β , commonly used to describe one-photon detachment with linearly polarized light.^{11,37,119,162} The PADs, and thus β , are generally eKE-dependent. Graphs (b) and (c) in Fig. 7.1 display the β values for selected cluster anions versus the total number of molecular moieties in each cluster. In (b), the β values represent the PADs integrated over a broad energy range representative of each image, covering about 80% of the corresponding spectral profile. It is recognized that the electronic-structural information contained in these data may be obscured by the eKE-dependence of the anisotropy parameter, as different data points in Fig. 7.1(b) correspond to the distributions integrated over different energy ranges and spectral profiles. To account at least partially for the eKE effects, the PADs were also analyzed within the limited eKE range consistent for all clusters studied, namely 0.12 to 0.53 eV. The corresponding β values are plotted in Graph (c) in Fig. 7.1. This energy interval was chosen to contain significant signals in all of the reported images. Since the range is relatively narrow and consistent throughout the data, Fig. 7.1(c) should give a more reliable insight into the changes in the electronic structure of the cluster anions with increasing homogeneous or heterogeneous solvation. However, it is emphasized that the qualitative behavior of the anisotropy parameter is the same in both Figs. 7.1(b) and (c), rather unaffected by the analysis method employed.

The data selected for presentation in Graphs (b) and (c) in Fig. 7.1 correspond to

three different cluster anion series: (i) the homogeneously solvated cluster anions $(\text{CO}_2)_n^-$, $n = 4-11$, corresponding to the first row of images in Fig. 7.1; (ii) the hydrated carbon dioxide anions $\text{CO}_2^-(\text{H}_2\text{O})_m$, $m = 2-5$, corresponding to the first column of images; and (iii) the mixed $[(\text{CO}_2)_n(\text{H}_2\text{O})_{n-1}]^-$, $n = 2-4$, cluster anions, corresponding to the main diagonal in the table of images in Fig. 7.1. To guide the eye, straight lines approximating the least-squares fits for each of the data series are also shown in Figs. 7.1(b) and (c). Some cluster anions, described by the general formula of series (i)-(iii), are not included in the Graphs, because the corresponding photoelectron spectra do not fall in the eKE range (0.12-0.53 eV) corresponding to Fig. 7.1(c). This is the reason for the exclusion of $(\text{CO}_2)_{12}^-$, $\text{CO}_2^-\cdot\text{H}_2\text{O}$, and $\text{CO}_2^-(\text{H}_2\text{O})_6$.

In both Graphs (b) and (c), the β values for series (i), the $(\text{CO}_2)_n^-$ cluster anions, remain substantially positive, without much systematic change as a function of cluster size. To the contrary, in series (ii), the $\text{CO}_2^-(\text{H}_2\text{O})_m$ clusters, stepwise hydration dramatically and monotonically lowers the degree of photoelectron anisotropy. As one might expect, series (iii) is an intermediate case, where the anisotropy of photodetachment diminishes with increasing cluster size, but not as rapidly as in the case of series (ii). Thus, it appears that the addition of CO_2 molecules does not significantly affect the photodetachment anisotropy, while hydration has a pronounced effect in rendering the PAD progressively more isotropic.

7.3 CORE SWITCHING $(\text{CO}_2)_n^-$ AND $[\text{CO}_2(\text{H}_2\text{O})_m]^-$

The $(\text{CO}_2)_n^-$ images in the top row of Fig. 7.1 yield energy-domain fitting parameters that are very close to those reported in earlier work.^{55,105} Thus it is reasonable to

base discussion of the observed PADs upon previously described cluster anion core structures. To recap for the $(\text{CO}_2)_n^-$ series, cluster anions composed of 6 and less monomers contain a dimer core, while clusters with $6 < n < 13$ are monomer core cluster anions.

There are two important comparisons to be made in the series of photoelectron images presented. The first is between the PADs corresponding to monomer versus dimer based clusters. This comparison sheds light on the electronic structures of the different cluster cores. The second is between the hydrated and non-hydrated cluster anions, highlighting the possible differences between the effects of hydration and solvation by carbon dioxide.

7.3.1 PADs of Monomer and Dimer Ionic Cores

A striking result is the similarity of the PADs of the dimer and monomer based clusters in the $(\text{CO}_2)_n^-$. The PAD relates to the structure of parent MO. One expects the dimer and the monomer based clusters to exhibit different PADs corresponding to the difference in HOMO and ionic core structure. Yet the images resulting from $(\text{CO}_2)_n^-$, $n = 4-12$ indicate similar PADs, top row of Fig. 7.1 The β values for the $(\text{CO}_2)_n^-$ series are all greater than 1, see Fig 7.1 (b) or (c). β for cluster with $n = 4$ and 5 are slightly less than for clusters with $n > 6$ but the difference is within the standard deviation of the data sets.

The similarity of the dimer and monomer based $(\text{CO}_2)_n^-$ clusters' PADs will be reconciled through careful qualitative analysis of the symmetries of the parent MOs using the s & p model. The PADs are also reconciled within the frame work of a linear

combination of molecular orbitals (LCMO) description of the dimer anion HOMO and a dual-source interference picture of the photodetached electrons to describe the photodetachment process.

In the cluster anions the excess electron localizes on the monomer or dimer core. Consequently, it is the core anion symmetry that is relevant to the PADs obtained. We initially assume that although the symmetry of the monomer or dimer anion core can be altered by solvation, their overall structures remain largely unchanged. The validity of this assumption will be explored.

The monomer-based clusters' core symmetry is C_{2v} . The $s\&p$ description of CO_2^- photodetachment is analogous to the CS_2^- case discussed in chapter 4. As with CS_2^- , the unpaired electron in CO_2^- resides in an orbital belonging to an A_1 symmetry species. The photodetached electron from an A_1 bound MO has three possible final-state symmetries, A_1 , B_1 , and B_2 , after considering electric-dipole transitions in the molecular frame (MF). The relative amplitudes depend on the orientation of the anion with respect to the laser field vector, defined in the lab frame (LF). Requiring ℓ to be ≤ 1 , the A_1 symmetric waves correspond to a partial s -wave and a partial p -wave aligned along the laser polarization axis. The B_1 and B_2 symmetry components correspond to partial p -waves oriented along the laser polarization which coincides with the z direction. These components overlap to give the final PAD pattern peaking along the z direction.

The covalent dimer anion can be addressed in a similar fashion. The dimer anion has a predicted D_{2d} symmetry structure with two bent CO_2 units linked by a covalent C-C bond.⁵⁹ This structure and corresponding HOMO is shown in Fig. 7.2 (a.1). Since this

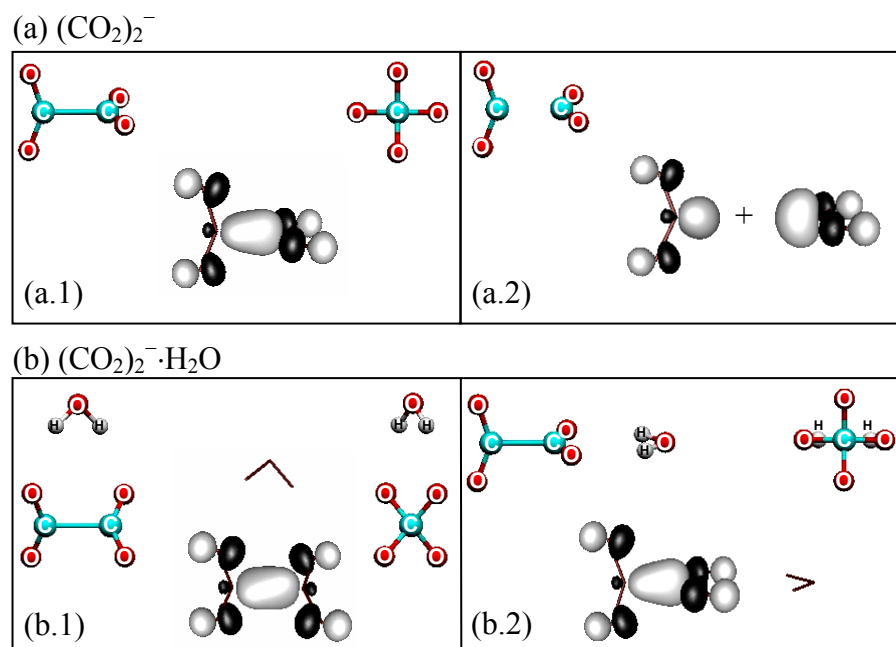


Figure 7.2 Molecular orbital plots for dimer based cluster anion HOMOs (a.1), (b.1), (b.2) and monomer anion HOMO (a.2). Geometries (shown above the HOMO for each species) are taken from Ref. ³ and correspond to the potential minima calculated at the MP2/6-31+G* level. Above left is the view perpendicular to CC bond axis and above right is along the CC bond axis. (a.1) $(\text{CO}_2)_2^-$, D_{2d} symmetry. (a.2) Two monomer CO_2^- HOMOs arranged with D_{2d} symmetry. (b.1) lowest energy $(\text{CO}_2)_2^- \cdot \text{H}_2\text{O}$ structure in which the dimeric core anion is distorted from D_{2d} to C_2 symmetry by the bridging H_2O group. (b.2) $(\text{CO}_2)_2^- \cdot \text{H}_2\text{O}$ with H_2O in the end position.

HOMO corresponds to an A_1 irreducible representation of the D_{2d} point group, the allowed free-electron symmetries are B_2 and E , depending upon the anion orientation relative to the laser polarization. The B_2 waves arise from anion orientations with non-zero projection of the C-C bond axis on the LF z axis. In the s & p approximation, B_2 symmetric waves correspond to p waves polarized along the C-C axis and predominantly along the z axis in the LF. The E symmetry waves are emitted from anions with non-zero perpendicular components of the C-C bond axis with respect to z . Again, s waves are not allowed, while the relevant p waves are polarized perpendicular to the C-C bond. In the LF these p waves may be polarized both in the z direction and perpendicular to it, making the predictions of the model less clear than in the monomer anion (C_{2v} symmetry) case. To arrive at more definitive conclusions supporting the parallel nature of the photodetachment process in the D_{2d} dimer anion one must evaluate the transition dipole matrix elements corresponding to different p waves.

The need for these calculations can be bypassed by considering the dimer anion structure within monohydrated clusters. As discussed below, the $(\text{CO}_2)_2^-$ core within these clusters is distorted from its D_{2d} symmetry. For example, in the structure shown in Fig. 7.2(b.1) the torsional angle between the two CO_2 groups is reduced to 75° due to the ionic hydrogen-bonding interaction of the water molecule with the dimer anion,³ reducing its symmetry to C_2 . Similarly, the dimer structure in Fig 7.2(b.2) experiences a hydration-induced closing of the OCO angle, leading to symmetry change from D_{2d} to C_{2v} . In each case the dimer anion HOMO still conforms to the totally symmetric representation of the respective point group. Of the D_{2d} , C_2 , and C_{2v} cases, the s & p description of the detach-

ment process is least ambiguous for the C_{2v} group, where the free electron can be shown to include mixtures of s and p waves, the latter polarized predominantly along Z .¹⁶³ Now consider that in all dimer anion structures discussed (the unperturbed D_{2d} , as well as the hydrated C_2 and C_{2v} structures) the detachment occurs from essentially the same HOMO. While the orbital is subject to solvent perturbations, their effect on its overall shape is not too great and the resulting PADs should be similar. Since the s & p analysis in the C_{2v} case unambiguously indicates a PAD peaking along the Z axis, similar outcomes are expected in detachment from the $(\text{CO}_2)_2^-$ HOMO, regardless of the detailed cluster structure. Thus, positive photoelectron anisotropy is to be expected for all dimer-based $(\text{CO}_2)_n^-$ and $(\text{CO}_2)_n^- \cdot \text{H}_2\text{O}$ clusters studied.

The above treatment only qualitatively indicates the direction the PADs from the dimer and monomer core anions, without satisfactorily addressing the qualitative similarities of the β values for each. To accomplish this we adopt a new approach using a two center detachment description. The $(\text{CO}_2)_2^-$ HOMO (ψ_{dimer}) can be thought of as a superposition of two monomer orbitals and hence the detachment from it can be described in terms of interference of electron waves originating from the two CO_2 moieties in the dimer anion. This correlation will enable us to compare the $(\text{CO}_2)_2^-$ and CO_2^- PADs. Using a LCMO approach and disregarding the normalization, we assume:

$$\psi_{\text{dimer}} \approx \psi_{\alpha} + \psi_{\beta}, \quad (7.1)$$

where $\psi_{\alpha,\beta}$ are the HOMOs of two (hypothetical) monomer anions (α and β) separated by the C-C bond (see Fig. 7.4). The monomer units and their orbitals transform into one another under a fourfold improper rotation about the C-C axis. Waves $\psi_{f,\alpha}$ and $\psi_{f,\beta}$

produced by detachment from ψ_α and ψ_β , respectively, give rise to a two-center description of the free-electron wavefunction $\psi_f = \psi_{f,\alpha} + \psi_{f,\beta}$.

Each of the monomers belongs to the C_{2v} point group and their individual HOMOs are of A_1 symmetry. Under the electric-dipole approximation, for an allowed transition $\langle \psi_{f,j} | z | \psi_j \rangle \neq 0$, where z is proportional to the active component of the dipole operator and $j = \alpha, \beta$. The symmetry species of z in the frames of α and β are determined by the orientation of the dimer frame and are given in Fig. 7.3. For orientation I, only B_2 waves are allowed from α , while β yields waves of B_1 symmetry. For orientation II, both monomer groups yield waves of A_1 symmetry.

Under the s and p approximation, $\psi_{f,\alpha}$ and $\psi_{f,\beta}$ are expanded in the basis of s , p , etc. partial waves emitted from centers α and β , respectively, and all components with $\ell > 1$ are disregarded.²⁷ For orientation I, this leaves only p waves, as s waves satisfy neither the B_2 nor B_1 restrictions obtained above. Transformed to the LF, the p waves of B_2 (for α) and B_1 (for β) symmetry correspond to the p_z waves sketched in Fig. 7.3. For orientation II, both s and p waves are allowed, with the p waves limited to p_z components only.

The phase shift between $\psi_{f,\alpha}$ and $\psi_{f,\beta}$ at their respective origins is determined by symmetry and largely unaffected by distance D between the emission centers. This assumption is well justified in the limit of $D \ll \lambda$, where $\lambda = 400$ nm. From symmetry, the overall free-electron wavefunction ψ_f must transform as the dipole component coincident with the laser polarization vector, because ψ_{dimer} is totally symmetric.

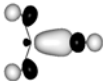

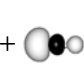
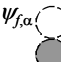



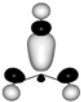

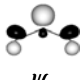



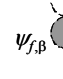
	Parent HOMO	LCMO representation	Free-electron dual-source <i>s</i> and <i>p</i> partial waves	
<u>Orientation I</u>				
		ψ_α  + ψ_β 	$\psi_{f,\alpha}$  + $\psi_{f,\beta}$  (I-a)	
		\vec{z} \vec{E}	$\psi_{f,\alpha}$  + $\psi_{f,\beta}$  (I-b)	
Dimer (D_{2d})	A_1		E	E
α (C_{2v})		A_1	B_2	B_2
β (C_{2v})		A_1	B_1	B_1
<u>Orientation II</u>				
		ψ_α  + ψ_β 	$\psi_{f,\alpha}$  + $\psi_{f,\beta}$  (II-a)	
		\vec{z} \vec{E}	$\psi_{f,\alpha}$  + $\psi_{f,\beta}$  (II-b)	
Dimer (D_{2d})	A_1		B_2	B_2
α (C_{2v})		A_1	A_1	A_1
β (C_{2v})		A_1	A_1	A_1

Figure 7.3 Qualitative treatment of $(\text{CO}_2)_2^-$ photodetachment. For each orientation I and II, the parent orbital (left column) is described as an LCMO superposition of the orbitals of two monomers α and β (second column). The partial wave pairs sketched on the right represent a dual-source description of the free-electron wavefunction in the limit of *s* and *p* components only. The symmetries of the bound and free electron wavefunctions and the laser polarization vector are given in the irreducible representations of the dimer and monomer point groups (D_{2d} and C_{2v} , respectively).

For orientation I, the z component of the dipole belongs to the E i.r. of the D_{2d} point group. Hence $\psi_f = \psi_{f,\alpha} + \psi_{f,\beta}$ must be of E symmetry, allowing for both constructive and destructive interference between $\psi_{f,\alpha}$ and $\psi_{f,\beta}$ (combinations I-a and I-b in Fig. 7.3), as well as for any intermediate phase shift. In addition, the amplitudes of $\psi_{f,\alpha}$ and $\psi_{f,\beta}$ are not constrained to be equal.

In a similar fashion, for orientation II the z dipole component belongs to the B_2 i.r. of the D_{2d} group and the overall wavefunction $\psi_f = \psi_{f,\alpha} + \psi_{f,\beta}$ is of B_2 symmetry. This requirement dictates that the s components of $\psi_{f,\alpha}$ and $\psi_{f,\beta}$ be phase-shifted by π , while the p_z waves contribute with the same sign. In addition, the $\psi_{f,\alpha}$ and $\psi_{f,\beta}$ amplitudes are equal. The relevant s and p waves are sketched in Fig. 7.3 (II-a and II-b).

Thus, the problem of $(\text{CO}_2)_2^-$ photodetachment is reduced to interference of s and p waves from two sources. These sources can be thought of as “centers of mass” of the monomer orbitals and thus separation D between them is in slight excess of the C-C bond length.⁵⁹ $D \approx 2 \text{ \AA}$ is a reasonable value to use.

The comparison of dimer and monomer anion cores requires an analysis of the interference pattern arising from the α and β centers in relation to the detachment description of the monomer. The de Broglie wavelength λ_e of the emitted electron's wavefunction is crucial in understanding the consequences of the interference pattern. At the energies characteristic of the detached electrons, 0.7 eV the λ_e is $\sim 15 \text{ \AA}$. At the $\sim 2 \text{ \AA}$ separation between the detachment centers they would appear to be overlapped. Hence when the phases of the waves are identical the PAD of the dimer would appear similar to that of the monomer. When the phase is opposite, the overall wave structure will differ

from the monomer wave emitted, but these differences would be minimized by destructive interference. Thus, the waves emitted with similar phases contribute the most to the dimer-anion PAD. At a qualitative level, this can explain the similar PADs observed for the monomer and dimer based $(\text{CO}_2)_n^-$.

7.3.2 Effects of Hydration and Solvation upon PADs

The photoelectron images in Fig. 7.1 decrease in size except when the cluster core shifts from dimer to monomer. Anisotropy of the PAD remains nearly unchanged upon solvation by CO_2 in contrast to the decline of anisotropy upon hydration. This subsection will describe a possible explanation for the contrasting effects of homogenous and heterogeneous solvation.

With the energetic effects accounted for, the changes in the β values in Fig. 7.1(c) are attributed primarily to the effect of solvation/hydration on the molecular orbital from which the photoelectrons originate. The $(\text{CO}_2)_n^-$, $n = 7-12$ cluster anions are known to have a monomer-anion core.^{55,56} The similarity of the anisotropy properties of the $(\text{CO}_2)_n^-$, $n = 7-12$, and $[\text{CO}_2(\text{H}_2\text{O})_m]^-$, $m = 1-2$ images suggests that the smallest hydrated clusters ($m \leq 2$) have a CO_2^- core.³⁰ In fact, the energetics of the observed photodetachment bands support CO_2^- core-based structures for all $[\text{CO}_2(\text{H}_2\text{O})_m]^-$ cluster anions studied. Namely, the eBE_{max} of the $[\text{CO}_2(\text{H}_2\text{O})_m]^-$, $m = 1-5$ photoelectron images summarized in Graph (a) in Fig. 7.1 (solid symbols) are consistent with hydration of CO_2^- , as well as with the ab initio calculations discussed below.

However, in the angular domain the similarity between the (i), (ii), and (iii) series diminishes rapidly with increasing cluster size, with the PADs becoming nearly isotropic

for clusters containing as few as 5-6 water molecules. To account for the loss of anisotropy with increasing hydration, the electronic structures of $[\text{CO}_2(\text{H}_2\text{O})_m]^-$ and other hydrated cluster anions need to be determined. One possibility is the excess electron is no longer localized on the CO_2 , being solvated by the water segment of the cluster instead. To obtain further insight, quantum chemical calculation using the GAUSSIAN 98 software package were carried out on $[\text{CO}_2(\text{H}_2\text{O})_m]^-$ cluster anions.

The ab initio geometry optimization was performed on several assumed initial geometries using the Gaussian 98 program⁷⁴ at MP2/6-31+G* level of theory. For $[\text{CO}_2(\text{H}_2\text{O})_2]^-$ the calculation resulted in two structures with very small energy difference. Therefore, to be more certain as which structure corresponds to the global minimum, the two structures were further optimized using MP2/6-31++G**. To calculate the total energy and the vertical detachment energy we used 6-311++G** basis sets with MP2 method.

The calculation generated several structural isomers for each cluster size and only the global minimum structures are presented in Fig. 7.4. Neither previous experimental nor theoretical results are available to allow evaluation of these predicted structures. Qualitatively, the structure for $m=2$ is similar to the one for $\text{O}_3^-(\text{H}_2\text{O})_2$ ¹⁶⁴ and the structures for $m=3$ and $m=5$ follow the same trend as the structures of hydrated iodide reported previously.^{139,165}

Our calculations predict that the inner solvation shell can contain up to four water molecules. When two water molecules solvate CO_2 , the first water molecule forms two hydrogen bonds to the oxygens on the opposite ends of the bent CO_2 to form a C_{2v}

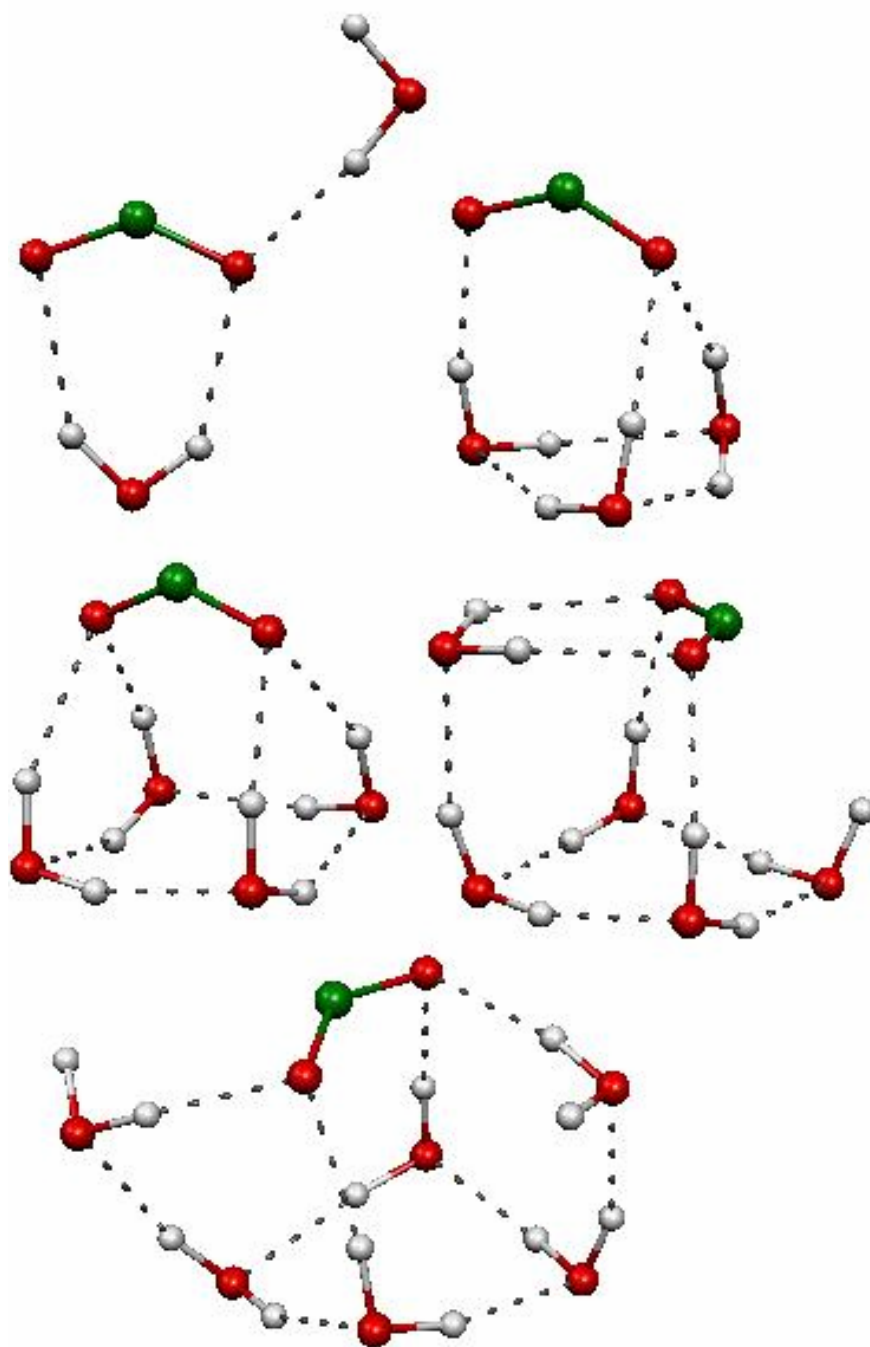


Figure 7.4 Predicted structures for CO₂(H₂O)_m Optimized by MP2/6-31+G* method.

symmetry structure, similar to the previously reported structure for $[\text{CO}_2(\text{H}_2\text{O})]^-$ ³ and the second water molecule forms one hydrogen bond to one of the oxygens of the CO_2 . Third water molecule expands the network into a six-member ring with all the dangling protons forming a hydrogen bond with the solute, CO_2 . A fourth water molecule completes the solvation sphere creating an eight-member ring and four H-bonds to the solute, two to each oxygen atom of the solute. Up on addition of the fifth water molecule, one water molecule interrupts the ring's interaction with the solute. It binds directly with the solute and it also accepts a hydrogen bond from the ring. Two of the ring's other dangling hydrogens bind to the solute while the fourth remains free. This could be due to the high ring-strain. The dynamic nature of these shells is illustrated by the similar stability of the two different locations for the sixth water. It will either attach directly to the solute or bind to the first shell creating structure in the second shell. Table 7.2 contains both experimental and calculated VDEs for clusters $[\text{CO}_2(\text{H}_2\text{O})_m]^-$. The exact experimental

Table 7.2. Total energies, eBE_{max} and VDE of $[\text{CO}_2(\text{H}_2\text{O})_m]^-$ cluster anions using the MP2/6-311++G** theory level and basis set or determined from photoelectron spectra through fitting with Gaussians.

Cluster Anion	Total Energy (a.u)	Calc VDE (eV)	Exp eBE_{max} (eV)	Mulliken Charge on CO_2
$[\text{CO}_2(\text{H}_2\text{O})_2]^-$	-340.7661871	2.28	2.315	-0.981
$[\text{CO}_2(\text{H}_2\text{O})_3]^-$	-417.0639828	2.49	2.66	-1.003
$[\text{CO}_2(\text{H}_2\text{O})_4]^-$	-493.3617186	2.78	2.85	-1.012
$[\text{CO}_2(\text{H}_2\text{O})_5]^-$	-569.6575299	3.10	3.02	-0.996
$[\text{CO}_2(\text{H}_2\text{O})_6]^-$	-645.9521948	3.50	3.1	-0.996

values of the VDE for $[\text{CO}_2(\text{H}_2\text{O})_{5,6}]^-$ cannot be determined since the output energy of the laser (3.1 eV) is below the VDE energy.

The calculated MOs for these structures suggest the electron remains on the CO_2 regardless of the extent of hydration, evident by the charge density provided in Table 7.2. Through examination of the most stable water cluster anions from previous theoretical studies and adding the energy of CO_2 and comparing them to the total energy of the hydrated carbon dioxide cluster anions the following picture unfolds. Taking the calculated total energies of the pure water cluster anions $(\text{H}_2\text{O})_3^- = -228.834301(\text{a.u.})^{166}$ (MP2/6311++G**) and $(\text{H}_2\text{O})_5^- = -381.21818(\text{a.u.})^{167}$ (PMP2/6311++G**) and adding the energy of CO_2 a comparison can be made with the calculated energies of the $[\text{CO}_2(\text{H}_2\text{O})_3]^-$, and $[\text{CO}_2(\text{H}_2\text{O})_5]^-$ clusters. The $[\text{CO}_2(\text{H}_2\text{O})_3]^-$, and $[\text{CO}_2(\text{H}_2\text{O})_5]^-$ are found to be -416.7930958 & -569.6594214 a.u. more stable than the corresponding hydrated electron clusters solvated by a neutral CO_2 (-416.37877 and -569.4242936 a.u.) Evidently the water does not solvate the electron. Perhaps with more diffuse basis sets the water would solvate the electron. The structure of the $(\text{H}_2\text{O})_5^-$ resembles our $[\text{CO}_2(\text{H}_2\text{O})_5]^-$ without the CO_2 . Larger and more diffuse basis sets should be used to determine the MO and the VDE. As is evident from previous anionic water calculations determining the structure is not trivial. For example, nearly five isoenergetic structures have been found for $(\text{H}_2\text{O})_6^-$.¹⁶⁸

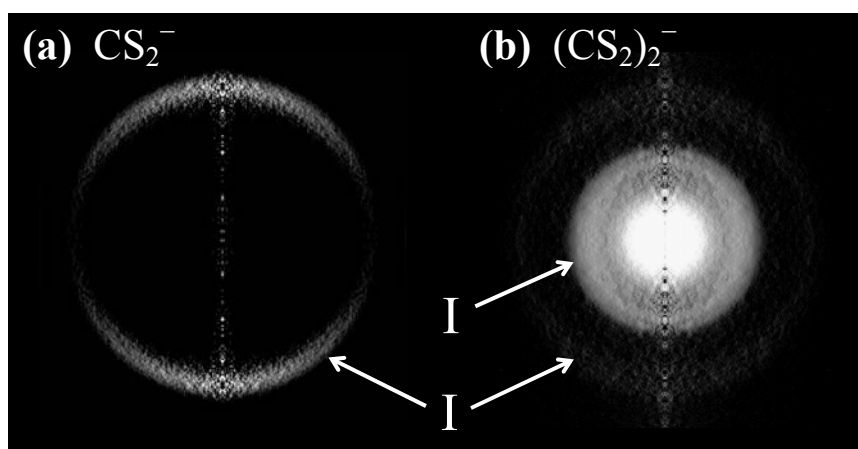


Figure 7.5. Abel-transformed 400 nm photoelectron images of (a) CS_2^- and (b) $(\text{CS}_2)_2^-$. The laser polarization is vertical. Arrows I point to the transitions corresponding to electron detachment from the CS_2^- HOMO (either in the isolated anion or in the $\text{CS}_2^- \cdot \text{CS}_2$

7.4 $(\text{CS}_2)_2^-$

The 400 nm Abel transformed photoelectron images obtained from CS_2^- and $(\text{CS}_2)_2^-$ are presented in Fig. 7.5. The Abel transforms assist in visual separation of the many transition of $(\text{CS}_2)_2^-$. The CS_2 image discussed in chapter 4 is shown again for comparison purposes.

The CS_2^- image has a single band (1) that has a VDE of 1.43 eV. The PAD is described by an anisotropy parameter $\beta = 0.60$, consistent with electron ejection from the a_1 HOMO of CS_2^- .^{26,27}

Several transition are revealed in the 400 nm image of $(\text{CS}_2)_2^-$. The outer band has a VDE of 1.65 eV and anisotropy parameter, $\beta = 0.34$ that corresponds to detachment from CS_2^- solvated by a CS_2 . No other transition in the image is associated with detachment from $\text{CS}_2^- \cdot \text{CS}_2$. The isotropic band in the center of the image is due to autodetachment from either the excited covalent dimer or a photofragment. Ring II is from direct photodetachment to the lowest energy state of the covalent $(\text{CS}_2)_2$ dimer, corresponding to a VDE ≈ 2.7 eV and $\beta = -0.17$. The differences between photoelectron images of covalent dimer, $(\text{CS}_2)_2^-$, and the monomer, CS_2^- , reveal the differences between HOMO of the dimer and a_1 HOMO of the monomer. As expected different MO species have different photoelectron signatures.

In light of the $(\text{CO}_2)_n^-$ results, where dimer and monomer cluster gave rise to markedly similar photoelectron images, the $(\text{CS}_2)_n^-$ results are intriguing. This discrepancy can be

understood as being due to a fundamental difference in the geometric and/or electronic structures of the dimer anions of CO_2 and CS_2 .

7.5 SUMMARY:

Photoelectron images of homogeneously solvated and hydrated carbon dioxide cluster anions were presented illustrating the effects of solvation on carbon dioxide. Homogeneous solvation does not affect the photoelectron angular distributions in carbon dioxide cluster anion. Contrarily hydration decreases the anisotropy signifying a shift in the electronic structure. Core-switching is observed which is evident by a jump in the $e\text{BE}_{\text{max}}$. β remains high even through the core changes from dimer to monomer. In Contrast, for the isovalent carbon disulfide the PAD produced from the dimer differs from the PAD of the monomer, which is a reflection of the difference of the electronic structure of the two dimers.

8 TIME-RESOLVED PHOTOELECTRON IMAGING

8.1 INTRODUCTION

The driving force of chemical reactions has long been investigated. Non-chemist have a tendency to consider reactions in terms of the movement of nuclei e.g. $ABC + h\nu \rightarrow A + BC$. However the nucleus motions depend upon the potential surface which arises due to the electrons. Electronic states are described by the corresponding wavefunctions. Eigenvalues and/or the separation between energy levels has been explored by traditional spectroscopy. Photoelectron imaging gives the ability to observe how these electronic wavefunctions evolve during a chemical reaction. As observed in previous chapters the photoelectron images are signatures of molecular orbitals. By observing the evolution of the photoelectron images we can characterize the potential surfaces the chemical reaction occurs upon.

The first time-resolved photoelectron imaging studies of trihalide anion dissociation are presented in this chapter. I_2Br^- was studied with 388 nm pump and 388 nm probe. The triiodide, I_3^- , has been investigated extensively as a model system for testing physical theories. Recent studies of ultrafast dynamics of the photodissociation of I_3^- in solution¹⁶⁹⁻¹⁷⁹ and in the gas phase^{137,180,181} demonstrate vibrational coherence in the I_2^- fragment and yield valuable information about dissipative phenomena involving highly excited molecules in solution. These experiments extended the earlier work on the photodissociation dynamics of HgI_2 in the gas phase¹⁸²⁻¹⁸⁵ and solution,¹⁸⁶⁻¹⁸⁹ and have motivated broad theoretical research on vibrational coherence and wavepacket dynamics, with and without the effects of solvation.^{172,190-195}

However I_3^- is limited in its application as a model due to its identical bonds, preventing selective bond breaking studies. It is also difficult to determine experimentally the probability of electron localization on a given I-atom in three-body $\text{I}_3^- \rightarrow 2\text{I} + \text{I}^-$ photodissociation. Only recently, through extensive modeling of time-dependent photoelectron spectra, have Neumark and co-workers shown that the I^- photofragment is most likely formed via concerted three-body dissociation along the I_3^- symmetric stretching coordinate.¹⁹⁶ In addition, photofragment kinetic energy release measurements by the same group have indicated that in three-body dissociation the excess electron localizes on the middle I-atom.¹⁹⁷

To overcome this limitation of I_3^- we examine the mixed halide, I_2Br^- , which offers more identifiable reaction pathways providing richer dynamics and photochemistry. A few studies of mixed trihalide anions have been reported. These include dissociation of I_2Br^- and IBr_2^- in solution.⁷ Also Raman and infrared spectroscopic measurements of I_2Br^- in solution have been reported.¹⁹⁸

The coexistence of structural isomers complicates the study of reaction pathways. I_2Br^- has two structural isomers, which are linear such as I-Br-I^- and I-I-Br^- . The most stable isomer is the one with the heaviest atom in the middle;^{199,200} hence, I-I-Br^- is the most stable.¹⁹⁹

In section 8.2.1, we will present preliminary results of time-resolved I_2^- experiments. This serves as a stepping stone for the mixed trihalide, I_2Br^- , presented in 8.2.2. Then the final section, 8.3, will be summary.

8.2 RESULTS

8.2.1 I_2^- Results

Bottom right of Fig 8.1 shows the potential energy curves of I_2^- and I_2 . In a photodissociation reaction a photon excites the molecule into an excited dissociative state that leads to $I^- + I$. Another photon probes the fragments. In the schematic shown in Fig 8.1 a pump laser of 800 nm excites the I_2^- and a probe laser (267 nm) photodetaches the electron from the excited state sampling the MO of the excited I_2^- system at a given instant.

A series of images of the photodissociation of I_2^- is provided in Fig. 8.1. The difference in delay between each image is 33 fs with the bottom corresponding to approximately -50 fs and the top image corresponding to ~450 fs. Near time zero the photoelectron image is an unresolved blur, but as the delay between the pump and the probe beams increases the images gradually resemble the photoelectron image of I^- . As shown in chapter 3, I^- photoelectron signature at 267 nm is two anisotropic rings with peak intensity perpendicular to the laser polarization with a separation of ~0.94 eV.

To the right of the images in Fig 8.1 is a contour plot of the photoelectron spectra as a function of time. At short delays the band near 1.6 eV is broad and weak. After ~300 fs the band intensifies and sharpens. A second band also grows in near 0.65 eV. The photodissociation of I_2^- has been a model for time-resolved anion photoelectron spectroscopy. It was the first negative ion dissociation to be studied using femtosecond photoelectron spectroscopy in 1996 by Neumark and its dynamics have been thoroughly characterized by subsequent experiments. Recently, Neumark also performed the first

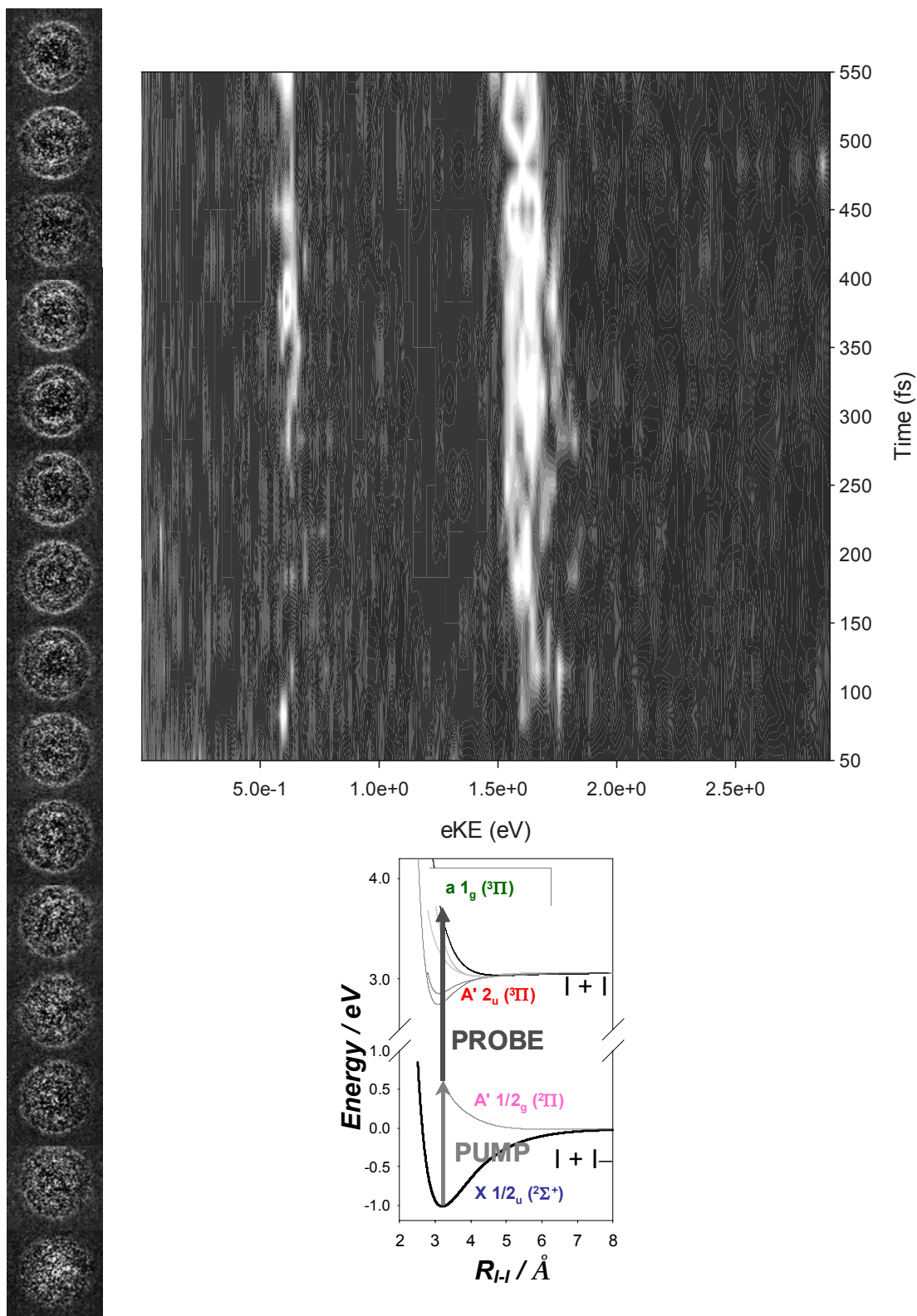


Figure 8.1 *Left* time-resolved photoelectron images of I_2^- each the time interval between images is 33 fs. The bottom image has a delay of approximately -50 fs, while the top is ~ 450 fs. *Top-right*: Contour spectra of the images with time as the y-axis. *Bottom*: Schematic of potential surfaces of I_2^- where arrows represent the photon energies of the pump and the probe beams.

time-resolved photoelectron imaging study of I_2^- . Therefore, our I_2^- results serves as a proof of principle and as an assessment of the abilities of our imaging spectrometer.

8.2.2 Γ^- channel of I_2Br^-

Upon excitation of I_2Br^- many ionic fragments may be created with a 388 nm photon: IBr^- , Γ^- , Br^- , I_2^- . From theoretical calculations and analogy with IBr_2^- and I_3^- ,^{181,199-202} all the fragments listed above are energetically accessible. With a 388 nm probe laser beam all ionic fragments will detach an electron, except Br^- . At the asymptotic limit (long pump-probe delays) the atomic-anion fragments are expected to yield relatively sharp photoelectron images. For the diatomic-anions the Frank-Condon effect must be considered. The photoelectron images may show contributions from one or more channels but in this chapter we will focus on the Γ^- channel. We observed a photoelectron band that tentatively could be I_2^- , however we reserve its analysis to future work.

Photoelectron images of photodissociation of I_2Br^- at a 388 nm pump and a 388 nm probe at a number of different delays are presented in Fig 8.2(a)-(e). Figure 8.2(f) displays an atomic Γ^- photoelectron image produced by one photon detachment at 388 nm. The photoelectron images in Fig. 8.2 (a)-(f) represent photoelectron clouds that have

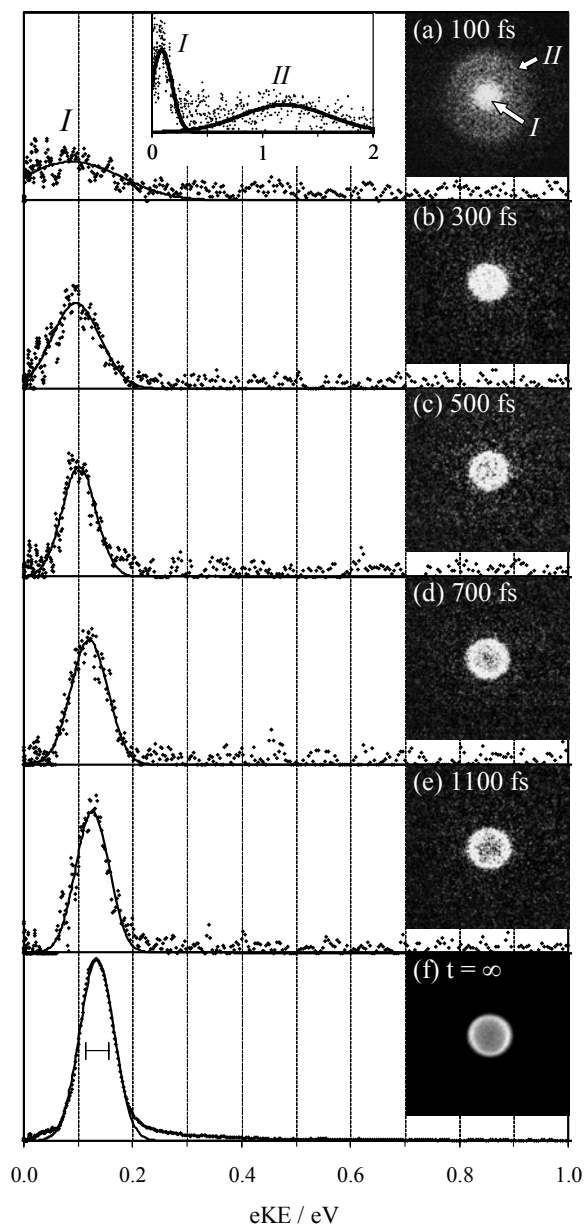


Figure 8.2 Two dimensional photoelectron images (shown on the right in order of increasing delay time) are Abel inverted to reproduce the photoelectron energy domain spectra (shown on the left) and the photoelectron angular distributions. The insert on the 100 fs spectrum shows an increased energy range, clearly indicating the presence of a second electronic transition as seen in the image by the outer ring. This outer ring is absent in all of the other (longer delay time) images. The peak in the 0.0-0.2 eV energy range becomes narrower and shifts to higher eKE as the delay time increases, becoming increasingly like that seen in atomic anion detachment. The final image in the series is from the single photon detachment of Γ^- at 388 nm which effectively represents an infinite delay time between the two lasers.

been projected onto the detector. Their energy and angular distributions can be reconstructed by an inverse Abel transform,¹⁶ which is performed by BASEX³⁶.

The delay-dependent changes observed in the images in Fig 8.2 (a)-(e) correspond to the evolution of the MO during the photodissociation of I_2Br^- . The image in Fig. 8.2 (a) exhibits two main features: a bright and relatively intense band near the image center (I) and a broad anisotropic band peaking with $\text{eKE} \sim 1.2$ eV (II). The latter is seen more clearly in the inset in Fig. 8.2(a), where the same 100 fs spectrum is shown on a different scale. With increased pump-probe delay, band (I) spatial extent increases and the center of the band diminishes in intensity forming a dark region in the center of the image by 700 fs, (Fig 8.2(d)). Gradually at longer pump-probe delays the photoelectron images (Fig. 8.2(e) at 1100fs) resemble the one photon photodetachment of I^- in Fig 8.2(f). The one photon photoelectron image of I^- is provided as a reference. It also reflects a single photodetachment transition from the anion to the $^2\text{P}_{3/2}$ ground state of the neutral. The upper spin orbit state, $^2\text{P}_{1/2}$ lies 0.94 eV higher in energy and is not accessible with 388 nm one-photon detachment. In the spectra, the low-eKE peak in Figs. 8.2(a)-(e) shifts to larger eKEs as the delay increases, while the width of the peak decreases, until both the peak position and width become very similar to those of the I^- spectrum in Fig. 8.2(f). Therefore, the hypothesis emerging from the inspection of the time-resolved photoelectron images in Figs. 8.2(a)-(e) is that they reflect the appearance of the I^- fragment in I_2Br^- photodissociation. Hence, the one-photon photoelectron image is a snapshot of the expected electronic signature for the dissociation of $\text{I}_2\text{Br}^- \rightarrow \text{I}^-$ at infinitely long delays where there is no interaction between the fragments.

Let us turn our attention to band (II). The anisotropic higher-eKE band (II) appears only at short pump-probe delays, i.e., in the 100 fs image in Fig. 8.2(a). It can be attributed to two different processes. First, because this signal appears when the pump and probe pulses overlap significantly in time, it may be due to coherent two-photon absorption by the parent anion. Such absorption is not a true pump-probe process, as both absorbed photons can be from either the pump or the probe beam, in addition to the possibility of simultaneous absorption of one pump and one probe photon. Signals due to the coherent pump-only and probe-only two-photon absorption are not properly accounted for by the background subtraction routine, because their intensity scales nonlinearly with laser power, resulting in the pump-only, probe-only, and pump-probe two-photon signals being non-additive when the two laser pulses are overlapped in time and space.

The second possible origin of band II in Fig. 8.2(a) is the contribution(s) of the I_2^- and/or IBr^- channel(s). We do not identify any other bands that could be attributed to these channels, even though their yield is expected to be significant at the pump wavelength used. If the higher eKE band in Fig. 8.2(a) is indeed due to the diatomic-anion channel(s), its apparent disappearance at longer delays can be due to a combination of dynamic, Franck-Condon, and possibly signal-to noise factors. The diatomic-anion fragments are formed in highly vibrationally excited states^{170,171,181,190,199,202,203} and rapid delocalization of the initially localized time-dependent wave packet^{173,204-208} leads to spreading of the pump-probe signal over a wide energy range. Thus, following the initial rise, the intensity of the pump-probe signals attributed to the diatomic-anion channels

drops in time¹⁹⁹ and the resulting diffuse bands¹⁸¹ are difficult to detect, compared to the sharp transitions associated with atomic-anion channels. The reaction channels yielding diatomic-anion fragments will be addressed in future work. Let us return to a quantitative analysis of the I^- channel.

The time-resolved spectra were fitted with Gaussians to extract peak positions and widths referred to as full width at half max (FWHM). These parameters are plotted in relationship to their corresponding pump-probe delay in Figs 8.3(a) and (b). The maximum peak position starts near 0.09 eV and approaches the asymptotic limit of 0.13-0.14 eV within ~ 1 ps, which corresponds to the detachment energy of I^- , 3.059 eV, subtracted from the 388 nm photon energy, 3.195 eV.

The experimental resolution in the relevant energy range is reflected in the atomic-anion spectrum in Fig. 8.2(f). The spectral width (FWHM = 0.07 eV) is a convolution of several broadening factors, such as the laser bandwidth [FWHM = 0.04 eV, indicated by a solid interval in Fig. 8.2 (f)] and the ion-beam velocity spread. With all factors considered, it is clear that at long delays the width of the spectral feature approaches the atomic limit.

The widths in Fig 8.3(b) decreases to 0.8 eV in less than 500 fs. Since this is of the same magnitude as our experimental temporal resolution (~ 250 fs), the convolution of the reaction kinetics with the pump probe cross-correlation function must be taken into account. This yields an upper boundary of the timescale involved in the reaction as approximately 300 fs.

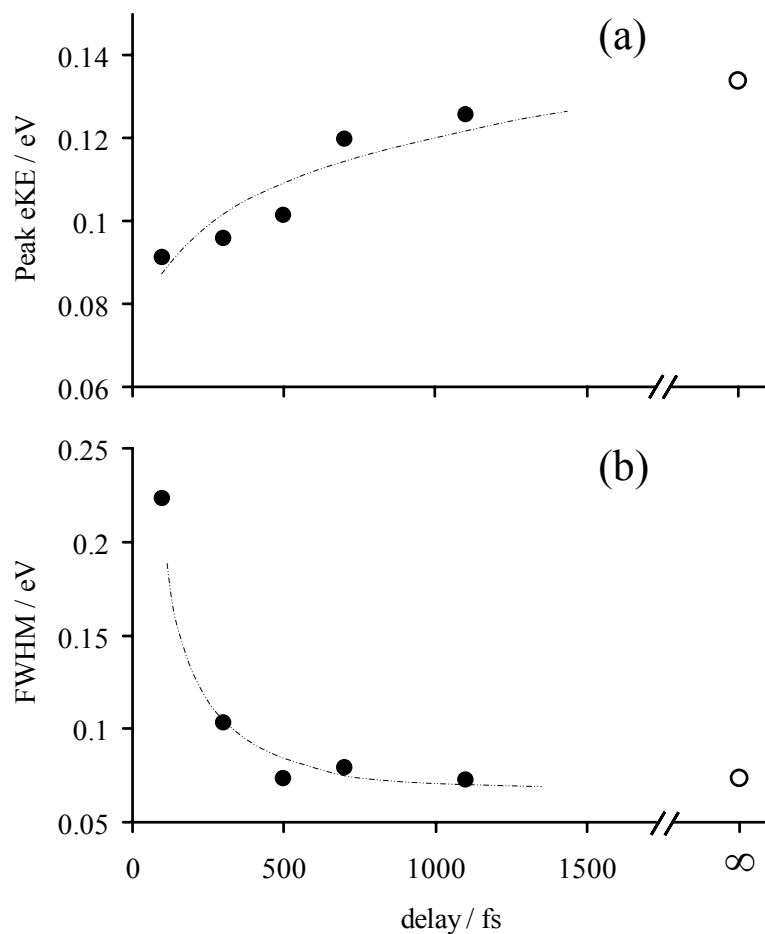


Figure 8.3 Evolution of the photoelectron band ascribed to the $\text{I}_2\text{Br}^- \rightarrow \Gamma$ channel (388 nm pump – 388 nm probe): (a) eKE corresponding to the transition maximum and (b) transition width (defined as FWHM) as functions of pump-probe delay. Filled symbols correspond to time-resolved data from I_2Br^- pump-probe measurements. Open symbols correspond to a one-photon measurement on isolated Γ , representing the $\text{I}_2\text{Br}^- \rightarrow \Gamma$ channel in the asymptotic limit of infinite delay. The peak positions and widths are determined by fitting the 0–0.2 eV band in the spectra in Fig. 8.2 with a gaussian function. The dashed trend lines, added merely to guide the eye, do not represent quantitative fits to the data.

The width evolution has two possible interpretations. First, one can postulate the excess electron localizes on the atomic fragment within the first 300 fs and the width is a reflection of the parent orbital shifting from a molecular orbital with homogeneous broadening to an atomic orbital. Second the width could be the result of inhomogeneous broadening due to the peak position drifting in time within the temporal profile of the pump-probe cross-correlation. These two interpretations are not necessarily exclusive of each other. However, the different timescales of the FWHM and peak-position evolution, revealed by comparing Figs. 8.3(a) and (b), favor the mechanism that relates the width of the photodetachment band to the evolving character of the parent orbital.

The evolution of the photodetached electron energy plotted in Fig. 8.3(a) indicates that interaction between the departing Γ^- and its counter-fragment(s) persists for ~ 1 ps, which is significantly longer than the time it takes to establish the atomic-anion character of the Γ^- fragment. The trend towards larger eKE with increasing pump-probe delay can be attributed to the gradually diminishing solvation of the Γ^- by the remaining neutral fragments. A different but equivalent view of this process is that the energetic shift is due to the evolving difference between the anion and neutral potentials along the reaction coordinate.

Therefore, the atomic-anion character is established within the first 300 fs, but the exit-channel interactions persist for up to ~ 1 ps. These time scales must be viewed in terms of the molecular level dynamics. In the case of I_3^- , Neumark and co-workers hypothesized that the Γ^- fragment is formed via a concerted three-body mechanism.^{181,202} Although the energetics of I_2Br^- are not so well known,^{199,200} the 388 nm pump should be

fairly close to the corresponding three-body channel threshold. If we assume, as a crude estimate, a ~ 0.1 eV kinetic-energy release to Γ^- , its exit-channel velocity will be ~ 4 Å/ps. If, on the other hand, the atomic anion is formed via the energetically lower $\Gamma^- + \text{IBr}$ channel,^{181,199,202} greater relative recoil velocities of the final fragments (in the ~ 10 Å/ps range) can be expected. These are asymptotic estimates; in dissociation on a repulsive potential, the fragment separation starts at a lower, accelerating rate. While the exact details are not known, within a direct dissociation mechanism in the above two energetic regimes the 300 fs timescale corresponds to a displacement of a few Angstroms away from the molecular-anion equilibrium. This is consistent with where the electronic identity of the fragments should have been defined.

The PADs are recovered from the time-resolved photoelectron images through integrating the signal intensity at each θ over the radial width of the image at half maximum of the peak height. The pump-probe PADs are described with the following equation:^{209,210}

$$I(\theta) \propto 1 + \beta_2 P_2(\cos \theta) + \beta_4 P_4(\cos \theta) \quad (8.1)$$

Where β_2 and β_4 are anisotropy parameters, and P_2 and P_4 are the second- and fourth-order Legendre polynomials, and θ is the angle between the laser polarization and the direction of the outgoing electron. The PADs from the photoelectron images in Fig. 8.2 are fitted with Eq. (1) using β_2 and β_4 as adjustable parameters. β_2 and β_4 at each pump-probe delay are plotted in Fig 8.4(a) and (b) respectively. The error bars are determined from the standard deviation of varying the sample widths for determining the anisotropy parameters, thus revealing the fluctuation within a data set. The uncertainties increase at

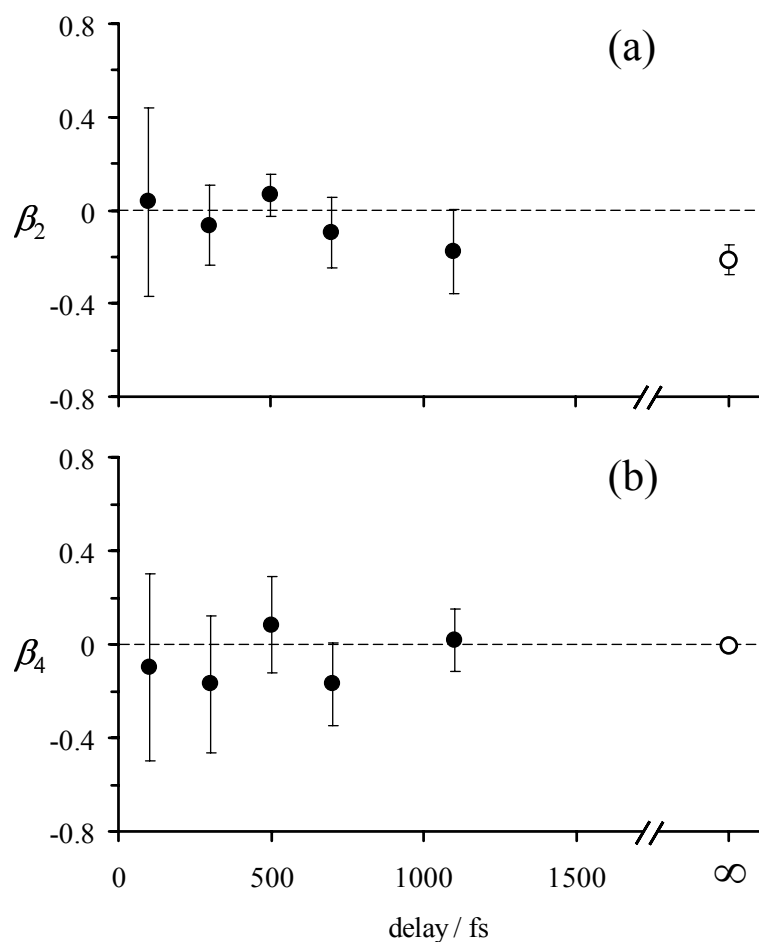


Figure 8.4 Evolution of the anisotropy parameters (a) β_2 and (b) β_4 as functions of pump-probe delay in I_2Br^- dissociation via the Γ^- channel (388 nm pump – 388 nm probe). Filled symbols correspond to time-resolved data; open symbols on the right represent one-photon (388 nm) detachment from isolated Γ^- , representing the $\text{I}_2\text{Br}^- \rightarrow \Gamma^-$ channel in the asymptotic limit of infinite delay. The anisotropy parameters were determined by fitting the 0–0.2 eV band in the photoelectron images shown in Fig. 8.2 using Eq. (1), as described in more detail in the text.

lower eKEs due to greater overlap of signal with center line noise caused by the inverse Abel transform.

Within our uncertainties β_4 does not stray from zero. Also of relevance is when β_4 is set to zero, β_2 does not change significantly and the quality of the fits with Eq. (1) does not decrease. This last observation is important because the last term in Eq. (1) arises from molecular-ensemble alignment in a two photon measurement. The first photon preferentially excites molecules whose dipole moment is aligned in the direction of the laser's polarization, thus preparing a partially aligned ensemble of excited intermediates that are probed by the second laser. The departing photofragments retain a memory of the parents' ensemble alignment producing a non-zero β_4 .^{209,210} However, in the case of the Γ^- channel, the asymptotic fragment is a closed-shell species. Its electronic wave function is spherically symmetric and therefore incapable of carrying memory of the parent ensemble alignment. Thus, the essentially zero values of β_4 in Fig. 8.4(b) are not unreasonable, at least at delays >300 fs, when the electronic identity of the Γ^- fragment has already been established.

The variation in β_2 with pump-probe delay shows that the image is isotropic up until 700 fs, see Fig. 8.4(a), whereupon β_2 increases in absolute magnitude toward the asymptotic value of -0.18 at 388 nm. The anisotropy parameter is known to be dependent upon energy. Hence, its variation in time could be a result of the changing energy of the detachment transition or the evolving nature of the Γ^- orbital being probed. To explore the roles of these factors, β_2 from time-resolved photodissociation of $\text{I}_2\text{Br} \rightarrow \Gamma^-$ are compared to one photon experimental values of β_2 for Γ^- . The comparison is shown in Fig. 8.5

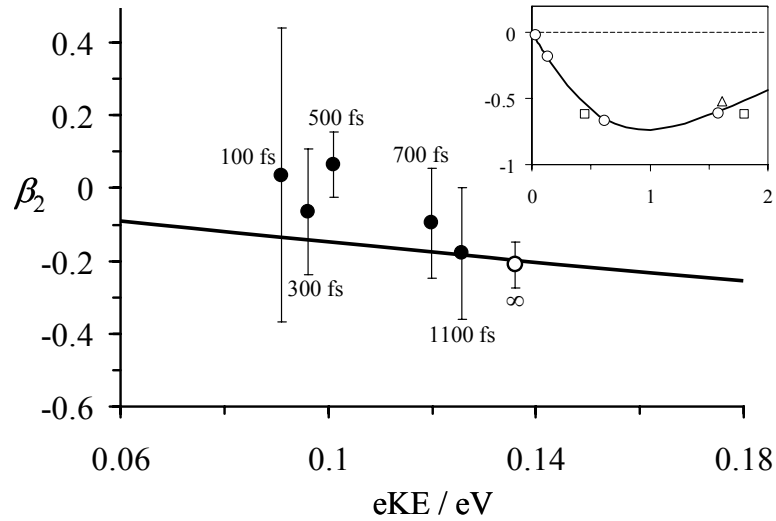


Figure 8.5 Comparison of the time-resolved β_2 values obtained in this work to the eKE-dependent values expected for one-photon detachment from I^- . In the main panel, filled symbols represent the time-resolved data with the corresponding pump-probe delays indicated next to the data points. The open circle corresponds to one-photon detachment from isolated I^- at 388 nm, representing the limit of infinite pump-probe delay in the I_2Br^- experiment. The solid line represents a fit to the one-photon data using the Hanstorp model,¹ as described in the text. The inset shows the one-photon detachment data for isolated I^- (symbols), for which the model parameters were optimized, and the fit curve (same as in the main panel) over a broad eKE-range. The open circles represent data obtained in this work. The open squares are from ref. 48 and the open triangle is from ref. 33.

where the solid line represents eKE-dependence of β_2 for I^- one photon photodetachment. This curve is obtained from fitting the available one photon data^{2,5} with an expression from Hanstorp et al.¹ that approximates the more precise Cooper and Zare treatment.^{11,37,119} The insert shows the fit over a broad energy range. The β_2 values from Fig 8.4(a) are shown in the main section of Fig 8.5 as symbols where they are plotted against the eKE peak position. Overall, the β_2 values obtained from this study, approach the β_2 obtained from photodetachment of I^- . However the uncertainties within our data especially at short delays do not allow us to draw conclusions. It is expected that further studies of the Br^- and I^- channels with increased photon energy will yield further insight into the evolution of the PAD within this reaction.

8.3 SUMMARY

Photodissociation of I_2Br^- yields photoelectron images that evolve to resemble photoelectron images of I^- within $\sim 1\text{ps}$. The 388 pump-probe photoelectron images reveal details of electronic structure transformation from the molecular anion to the atomic-anion fragment. A narrowing of the spectral profile occurs by 300 fs and the photoelectron energy increases toward the corresponding asymptotic limit by $\sim 1\text{ps}$ as the pump-probe delay is increased. The PAD also evolves, reflecting the formation of I^- . The shorter time scale reflects the localization of the electron upon the atomic fragment while the longer one denotes the persistent interaction among separating fragments, which will affect the energetics of photodetachment and the PAD. Hence, the photodissociation dynamics can be divided into two phases. The early stage involves the localization of the

wavefunction from a molecular orbital to an atomic orbital. It is during this phase that the electronic identity of the fragments is being defined. During the second stage long range interactions are influencing the wavefunctions of the exiting fragments which are reflected in the energetics and angular distributions of the photoelectron images.

9 FUTURE DIRECTIONS

In summary the Sanov group has developed a femtosecond negative-ion photoelectron imaging spectrometer. The photoelectron images serve as fingerprints of molecular orbitals through which we can trace not only the energy eigen values but also the symmetry of the wave functions as they evolve in time and upon solvation. After calibrating the spectrometer with images of atomic anions, we leaped into imaging molecular anions where we developed methods to qualitatively analyze photoelectron angular distribution. Building upon the molecular studies we imaged homogenous and heterogeneous cluster anions. After overcoming some obstacles we attained our first time resolved images. There are two directions to go: the first is in the cluster domain, and the second is in the time-resolved domain.

9.1 CLUSTERS

In the clusters experiments of the isovalent family of molecules OCS^- , CS_2^- and CO_2^- future work should include sequent hydration of $(\text{OCS})_n^-$ and $(\text{CS}_2)_n^-$ cluster anions with a careful study of the change in photoelectron angular distributions upon hydration. Does the anisotropy diminish as in CO_2 cluster anions? Also the study of pure water cluster anions would be interesting to contrast with the $[\text{CO}_2(\text{H}_2\text{O})_n]^-$. This would assist in the interpretation of the current $[\text{CO}_2(\text{H}_2\text{O})_n]^-$ cluster results allowing for the discernment of charge localization. Does the charge localize on the water molecules or is it shared between the carbon dioxide and water molecules? Time resolved experiments will assist with understanding the decrease of anisotropy in the $[\text{CO}_2(\text{H}_2\text{O})_n]^-$ clusters images. These would allow us to observe the charge transfer to solvent transition or other dynamics that

occur in these systems. A look at larger clusters, such as $N > 13$ in the $(\text{CO}_2)_n^-$ series, would allow for the characterization of core switching in the $(\text{CO}_2)_n^-$ series at 14 where the core shifts from a monomer back to the dimer core. Core switching is thought to be a mechanism for faster-than-diffusion hopping of negative charge dynamics in liquid and supercritical CO_2 .²¹¹ Applying higher photon energy to the $[\text{CO}_2(\text{H}_2\text{O})_n]^-$ series would be extremely useful in tracking down the vertical detachment energies. Plus the possibility of more hydrated clusters can be studied at higher photon energies.

It would be interesting to explore other cluster species that are relevant in atmospheric processes with an attempt to understand green house gases and ozone depletions. Another area of interesting clusters would be metal cluster with the focus of the switching point between molecular and bulk properties.

In addition to looking at different cluster species the instrument needs further development. Installation of a higher repetition rate nozzle would increase the signal to noise ratio in the images allowing for shorter collection times and better image quality. Currently the repetition rate of the nozzle is 70 *Hz* and the laser repetition is 1000 *Hz*. In other words 90% of our laser pulses are not doing anything but as we increase repetition rate of the pulsed nozzle we must ensure that the vacuum pumps are not overloaded. A piezoelectric pulsed nozzle can extend our repetition rate up to 500 *Hz*. Another improvement would be the addition of a secondary mass spectrometry to identify the photofragments. This capability will increase the information we attain about a system's dynamics by allowing us to detect the ion fragments of the photodissociation reactions. In cases where two anions have similar electron affinities but different masses this will

assist in identification of the photodissociation products. A similar approach would be coincidence imaging where both the fragments and the photoelectrons are imaged. Here additional information in regards to the energetics of the photofragment is also obtained and can be correlated to the photoelectronic signal.

9.2 TIME RESOLVED EXPERIMENTS

Currently we are studying the photodissociation of I_2^- and IBr^- with 390 nm pump and 390 nm probe. We have also studied them at 790 nm pump and 390 nm probe. In essence, we have imaged the potential surface on which the photodissociation is occurring. In particular, the dynamic nature of the photoelectron angular distribution has been quite striking. It takes longer for the images resulting from photodissociation of I_2^- to resemble I^- than the fragments of IBr^- due to symmetry constraints. Currently we are extending the delay between the pump and probe in I_2^- photodissociation to better characterize this behavior of delocalization of wave function at greater time intervals. Future experiments of photodissociation of other homo and heteronuclear dihalides e.g. Cl_2^- , Br_2^- , BrCl^- , etc would assist in characterizing this behavior.

The next logical step after diatomics would be triatomics and larger molecules that are chemically interesting. Combustion processes and atmospheric reactions would be sources for interesting molecules to study with photoelectron imaging; some of these would include HONO^- , NO^- , NO_2^- . Once we characterize these molecules then we should try to simulate them in condensed phase environments. Hence the next step would be time-resolved photoelectron imaging of solvated cluster anions. Studying these systems from an electronic perspective, allows for a deeper understanding of chemical reactivity

and bonding allowing for test of theory. Time-resolved cluster anion photoelectron imaging bridges the gap between gas phase and condensed phase environments.

10 REFERENCES

- (1) Hanstorp, D.; Bengtsson, C.; Larson, D. J. *Phys. Rev. A* **1989**, *40*, 670-675.
- (2) Davis, A. V.; Wester, R.; Bragg, A. E.; Neumark, D. M. *J. Chem. Phys.* **2003**, *118*, 999-1002.
- (3) Saeki, M.; Tsukuda, T.; Iwata, S.; Nagata, T. *J. Chem. Phys.* **1999**, *111*, 6333-6344.
- (4) Lahaye, J. G.; Vandenhoute, R.; Fayt, A. *J. Mol. Spectrosc.* **1987**, *123*, 48-83.
- (5) Gilles, M. K.; Ervin, K. M.; Ho, J.; Lineberger, W. C. *J. Phys. Chem.* **1992**, *96*, 1130-1141.
- (6) Gutsev, G. L.; Bartlett, R. J.; Compton, R. N. *J. Chem. Phys.* **1998**, *108*, 6756-6762.
- (7) Martin, W. C.; Musgrove, A.; Kotochigova, S.; Sansonetti, J. E.; Vol. 2004.
- (8) Martin, W. C.; Zalubas, R.; Musgrove, A. *Journal of Physical and Chemical Reference Data* **1990**, *19*, 821-880.
- (9) Ervin, K. M.; Lineberger, W. C. In *Advances in Gas Phase Ion Chemistry*; Adams, N. G., Babcock, L. M., Eds.; JAI Press: Greenwich, 1992; Vol. 1, p 121.
- (10) Chandler, D. W.; Houston, P. L. *J. Chem. Phys.* **1987**, *87*, 1445-1447.
- (11) Cooper, J.; Zare, R. N. *J. Chem. Phys.* **1968**, *49*, 4252.
- (12) Reed, K. J.; Zimmerman, A. H.; Andersen, H. C.; Brauman, J. I. *J. Chem. Phys.* **1976**, *64*, 1368-1375.
- (13) Suzuki, T.; Wang, L.; Kohguchi, H. *J. Chem. Phys.* **1999**, *111*, 4859-4861.

- (14) Davies, J. A.; LeClaire, J. E.; Continetti, R. E.; Hayden, C. C. *J. Chem. Phys.* **1999**, *111*, 1-4.
- (15) Davies, J. A.; Continetti, R. E.; Chandler, D. W.; Hayden, C. C. *Phys. Rev. Lett.* **2000**, *84*, 5983-5986.
- (16) Heck, A. J. R.; Chandler, D. W. *Ann. Rev. Phys. Chem.* **1995**, *46*, 335-372.
- (17) Houston, P. L. *Accts. Chem. Res.* **1995**, *28*, 453-460.
- (18) Zyrianov, M.; Droz-Georget, T.; Reisler, H. *J. Chem. Phys.* **1999**, *110*, 2059-2068.
- (19) Ahmed, M.; Blunt, D.; Chen, D.; Suits, A. G. *J. Chem. Phys.* **1997**, *106*, 7617-7624.
- (20) Parker, D. H.; Eppink, A. T. J. B. *J. Chem. Phys.* **1997**, *107*, 2357-2362.
- (21) Baguenard, B.; Pinare, J. C.; Lepine, F.; Bordas, C.; Broyer, M. *Chem. Phys. Lett.* **2002**, *352*, 147-153.
- (22) Baguenard, B.; Pinare, J. C.; Bordas, C.; Broyer, M. *Phys. Rev. A* **2001**, *63*, 023204.
- (23) Bragg, A. E.; Wester, R.; Davis, A. V.; Kammrath, A.; Neumark, D. M. *Chem. Phys. Lett.* **2003**, *376*, 767-775.
- (24) Bragg, A. E.; Verlet, J. R. R.; Kammrath, A.; Neumark, D. M. *J. Chem. Phys.* **2004**, *121*, 3515-3526.
- (25) Neumark, D. M. *Ann. Rev. Phys. Chem.* **2001**, *52*, 255-277.
- (26) Surber, E.; Sanov, A. *J. Chem. Phys.* **2002**, *116*, 5921-5924.
- (27) Surber, E.; Mabbs, R.; Sanov, A. *J. Phys. Chem. A* **2003**, *107*, 8215-8224.

- (28) Surber, E.; Ananthavel, S. P.; Sanov, A. *J. Chem. Phys.* **2002**, *116*, 1920-1929.
- (29) Surber, E.; Sanov, A. *J. Chem. Phys.* **2003**, *118*, 9192-9200.
- (30) Mabbs, R.; Surber, E.; Velarde, L.; Sanov, A. *J. Chem. Phys.* **2004**, *120*, 5148-5154.
- (31) Mabbs, R.; Surber, E.; Sanov, A. *Chem. Phys. Lett.* **2003**, *381*, 479-485.
- (32) Mabbs, R.; Pichugin, K.; Surber, E.; Sanov, A. *J. Chem. Phys.* **2004**, *121*, 265-272.
- (33) Johnson, M. A.; Lineberger, W. C. In *Techniques for the Study of Ion Molecule Reactions*; Farrar, J. M., Saunders, W. H., Eds.; Wiley: New York, 1988, pp 591-635.
- (34) Wiley, W. C.; McLaren, I. H. *Rev. Sci. Instr.* **1955**, *26*, 1150.
- (35) Posey, L. A.; Deluca, M. J.; Johnson, M. A. *Chem. Phys. Lett.* **1986**, *131*, 170-174.
- (36) Dribinski, V.; Ossadtchi, A.; Mandelshtam, V. A.; Reisler, H. *Rev. Sci. Instr.* **2002**, *73*, 2634-2642.
- (37) Cooper, J.; Zare, R. N. *J. Chem. Phys.* **1968**, *48*, 942-943.
- (38) Wigner, E. P. *Phys. Rev.* **1948**, *73*, 1002-1009.
- (39) Hotop, H.; Lineberger, W. C. *J. phys. chem. Ref. Data* **1985**, *14*, 731.
- (40) *CRC Handbook of Chemistry and Physics*; 81 ed.; CRC Press: Boca Raton, Florida, 2000.
- (41) *CRC Handbook of Chemistry and Physics*; 84 ed.; CRC Press: Boca Raton, Florida, 2004.
- (42) Moran, S.; Ellison, G. B. *J. Phys. Chem* **1988**, *92*, 1794-1803.

- (43) Tsukuda, T.; Hirose, T.; Nagata, T. *Chem. Phys. Lett.* **1997**, 279, 179-184.
- (44) Swope, W. C.; Lee, Y.-P.; Schaefer, H. F., III *J. Chem. Phys.* **1979**, 70, 947-953.
- (45) Number 69 (July 2001 Release) ed.
- (46) Celotta, R. J.; Bennett, R. A.; Levine, J.; Hall, J. L.; Siegel, M. W. *Phys. Rev. A* **1972**, 6, 631-642.
- (47) Burch, D. S.; Smith, S. J.; Branscomb, L. M. *Phys. Rev.* **1958**, 112, 171-175.
- (48) Lin, P.; Lucchese, R. R. *J. Chem. Phys.* **2001**, 114, 9350-9360.
- (49) Sherwood, C. R.; Garner, M. C.; Hanold, K. A.; Strong, K. M.; Continetti, R. E. *J. Chem. Phys.* **1995**, 102, 6949-6952.
- (50) Ervin, K. M.; Anusiewicz, W.; Skurski, P.; Simons, J.; Lineberger, W. C. *J. Phys. Chem. A* **2003**, 107, 8521-8529.
- (51) Oakes, J. M.; Ellison, G. B. *Tetrahedron* **1986**, 42, 6263-6267.
- (52) Suzuki, I. *Bull. Chem. Soc. Jpn.* **1975**, 48, 1685-1690.
- (53) Castleman, A. W.; Bowen, K. H. *J. Phys. Chem.* **1996**, 100, 12911-12944.
- (54) Maeyama, T.; Oikawa, T.; Tsumura, T.; Mikami, N. *J. Chem. Phys.* **1998**, 108, 1368-1376.
- (55) DeLuca, M. J.; Niu, B.; Johnson, M. A. *J. Chem. Phys.* **1988**, 88, 5857-5863.
- (56) Tsukuda, T.; Johnson, M. A.; Nagata, T. *Chem. Phys. Lett.* **1997**, 268, 429-433.
- (57) Bowen, K. H.; Eaton, J. G. In *The Structure of Small Molecules and Ions*; Naaman, R., Vager, Z., Eds.; Plenum: New York, 1988, pp 147-169.
- (58) Hiraoka, K.; Fujimaki, S.; Aruga, G.; Yamabe, S. *J. Phys. Chem.* **1994**, 98, 1802-1809.

- (59) Fleischman, S. H.; Jordan, K. D. *J. Phys. Chem.* **1987**, *91*, 1300-1302.
- (60) Sanov, A.; Nandi, S.; Jordan, K. D.; Lineberger, W. C. *J. Chem. Phys.* **1998**, *109*, 1264-1270.
- (61) Alexander, M. L.; Johnson, M. A.; Levinger, N. E.; Lineberger, W. C. *Phys. Rev. Lett.* **1986**, *57*, 976-979.
- (62) Alexander, M. L. In *Department of Chemistry*; University of Colorado: Boulder, 1987, p 170.
- (63) Klots, C. E.; Compton, R. N. *J. Chem. Phys.* **1977**, *67*, 1779-1780.
- (64) Klots, C. E.; Compton, R. N. *J. Chem. Phys.* **1978**, *69*, 1636.
- (65) Knapp, M.; Kreisle, D.; Echt, O.; Sattler, K.; Recknagel, E. *Surf. Sci.* **1985**, *156*, 313.
- (66) Knapp, M.; Echt, O.; Kreisle, D.; Mark, T. D.; Recknagel, E. *Chem. Phys. Lett.* **1986**, *126*, 225.
- (67) Stamatovic, A.; Leiter, K.; Ritter, W.; Stephan, K.; Mark, T. D. *J. Chem. Phys.* **1985**, *83*, 2942.
- (68) Langosh, H.; Haberland, H. *Z. Physik D* **1986**, *2*, 243.
- (69) Kondow, T.; Mitsuke, K. *J. Chem. Phys.* **1985**, *83*, 2612-2613.
- (70) Kondow, T. *J. Phys. Chem.* **1987**, *91*, 1307.
- (71) Misaizu, F.; Mitsuke, K.; Kondow, T.; Kuchitsu, K. *J. Chem. Phys.* **1991**, *94*, 243-249.
- (72) Kraft, T.; Ruf, M. W.; Hotop, H. *Z. Phys. D* **1989**, *14*, 179.

(73) Compton, R. N.; Reinhardt, P. W.; Cooper, C. D. *J. Chem. Phys.* **1975**, *63*, 3821.

(74) Frisch, M. J.; Trucks, G. W.; Schlegel, H. B.; Scuseria, G. E.; Robb, M. A.; Cheeseman, J. R.; Zakrzewski, V. G.; Montgomery, J. A.; Stratmann, R. E.; Burant, J. C.; Dapprich, S.; Millam, J. M.; Daniels, A. D.; Kudin, K. N.; Strain, M. C.; Farkas, O.; Tomasi, J.; Barone, V.; Cossi, M.; Cammi, R.; Mennucci, B.; Pomelli, C.; Adamo, C.; Clifford, S.; Ochterski, J.; Petersson, G. A.; Ayala, P. Y.; Cui, Q.; Morokuma, K.; Malick, D. K.; Rabuck, A. D.; Raghavachari, K.; Foresman, J. B.; Cioslowski, J.; Ortiz, J. V.; Stefanov, B. B.; Liu, G.; Liashenko, A.; Piskorz, P.; Komaromi, I.; Gomperts, R.; Martin, R. L.; Fox, D. J.; Keith, T.; Al-Laham, M. A.; Peng, C. Y.; Nanayakkara, A.; Gonzalez, C.; Challacombe, M.; Gill, P. M. W.; Johnson, B. G.; Chen, W.; Wong, M. W.; Andres, J. L.; Head-Gordon, M.; Replogle, E. S.; Pople, J. A.; Rev. A.7 ed.; Gaussian, Inc.: Pittsburgh, PA, 1998.

(75) Curtiss, L. A.; Redfern, P. C.; Raghavachari, K.; Pople, J. A. *J. Chem. Phys.* **1998**, *109*, 42-55.

(76) Møller, C.; Plesset, M. S. *Phys. Rev.* **1934**, *46*, 618.

(77) Pople, J. A.; Seeger, R.; Krishnan, R. *Int. J. Quantum Chem. Symp.* **1977**, *11*, 149.

(78) Pople, J. A.; Headgordon, M.; Raghavachari, K. *J. Chem. Phys.* **1987**, *87*, 5968-5975.

(79) Bartlett, R. J. In *Annu. Rev. Phys. Chem.*; Rabinovitch, B. S., Schurr, J. M., Strauss, H. L., Eds.; Annual Reviews, Inc.: Palo Alto, CA, 1981; Vol. 32, pp 359-402.

- (80) Pople, J. A.; Binkley, J. S.; Seeger, R. *Int. J. Quantum Chem.* **1976**, 1-19.
- (81) Purvis, G. D.; Bartlett, R. J. *J. Chem. Phys.* **1982**, 76, 1910-1918.
- (82) Scuseria, G. E.; Schaefer, H. F. *J. Chem. Phys.* **1989**, 90, 3700-3703.
- (83) Scuseria, G. E.; Janssen, C. L.; Schaefer, H. F. *J. Chem. Phys.* **1988**, 89, 7382-7387.
- (84) Curtis, R. A.; Farrar, J. M. *J. Chem. Phys.* **1989**, 90, 862-870.
- (85) Curtiss, L. A.; Raghavachari, K.; Redfern, P. C.; Rassolov, V.; Pople, J. A. *J. Chem. Phys.* **1998**, 109, 7764-7776.
- (86) Curtiss, L. A.; Raghavachari, K.; Trucks, G. W.; Pople, J. A. *J. Chem. Phys.* **1991**, 94, 7221-7230.
- (87) Curtiss, L. A.; Raghavachari, K.; Redfern, P. C.; Pople, J. A. *J. Chem. Phys.* **1997**, 106, 1063-1079.
- (88) Curtiss, L. A.; Raghavachari, K.; Redfern, P. C.; Pople, J. A. *J. Chem. Phys.* **2000**, 112, 7374-7383.
- (89) Tschumper, G. S.; Schaefer, H. F. *J. Chem. Phys.* **1997**, 107, 2529-2541.
- (90) Becke, A. D. *Phys. Rev. A* **1988**, 38, 3098-3100.
- (91) Becke, A. D. *J. Chem. Phys.* **1993**, 98, 5648-5652.
- (92) Lee, S.; Hynes, J. T. *J. Chem. Phys.* **1988**, 88, 6863-6869.
- (93) Adamo, C.; Barone, V. *J. Chem. Phys.* **1998**, 108, 664-675.
- (94) Schlegel, H. B. *J Comput Chem* **1982**, 3, 214-218.
- (95) Csaszar, P.; Pulay, P. *J Mol Struct* **1984**, 114, 31-34.

- (96) Haberland, H.; Ludewigt, C.; Schindler, H. G.; Worsnop, D. R. *J. Chem. Phys.* **1984**, *81*, 3742-3744.
- (97) Haberland, H.; Schindler, H. G.; Worsnop, D. R. *Berichte Der Bunsen-Gesellschaft-Physical Chemistry Chemical Physics* **1984**, *88*, 270-272.
- (98) Armbruster, M.; Haberland, H.; Schindler, H. G. *Phys. Rev. Lett.* **1981**, *47*, 323-326.
- (99) Bailey, C. G.; Kim, J.; Johnson, M. A. *J. Phys. Chem.* **1996**, *100*, 16782-16785.
- (100) Ayotte, P.; Weddle, G. H.; Bailey, C. G.; Johnson, M. A.; Vila, F.; Jordan, K. D. *J. Chem. Phys.* **1999**, *110*, 6268-6277.
- (101) Kim, J.; Becker, I.; Cheshnovsky, O.; Johnson, M. A. *Chem. Phys. Lett.* **1998**, *297*, 90-96.
- (102) Lee, G. H.; Arnold, S. T.; Eaton, J. G.; Sarkas, H. W.; Bowen, K. H.; Ludewigt, C.; Haberland, H. *Zeitschrift Fur Physik D-Atoms Molecules and Clusters* **1991**, *20*, 9-12.
- (103) Posey, L. A.; Deluca, M. J.; Campagnola, P. J.; Johnson, M. A. *J. Phys. Chem.* **1989**, *93*, 1178-1181.
- (104) Coe, J. V.; Lee, G. H.; Eaton, J. G.; Arnold, S. T.; Sarkas, H. W.; Bowen, K. H.; Ludewigt, C.; Haberland, H.; Worsnop, D. R. *J. Chem. Phys.* **1990**, *92*, 3980-3982.
- (105) Tsukuda, T.; Saeiki, M.; Kimura, R.; Nagata, T. *J. Chem. Phys.* **1999**, *110*, 7846-7857.
- (106) Nagata, T.; Yoshida, H.; Kondow, T. *Chem. Phys. Lett.* **1992**, *199*, 205-210.

- (107) Nagata, T.; Yoshida, H.; Kondow, T. *Z. Phys. D* **1993**, *26*, 367-369.
- (108) Klots, C. E. *J. Chem. Phys.* **1979**, *71*, 4172-4172.
- (109) Keesee, R. G.; Castleman, A. W. *Journal of Physical and Chemical Reference Data* **1986**, *15*, 1011-1071.
- (110) Castleman, A. W.; Keesee, R. G. *Ann. Rev. Phys. Chem.* **1986**, *37*, 525-550.
- (111) Jortner, J.; Even, U.; Goldberg, A.; Schek, I.; Raz, T.; Levine, R. D. *Surf. Rev. Lett.* **1996**, *3*, 263-280.
- (112) Andersen, J. U.; Bonderup, E.; Hansen, K. *J. Phys. B* **2002**, *35*, R1-R30.
- (113) Wurz, P.; Lykke, K. R. *J. Phys. Chem.* **1992**, *96*, 10129-10139.
- (114) Zhao, Y. X.; Debeer, E.; Xu, C. S.; Taylor, T.; Neumark, D. M. *J. Chem. Phys.* **1996**, *105*, 4905-4919.
- (115) Surber, E.; Sanov, A. *Phys. Rev. Lett.* **2003**, *90*, 093001.
- (116) Klots, C. E. *J. Chem. Phys.* **1994**, *100*, 1035-1039.
- (117) Andersen, J. U.; Bonderup, E.; Hansen, K. *J. Chem. Phys.* **2001**, *114*, 6518-6525.
- (118) Nandi, S.; Sanov, A.; Delaney, N.; Faeder, J.; Parson, R.; Lineberger, W. C. *J. Phys. Chem. A* **1998**, *102*, 8827-8835.
- (119) Cooper, J.; Zare, R. N. In *Atomic collision processes*; Geltman, S., Mahanthappa, K. T., Brittin, W. E., Eds.; Gordon and Breach, Science Publishers: New York, London, Paris, 1968; Vol. XI-C, pp 317-337.
- (120) Kowal, M.; Gora, R. W.; Roszak, S.; Leszczynski, J. *J. Chem. Phys.* **2001**, *115*, 9260-9265.

- (121) Baessmann, C.; Boesl, U.; Yang, D.; Drechsler, G.; Schlag, E. W. *Int. J. Mass Spect. Ion Proc.* **1996**, *159*, 153-167.
- (122) Lehr, L.; Zanni, M. T.; Frischkorn, C.; Weinkauff, R.; Neumark, D. M. *Science* **1999**, *284*, 635.
- (123) Serxner, D.; Dessent, C. E. H.; Johnson, M. A. *J. Chem. Phys.* **1996**, *105*, 7231-7234.
- (124) Kelley, J. A.; Weber, J. M.; Lisle, K. M.; Robertson, W. H.; Ayotte, P.; Johnson, M. A. *Chem. Phys. Lett.* **2000**, *327*, 1-6.
- (125) Markovich, G.; Pollack, S.; Giniger, R.; Cheshnovsky, O. *J. Chem. Phys.* **1994**, *101*, 9344-9353.
- (126) Bailey, C. G.; Kim, J.; Dessent, C. E. H.; Johnson, M. A. *Chem. Phys. Lett.* **1997**, *269*, 122-127.
- (127) Bassmann, C.; Boesl, U.; Yang, D.; Drechsler, G.; Schlag, E. W. *Int. J. Mass Spectrometry and Ion Processes* **1996**, *159*, 153-167.
- (128) Ayotte, P.; Bailey, C. G.; Weddle, G.; Johnson, M. A. *J. Phys. Chem. A* **1998**, *102*, 3067-3071.
- (129) Hiraoka, K.; Mizuse, S.; Yamabe, S. *J. Phys. Chem.* **1988**, *92*, 3943-3952.
- (130) Jortner, J.; Ottolenghi, M.; Stein, G. *J. Phys. Chem.* **1964**, *68*, 247-&.
- (131) Corcelli, S. A.; Kelley, J. A.; Tully, J. C.; Johnson, M. A. *J. Phys. Chem. A* **2002**, *106*, 4872-4879.
- (132) Kim, J.; Lee, H. M.; Suh, S. B.; Majumdar, D.; Kim, K. S. *J. Chem. Phys.* **2000**, *113*, 5259-5272.

- (133) Cabarcos, O. M.; Weinheimer, C. J.; Lisy, J. M. *J. Chem. Phys.* **1999**, *110*, 5-8.
- (134) Cabarcos, O. M.; Lisy, J. M. *Chem. Phys. Lett.* **1996**, *257*, 265-272.
- (135) Xantheas, S. S. *J. Phys. Chem.* **1996**, *100*, 9703-9713.
- (136) Zhao, X. G.; Gonzalez-Lafont, A.; Truhlar, D. G.; Steckler, R. *J. Chem. Phys.* **1991**, *94*, 5544-5558.
- (137) Johnson, M. S.; Kuwata, K. T.; Wong, C.-K.; Okumura, M. *Chem. Phys. Lett.* **1996**, *260*, 551-557.
- (138) Choi, J.-H.; Kuwata, K. T.; Cao, Y.-B.; Okumura, M. *J. Phys. Chem. A* **1998**, *102*.
- (139) Vila, F. D.; Jordan, K. D. *J. Phys. Chem. A* **2002**, *106*, 1391-1397.
- (140) Chen, H. Y. S.; W.S. *J. Am. Chem. Soc.* **2000**, *122*, 7534-7542.
- (141) Lee, H. M.; Suh, S. B.; Kim, K. S. *J. Chem. Phys.* **2003**, *119*, 7685-7692.
- (142) Irle, S.; Bowman, J. M. *J. Chem. Phys.* **2000**, *113*, 8401-8403.
- (143) Dorsett, H. E.; Watts, R. O.; Xantheas, S. S. *J. Phys. Chem. A* **1999**, *103*, 3351-3355.
- (144) Zhan, C.-G.; Dixon, D. A. *J. Phys. Chem. A* **2004**, *108*, 2020-2029.
- (145) Zhan, C.-G.; Iwata, S. *Chem. Phys. Lett.* **1995**, *232*, 72-78.
- (146) Arshadi, M. Y., R.; Kebarle, Paul *J. Phys. Chem.* **1970**, *74*, 1475-1482.
- (147) Davis, A. V. Z., M. T.; Frischkorn, C.; Neumark, D. M. *J. Electron Spectrosc. Relat. Phenom.* **2000**, *108*, 203-211.

- (148) Ayotte, P.; Weddle, G. H.; Johnson, M. A. *J. Chem. Phys.* **1999**, *110*, 7129-7132.
- (149) Ayotte, P.; Weddle, G. H.; Kim, J.; Johnson, M. A. *J. Am. Chem. Soc.* **1998**, *120*, 12361-12362.
- (150) Combariza, J. E.; Kestner, N. R.; Jortner, J. *J. Chem. Phys.* **1994**, *100*, 2851-2864.
- (151) Weber, J. M.; Kelley, J. A.; Robertson, W. H.; Johnson, M. A. *J. Chem. Phys.* **2001**, *114*, 2698-2706.
- (152) Weber, J. M.; Kelley, J. A.; Nielsen, S. B.; Ayotte, P.; Johnson, M. A. *Science* **2000**, *287*, 2461-2463.
- (153) Seta, T.; Yamamoto, M.; Nishioka, M.; Sadakata, M. *J. Phys. Chem. A* **2003**, *107*, 962-967.
- (154) Robinson, E. M. C.; Holstein, W. L.; Stewart, G. M.; Buntine, M. A. *Phys. Chem. Chem. Phys.* **1999**, *1*, 3961-3966.
- (155) Lee, H. M.; Kim, K. S. *Mol. Phys.* **2002**, *100*, 875-879.
- (156) Robertson, W. H.; Diken, E. G.; Price, E.; Shin, J.-W.; Johnson, M. A. *Science* **2003**, *299*, 1367-1372.
- (157) Myshakin, E. M.; Jordan, K. D.; Robertson, W. H.; Weddle, G. H.; Johnson, M. A. *J. Chem. Phys.* **2003**, *118*, 1735-1746.
- (158) Robertson, W. H.; Price, E.; Weber, J. M.; Shin, J.-W.; Weddle, G. M.; Johnson, M. A. *J. Phys. Chem. A* **2003**, *107*, 6527-6532.

- (159) Cooper, C. D.; Compton, R. N. *Chemistry and Physics of Lipids* **1972**, *14*, 29-&.
- (160) Cooper, C. D.; Compton, R. N. *J. Chem. Phys.* **1973**, *59*, 3550-3565.
- (161) Sanov, A.; Lineberger, W. C.; Jordan, K. D. *J. Phys. Chem. A* **1998**, *102*, 2509-2511.
- (162) Zare, R. N. *Mol. Photochem.* **1972**, *4*, 1.
- (163) Surber, E.; Mabbs, R.; Sanov, A. *J. Phys. Chem. A* **2003**, *107*, 8215-8224.
- (164) Bentley, J.; Collins, J. Y.; Chipman, D. M. *Journal of Physical Chemistry A* **2000**, *104*, 4629-4635.
- (165) Ayotte, P.; Weddle, G. H.; Kim, J.; Kelley, J.; Johnson, M. A. *Journal of Physical Chemistry A* **1999**, *103*, 443-447.
- (166) Chen, H. Y.; Sheu, W. S. *J. Chem. Phys.* **2001**, *115*, 10678-10684.
- (167) Kulkarni, S. A.; Bartolott, L. J.; Pathak, R. K. *J. Chem. Phys.* **2000**, *113*, 2697-2700.
- (168) Kim, J.; Kim, K. S. *J. Chem. Phys.* **1998**, *109*, 5886-5895.
- (169) Banin, U.; Waldman, A.; Ruhman, S. *J. Chem. Phys.* **1992**, *96*, 2416-2419.
- (170) Banin, U.; Kosloff, R.; Ruhman, S. *Isr. J. Chem.* **1993**, *33*, 141-156.
- (171) Banin, U.; Ruhman, S. *J. Chem. Phys.* **1993**, *98*, 4391-4403.
- (172) Benjamin, I.; Banin, U.; Ruhman, S. *J. Chem. Phys.* **1993**, *98*, 8337-8340.
- (173) Banin, U.; Bartana, A.; Ruhman, S.; Kosloff, R. *J. Chem. Phys.* **1994**, *101*, 8461-8481.

- (174) Banin, U.; Kosloff, R.; Ruhman, S. *Springer Series in Chemical Physics (Ultrafast Processes)* **1994**, *IX*, 68-69.
- (175) Gershgoren, E.; Gordon, E.; Ruhman, S. *J. Chem. Phys.* **1997**, *106*, 4806-4809.
- (176) Gershgoren, E.; Banin, U.; Ruhman, S. *J. Phys. Chem. A* **1998**, *102*, 9-16.
- (177) Kühne, T.; Vöhringer, P. *Springer Series in Chemical Physics (Ultrafast Processes)* **1996**, *X*, 249-250.
- (178) Kühne, T.; Vöhringer, P. *J. Phys. Chem. A* **1998**, *102*, 4177-4185.
- (179) Kühne, T.; Kuster, R.; Vöhringer, P. *Chem. Phys.* **1998**, *233*, 161-178.
- (180) Zanni, M. T.; Greenblatt, B. J.; Davis, A. V.; Neumark, D. M. *Proc. SPIE* **1998**, *3271*, 196-207.
- (181) Zanni, M. T.; Greenblatt, B. J.; Davis, A. V.; Neumark, D. M. *J. Chem. Phys.* **1999**, *111*, 2991-3003.
- (182) Dantus, M.; Bowman, R. M.; Baskin, J. S.; Zewail, A. H. *Chem. Phys. Lett.* **1989**, *159*, 406-412.
- (183) Dantus, M.; Bowman, R. M.; Gruebele, M.; Zewail, A. H. *J. Chem. Phys.* **1989**, *91*, 7437-7450.
- (184) Bowman, R. M.; Dantus, M.; Zewail, A. H. *Chem. Phys. Lett.* **1989**, *156*, 131-137.
- (185) Pedersen, S.; Baumert, T.; Zewail, A. H. *J. Phys. Chem.* **1993**, *97*, 12460-12465.

- (186) Pugliano, N.; Palit, D. K.; Szarka, A. Z.; Hochstrasser, R. M. *J. Chem. Phys.* **1993**, *99*, 7273-7276.
- (187) Pugliano, N.; Szarka, A. Z.; Gnanakaran, S.; Triechel, M.; Hochstrasser, R. M. *J. Chem. Phys.* **1995**, *103*, 6498-6511.
- (188) Pugliano, N.; Szarka, A. Z.; Hochstrasser, R. M. *J. Chem. Phys.* **1996**, *104*, 5062-5079.
- (189) Gnanakaran, S.; Lim, M.; Pugliano, N.; Volk, M.; Hochstrasser, R. M. *Journal of Physics-Condensed Matter* **1996**, *8*, 9201-9220.
- (190) Ashkenazi, G.; Banin, U.; Bartana, A.; Kosloff, R.; Ruhman, S. *Adv. Chem. Phys.* **1997**, *100*, 229-315.
- (191) Bartana, A.; Banin, U.; Ruhman, S.; Kosloff, R. *Chem. Phys. Lett.* **1994**, *229*, 211-217.
- (192) Benjamin, I. *J. Chem. Phys.* **1995**, *103*, 2459-2471.
- (193) Benjamin, I.; Barbara, P. F.; Gertner, B. J.; Hynes, J. T. *J. Phys. Chem.* **1995**, *99*, 7557-7567.
- (194) Lynden-Bell, R. M.; Kosloff, R.; Ruhman, S.; Danovich, D.; Vala, J. *J. Chem. Phys.* **1998**, *109*, 9928-9937.
- (195) Sato, H.; Hirata, F.; Myers, A. B. *J. Phys. Chem. A* **1998**, *102*, 2065-2071.
- (196) Zanni, M. T.; Batista, V. S.; Greenblatt, B. J.; Miller, W. H.; Neumark, D. M. *J. Chem. Phys.* **1999**, *110*, 3748.
- (197) Choi, H.; Bise, R. T.; Hoops, A. A.; Neumark, D. M. **1999**, in preparation.
- (198) Maki, A. G.; Forneris, R. *Spectrochimica Acta A* **1967**, *23*, 867-880.

- (199) Sanov, A.; Sanford, T.; Butler, L. J.; Vala, J.; Kosloff, R.; Lineberger, W. *C. J. Phys. Chem. A* **1999**, *103*, 10244-10254.
- (200) Ogawa, Y.; Takahashi, O.; Kikuchi, O. *J. Mol. Struct. (Theochem)* **1998**, *429*, 187-196.
- (201) Ogawa, Y.; Takahashi, O.; Kikuchi, O. *J. Mol. Struct. (Theochem)* **1998**, *424*, 285-292.
- (202) Choi, H.; Bise, R. T.; Hoops, A. A.; Neumark, D. M. *J. Chem. Phys.* **2000**, *113*, 2255-2262.
- (203) Banin, U.; Kosloff, R.; Ruhman, S. *Chem. Phys.* **1994**, *183*, 289-307.
- (204) Bohr, N. *Z. Phys.* **1923**, *13*, 117.
- (205) Schrödinger, E. *Naturwiss.* **1926**, *14*, 664.
- (206) Landau, L. D.; Lifshitz, E. M. *Quantum Mechanics: Nonrelativistic Theory*; 3rd ed. ed.; Pergamon Press: Oxford, 1977.
- (207) Averbukh, I. S.; Perelman, N. F. *Sov. Phys. Usp.* **1991**, *34*, 572-591.
- (208) Averbukh, I. S.; Perelman, N. F. *Physics Letters A* **1989**, *139*, 449-453.
- (209) Leahy, D. J.; Reid, K. L.; Zare, R. N. *J. Chem. Phys.* **1991**, *95*, 1757.
- (210) Reid, K. L.; Underwood, J. G. *J. Chem. Phys.* **2000**, *112*, 3643.
- (211) Shkrob, I. A.; Sauer, M. C. *Journal of Physical Chemistry B* **2001**, *105*, 7027-7032.